High-Resolution Water Isotope Records from West Antarctic Ice Cores: Interpretations of Climatic, Glaciological, and Diffusional Processes

by

Tyler Robert Jones

B.S. Civil Engineering, University of Colorado, 2006

M.S. Biogeochemistry, University of Colorado Boulder, 2010

A thesis submitted to the

Faculty of the Graduate School of the

University of Colorado in partial fulfillment

of the requirement for the degree of

Doctor of Philosophy

Environmental Studies Program

2015

This thesis entitled:

High-Resolution Water Isotope Records from West Antarctic Ice Cores: Interpretations of Climatic, Glaciological, and Diffusional Processes

written by Tyler Robert Jones

has been approved for the Environmental Studies Program

_____

Dr. James W. C. White

_____

Dr. Thomas M. Marchitto, Jr.

_____

Dr. Lisa Dilling

_____

Dr. Trevor Popp

_____

Date

The final copy of this thesis has been examined by the signatories, and we find that both the content and the form meet acceptable presentation standards of scholarly work in the above mentioned discipline.

Abstract

Jones, Tyler Robert (Ph.D., Environmental Studies)

High-Resolution Water Isotope Records from West Antarctic Ice Cores: Interpretations of Climatic, Glaciological, and Diffusional Processes

Thesis directed by Professor James W. C. White

To place current climate change in context, it is necessary to study geologic proxy records that extend beyond historical documentation. One such proxy is polar ice cores, which contain climatic information many thousands of years into the past. In East Antarctica, a ~700,000 year ice core record shows that Earth climate has shifted between glacial (cold) and inter-glacial (warm) conditions seven times, mirrored by atmospheric CO_2 concentrations. In Greenland, ~100,000 year ice core records show that climate has changed abruptly within years to decades. These long-term and short-term changes frame our understanding of the climate system, and allow for informed predictions about future climate change.

In this dissertation, we study a number of ice core records from West Antarctica. We first present a series of seven shallow ice cores from Siple Dome, West Antarctica. The shallow cores are used to investigate high-frequency variability in water isotopes (a proxy for local temperature and regional atmospheric circulation). Although the shallow cores span only 60 km, a microclimate effect causes distinct differences across the dome - an effect that should be considered in the interpretations of longer ice cores taken from coastal West Antarctic locations. We then shift focus to the analysis of an ultra-high resolution water isotope record from the inland West Antarctic Ice Sheet (WAIS) Divide ice core (WDC). This record was analyzed using

laser absorption spectroscopy, consists of over 24 million data points, and extends to 68,000 years before present. It is the highest-resolution and longest continuous ice core climate record ever recovered from Antarctica. A number of analyses are performed, including: 1) Quantification of diffusional processes, 2) Reconstruction of high-frequency decadal and sub-decadal oscillations, and 3) Analysis of low-frequency millennial-scale oscillations.

The results of the WDC water isotope study hold important insight into Antarctic climate patterns. The annual signal is found to trend with solar insolation over the last 10 thousand years. The strength of 2 to 15-year variability – which may originate as part of the El Niño Southern Oscillation (ENSO) in the tropical Pacific Ocean - exhibits distinct differences between the most recent glacial and interglacial periods. At the millennial-scale, variability appears to be partially driven by solar activity. A regular oscillation (of solar origin or otherwise) is evident in the water isotope record for the last 68 thousand years, and may hold clues to the initiation of abrupt climate change events documented in Greenland ice cores. Ultimately, the resolution of the WDC record allows for the assessment of climate change on the order of a presidential term (4 years) or less over most of the last glacial-interglacial cycle. More importantly, the results provide context for current and future anthropogenic climate change by defining natural variability in the past.

To my family

Acknowledgments

After spending many years working on the highly collaborative WAIS Divide ice coring project, it is exceptionally difficult to convey my gratitude to all the people who have helped me during my PhD. I'll try my best, but will undoubtedly fall short in my acknowledgments. Thank you… to my family for never ending support… to my advisor Jim White, for taking a chance on a guy who didn't know a lot, keeping science fun, being accessible, knowing how to simplify and tell a story, cultivating a creative intellectual spirit, helping me with my first teaching experiences, taking his shoes off in meetings and acting like one of the students, being the smartest person I know yet always remaining humble, making me a better scientist, affording me incredible opportunities, and most importantly, never giving up on me or any of his students… to my committee (in alphabetical order: Giff, Jim, Lisa, Tom, Trevor, and previously, Ben) for all the interactions and assistance over the years, whether in class, over email, on an ice sheet, or anywhere in between… to Bruce for being a lab wizard, a field expert, and a technical guru on all things related to ice coring, life, positivity, and beyond, plus sharing his knowledge of "survival" on the ice sheet, managing so many people so well, enjoying good coffee, and always having good stories to tell… to Valerie for being a science all-star, an excellent dancer, and the producer (with Bruce) of one of the best ice core records of all time… to all my lab mates (in alphabetical order: Amy, Andrea, Bruce, Caroline, Doc, Emily, Isaac, Jason, Jim, Owen, Sylvia, Valerie, Vas) for all the scientific help, funny lunches, and friendship… to Kurt Cuffey for kindly telling me my scientific poster at the 2013 WAIS meeting was fatally flawed, and then proceeding to help me with complicated mathematical formulae, sometimes explaining concepts multiple times, but always keeping our interactions kind and fun, many times sending pictures with his emails from far away places, and always having a good joke, the best of which is the

portrayal of his textbook *The Physics of Glaciers* at "actual size," stuck prominently to the side of a gigantic granite face… to Eric Steig for meeting in many time zones to discuss isotopic interpretations, hosting me at his lab multiple times, always making other people feel important, teaching with passion, and founding a really helpful science website called RealClimate… to Rebecca Safran for trusting me to be a co-teacher of *Climate Change Filmmaking*, my first experience as an instructor of record at the college level, and then being a friend… to the NSF for funding ice core research topics and making my PhD possible… to the WAIS Divide community for awesome yearly meetings, great science, and camaraderie… to the Centre for Ice and Climate in Denmark for hosting me multiple times, once at the NEEM ice core camp, and introducing me to varying Danish foods and customs… to the friendly lab dogs for always wagging their tails… to the fish in the tank by the fridge for being good pets… to INSTAAR for having a surfing polar bear logo and for being a fantastic institute for collaboration… to ENVS for teaching me about science, policy, and ethics, and more importantly, how to think about the world… to Boulder for keeping me healthy and grounded…

Table of Contents

Chapter 1

Introduction

1.1. Motivation for this Dissertation

The polar ice sheets contain a vast archive of geochemical information that can be utilized to understand Earth's past climate. One of the primary methods for studying paleoclimate in polar regions is the extraction of ice cores. Depending on the region, some ice cores can be more than 10,000 feet long – prompting the popular nickname "Two-Mile Time Machines" – and can date to over 700,000 years ago. Ice cores are particularly useful for high-resolution sampling over timescales relevant to humans, such as climatic changes that occur over the length of a presidential term, and can inform about temperature, atmospheric circulation, greenhouse gases, dust distribution, and many other physical processes. In general, ice cores define variability in the Earth climate system, which may be abrupt or gradual, and provide context for current and future anthropogenic climate changes.

The overall objective of this dissertation is to present high-resolution paleoclimate records of climate change as recorded by variations in water molecules from a number of West Antarctic ice cores. First, an array of shallow ice cores at Siple Dome is analyzed to determine the feasibility of interpreting high-frequency oscillations in coastal locations of

West Antarctica. Second, an inland deep ice core is analyzed at unprecedented sampling density and temporal-resolution due to relatively high snow accumulation rates and favorable ice sheet dynamics compared with other ice cores. The information contained in the inland ice core extends to ~60 ka bp, comprising ice recovered from the surface of the ice sheet to within meters of bedrock. An annually resolved dating scheme has been developed to ~29 ka bp, allowing for important time-based analyses spanning the glacial-interglacial transition and other important time-periods actively studied by the paleoclimate community.

The primary contributions of this research are: 1) An exploration of high-frequency signals and microclimate from seven shallow Siple Dome ice cores, located in a coastal location off the Ross Ice Shelf in West Antarctica; 2) The completion of the West Antarctic Ice Sheet Divide ice core (WDC) water isotope record to ~60 ka bp, which is the highest-resolution water isotope record recovered to date that includes Pleistocene ice (the record was analyzed on a new generation of continuous ice melting Cavity Ring-Down Laser Spectroscopy (CRDS) systems); 3) Analysis and modeling of water isotope diffusion at WDC to ~29 ka bp for interpretation of glaciological and paleoclimatic processes; and 4) The first continuous analysis of high-frequency oscillations (between 2-15 years) dating to ~29 ka bp, as determined from the WDC water isotope record.

1.2. Earth Climate in Context

For the last ~4 billion years of Earth climate history, the planet has alternated

between hothouse and icehouse conditions. A hothouse Earth (occurring 80% of the time) has no frozen water on land surfaces. One such hothouse occurrence was ~52-53 million years ago. During this time, Ellesmere Island in Canada's High Arctic (~79°N) shows evidence of lush swamp forests inhabited by turtles, alligators, primates, tapirs, and hippo-like Coryphodon in an ecological setting that never went below freezing (Eberle et al., 2010). This tropical-Arctic setting stands in stark contrast to the frozen (yet thawing) Arctic of today. Like present day Earth, icehouse conditions (occurring 20% of the time) arise when frozen water exists on land surfaces in the form of ice sheets. There is also some evidence to suggest that the Earth has been almost completely frozen in the deep past, similar to a "snowball" flying through space (Hoffman and Schrag, 2000).

The time period in Earth's past that is most relevant to our future as humans coincides with a grouping of hominin fossils from the species *Homo erectus*[1]. *H. erectus* appears in the fossil record about 1.9 million years ago, and because of its walking gate and bone structure, has been referred to as "Upright Man" (reviewed by Antón, 2003). So, putting billions of years of Earth climate history aside, our most recent upright ancestor appeared on Earth less than ~2 million years ago, and our evolutionary history is tied to the climatic conditions our ancestors experienced until present. The remainder of this introduction will focus heavily on the recent geologic past, with special emphasis on the ice core paleoclimate record extending to ~800 ka bp. Over this time period, human-like species evolved into *Homo Sapien*, meaning "Wise Man".

[1] A rough lineage of skulls related to human ancestors in temporal order includes:
1) Gorilla, 2) Australopithecus, 3) Homo erectus, 4) Neanderthal (La Chapelle aux Saints), 5) Steinheim Skull, and 6) Modern Homo sapiens.

1.2.1. Gradual Variations in Climate

Over millennial time scales, changes in the Earth's orbit, and consequent changes in solar energy input to Earth, cause global climate changes, which alter the face of the planet through growth and recession of ice sheets. For the last 800,000 years, ice core records from Antarctica reveal repeated glacial-interglacial cycles operating at 100ka intervals (Figure 1.1). Cold periods (glacial periods) persisted for ~90ka during each cycle and were interrupted by short ~10ka duration warm periods (interglacial periods). The pacing of glacial-interglacial transitions is related to variations in Earth's orbit. Small changes in the amount of insolation received in the northern latitudes (at about 65° north) causes snow to melt or persist throughout the summer months (Milankovitch, 1941), which can give rise to ice ages or cause ice to melt away. There are three important cyclical parameters that cause changes in insolation incident on Earth's surface, including: 1) The obliquity (tilt) of Earth's axis at 41ka cycles, 2) The precession of the equinoxes at 19 ka, 22 ka and 24 ka cycles, and 3) The eccentricity of Earth's orbit at 95 ka, 125 ka, and 400 ka cycles. In ice cores, a strong ~100ka cycle is related to eccentricity, although tilt and precession cycles are also evident.

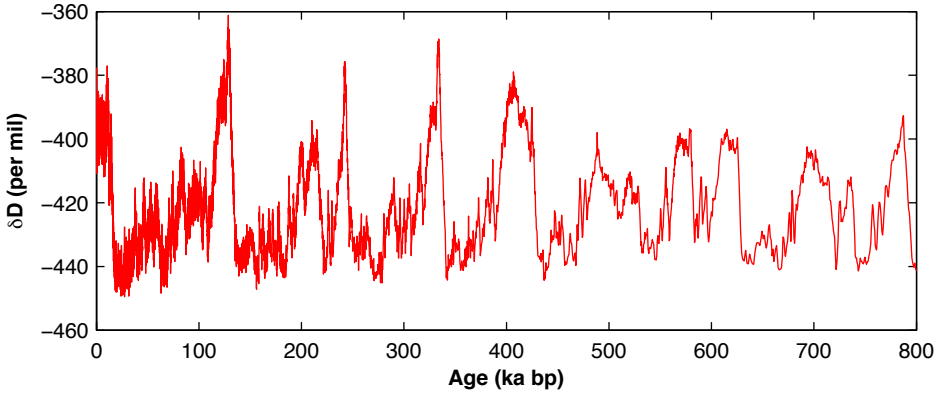

Figure 1.1. *A δD record from the European Project for Ice Coring in Antarctica Dome C (EPICA Dome C) ice core showing 800 ka of glacial-interglacial transitions. Less negative δD values correspond to warmer temperatures, while more negative δD values correspond to colder temperatures.*

1.2.2. Abrupt Climate Change

Superimposed on long-term orbital forcing, Greenland ice cores have revealed twenty-five abrupt climate warmings occurring during the last glacial cycle at roughly ~1.5 to 4.0 ka intervals. These abrupt climate changes are known as Dansgaard-Oeschger events (D-O events). During certain cold periods between D-O events, ice-rafted debris is evident in North Atlantic sediment cores at roughly ~5 to 10 ka intervals, known as Heinrich (H) events. During H events, large discharges of glaciers from the Hudson Bay region of Canada carried sediment into the North Atlantic, which eventually fell to the ocean floor as the icebergs melted (Bond and Lotti, 1995). Although DO and H events are evident in many global geologic records, neither are strictly periodic, nor do they occur linearly in time and space (Figure 1.2).

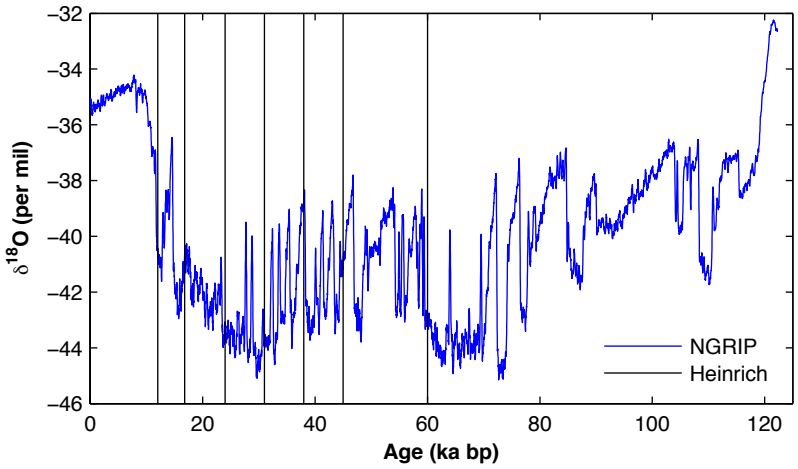

Figure 1.2. *The NGRIP ice core $\delta^{18}O$ record for the last 120 ka. Abrupt D-O warming events are evident during the last glacial period as less negative $\delta^{18}O$ excursions (North Greenland Ice Core Project members, 2004). Heinrich events are shown by the thin black lines, corresponding to times of elevated ice-rafted material in the DSDP 609 North Atlantic deep sea sediment core (Bond and Lotti, 1995).*

D-O events follow a characteristic evolution of abrupt initial warming, followed by gradual cooling, and terminated by rapid temperature decline back to full stadial conditions. However, not all D-O events behave the same way. For example, the duration of warm periods are variable, such as the length of D-O events 19 and 20, which are an order of magnitude longer than D-O events 3 and 4. Long D-O events are generally preceded by H events, such as D-O events 8 and 12 preceded by H events 4 and 5, respectively. The best studied abrupt climate changes occurred at the beginning and end of the Younger Dryas (YD) cold period (Figure 1.3). The YD began at ~12.7-12.8 ka bp and ended abruptly at ~11.5 ka bp (D-O event 0), during which time the northern hemisphere was affected by cold, windy and dry conditions (Alley, 2000). The first indication of the YD cold period came from fossil pollen of *dryas octapedula* (White Dryas) in late-glacial age peat layers from northern Europe. White Dryas is known to

grow in the cold Arctic tundra, and multiple pollen layers show that northern Europe alternated between boreal and tundra conditions. The pollen layers are named the Oldest Dryas, Older Dryas and Younger Dryas.

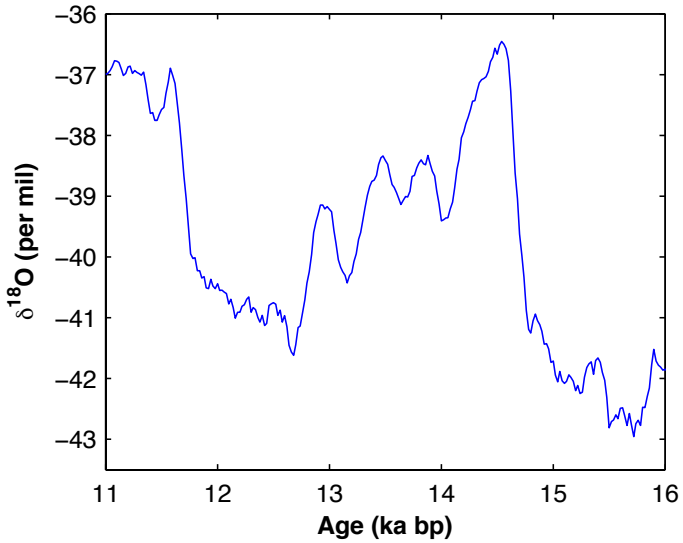

Figure 1.3. *Graph of the Younger Dryas (YD) as recorded in the NGRIP ice core $\delta^{18}O$ record. The YD was a cold period that began at ~12.7-12.8 ka bp and ended abruptly at ~11.5 ka bp. The preceding warm period centered at ~14.5 ka bp is known as the Bølling-*Allerød *(BA) interstadial. Notice the abrupt warming that ended the YD around ~11.5 ka (D-O event 0).*

Greenland ice cores at Camp Century (northwest Greenland) and Dye 3 (south central Greenland) were the first ice cores to confirm the YD climate reversal. Subsequent coring at GRIP and GISP2 (both in central Greenland) showed results were reproducible at adjacent coring sites. More recent coring at NGRIP (north central Greenland) and NEEM (northwest Greenland) show the YD signal was pervasive across the entire Greenland ice sheet.

1.2.3 The Younger Dryas

The most striking aspect of the YD was the abruptness with which it ended. At the YD termination (reviewed by Alley, 2000), the GISP2 ice core shows accumulation rates doubled in one to a few years and local temperatures increased 10±4°C (18±7°F) in several decades or less. That temperature change is analogous to moving from Arizona to Maine (based on statewide average temperatures from 1971-2000 as reported by the NOAA Climatic Data Center). In addition, data-driven modeling for central Greenland shows a factor of three decrease in sea-salt (theorized to be a proxy for wind-blown "frost flowers" from newly formed sea ice), a factor of seven decrease in calcium (proxy for dust from central Asia), and a factor of seven decrease in 3-10 micron dust (proxy for windiness). In the GRIP ice core, atmospheric methane concentrations increased from 475 ppbv to 750 ppbv (proxy for boreal, sub-tropical and tropical wetlands). Significant changes in atmospheric CO_2 concentrations did not occur in Greenland, although they are likely masked by orbital scale increases in CO_2 during the glacial termination. At the termination of the YD in the GISP2 ice core, warming proceeded in two-distinct steps over ~50 years and multi-parameter records show a series of five-year step changes (Taylor et al., 1997). In a high-resolution study of the NGRIP ice core, the final two abrupt warmings of the glacial period occurred in multiple ocean-atmosphere reorganizations (Steffensen et al., 2008).

1.2.4 Deciphering a Global Signal

Although the exact ~1,500 year quasi-cyclical forcing mechanism of D-O events

is still unexplained, the likely origin is either solar activity (Bond et al., 2001; Clement et al., 2001; Rahmstorf, 2003; Braun et al., 2005; Rial and Saha, 2009) or mechanisms internal to the Earth system (van Kreveld et al., 2000; Clark et al., 2001). Broecker (2003) and Clement et al. (2001) summarize North Atlantic and tropical abrupt climate change triggers (either solar or Earthly in origin), respectively. One theory suggests freshwater input to the North Atlantic triggers changes in the mode of the thermohaline overturning circulation (TOC), which alters northern/southern hemisphere heat budgets (termed the bipolar see saw by Broecker, 1998) and eventually causes global climate change. The other theory suggests that shifts in the tropical ocean-atmosphere system, such as in the regions where ENSO occurs, trigger widespread climate change. For either theory, a semi-cyclical causation mechanism must explain D-O and H events, such that immediate atmospheric impacts propagate globally.

Irrespective of a North Atlantic or tropical trigger, sudden freshwater additions to the North Atlantic after H and D-O events have been implicated in reductions of the TOC and increased sea ice formation (reviewed by Hemming, 2004). Atmospheric modeling studies show that when sea ice covers the North Atlantic, the tropical rain belt shifts southward (Chiang et al., 2003). Broecker (1998) categorizes the effects of pronounced sea ice formation in the North Atlantic: Europe would experience highly seasonal climate; increased snow cover in Asia would weaken or stop heat driven monsoons; atmospheric circulation, ocean currents and precipitation would change in the tropical regions; dampened climate affects would be seen in other far-field southern hemisphere locations; and warmings would occur in Antarctica due to the bi-polar see saw.

H events are thought to cause weakening or complete shutdown of TOC, whereas

D-O events only weaken the overturning (Broecker, 2006). As a result, H events likely cause greater equatorward extension of sea ice in the North Atlantic than do D-O events. More pronounced southward extension of sea ice results in a shift in the polar front and rain belts to lower latitudes. Due to these differences, the global extent and magnitude of D-O and H events, according to climate proxies, varies (Figure 1.4). In Greenland ice, D-O events are prominent, but H events do not appear significantly (Dansgaard et al., 1993). Conversely, Antarctic ice cores show warm events during H iceberg discharges and dampened D-O event signals (Blunier and Brook, 2001). In the Caribbean's Cariaco Basin, D-O events dominate (Peterson et al., 2000). In central Florida (Grimm et al., 1993) and eastern Brazil (Wang et al., 2004), only H impacts are evident. In other studies from the western Mediterranean (Cacho et al., 1999), the Arabian Sea (Altabet et al., 2002) and Chinese stalagmites (Wang et al., 2001), both D-O and H events appear, but H events tend to dominate.

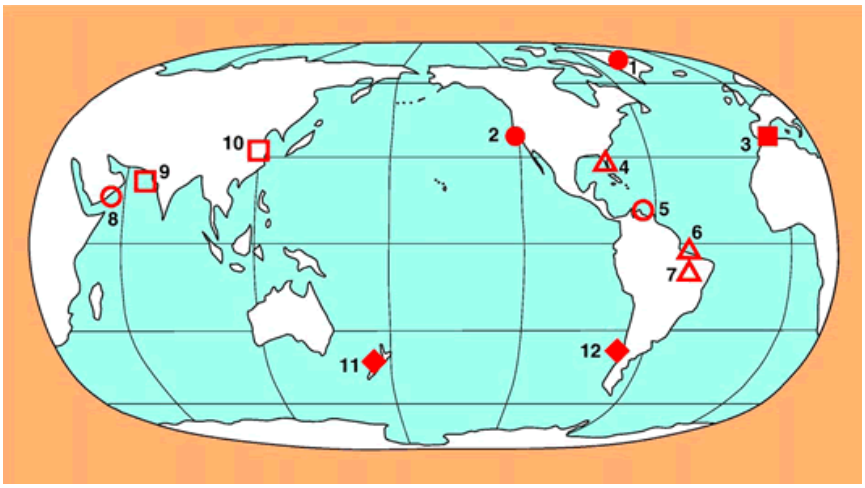

Figure 1.4. *Global extent of D-O and H events (Broecker, 2006). Records indicated by circles are dominated by D-O events; triangles by H events; squares by both D-O and H events, but the H events have a stronger signal; diamonds show sites in the southern hemisphere which appear to follow the deglacial pattern recorded in Antarctic ice rather than that recorded in Greenland ice; filled symbols show sites where the record appears to be dominated by temperature changes; and open symbols shows sites where rainfall changes appear to dominate.*

The sum of research has shown that D-O and H event appear globally in different geologic records, albeit in different ways relative to varying internal Earth processes. The exact cause of D-O event warming is currently unknown, but well studied with numerous explanatory mechanisms often implicating TOC. It is also unknown whether the trigger mechanism for these abrupt events occurs in the tropics or polar regions. However, more recent ice core research has shown that the Northern Hemisphere (i.e. the Arctic) leads the Southern Hemisphere (i.e. the Antarctic), lending evidence that freshwater forcing may be the trigger mechanism for abrupt climate change events (Buizert, 2015).

1.3. Human Civilization and Climate

Ice core research (and other geologic archives) have shown that natural variability related to Earth's orbit around the sun has dominated long-term paleoclimate, but also that abrupt climate changes occur regularly on timescales similar to a presidential term. These documented climate changes shaped human evolution, and played a central role in the rise and fall of human civilization. Humans can generally adapt to long-term change (i.e. change occurring over many generations of humans), but abrupt climate change (i.e. change occurring well within the span of a human lifetime) can have profound impacts on human civilization (summarized by de Menocal, 2001). Archeological evidence and climate proxies have been used to document the abrupt climate-related collapse of the Akkadian empire in Mesopotamia 4,200 years ago (Weiss et al., 1993), the Mayan civilization in central America 1,500 years ago (Gill, 2000; Hodell et al., 1995; 2005), and the Anasazian Indian culture of the American southwest 700 years ago (Axtell, et al., 2002). These collapses, while complex in nature, appear to be related by the onset of drought.

Similar abrupt climate change risk exists for current societies. In 2002, the Committee on Understanding and Monitoring Abrupt Climate Change (CACC) as part of the National Research Council (NRC) stated that human activities could trigger abrupt climate change (NRC, pg. 18, 2002). In a more recent report by the CACC (NRC, 2013), the authors find that abrupt climate changes are already happening on Earth. These include the disappearance of late-summer Arctic sea ice and increases in extinction threat for marine and terrestrial species. The 2013 report also defines an abrupt climate impact as "ongoing changes that, when certain thresholds are crossed, can cause abrupt impacts

for society and ecosystems." An example of an abrupt climate impact would be the slow rise of sea level eventually reaching a threshold that causes flooding in a subway system. This occurred in the New York subway during Hurricane Sandy in 2012.

The research on abrupt climate change has come full circle. Upon the astonishing discovery in the 1960's of 25 abrupt climate change events in Greenland ice cores, which many researchers originally doubted, we now find ourselves facing abrupt climate change and abrupt climate impacts occurring in our own time. The Intergovernmental Panel on Climate Change has stated in the 5th and final Assessment Report that "Human influence on the climate system is clear and growing, with impacts observed on all continents. If left unchecked, climate change will increase the likelihood of severe, pervasive and irreversible impacts for people and ecosystems" (IPCC, 2013). Indeed, much research points towards this outcome. In the coming decades, temperatures on Earth will exceed the range that most living species have experienced in at least the last 5 million years (NRC, 2013; Figure 1.5), which includes *H. Sapiens* – remember, our distant "upright" relative *H. Erectus* appears in the fossil record ~1.9 million years ago. Other research has found that a section of the West Antarctic ice sheet has reached a point of inevitable collapse, which would raise sea levels by three feet or more, perhaps over the next 200 years (Joughin et al., 2014, Rignot et al., 2014). Estimates of sea level rise from the IPCC range from 1.7 – 3.2 feet by 2100 under high-emissions scenarios (IPCC, 2013), a conservative estimate that hardly takes into account the onset of West Antarctic ice sheet collapse or potential accelerated melting in Greenland (Rignot et al., 2014). Under these scenarios, the near-future livability of major cities like Miami-Fort Lauderdale and New York City will change drastically or even cease to exist due to abrupt climate impacts

(Motta and White, 2014). There are many other examples of the potential future effects of climate change, most of which are summarized in the NRC (2013) report or the IPCC AR5 (2013) report.

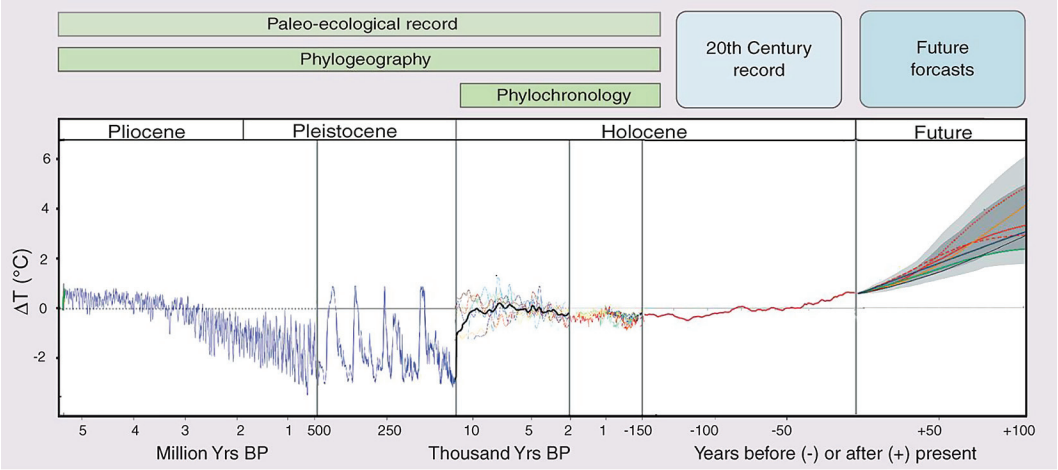

Figure 1.5. *Temperature reconstruction and future temperature projections on Earth. Note the varying timescales. In the near future, temperatures on Earth are expected to exceed those experienced by most living creatures at any point in the last 5 million years. Figure from Moritz and Agudo, 2013.*

So, the question now is how humans will respond in the face of overwhelming scientific evidence for anthropogenic climate change (and other issues like pollution and the overuse of resources) that threatens our civilization, most organisms, and all ecosystems. Some of the changes we will face may be too abrupt for adaptation, even with forward-looking policy. There are also ethical questions to consider, such as the fairness of limiting developing countries' greenhouse gas emissions or inter-generational equity for a livable world. Perhaps the inability of some humans to see long-term will be a major downfall for our future world, or perhaps human ingenuity and fairness will

overcome the status quo. Science should continue to inform ethical discourse and policy-making decisions. This dissertation is a very small, but extensively researched, extension of that goal.

1.4. Thesis Impetus

The remainder of this introduction chapter will focus on the science of water isotopes in ice cores, which are used primarily as a proxy for past near surface atmospheric temperature, atmospheric circulation, and sea surface temperatures in the moisture source regions supplying precipitation to an ice core location. To fully understand the water isotope record requires a diffusion correction. Diffusion occurs primarily in the upper ~70-90 meters of the ice sheet (known as firn) within a porous network of ice that allows for the movement of water molecules between solid and vapor phase. This process causes the higher-frequencies in the water isotope record to be dampened or eliminated relative to the original signal. An estimate of the original signal can be determined using spectral analysis (i.e. frequency analysis) techniques. The retrieval and sampling of ice cores, the measurement of water isotope values, diffusion correction, and paleoclimate interpretation are central to the research goals in this document. A partial emphasis is placed on climate analysis at timescales that matter to humans. We develop high-resolution ice core records from two locations in West Antarctica, including a coastal site and an inland site. The ice cores and associated research are explained below, while more in depth explanations are found in later chapters of this dissertation.

1.4.1. Siple Dome Ice Core

The Siple Dome ice core (SD) is located ~130 km east of the Siple Coast and Ross Ice Shelf in West Antarctica. SD was drilled as part of the West Antarctic Ice Sheet (WAIS) initiative managed by the National Science Foundation (NSF) Office of Polar Programs (OPP). Originally one of two deep WAIS initiative ice cores (the other being the inland and more elevated WAIS Divide), Siple Dome's coastal location in the Pacific sector of West Antarctica was selected in part to study regional climate signals. We evaluate a series of shallow ice cores drilled at sites across the dome to better characterize small-scale patterns in relationship with local climate variability. Ultimately, we assess the feasibility of long-term climate reconstruction using coastal ice core sites in West Antarctica. Drilling at Siple Dome was completed in January, 1999.

1.4.2. West Antarctic Ice Sheet Divide Ice Core

The WAIS Divide ice core (WDC) is located inland of SD and ~24 km from the ice flow divide in the Pacific sector of West Antarctica. The WDC was the second WAIS initiative core to be drilled, benefitting from advances in technology and a much larger synergistic effort across varying academic institutions, foundations, and planning offices. The WAIS Divide location was chosen due to favorable ice flow dynamics, individually identifiable annual layers dating into the last glacial period, and an ice accumulation rate sufficient to reduce the ice age-gas age difference to less than 500 years. We utilize a new continuous liquid water sampling system for analysis of the WDC, resulting in the

highest-resolution water isotope record yet recovered from the Antarctic continent. An annually dated chronology based upon layer counting, electrical conductivity, and ionic compounds extends to 29 ka bp. We correct the water isotope record for diffusion, determine diffusion lengths, and ultimately report on the first continuous high-frequency (i.e. 2-15 years oscillations) geologic record in Antarctica dating to 29 ka bp. A firn and deep ice diffusion model are used to understand the physical constraints of diffusion on the water isotope record. Drilling at WAIS Divide was completed in December, 2011.

1.5. Stable Water Isotopes as Climate Tracers

Stable isotopes are non-radioactive versions of the same chemical element, where each element exhibits the same number of protons but different numbers of neutrons. Water is composed of different stable isotopes including $^{1}H_{2}{}^{16}O$, $^{1}H^{2}H^{16}O$, and $^{1}H_{2}{}^{18}O$; all of which exist naturally in different amounts. The average abundance of hydrogen (^{1}H) and deuterium (D or ^{2}H) is 99.984% and 0.0156%, respectively, while the average abundance of oxygen-16 (^{16}O) and oxyegen-18 (^{18}O) is 99.763% and 0.1995%, respectively (Hoefs, 2004). The differing molecular weights and abundances cause about 1 out of every 500 water molecules to be of the heavier variety.

The partitioning of stable water isotopes between phase changes and within different hydrologic reservoirs is the fundamental basis for water isotope geochemistry. Due to differences in molecular weight, heavier isotopes prefer to exist in lower energy states during phase changes. In the ocean atmosphere system, evaporation causes water molecules containing ^{1}H and ^{16}O to preferentially, but not exclusively, evaporate from the

oceans relative to ^{2}H and ^{18}O, respectively. Likewise, condensation causes water containing ^{2}H and ^{18}O to preferentially precipitate from clouds, leaving ^{1}H and ^{16}O behind. The process of differential movement of stable isotopes is known as isotopic fractionation.

Isotopic fractionation of water molecules is expressed in delta notation (δ), which is defined as the parts per mil ($^{o}/_{oo}$) departure from a scientifically defined standard. For isotopes of water, Vienna Standard Mean Ocean Water (VSMOW) is used (defined as 0.00 $^{o}/_{oo}$). The δD or $\delta^{18}O$ values are expressed using the following equation:

$$\delta_{sample} = 1000\left[\left(\frac{R_{sample}}{R_{VSMOW}}\right) - 1\right] \quad (1)$$

where R is the ratio $^{18}O/^{16}O$ or $^{2}H/^{1}H$ in the sample or standard.

Deuterium and oxygen-18 concentrations generally covary in time and space. The relationship between δD and $\delta^{18}O$ of precipitation has been empirically determined to be:

$$\delta D = 8\,\delta^{18}O + 10 \quad (2)$$

where δD and $\delta^{18}O$ are derived from isotopes of water in rain and snow at varying locations on the Earth's surface (Figure 1.6), otherwise known as the Global Meteoric Water Line (GMWL; Craig, 1961).

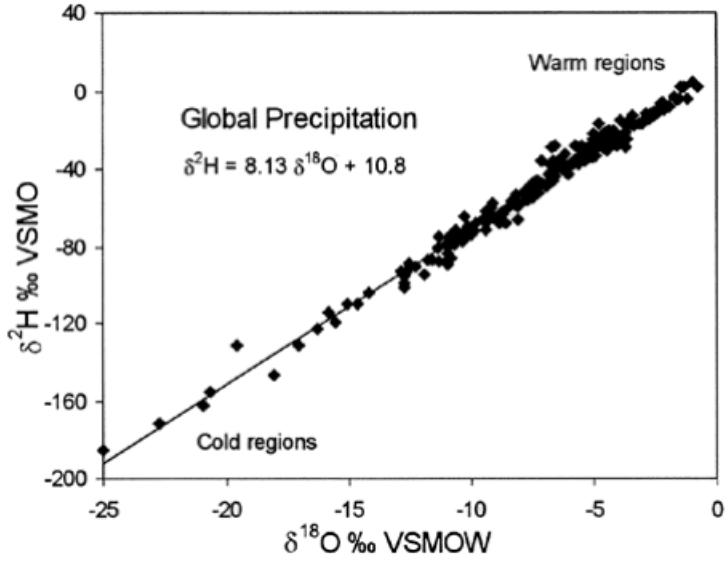

Figure 1.6. *Graph of the Global Meteoric Water Line (Clark and Fritz, 1997). Note the progression from warm regions (low latitudes) to cold regions (high latitudes).*

The isotopic composition of global meteoric water is strongly correlated with surface temperature (Dansgaard, 1964; Figure 1.7). The global correlation between $\delta^{18}O$, δD, and surface temperature has been empirically defined as:

$$\delta^{18}O = 0.69\ T_{average} - 13.6 \quad (3)$$

$$\delta D = 5.6\ T_{average} - 100 \quad (4)$$

where $T_{average}$ is the mean annual surface temperature at the collection site. In cold regions, the fractionation between water vapor and condensate is strongest, such that δD and $\delta^{18}O$ are more strongly depleted at high latitudes.

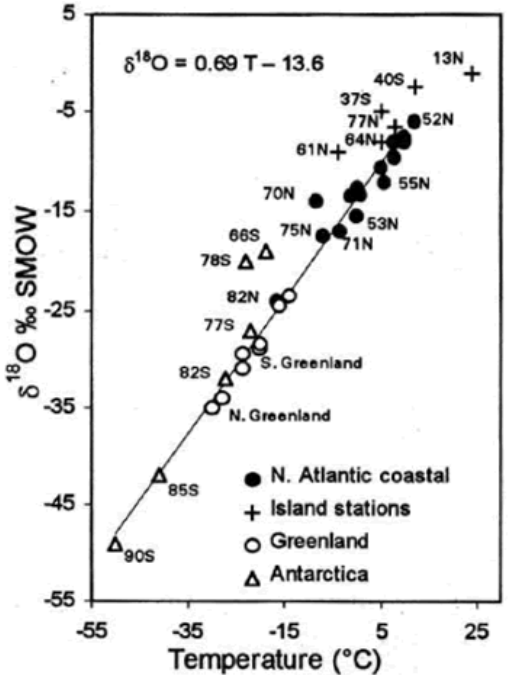

Figure 1.7. *Graph of the temperature vs. $\delta^{18}O$ relationship for precipitation (Clarke and Fritz, 1997). Note the values of $\delta^{18}O$ in Greenland and Antarctica are some of the most depleted.*

1.5.1. Rayleigh Distillation

Dansgaard (1964) describes a simple Rayleigh model to characterize condensation in open systems. For in-cloud processes, liquid water condenses in isotopic equilibrium with its parent vapor, and is then permanently removed from the system as precipitation. The Rayleigh expression is defined as:

$$\frac{\mathrm{R}}{R_i} = f^{(\alpha-1)} \tag{5}$$

where R is the isotopic ratio ($^{18}O/^{16}O$ or $^{2}H/^{1}H$), R_i is the initial ratio, f is the fraction of

vapor remaining in an air parcel, and α is an empirically defined fractionation factor between liquid and vapor (which is a function of temperature).

In a given parcel of air, the overall depletion of heavy isotopes is directly related to the fraction of vapor remaining, which itself is dependent on the temperature of the air column (Figure 1.8). When water vapor is cooled to its dew point, condensation occurs causing precipitation events, and consequently less water vapor is held in the parcel of air. As water vapor moves poleward, air temperatures progressively become colder causing additional precipitation events. At high latitudes, and after many precipitation events, a parcel of air becomes depleted in heavy isotopes, to an extent that can be directly linked to temperature on Earth.

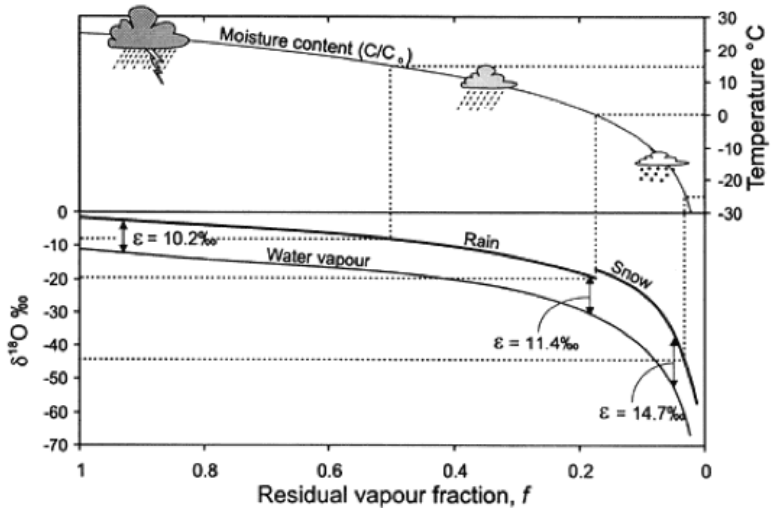

Figure 1.8. *Graph of the temperature vs. $\delta^{18}O$ relationship for precipitation (Clarke and Fritz, 1997). Note the values of $\delta^{18}O$ in Greenland and Antarctica are some of the most depleted.*

Merlivat and Jouzel (1979) further characterize an ideal model of isotopic fractionation during evaporation. Equilibrium fractionation, related to the bond strength formed by different water isotopes, occurs in a thin saturated boundary layer at the ocean-atmosphere interface. Kinetic fractionation, related to the diffusive speed of different water isotopes, occurs across an unsaturated transition zone near the ocean surface, which eventually becomes well mixed in the open-air column. If relative humidity in the transition zone is high, little or no kinetic fractionation occurs, and equilibrium processes dominate. However, evaporation processes at the ocean surface occur under non-equilibrium conditions, depleting the water surface and boundary layer of the more diffusive species (e.g. $^{1}H_{2}^{16}O$) and leaving the ocean reservoir enriched in heavy water isotopes (e.g. $^{1}H^{2}H^{16}O$ and $^{1}H_{2}^{18}O$).

A number of factors are known to affect Antarctic δ values, including: 1) Additional poleward evaporation and enrichment of isotopic signals in a parcel of vapor, which limits variability of over the ice sheets (Hendricks et al., 2000; Noone and Simmonds, 2002); 2) Katabatic winds that transport isotopically depleted inland snow towards the coast (Bromwich et al., 1993); 3) Additional kinetic isotopic fractionation during condensation of snow crystals in supersaturated air masses (Jouzel and Merlivat, 1984); 4) Changes in temperature and/or location of the primary moisture source region (Kavanaugh and Cuffey, 2003); 5) Intermittency and seasonality of precipitation (Jouzel et al., 1997); 6) Changes in the strength and/or height of the inversion layer (discussed in Blunier et al., 1998 and Kavanaugh and Cuffey, 2003); and 7) Drift of snow accumulation waves at oscillations between 2.5 and 100 years (Ekaykin et al., 2002). The SD and WDC water isotope records are likely affected by all of these factors, thus

being integrators of West Antarctic mean climate.

1.5.2. Deviation from Equilibrium Conditions

Deuterium excess (dxs) can be used as a proxy for conditions in the regions providing moisture to ice core sites. In general, changes in dxs result from sea surface temperature changes at the vapor source or a change in the vapor source location. To describe dxs, the GMWL can be written more generally as:

$$\mathrm{dxs} = \delta\mathrm{D} - 8\,\delta^{18}O \tag{6}$$

Kinetic effects associated with evaporation at the ocean surface control the dxs parameter (Dansgaard, 1964). For example, $^{1}H^{2}H^{16}O$ (mass of 19) will have a higher diffusivity rate than $^{1}H_{2}{}^{18}O$ (mass of 20), resulting in higher dxs values during deviation from equilibrium conditions.

The initial isotope concentration in an air parcel will have a dxs value that is a function of SST, relative humidity and wind speed (Jouzel and Merlivat, 1984). Relative humidity (RH) is the ratio of actual water vapor content in air to its total holding capacity at a given temperature (i.e. warmer air can hold more moisture). For a set water vapor content, RH will lower as temperature increases, since the warmer air can hold more water vapor. Under conditions of 100% RH (air saturated with vapor), diffusion between the atmosphere and the ocean is equal in both directions and no net kinetic fractionation occurs. However, when relative humidity is below saturation, diffusion from the ocean to

the atmosphere will occur, preferentially selecting the faster diffusing molecules of water.

When SST is warming (which corresponds to decreasing RH in the transition zone), dxs values will increase, whereas cooling SST (which corresponds to increasing RH in the transition zone) will produce lower dxs. High wind speeds will also lower the dxs value, since the transition above the ocean surface becomes more turbulent and less diffusive, meaning that mass differences in water molecules are unable to exert themselves through diffusion. Of the variables effecting dxs, studies have shown that SST is the primary determinant of dxs values in Greenland and Antarctic snow (Johnsen et al., 1989; Petit et al., 1991; respectively). In most cases, δ and dxs are anti-phased in Greenland and Antarctic ice cores, due to expansion or contraction of the polar front during coolings and warmings in polar regions, respectively.

1.5.3. Water Isotope Relationship to Temperature

Of particular importance when analyzing the isotopic record in ice cores is the δ-temperature relationship. The water isotope paleothermometer is derived from empirical measurements of the fractionation factor (α), which varies at different temperatures. For ^{18}O phase changes from water to vapor, α is defined as:

$$\alpha_{water-vapor} = \frac{\left(\frac{^{18}O}{^{16}O}\right)_{water}}{\left(\frac{^{18}O}{^{16}O}\right)_{vapor}} \tag{7}$$

Local temperature has been shown to reliably control the water isotopic composition in

accumulated snow, except in places where the δ-temperature relation changes over time and space (reviewed by Jouzel et al., 1997).

For Greenland precipitation, α is not constant through time, and other calibrations from borehole temperature profiles or nitrogen/argon thermal isotopic fractionation of trapped gases in the ice are necessary to resolve past temperature. For example, one study of $\delta^{15}N$ and $\delta^{40}Ar$ shows water isotopes underestimate temperature at NGRIP by a factor of two during D-O events 18, 19, 20, 23, and 24 (Landais et al., 2004). In Antarctica, δ values can reliably capture most temperature variations within (-)10% to (+)30% (Jouzel et al., 2003).

1.6. Dissertation Format

This doctoral dissertation comprises research related mainly to ice cores from West Antarctica. Four unique scientific papers are presented that have been or will be published in international peer-reviewed scientific journals. Each paper comprises a dissertation chapter. Chapter 2 is a reformatted version of a published paper while Chapters 3, 4, and 5 may undergo further refinement before publication. In the final chapter (Chapter 6), key findings are summarized, and a discussion is put forth for near-term future research. Many additional scientific research papers can result from the aggregate of this research.

1.7. References

Alley, R. B. (2000). The Younger Dryas cold interval as viewed from central Greenland. *Quaternary Science Reviews*, 19(1), 213-226.

Altabet, M. A., Higginson, M. J., & Murray, D. W. (2002). The effect of millennial-scale changes in Arabian Sea denitrification on atmospheric CO_2. *Nature*, *415*(6868), 159-162.

Antón, S. C. (2003). Natural history of Homo erectus. *American journal of physical anthropology*, 122(S37), 126-170.

Axtell, R. L., Epstein, J. M., Dean, J. S., Gumerman, G. J., Swedlund, A. C., Harburger, J., Chakravarty, S., Hammond, R., Parker, J., & Parker, M. (2002). Population growth and collapse in a multiagent model of the Kayenta Anasazi in Long House Valley. *Proceedings of the National Academy of Sciences of the United States of America,* 99(Suppl 3), 7275-7279.

Blunier, T., Chappellaz, J., Schwander, J., Dällenbach, A., Stauffer, B., Stocker, T. F., Raynaud, D., Jouzel, J., Clausen, H. B., Hammer, C. U., & Johnsen S. J. (1998). Asynchrony of Antarctic and Greenland climate change during the last glacial period. *Nature*, 394(6695), 739-743.

Blunier, T., & Brook, E. J. (2001). Timing of millennial-scale climate change in Antarctica and Greenland during the last glacial period. *Science*, *291*(5501), 109-112.

Bond, G. C., and R. Lotti (1995), Iceberg discharges into the North Atlantic on millennial time scales during the last glaciation, *Science*, 267, 1005–1010.

Bond, G., Kromer, B., Beer, J., Muscheler, R., Evans, M. N., Showers, W., Hoffman,S., Lotti-Bond, R., Hajdas, G., & Bonani, G. (2001). Persistent solar influence on North Atlantic climate during the Holocene. *Science*, 294(5549), 2130-2136.

Braun, H., Christl, M., Rahmstorf, S., Ganopolski, A., Mangini, A., Kubatzki, C., Roth, K., & Kromer, B. (2005). Possible solar origin of the 1,470-year glacial climate cycle demonstrated in a coupled model. *Nature*, 438(7065), 208-211.

Broecker, W. S. (1998). Paleocean circulation during the last deglaciation: a bipolar seesaw?. *Paleoceanography*, 13(2), 119-121.

Broecker, W. S. (2003). Does the trigger for abrupt climate change reside in the ocean or in the atmosphere?. *Science*, 300(5625), 1519-1522.

Broecker, W. S. (2006). Abrupt climate change revisited. Global and Planetary Change, 54(3), 211-215.

Bromwich, D. H., Carrasco, J. F., Liu, Z., & Tzeng, R. Y. (1993). Hemispheric atmospheric variations and oceanographic impacts associated with katabatic surges across the Ross Ice Shelf, Antarctica. *Journal of Geophysical Research: Atmospheres* (1984–2012), 98(D7), 13045-13062.

Buizert, Christo, et al. (2015). Precise interhemispheric phasing of abrupt climate change during the last ice age. *Nature*. Manuscript in press.

Cacho, I., Grimalt, J. O., Pelejero, C., Canals, M., Sierro, F. J., Flores, J. A., & Shackleton, N. (1999). Dansgaard‐Oeschger and Heinrich event imprints in Alboran Sea paleotemperatures. *Paleoceanography*, 14(6), 698-705.

Chiang, J. C., Biasutti, M., & Battisti, D. S. (2003). Sensitivity of the Atlantic intertropical convergence zone to last glacial maximum boundary conditions. *Paleoceanography*, 18(4).

Clark, I. & Fritz, P. (1997). *Environmental isotopes in Hydrogeology*. Lewis Publishers. New York.

Clark, P. U., Marshall, S. J., Clarke, G. K., Hostetler, S. W., Licciardi, J. M., & Teller, J. T. (2001). Freshwater forcing of abrupt climate change during the last glaciation. *Science*, 293(5528), 283-287.

Clement, A. C., Cane, M. A., & Seager, R. (2001). An Orbitally Driven Tropical Source for Abrupt Climate Change*. *Journal of Climate*, *14*(11), 2369-2375.

Craig, H. (1961). Isotopic variations in meteoric waters. *Science*, (133), 1702-3.

Dansgaard, W. (1964). Stable isotopes in precipitation. *Tellus*, 16(4), 436-468.

Dansgaard, W., Johnsen, S. J., Clausen, H. B., Dahl-Jensen, D., Gundestrup, N. S., Hammer, C. U., Hvidberg, C. S., Steffensen, J. P., & Bond, G. (1993). Evidence for general instability of past climate from a 250-kyr ice-core record. *Nature*, 364(6434), 218-220.

de Menocal, P. B. 2001. Cultural responses to climate change during the late Holocene. *Science* 292:667–73.

Eberle, J. J., Fricke, H. C., Humphrey, J. D., Hackett, L., Newbrey, M. G., & Hutchison, J. H. (2010). Seasonal variability in Arctic temperatures during early Eocene time. *Earth and Planetary Science Letters*, 296(3), 481-486.

Ekaykin, A. A., Lipenkov, V. Y., Barkov, N. I., Petit, J. R., & Masson-Delmotte, V. (2002). Spatial and temporal variability in isotope composition of recent snow in the vicinity of Vostok station, Antarctica: implications for ice-core record interpretation. *Annals of Glaciology*, 35(1), 181-186.

Gill, R. B. *The great Maya droughts: water, life, and death*. UNM Press, 2001.

Grimm, E. C., Jacobson Jr, G. L., Watts, W. A., Hansen, B. C., & Maasch, K. A. (1993). A 50,000-Year Record of Climate Oscillations from Florida and its Temporal Correlation. *Science*, 261(5118), 198-200.

Hemming, S. R. "Heinrich events: Massive late Pleistocene detritus layers of the North Atlantic and their global climate imprint." *Reviews of Geophysics* 42.1 (2004).

Hendricks, M. B., D. J. DePaolo, and R. C. Cohen (2000), Space and time variation of δ18O and δD in precipitation: Can paleotemperature be estimated from ice cores?, *Global Biogeochem. Cycles,* 14(3), 851–861

Hodell, D. A., Curtis, J. H., & Brenner, M. (1995). Possible role of climate in the collapse of Classic Maya civilization. *Nature*, *375*(6530), 391-394.

Hoffman, P. F., & Schrag, D. P. (2000). Snowball earth. *Scientific American*, *282*(1), 68-75.

IPCC, 2013: Climate Change 2013: *The Physical Science Basis. Contribution of Working Group I to the Fifth Assessment Report of the Intergovernmental Panel on Climate Change* [Stocker, T.F., D. Qin, G.-K. Plattner, M. Tignor, S.K. Allen, J. Boschung, A. Nauels, Y. Xia, V. Bex and P.M. Midgley (eds.)]. Cambridge University Press, Cambridge, United Kingdom and New York, NY, USA, 1535 pp.

Johnsen, S. J., Dansgaard, W., & White, J. W. C. (1989). The origin of Arctic precipitation under present and glacial conditions. *Tellus B*, *41*(4), 452-468.

Joughin, I., Smith, B. E., & Medley, B. (2014). Marine Ice Sheet Collapse Potentially Under Way for the Thwaites Glacier Basin, West Antarctica. *Science*, *344*(6185), 735-738.

Jouzel, J., & Merlivat, L. (1984). Deuterium and oxygen 18 in precipitation: Modeling of the isotopic effects during snow formation. *Journal of Geophysical Research: Atmospheres (1984–2012)*, *89*(D7), 11749-11757.

Jouzel, J., Alley, R. B., Cuffey, K. M., Dansgaard, W., Grootes, P., Hoffmann, G., Johnsen, S. J., Koster, R. D., Peel, D., Shuman, A., Stievenard, M., Stuiver, M., & White, J. (1997). Validity of the temperature reconstruction from water isotopes in ice cores. J*ournal of Geophysical Research: Oceans* (1978–2012), 102(C12), 26471-26487.

Jouzel, J., Vimeux, F., Caillon, N., Delaygue, G., Hoffmann, G., Masson‐Delmotte, V., & Parrenin, F. (2003). Magnitude of isotope/temperature scaling for interpretation of central Antarctic ice cores. *Journal of Geophysical Research: Atmospheres* (1984–2012), 108(D12).

Kavanaugh, J. L., & Cuffey, K. M. (2003). Space and time variation of δ18O and δD in Antarctic precipitation revisited. *Global Biogeochemical Cycles*, *17*(1).

Kreveld, S. V., Sarnthein, M., Erlenkeuser, H., Grootes, P., Jung, S., Nadeau, M. J., Pflaumann, U., & Voelker, A. (2000). Potential links between surging ice sheets, circulation changes, and the Dansgaard‐Oeschger Cycles in the Irminger Sea, 60–18 Kyr. *Paleoceanography*, 15(4), 425-442.

Landais, A., Barnola, J. M., Masson‐Delmotte, V., Jouzel, J., Chappellaz, J., Caillon, N., Huber, C., Leuenberger, M., & Johnsen, S. J. (2004). A continuous record of temperature evolution over a sequence of Dansgaard‐Oeschger events during Marine Isotopic Stage 4 (76 to 62 kyr BP). *Geophysical Research Letters*, 31(22).

Merlivat, L., & Jouzel, J. (1979). Global climatic interpretation of the deuterium‐oxygen 18 relationship for precipitation. *Journal of Geophysical Research: Oceans (1978–2012)*, *84*(C8), 5029-5033.

Milankovitch, M. *Kanon der Erdebestrahlung und seine anwendung auf das eiszeitenproblem*. *Königlich Serbische Akademie*, 1941.

Moritz, C., & Agudo, R. (2013). The future of species under climate change: resilience or decline?. *Science*, *341*(6145), 504-508.

Motta, R., & White, J. W. C. "A Tale of Two Cities: Miami, New York & Life on the Edge." *Climate Central*. Climate Central, 22 August 2014. Web. 05 January 2015. <http://www.climatecentral.org/news/sea-level-rise-miami-new-york-17925>.

Noone, D., & Simmonds, I. (2002). Associations between $\delta^{18}O$ of Water and Climate Parameters in a Simulation of Atmospheric Circulation for 1979-95. *Journal of Climate*, *15*(22), 3150-3169.

Noone, D. (2008). The influence of midlatitude and tropical overturning circulation on the isotopic composition of atmospheric water vapor and Antarctic precipitation. *Journal of Geophysical Research: Atmospheres (1984–2012)*,*113*(D4).

North Greenland Ice Core Project members. (2004). High-resolution record of Northern Hemisphere climate extending into the last interglacial period. *Nature*, v.431, No. 7005, pp. 147-151

NRC (National Research Council). 2002. *Abrupt Climate Change: Inevitable Surprises*. Washington, DC: National Academy Press.

NRC (National Research Council). 2013. *Abrupt Impacts of Climate Change: Anticipating Surprises.* Washington, DC: National Academy Press.

Peterson, L. C., Haug, G. H., Hughen, K. A., & Röhl, U. (2000). Rapid changes in the hydrologic cycle of the tropical Atlantic during the last glacial. *Science*, 290(5498), 1947-1951.

Petit, J. R., White, J. W. C., Young, N. W., Jouzel, J., & Korotkevich, Y. S. (1991). Deuterium excess in recent Antarctic snow. *Journal of Geophysical Research: Atmospheres* (1984–2012), 96(D3), 5113-5122.

Rahmstorf, S. (2003). Timing of abrupt climate change: A precise clock. *Geophysical Research Letters*, *30*(10).

Redman, C. L. (1978). *The rise of civilization: from early farmers to urban society in the ancient Near East*. San Francisco: WH Freeman.

Rial, J. A., & Saha, R. (2011). Modeling abrupt climate change as the interaction between sea ice extent and mean ocean temperature under orbital insolation forcing. *Abrupt Climate Change: Mechanisms, Patterns, and Impacts*, 57-74.

Rignot, E., Mouginot, J., Morlighem, M., Seroussi, H., & Scheuchl, B. (2014). Widespread, rapid grounding line retreat of Pine Island, Thwaites, Smith, and Kohler glaciers, West Antarctica, from 1992 to 2011. *Geophysical Research Letters*.

Steffensen, J. P., Andersen, K. K., Bigler, M., Clausen, H. B., Dahl-Jensen, D., Fischer, H., Goto-Azuma, K., Hansson, M., Johnsen, S. J., Jouzel, J., Masson-Delmotte, V., Popp, T., Rasmussen, S. O., Rothlisberger, R., Ruth, U., Stauffer, B., Siggaard-Andersen, M. L., Sveinbjornsdottir, A. E., Svensson, A., & White, J. W. (2008). High-resolution Greenland ice core data show abrupt climate change happens in few years. *Science*, 321(5889), 680-684.

Taylor, K. C., Mayewski, P. A., Alley, R. B., Brook, E. J., Gow, A. J., Grootes, P. M., ... & Zielinski, G. A. (1997). The Holocene-Younger Dryas transition recorded at Summit, Greenland. *Science*, 278(5339), 825-827.

Wang, Y. J., Cheng, H., Edwards, R. L., An, Z. S., Wu, J. Y., Shen, C. C., & Dorale, J. A. (2001). A high-resolution absolute-dated late Pleistocene monsoon record from Hulu Cave, China. *Science*, 294(5550), 2345-2348.

Wang, X., Auler, A. S., Edwards, R. L., Cheng, H., Cristalli, P. S., Smart, P. L., Richards, D. A., & Shen, C. C. (2004). Wet periods in northeastern Brazil over the past 210 kyr linked to distant climate anomalies. *Nature*, 432(7018), 740-743.

Weiss, H., Courty, M. A., Wetterstrom, W., Guichard, F., Senior, L., Meadow, R., & Curnow, A. (1993). The genesis and collapse of third millennium north Mesopotamian civilization. *SCIENCE-NEW YORK THEN WASHINGTON-*, 261, 995-995.

Chapter 2

Siple Dome Shallow Ice Cores: A Study in Coastal Dome Microclimatology[2]

Abstract

Ice cores at Siple Dome, West Antarctica, receive the majority of their precipitation from Pacific Ocean moisture sources. Pacific climate patterns, particularly the El Niño–Southern Oscillation (ENSO) and the Southern Annular Mode (SAM), affect local temperature, atmospheric circulation, snow accumulation, and water isotope signals at Siple Dome. We examine borehole temperatures, accumulation, and water isotopes from a number of shallow ice cores recovered from a 60 km north–south transect of the dome. The data reveal spatial gradients partly explained by orographic uplift, as well as microclimate effects that are expressed differently on the Pacific and inland flanks. Our analyses suggest that while an ENSO and SAM signal are evident at Siple Dome, differences in microclimate and possible post-depositional movement of snow makes climate reconstruction problematic, a conclusion that should be considered at other West Antarctic coastal dome locations.

[2] Jones, T. R., White, J. W. C., & Popp, T. (2014). Siple Dome shallow ice cores: a study in coastal dome microclimatology. *Climate of the Past*, 10(3), 1253-1267.

2.1. Introduction

The Siple Dome ice core was drilled as part of the West Antarctic Ice Sheet (WAIS) initiative managed by the National Science Foundation (NSF) Office of Polar Programs (OPP). Originally one of two deep WAIS initiative ice cores (the other being the inland and more elevated WAIS Divide), Siple Dome's coastal location in the Pacific sector of Antarctica was selected in part to study regional climate signals. In this study, we evaluate a series of shallow ice cores drilled at sites across the dome to better characterize small scale patterns in relationship with local climate variability as well as determine the feasibility of long-term climate reconstruction using coastal ice core sites in West Antarctica (WA).

2.1.1. Site Description

Siple Dome is located in WA on the Siple Coast at approximately 81°40'S and 148°49'W (Figure 2.1). The Siple Coast contains five major ice streams (A-E), which drain part of the WAIS, and is immediately adjacent to the Ross Ice Shelf. Siple Dome is located between ice streams C and D. Drill sites include two cores on the north flank of the dome facing the Pacific Ocean (E and G), three cores from the summit of the dome (B, C and D), and two cores on the south flank of the dome facing inland (H and F) (Figure 2.1). The maximum slope across the study area is relatively flat at 7.2 m/km. Table 2.1 summarizes the details for each ice core location.

Table 2.1.
The Siple Dome shallow ice core sites (B–H) and borehole temperature measurement sites (G, B, H, J) used in this study.

Site	Data Type	Latitude (degrees)	Longitude (degrees)	Length of ice record (years)	Bottom depth (m)
E	Ice	81°18.14'S	148d°18.14'W	1908–1995	20
G	Ice/temp	81°34.25'S	148°35.85'W	1917–1995	20
D	Ice	81°38.73'S	148°47.16'W	1901–1995	20
C	Ice	81°39.30'S	148°47.66'W	1836–1995	30
B	Ice/temp	81°39.53'S	148°48.72'W	1657–1995	54
H	Ice/temp	81°44.37'S	148°58.61'W	1898–1995	20
F	Ice	81°54.51'S	149°20.22'W	1872–1995	20
J	Temp	81°55.50'S	149°22.58'W		

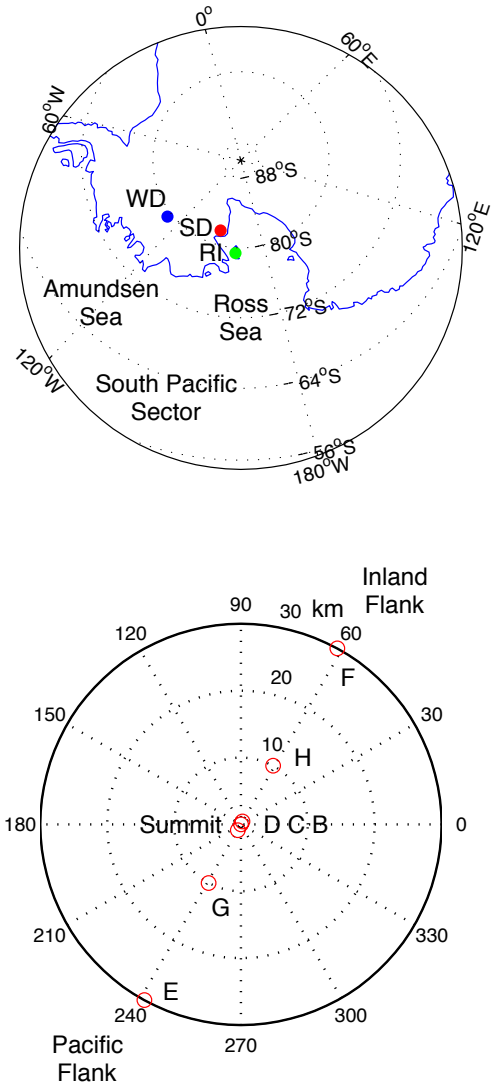

Figure 2.1. *Top panel: map of Antarctica centered on the Ross Sea region. The red dot is Siple Dome (SD), the blue dot is the WAIS Divide (WD), and the green dot is Roosevelt Island (RI). WD and RI are recently drilled ice cores in close proximity to Siple Dome. Bottom panel: local map of Siple Dome including grid locations of shallow ice cores B–H. The Pacific flank cores are to the north of the dome summit, and the inland flank cores are to the south of the dome summit.*

2.1.2. Antarctic Teleconnection

The Siple Dome region is centrally located to study all of the effects connected to the El Niño-Southern Oscillation (ENSO), the Southern Annular Mode (SAM), and the

Amundsen Sea Low Pressure Area (ASL). Previous studies have shown that teleconnected ENSO climate signals are pervasive across the Antarctic continent (Turner, 2004). In WA, ENSO has been shown to affect atmospheric circulation, local temperature, and snow accumulation (Delaygue et al., 2000; Bromwich et al., 2004; Guo et al., 2004; Schneider et al., 2004). A positive correlation exists between ENSO and the SAM during times of strong teleconnection (Fogt and Bromwich, 2006), such that the SAM Index expresses both high-latitude and tropical climate variability (Ding et al., 2012). In turn, the SAM influences the depth of the ASL, and both the location and depth of the ASL affects the climatology of the Ross Sea region and the interior of West Antarctica by influencing storm tracks (Turner et al., 2013).

Research by Hosking et al. (2013) shows that ~25% of variance expressed in the SAM index is related to ENSO variations. However, the exact location, phasing, and climate forcing of the ASL in relation to ENSO has been the topic of numerous studies. Turner et al. (2013) showed that the ASL is significantly deeper during La Niña as compared to El Niño, but the zonal location of the ASL is not statistically different during either ENSO phase. Bertler et al. (2006) showed that the ASL causes near surface temperature anomalies in the eastern Ross Sea, resulting in a net cooling during El Niño events and a net warming during La Niña events. Fogt and Bromwich (2006) found that positive SAM index years are more likely during strong La Niña years, while Bromwich et al. (1993) found a connection between katabatic surges over inland WA and across the Ross Ice Shelf during El Niño events.

2.1.3. Accumulation at Siple Dome

Satellite microwave observations at Siple Dome first suggested a north to south decrease in accumulation rates (Zwally and Gloersen, 1977). Subsequent studies by Bromwich (1988) concluded that orographic processes controlled the distribution of snow across Siple Dome from storms originating in the Ross and Amundsen Seas. Radar stratigraphy was later used to confirm a northward migration of the flow divide (Nereson et al., 1998), and modeling of the radar layer spacing at millennial resolution showed a 70% decrease in accumulation from north-south across the Dome (Nereson et al., 2000). A recent accumulation study derived from the analysis of beta radioactivity in shallow firn cores showed that accumulation is greatest 30 km N of Siple Dome and decreases by half at 30 km S, based on net accumulation averages from 1955-1997 (Hamilton, 2002).

2.1.4. Water Isotopes

To study the effects of ENSO, SAM, and the ASL at Siple Dome, we utilize water isotopes as a climate tracer. The isotopic composition of water molecules is expressed in delta notation (δ) relative to VSMOW using the following equation:

$$\delta_{sample} = 1000\left[\left(\frac{R_{sample}}{R_{VSMOW}}\right) - 1\right] \quad (1)$$

where R is the isotopic ratio $^{18}O/^{16}O$ or H^2/H^1 in the sample or VSMOW. The δD and $\delta^{18}O$ isotopic composition of precipitation is related to the temperature at which condensation occurs in a cloud (Dansgaard, 1964).

A number of factors are known to affect Antarctic δ values, including: 1) Additional poleward evaporation and enrichment of isotopic signals in a parcel of vapor, which limits variability of δ over the ice sheets (Hendricks et al., 2000; Noone and Simmonds, 2002); 2) Katabatic winds that transport isotopically depleted inland snow towards the coast (Bromwich et al., 1993); 3) Additional kinetic isotopic fractionation during condensation of snow crystals in supersaturated air masses (Jouzel and Merlivat, 1984); 4) Changes in temperature and/or location of the primary moisture source region (Kavanaugh and Cuffey, 2003); 5) Intermittency and seasonality of precipitation (Jouzel et al., 2007); 6) Changes in the strength and/or height of the inversion layer (discussed in Blunier et al., 1998 and Kavanaugh and Cuffey, 2003); and 7.) Drift of snow accumulation waves at oscillations between ~2.5-100 years (Ekaykin et al., 2002). Isotopes at Siple Dome are assumed to be affected by all of these factors, thus being an integrator of the region's mean climate.

2.1.5. This Study

For a typical ice core location, shallow ice cores are used to extract a common climatic signal and determine the amount of climatic variability. Ideally, a deep ice core location will not exhibit large-scale variability over short distances as determined by shallow ice cores. In this study, we analyze a series of seven shallow ice cores (B - H)

spanning a 60 km north-south transect of Siple Dome. Our measurements of water isotopes, borehole temperatures, and net accumulation rates span the years 1920-1995 for Cores C-H, as well as the years 1657-1995 for Core B (in the same location as the Siple Dome deep ice core). We use a number of methods to analyze the connection between water isotopes, net accumulation, and climate oscillations like ENSO and SAM, including time series analysis, principal component analysis, and cross wavelet transform. Our study shows that Siple Dome exhibits significant climate variability over the 60 km transect, and that a common climate signal cannot be extracted from the shallow ice cores for the time period in question (1920-1995). These results lead to important considerations for the interpretation of ice core records on coastal dome locations in West Antarctica.

2.2. Methods

2.2.1. Field and Laboratory

Siple Dome shallow cores B-H were drilled in the 1996-1997 field season to explore the spatial variability of various climatic and meteorological signals. Following extraction, these cores were analyzed for stable hydrogen and oxygen isotopes of water (Steig and White, 2003). The ice was sampled at the National Ice Core Laboratory (NICL) in Lakewood, Colorado and isotopically analyzed at the Institute of Arctic and Alpine Research (INSTAAR) Stable Isotope Lab (SIL) at the University of Colorado.

The SIL analyzed both δD and $\delta^{18}O$ values of water using SIRA Prism Micromass mass spectrometers. Hydrogen isotopic ratios were determined using an automated direct

injection uranium reduction system (Vaughn et al., 1998) with an uncertainty of ± 1.0 ‰. Oxygen isotopic ratios were determined with an automated version of the traditional CO_2/H_2O equilibration method (Epstein and Mayeda, 1953) with an uncertainty of ±0.1‰. The shallow ice cores were sampled at 5 cm increments, yielding sub-annual temporal resolution (approximately 2-6 samples per year) until the year 1920. High temporal resolution data for Core B extends as far back as 1657.

A depth-age dating scheme for the Siple Dome shallow ice cores was developed by Alley (2003). The dating of the ice cores was performed using visual stratigraphy on a light table over fluorescent tubes (after the core had been sectioned longitudinally). Indicators were used to determine how obvious dating choices were: 3=clear indication, 2=fair indication, and 1=poor indication. Even when the choice of a depth-age was not obvious, stratigraphy was 'forced' towards an expected value. For the age interval 1920-1995 (0 to ~17 meters), Core B, C, D, E, F, G, and H had sixteen poor indications, twenty-four poor indications, seven poor indications, twenty-three poor indications, nine poor indications, fourteen poor indications, and nine poor indications, respectively. For Core B at depths of 23-100 meters, two independent estimates of annual layer counting were conducted. Control group one counted 75 years while control group two counted 71 years, resulting in a difference of about 5%. Alley (2003) suggests that absolute accuracy is 10% or better for all shallow ice cores, meaning that from 1920-1995 the absolute dating may be off by about 4 years, or on average one wrong pick every ~19 years.

In this study, we employ a number of field and laboratory measurements for interpretation of the isotopic and net accumulation records. Twenty-meter borehole temperatures taken by Clow (1996) constrain the mean annual temperature and local

climate at Siple Dome. The borehole measurements were taken at a depth not influenced by seasonal fluctuations in surface temperature with an uncertainty of ±0.003°C. Borehole temperature data is not available for Core E on the North flank (Pacific facing) and Core F on the South Flank (Inland facing), so we estimate these values using the other known borehole temperatures and the local atmospheric lapse rate of 0.82°C/100m (Shimizu, 1964). Net accumulation rates were determined from the volume of snow per year in the ice core, based on the depth-age dating scheme by Alley (2003), and a 3rd order polynomial fit of one-meter density measurements taken by Lamorey (2003). The polynomial fit introduces less than a 0.1% error to the known one-meter density measurements, while the densities in between are interpolated. The uncertainty of net accumulation is then dependent on the depth-age dating scheme. The standard error of the net accumulation mean for Core E, G, D, C, B, H, and F is 0.2, 0.2, 0.3, 0.2, 0.2, 0.2, and 0.2 cm yr^{-1} ice eq., respectively. All local climate information, including elevation, borehole temperatures, net accumulation, and water isotopes, is shown in Table 2.2.

Table 2.2.
Siple Dome shallow ice core data summary. The δD, δD standard deviation (SD), net accumulation, and net accumulation standard deviation values pertain to the time period 1920–1995.

Site	Location (km)	Elevation (m a.s.l.)	Borehole Temp. (°C at 20 m depth)	δD (per mil)	δD SD (per mil)	Net Accum. (cm yr^{-1} ice eq.)	Net Accum. SD (cm yr^{-1} ice eq.)
E	30N	400		−199.1	16	11.7	3.6
G	10N	590	−24.79	−202.4	14.8	13.4	4.2
D	1N	615		−205.4	13.9	11	4.4
C	0	615		−203.0	14.1	11.2	3.1
B	0.5S	615	−25.12	−202.3	13.9	11.1	3
H	10S	590	−25.33	−207.5	13.8	9.3	2.9
F	30S	450		−220.2	11.2	8.2	3.1
J	32S	435	−24.22				

2.2.2. Data and Procedures

We compare δD to the Niño3.4 Index (Niño34), the Southern Annular Mode Index (SAM Index), and the ASL Actual Central Pressure Index (ASL Index). Niño34 is a proxy for sea surface temperatures (SST) in the region of the tropical Pacific bounded by 120°W-170°W and 5°S- 5°N (Trenberth, 1997). Niño34 provides a reliable record of ENSO dating back to 1950. The SAM Index is defined as the leading principal component of 850 hPa geopotential height anomalies poleward of 20°S (Thompson and Wallace, 2000), providing a short record of opposing pressure anomalies centered in the Antarctic near 40°S to 50°S. The SAM Index provides a reliable record dating back to 1979 and is a leading mode of climate variability in the high southern latitudes. The ASL Index describes the monthly and seasonal variability of the ASL relative central pressure

and location reconstructed from ERA-Interim Reanalyses dating back to 1979 (Hosking et al., 2013). The ASL Index is strongly correlated ($p < 0.01$) to the SAM for all seasons. Due to the strong correlation, we choose to use the SAM Index (rather than the ASL Index) throughout the rest of this paper for comparison to Siple Dome shallow ice cores.

Frequency analysis of the water isotope records was performed using a crosswavelet (XWT) coherence Matlab package (Grinsted, 2004 and Torrence and Compo, 1998). The XWT changes one-dimensional time series into time-frequency space, creating a two dimensional image of cross-modal variability and phase lag through time. The wavelet power is based on a red noise background spectrum. In our analysis, we place emphasis on the δD of Core B (δD_B), the longest shallow ice core (dating to 1657), which was drilled in the same location as the deep Siple Dome ice core.

2.3. Results and Discussion

2.3.1. Net Accumulation

Previous modeling at 1,000 to 10,000 year timescales shows asymmetry in Siple Dome north-south accumulation existed for many thousands of years into the past (Nereson et al., 2000). Our study confirms these findings at smaller and more recent timescales, and we find agreement with other near-term accumulation studies on Siple Dome. Table 2.3 shows a comparison of net accumulation rates from 1955-1995 found by Hamilton (2002) in comparison to this study. Hamilton (2002) used detection of elevated levels of gross beta radioactivity at the 1955 bomb testing reference horizon to infer averaged accumulation rates, whereas we use an estimation of net accumulation

based on depth-age dating and density profiles. Uncertainty of net accumulation measurements in the Hamilton (2002) study was determined using density profiles from snow pits and submergence-velocity, or the "coffee-can" technique. This method entails repeat GPS surveys over a 3-year period of markers installed at 5 to 20 meters depth in the firn, which are used to quantify measurement repeatability and the steadiness of firn densification and accumulation rate. Hamilton (2002) assigned a maximum uncertainty on net accumulation measurements of about 1.4 cm yr^{-1} ice eq. In this study, the standard error of the net accumulation mean (1955-1995) for each ice core varies between 0.3 - 0.4 cm yr^{-1} ice eq., and the overall uncertainty would depend on the accuracy of the depth-age scale, the accuracy of one-meter density measurements, and alteration of the original signal due to post-depositional processes (discussed by Fisher et al., 1985 and Frezzotti et al., 2007).

Table 2.3.
Comparison of Siple Dome net accumulation rate studies from 1955 to 1995, expressed as water equivalents. The standard deviation of net accumulation is also shown for this study. The Hamilton (2002) study standard deviation is not available because the data is not a time series, but rather a long-term average based on the 1955 bomb testing reference horizon.

Site (Distance from the divide)	Hamilton (2002) (cm yr^{-1} ice eq.)	This Study (cm yr^{-1} ice eq.)	This Study SD (cm yr^{-1} ice eq.)
30 km N	15.5		4
10 km N	14	13.4	4.5
0 km	12.1	11.2	3.1
10 km S	10.4	9.3	2.7

Hamilton (2002) accumulation values differ with this study by about ~25% at 30 km N and 20% at 10 km S, whereas the other locations differ by 4% or less. The net accumulation values may differ due to differences in geographic measurement locations, uncertainty in the depth-age dating scheme used in this study, post-depositional processes, or varying methodologies for calculating the density profile. In this study, we find that the standard deviation of net accumulation between 1955-1995 for each ice core site varies between 2.7 to 4.5 cm yr^{-1} ice eq. (Table 2.3). The highest net accumulation value occurs at 10 km N, suggesting that increased Pacific Flank accumulation rates (and northward migration of the Dome) persisted towards the present at sub-centennial timescales. It is not clear why net accumulation is greatest at 10 km N (Core G) and not 30 km N (Core E). One possibility is that the area around Core E is not cold enough to allow local condensation, which instead occurs further inland, at higher elevations. A second possibility is that an inversion layer forms during certain parts of the year at Siple Dome, which tends to cap air masses, and eventual precipitation, at elevations above Core E. A final possibility is that surface winds move snow after deposition, producing uneven loading due to Dome topography. The time series of net accumulation and water isotopes are shown in (Figure 2.2).

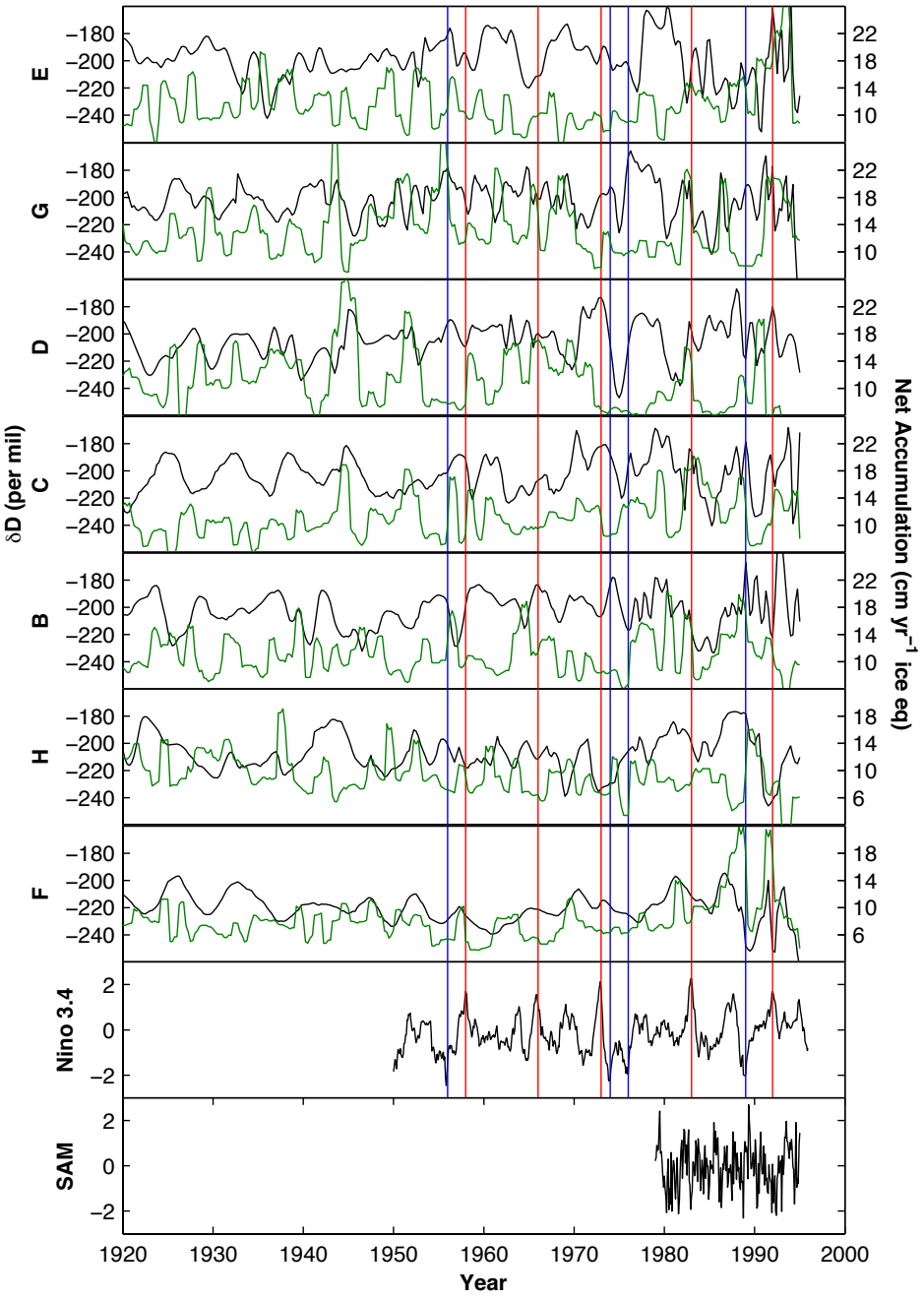

Figure 2.2. *Siple Dome shallow ice core D (black lines) and net accumulation records (green lines). The Niño 3.4 and SAM indexes are also shown. Strong El Niño years (red lines) and strong La Niña years (blue lines) are defined as 5 consecutive months greater than or less than 1.5°C sea surface temperature anomalies for the Niño 3.4 region, respectively.*

2.3.2. Borehole Temperatures

Shallow 20 m borehole temperature observations (uncertainty of ±0.003°C) reveal two distinct temperature gradients across Siple Dome, including a cold regime on the Inland Flank and a warmer regime on the Dome Summit and Pacific Flank (Figure 2.3). The borehole temperature at Core G (10 km N) relative to Core B (0.5 km S) falls within 0.13°C from that expected by the local atmospheric lapse rate of 0.82°C/100m (Shimizu, 1964). The borehole temperature at Core J (32 km S) relative to Core H (10 km S) is colder by 0.05°C than would be predicted by the local adiabat.

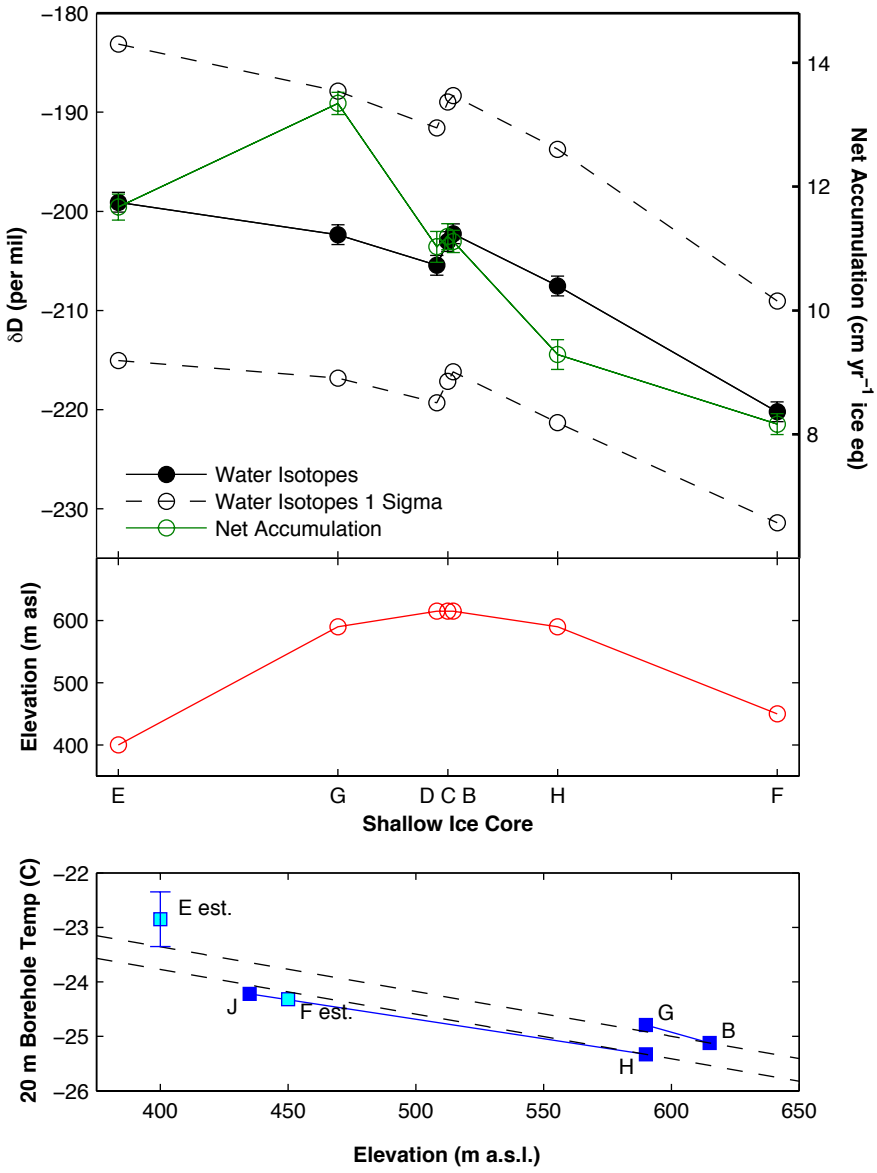

Figure 2.3. *Top panel: shallow ice core mean δD (solid black line, uncertainty bars attached), δD standard deviation (black dashed line), and mean net accumulation (solid green line, standard error bars attached) on Siple Dome from 1920 to 1995. Middle panel: the elevation profile of shallow ice cores at Siple Dome. Bottom panel: shallow 20m borehole temperatures recorded at Siple Dome. Dark blue squares denote temperature measurements. Blue lines designate temperature trends. Dashed black lines designate adiabats (0.82°C/100m). No borehole temperature was taken in the vicinity of core E (30 km north) or core F (30 km south). These temperature values (light blue squares) are estimated using adiabats and temperature trends.*

We estimate borehole temperature values at Core E and Core F relative to the local atmospheric lapse rate and the borehole temperature measurement trends between sites G to L and J to H, respectively. For Core E (30 km N, 400 m a.s.l.), we estimate a temperature range of -23.23 to -22.28°C. For Core F (450 m a.s.l.), we estimate a value of -24.32°C. We find a temperature difference between 30 km N and 30 km S of about 1.09-2.04°C. If the temperature trend on the Inland Flank is extrapolated to 400 meters a.s.l. using the atmospheric lapse rate, the difference in temperature at 400 m a.s.l. between the Pacific and Inland Flank would be about 0.7-1.6°C. The difference in temperatures suggests variable forcing mechanisms acting on either side of the Dome that could influence the water isotope and net accumulation records. We discuss this concept later in the paper.

2.3.3. Water Isotopes

If we assume that near-surface temperature is controlling water isotopes at Siple Dome, then we would expect a linear δ-temperature (δ-T) relationship. This is not the case. We test the δ-T relation by using an Antarctic correlation of 6.34‰ ± 0.09‰ per 1°C (Masson-Delmotte et al., 2008). There is not enough information to construct a local δ-T spatial slope at Siple Dome, but for this study an estimate of the slope will suffice.

The temperature difference range between Core B (Dome) and Core E (Pacific) is estimated to be 1.89-2.84°C, which corresponds to δD expected isotope depletions on the Dome Summit of about 12.0‰ -18.0‰, respectively. However, the actual difference between δD_B and δD_E is only 3.2‰ (Figure 2.3), meaning that the water isotopes are too

heavy on the Dome Summit in relation to elevation-based temperature estimates at Core E. The δ-T discontinuity is more pronounced on the Inland Flank. The borehole temperature estimate at Core F (Inland) is warmer than Core B (Dome), suggesting that water isotopes should be heavier at Core F (Inland). In fact, the isotopes are significantly depleted compared to Core B by -17.9‰ (Figure 2.3). These discrepancies show that a linear δ-T relation is too simplistic to explain climate at Siple Dome over the time period 1920-1995.

2.3.4. δD Standard Deviation

Siple Dome shallow ice cores show a relatively linear decrease in δD standard deviation from north to south. At 30 km N, the water isotope signal is amplified with a standard deviation of 16.0‰, whereas at 30 km S the water isotope signal is dampened with a standard deviation of 11.9‰. The loss of signal moving southward across the Dome can be related to a number of contributing factors, including: 1) Erosion of the original summer-winter water isotope signal due to diffusion in the firn (Cuffey and Steig, 1998). For example, shallow ice core sites with low accumulation (i.e. Core F, Inland) would have more pronounced diffusion and a smaller standard deviation than an ice core site with high accumulation (i.e. Core E, Pacific). 2) Interannual variations in climate that can be more or less pronounced over a certain time period and which may have different effects on each shallow ice core site. For example, the Pacific Flank and Dome Summit may experience more storm systems on average taking a direct path from the Ross and Amundsen Seas (i.e. less snow events leading to an amplified δD signal and

high standard deviations), while the Inland Flank could experience more storm systems on average that follow an indirect cross-continental route (i.e. more snow events leading to a dampened δD signal and low standard deviations). 3) Intermittency of precipitation at a given shallow ice core site relative to other sites, such as the seasonality of precipitation discussed by Jouzel et al. (2007). 4) Variations in net accumulation and water isotopes related to post-depositional processes. For example, the dampened inland water isotope signal at Core F may be related to katabatic winds traveling from inland WA towards the coast (Bromwich et al., 1993). The cold katabatic winds would tend to sink and flow along the valleys towards the coast, bringing isotopically lighter wind blown snow with low δD standard deviation from higher elevations in the interior of Antarctica.

2.3.5. Principal Component Analysis

Principal Component Analysis (PCA) was performed using all seven shallow ice core δD records (Figure 2.4). The first five components of the PCA explain 22%, 17%, 16%, 14%, and 13% of the total δD variance. This suggests that multiple processes control the stable isotopes of snow, and importantly that no single process dominates. The bi-plot of component 1 vs. component 2 shows vector representations of the coefficients of the δD records on the first two principal components. For component 1 on the vertical axis, Core F and Core H (Inland) have negative coefficients, whereas Cores E, G, D, C, and B (Pacific and Summit) have positive coefficients. Component 1 shows a fundamental difference in Pacific and Summit δD records versus Inland δD records, an

occurrence that we also see in borehole temperature measurements and discrepancies in water isotopes. For component 2 on the horizontal axis, Core B and Core E have negative coefficients, and Cores G, C, D, H, and F have positive coefficients. It is unclear why Core B and Core E would be unique in component 2. Perhaps the differences arise during post depositional processes resulting from oscillations in snow waves on the surface of the ice sheet (Ekaykin et al., 2002) or by some other unknown forcing.

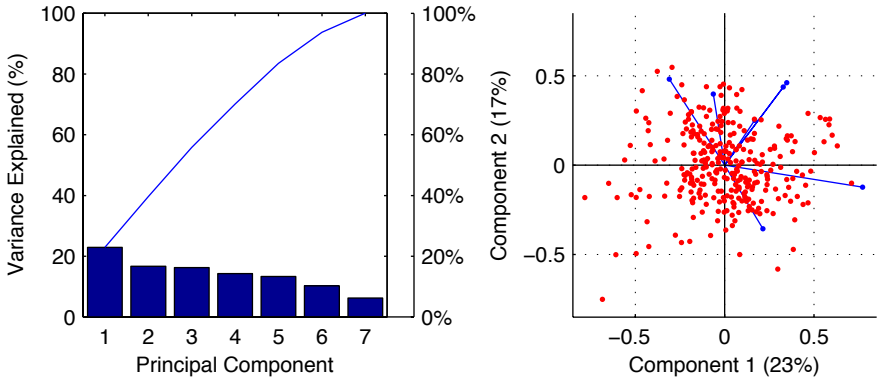

Figure 2.4. *Left panel: principal component analysis of the Siple Dome shallow ice core D records. Right panel: biplot of component 1 vs. component 2.*

Some correlation exists between certain principal components and the Niño34 and SAM Indexes (Figure 2.5). The SAM Index and PC3 are significantly correlated (p-value < 0.05) with an R-value of 0.25. The Niño34 Index and PC5 are significantly correlated (p-value < 0.05) with an R-value of 0.19. These results suggest ENSO and SAM have a role in the water isotope signal at Siple Dome, but PC1, PC2, and PC4 exhibit additional complexity that is not readily explained.

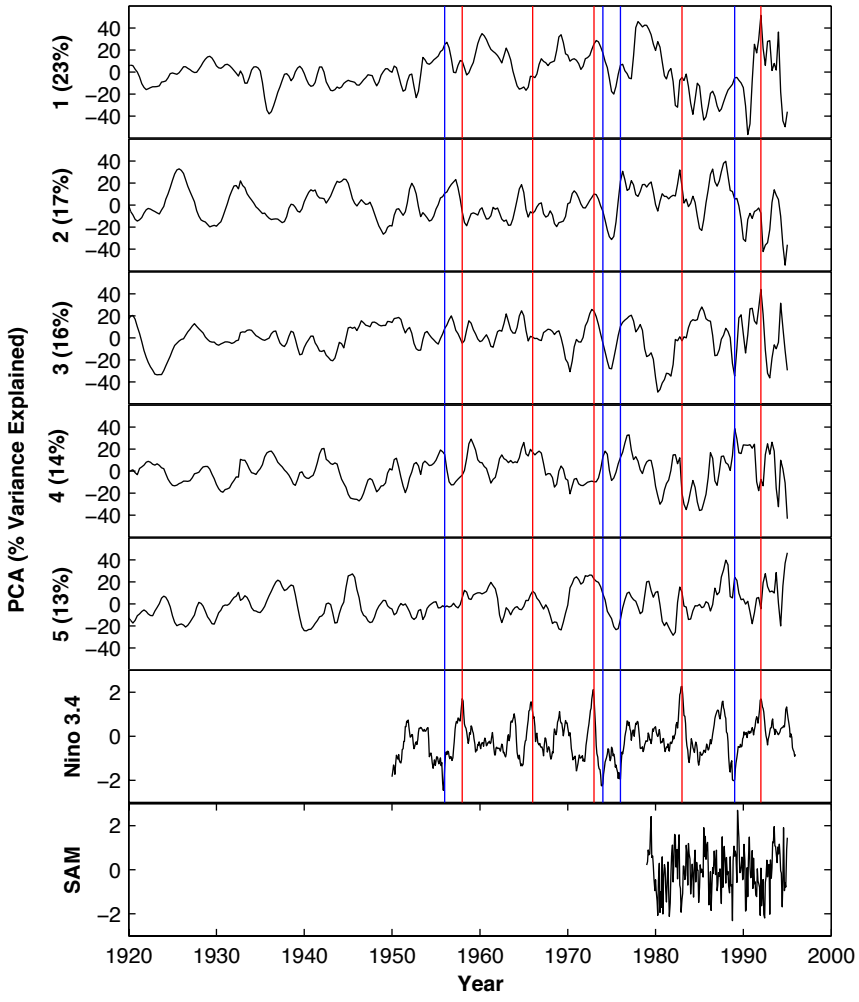

Figure 2.5. *The first 5 principal components of the shallow ice core δD records are compared with the Niño 3.4 and SAM indexes. Strong El Niño years (red lines) and strong La Niña years (blue lines) are defined as 5 consecutive months greater than or less than 1.5°C sea surface temperature anomalies for the Niño 3.4 region, respectively.*

2.3.6. Time Series Analysis

We compare time series records of net accumulation and water isotopes using correlation matrices (Table 2.4). We find that none of the net accumulation or water isotope time series correlate amongst themselves. For example, Core C (0 km) and Core B (0.5 km S) are only separated by 0.5 km, yet the correlation values for C vs. B net

accumulation and C vs. B water isotopes are -0.05 and 0.09, respectively. The Pearson values for these correlations are insignificant ($p > 0.05$). The most correlated net accumulation time series (significant p-value < 0.05) are Core E (30 km N) and Core F (30 km S) with an R-value of 0.26. The most correlated water isotope time series (significant p-value < 0.05) are Core E (30 km N) and Core C (0 km) with an R-value of 0.20. Neither correlation implies causation.

Table 2.4.
Siple Dome correlation matrix for shallow ice core water isotope δD time series (bottom left of matrix) and net accumulation (top right of matrix). Values with a star indicate significant Pearson's correlation values of less than 0.05. Only similar time series should be interpreted from the table (i.e. acc with acc and iso with iso, but not acc with iso).

	E acc	**G acc**	**D acc**	**C acc**	**B acc**	**H acc**	**F acc**	
E iso	–	0.04	−0.09	0.08	−0.02	−0.02	0.26*	**E acc**
G iso	0.13*	–	0.06	0.06	−0.12*	−0.17*	−0.03	**G acc**
D iso	0.02	0.13*	–	0.04	−0.01	0.13*	−0.08*	**D acc**
C iso	0.20*	0.05	0.09	–	−0.05	−0.18*	0.19*	**C acc**
B iso	0.09	0.04	−0.11	0.09	–	−0.05	0.19*	**B acc**
H iso	−0.20*	−0.02	−0.09	0.05	−0.03	–	−0.15	**H acc**
F iso	−0.05	0.08	−0.13*	0.18*	−0.22*	0.19*	–	**F acc**
	E iso	**G iso**	**D iso**	**C iso**	**B iso**	**H iso**	**F iso**	

It is counterintuitive that shallow ice cores so closely separated would have such differing net accumulation and water isotope histories. Assuming precipitation rates are the same at the time of deposition between sites C and B, post-depositional processes (i.e. snow waves or wind loading) may be altering the net accumulation signal. If post depositional processes in fact change net accumulation, then a similar outcome would be

expected for the water isotope records, which we observe. To achieve a coherent record amongst the shallow ice cores, the water isotope signals would have to be smoothed, which would reduce or eliminate yearly, bi-yearly, decadal, and sub-centennial oscillations.

We also compare time series records of net accumulation and water isotopes to the Niño34 and SAM Indexes (Figure 2.2). We define strong El Niño years (red lines) and strong La Niña years (blue lines) as 5 consecutive months greater than or less than 1.5°C sea surface temperature anomalies for the Niño34 region, respectively. We find that both water isotope and net accumulation shallow ice core records do not share a common signature with any of the strong ENSO events. Individual time series correlation values for both water isotopes and net accumulation versus either Niño34 or SAM vary within about -0.30 to 0.30 (Table 2.5). Most time series correlations are insignificant ($p > 0.05$). Some portions of the time series go into and out of phase with the Niño34 or SAM Indexes, so correlation is higher for certain parts of the record and lower for others.

Table 2.5.
Siple Dome correlation values for both water isotope δD and net accumulation versus either Niño34 or SAM. Values with a star indicate significant Pearson's correlation values of less than 0.05.

-	E iso	G iso	D iso	C iso	B iso	H iso	F iso
Niño34	−0.12	−0.1	0.08	0.12	0.01	−0.13	0.11
SAM	−0.05	0.09	0.17	0.01	−0.28*	−0.04	−0.16
-	**E acc**	**G acc**	**D acc**	**C acc**	**B acc**	**H acc**	**F acc**
Niño34	0.19*	0.08	0.08	0.06	0.08	−0.05	0.17*
SAM	−0.07	−0.03	−0.16	0.17	−0.27*	0.04	−0.24

2.3.7. Cross Wavelet Transform

Since the PCA components relate to the entire array of seven shallow ice cores, we perform cross-spectral wavelet analysis (XWT) on a single ice core location. The XWT of the δD_B record versus net accumulation, Niño34, and SAM is shown in Figure 2.6. The δD_B and Core B net accumulation XWT from 1657-1995 has strong, significant, and non-continuous power in oscillations at 2-5 years and strong, non-significant, continuous power in oscillations between 16-32 years. The δD_B and Niño34 XWT from 1950-1995 shows strong, significant, and continuous power in oscillations ranging from 2-7 years. The δD_B and SAM XWT from 1979-1995 shows strong, significant, and continuous power in oscillations at 1-3 years from about 1988-1995. All shallow ice core XWT results can be found in Appendix A and show similar results.

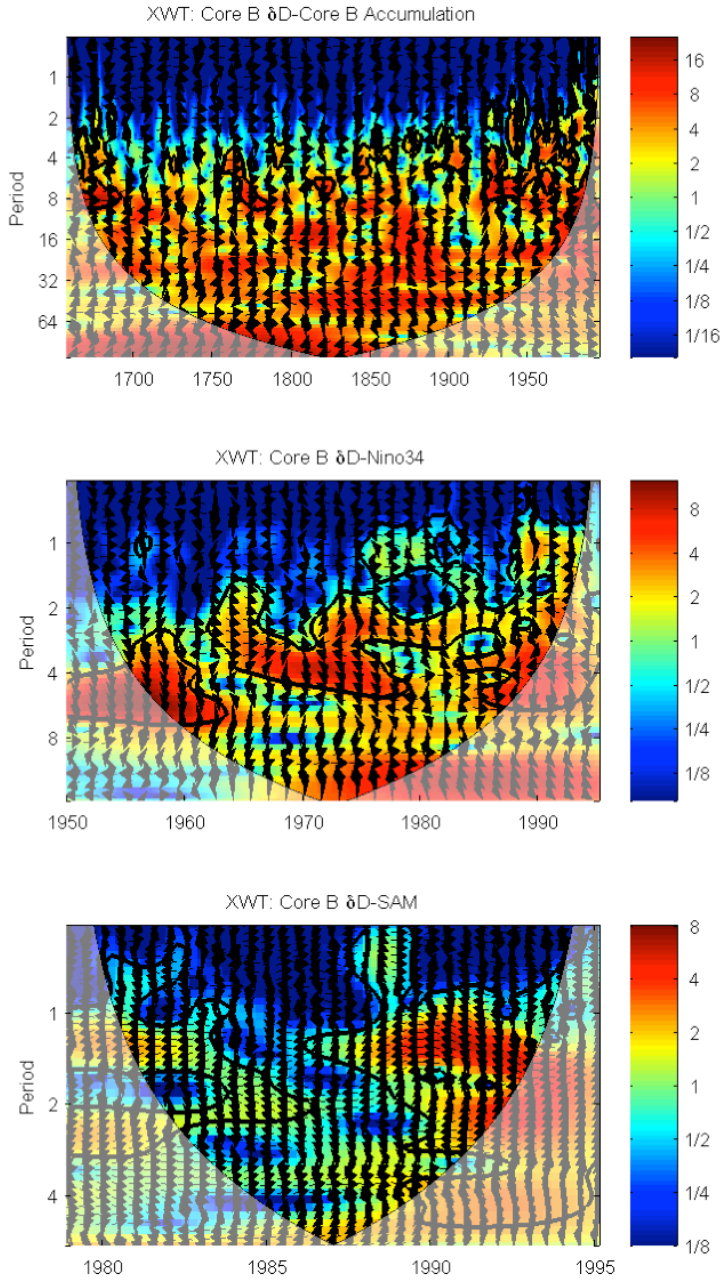

Figure 2.6. *XWT plot of regions in time–frequency space where the time series in question show high common power. The phase arrows show the relative phasing of the time series (right: in-phase, left: anti-phase, down: X leading Y by 90°, up: Y leading X by 90°). Top panel: core B δD and core B net accumulation XWT from 1657 to 1995. Middle panel: core B δD and Niño 3.4 XWT from 1950 to 1995. Bottom panel: core B δD and SAM XWT from 1979 to 1995. All shallow ice core XWT plots can be found in Appendix A.*

The fact that Core B XWT exhibits ENSO-type frequencies is not surprising since ENSO oscillations can be found in may of the world's time series. In short, ENSO is intrinsically a part of global climate. We note that while the XWT analysis for δD_B versus net accumulation, Niño34, and SAM finds common power at varying periodicities, the oscillations go into and out of phase throughout the entire record (as interpreted in the phase arrows). In other words, common oscillations at high power are not phase locked, and cannot be interpreted as a link between any of the time series. The XWT plots show that while ENSO and SAM likely affect climate at Siple Dome, the Siple Dome water isotope record is not a useful ENSO or SAM proxy on the first order.

2.3.8. Climate Signal

We find that the climatology of Siple Dome expressed in water isotopes, net accumulation, and borehole temperatures is highly complex. Although one of the original goals of the West Antarctic Ice Sheet initiative was to reconstruct regional climate oscillation signals such as ENSO, we can find no direct transect-wide relation amongst the water isotope or net accumulation time series with strong El Niño, strong La Niña, or SAM events. However, we do find significant correlations between the SAM Index and PC3 (R-value of 0.25) and between the Niño34 Index and PC5 (R-value of 0.19). The XWT analysis also shows that shallow ice cores share common power with ENSO and SAM, but are not phase locked. This suggests that both ENSO and SAM are superimposed on a water isotope signal that is affected by many other climatic forcings.

Orographic uplift alone does not control isotope values at Siple Dome because shallow ice core δD values do not conform with elevation and borehole temperatures. As Component 1 of the PCA and borehole temperatures suggest, there may be fundamental differences in climate on the Pacific and Inland Flanks. The exact nature of these mechanisms is unknown. Perhaps the Inland Flank is more influenced by katabatic winds originating from the interior of WA, while the Pacific Flank is more influenced by weather systems originating in the Amundsen and Ross Seas. Differences in post-depositional processes (snow waves and/or wind scouring) may also play a role.

In a study of net accumulation signals at Talos Dome, Frenzzotti et al. (2007) found that spatial variability at the km scale is one order of magnitude higher than temporal variability at the multi-decadal/century scale for ice core sites with net accumulation less than 20 cm yr^{-1} ice eq. All shallow ice core sites at Siple Dome fall within this range. We find that significant variations in net accumulation and water isotopes occur at distances as close as 0.5 km, which as Frenzzotti et al. (2007) shows, may be more influenced by sub-kilometer ice sheet morphology than a true climate signal. This suggests that high-frequency oscillations (multi-year) in the net accumulation and water isotope time series cannot be interpreted solely as a local or regional climate signal. Frenzzotti et al. (2007) also shows that accumulation hiatuses can occur at sites with net accumulation lower than 12 cm yr^{-1} ice eq. This finding pertains to all shallow ice core sites at Siple Dome except Core G. Gaps in accumulation could cause misidentification of annual layers in ice core dating, as well as inaccuracies in statistical analysis of ice core time series records. This should be considered when interpreting deep

ice cores in locations with low net accumulation or marked variations in shallow ice core signals over small distances.

2.4. Conclusions

Analysis of seven shallow ice cores spanning a relatively flat 60 km north-south transect of Siple Dome have been analyzed for borehole temperatures, net accumulation, and water isotopes. Multiple statistical analysis methods reveal a complex micro climate. We find that Siple Dome has two distinct temperature profiles, including a warmer temperature regime on the Pacific Flank and Dome Summit, and a colder temperature regime on the Inland Flank. Water isotope values do not conform directly to temperature measurements, nor do any of the water isotope and net accumulation times series show strong agreement amongst themselves or to extra-polar climate forcings like the El Niño-Southern Oscillation and the Southern Annular Mode. We find indications that post-depositional snow movements may convolute both water isotope and net accumulation time series.

Due to the complexity of climate in the region, our findings suggest caution in interpreting high-frequency water isotope and net accumulation signals in the coastal dome locations of West Antarctica. Ongoing research at WAIS Divide (an inland ice core site) and Roosevelt Island (a coastal ice core site on an island in the Ross Sea) may give better indications whether the amount of climate variability observed at Siple Dome is unique to Siple Dome, occurs at other coastal dome locations (i.e. Roosevelt Island), or is more widespread across the West Antarctic region (i.e. WAIS Divide). Understanding the

amount of variability at an ice core location can better inform interpretations of climate signals seen in deep ice cores.

2.5. Appendix A: Cross-spectral wavelet analysis

Plots of cross-spectral wavelet analysis (XWT) for shallow ice core δD records versus net accumulation, Niño 34, and SAM. The XWT changes one-dimensional time series into time-frequency space, creating a two-dimensional image of cross-modal variability and phase lag through time. The wavelet power is based on a red noise background spectrum. The phase arrows show the relative phasing of the time series (right: in-phase, left: anti-phase, down: X leading Y by 90°, up: Y leading X by 90°).

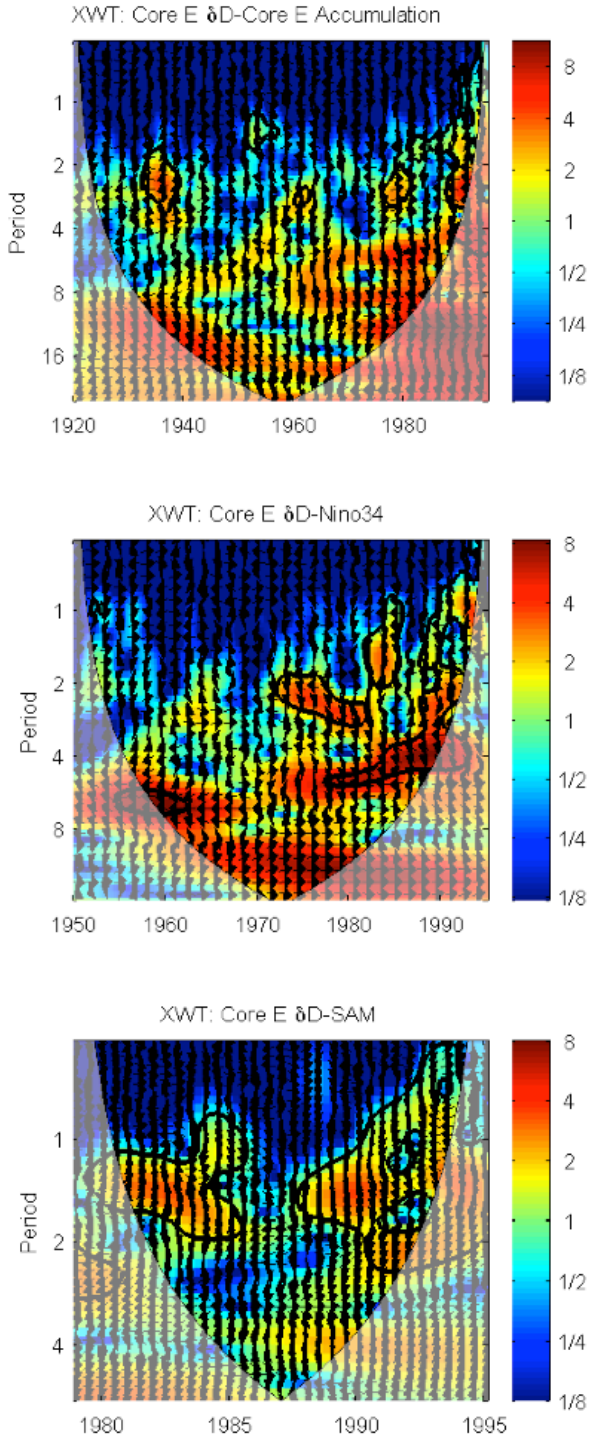

Figure 2.7. *Top panel: core E δD and core E net accumulation XWT from 1657 to 1995. Middle panel: core E δD and Niño 3.4 XWT from 1950 to 1995. Bottom panel: core E δD and SAM XWT from 1979 to 1995.*

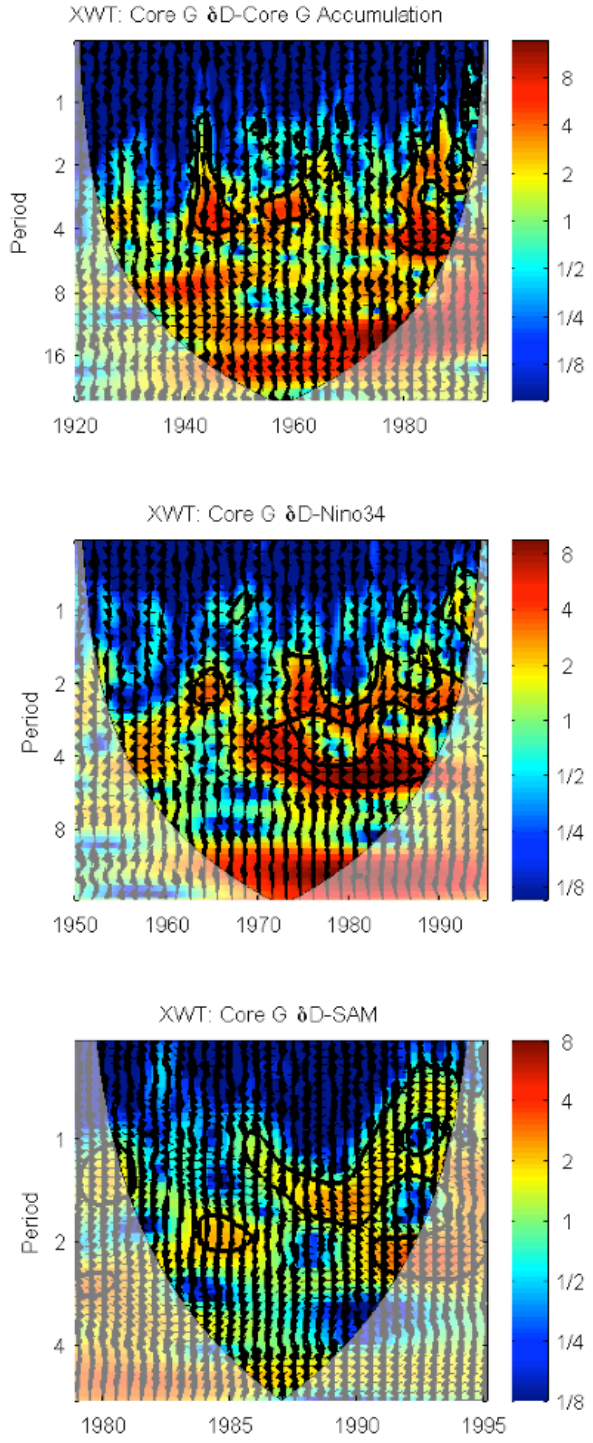

Figure 2.8. *Top panel: core G δD and core G net accumulation XWT from 1657 to 1995. Middle panel: core G δD and Niño 3.4 XWT from 1950 to 1995. Bottom panel: core G δD and SAM XWT from 1979 to 1995.*

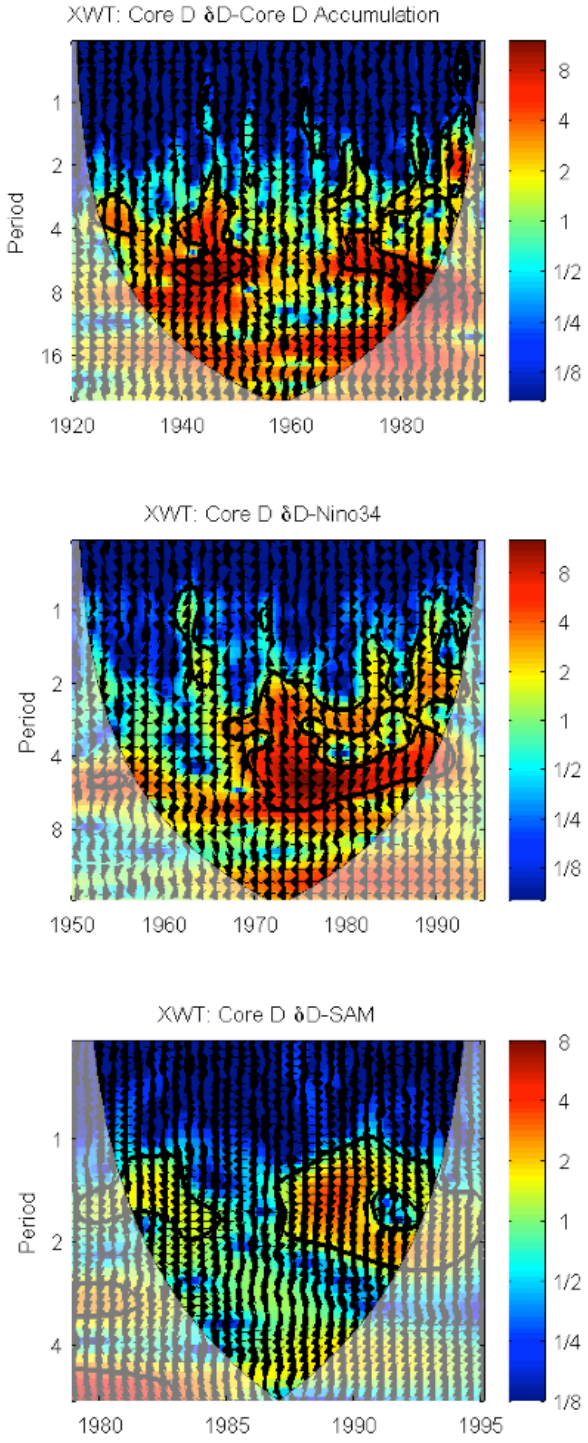

Figure 2.9. *Top panel: core D δD and core D net accumulation XWT from 1657 to 1995. Middle panel: core D δD and Niño 3.4 XWT from 1950 to 1995. Bottom panel: core D δD and SAM XWT from 1979 to 1995.*

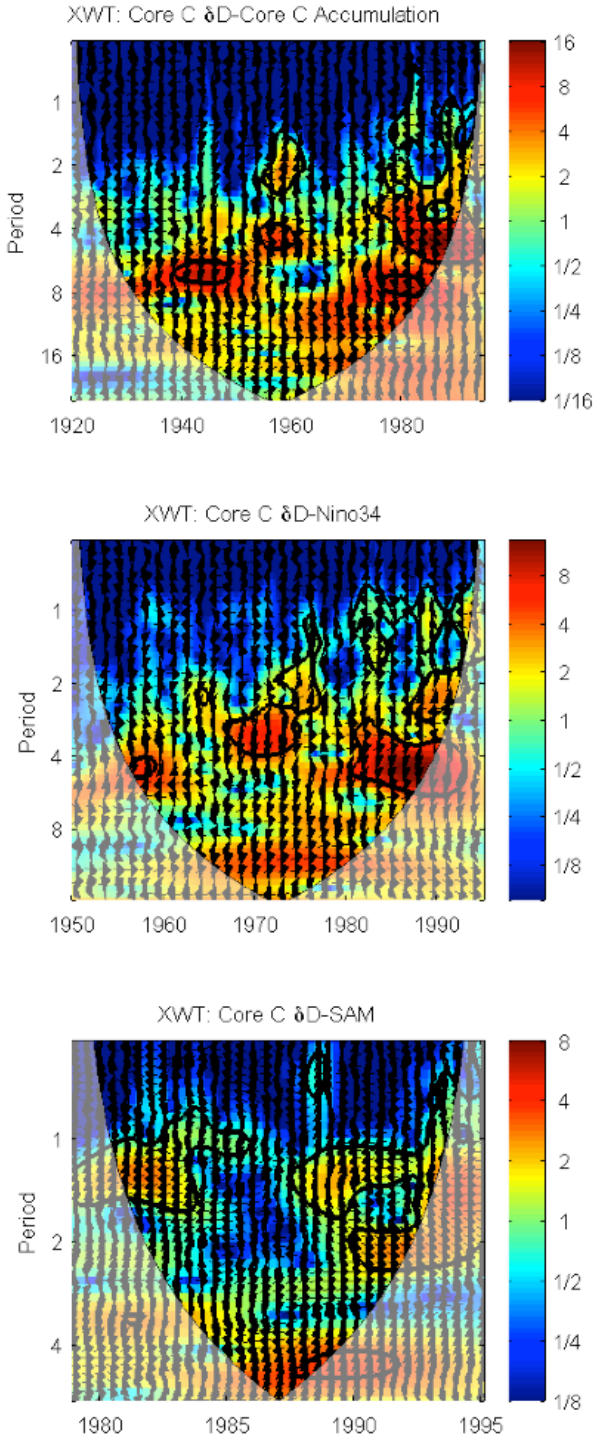

Figure 2.10. *Top panel: core C δD and core C net accumulation XWT from 1657 to 1995. Middle panel: core C δD and Niño 3.4 XWT from 1950 to 1995. Bottom panel: core C δD and SAM XWT from 1979 to 1995.*

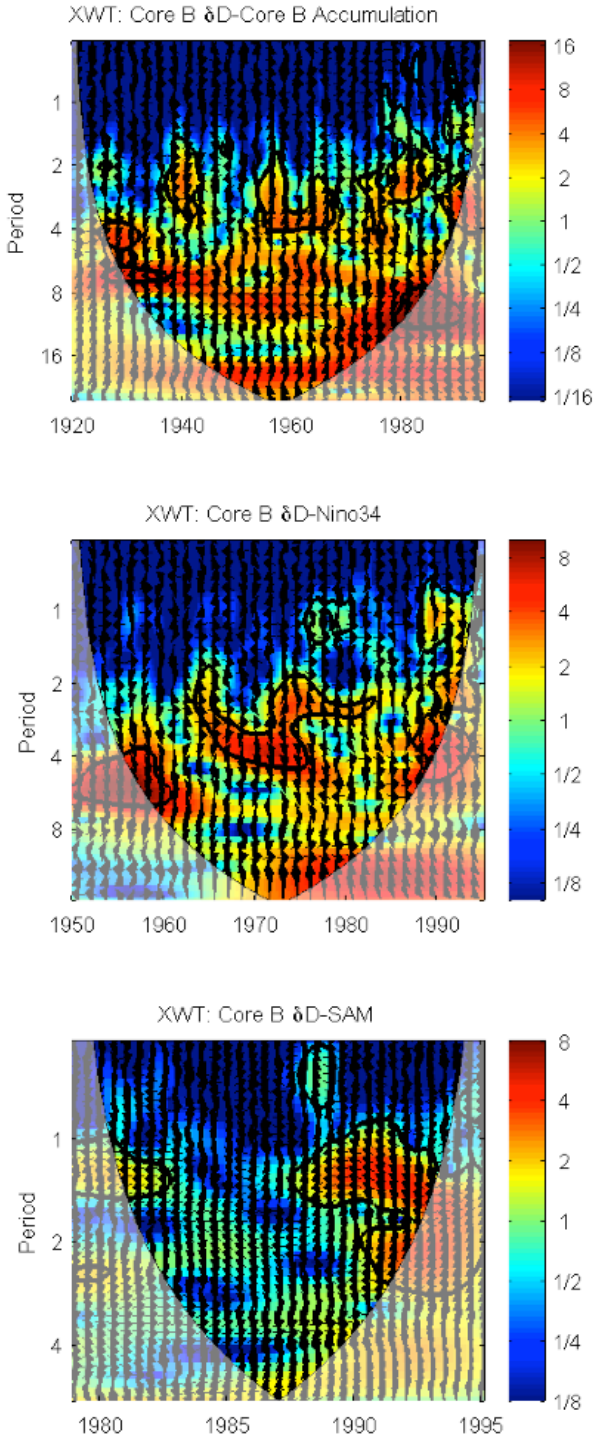

Figure 2.11. *Top panel: core B δD and core B net accumulation XWT from 1657 to 1995. Middle panel: core B δD and Niño 3.4 XWT from 1950 to 1995. Bottom panel: core B δD and SAM XWT from 1979 to 1995.*

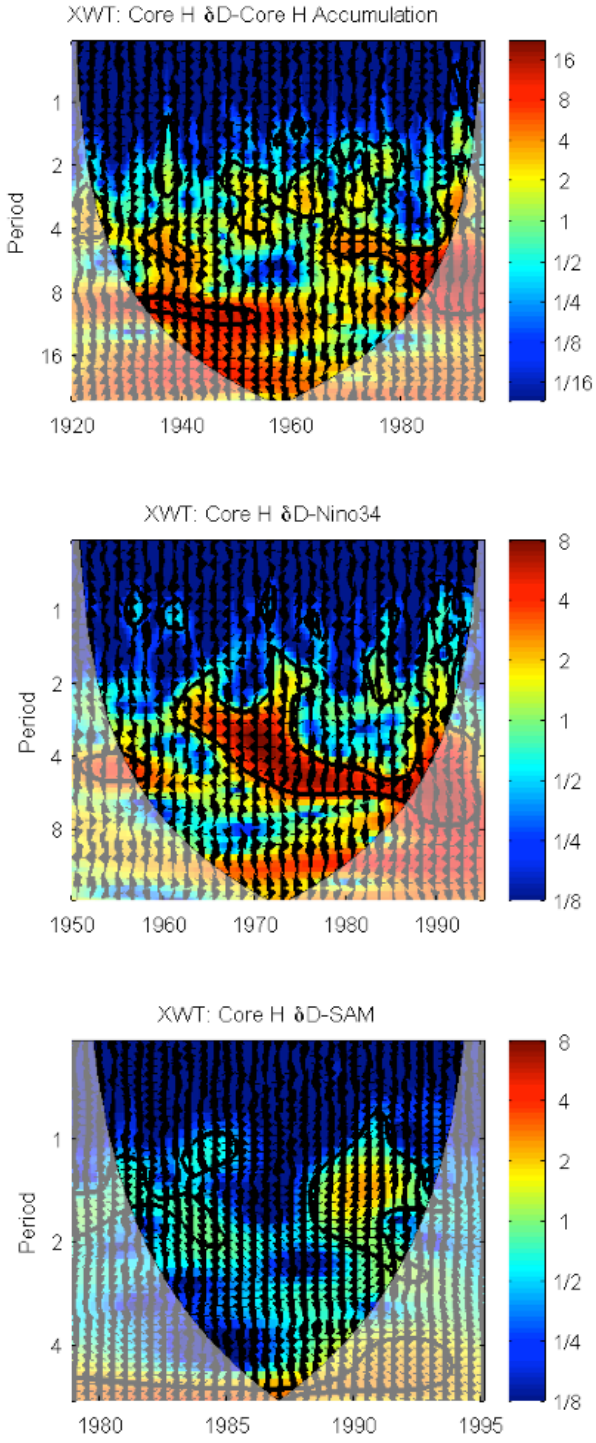

Figure 2.12. *Top panel: core H δD and core H net accumulation XWT from 1657 to 1995. Middle panel: core H δD and Niño 3.4 XWT from 1950 to 1995. Bottom panel: core H δD and SAM XWT from 1979 to 1995.*

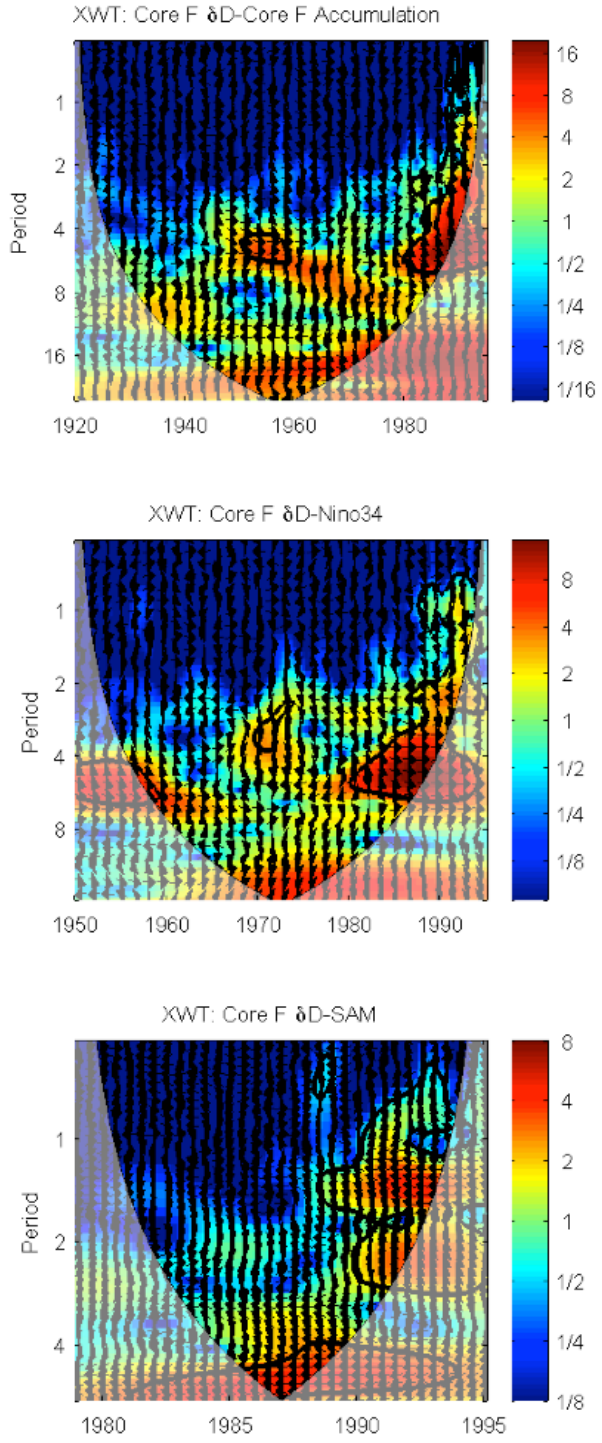

Figure 2.13 *Top panel: core F δD and core F net accumulation XWT from 1657 to 1995. Middle panel: core F δD and Niño 3.4 XWT from 1950 to 1995. Bottom panel: core F δD and SAM XWT from 1979 to 1995.*

2.6. References

Alley, R. (2003) Visible Stratigraphic Dating, Siple Dome and Upstream C Cores. *National Snow and Ice Data Center*, Boulder, Colorado USA, http://www.nsidc.org

Bertler, N. A., Barrett, P. J., Mayewski, P. A., Fogt, R. L., Kreutz, K. J., & Shulmeister, J. (2004). El Niño suppresses Antarctic warming. *Geophysical Research Letters*, 31(15).

Bertler, N. A. N., Naish, T. R., Mayewski, P. A., & Barrett, P. J. (2006). Opposing oceanic and atmospheric ENSO influences on the Ross Sea Region, Antarctica. *Advances in Geosciences*, 6, 83-86.

Blunier, T., Chappellaz, J., Schwander, J., Dällenbach, A., Stauffer, B., Stocker, T. F., Raynaud, D., Jouzel, J., Clausen, H. B., Hammer, C. U., & Johnsen S. J. (1998). Asynchrony of Antarctic and Greenland climate change during the last glacial period. *Nature*, 394(6695), 739-743.

Bromwich, D. H. (1988). Snowfall in high southern latitudes. *Reviews of Geophysics,* 26(1), 149-168.

Bromwich, D. H., Rogers, A. N., Kållberg, P., Cullather, R. I., White, J. W., & Kreutz, K. J. (2000). ECMWF Analyses and Reanalyses Depiction of ENSO Signal in Antarctic Precipitation*. *Journal of Climate*, 13(8), 1406-1420.

Bromwich, D. H., Monaghan, A. J., & Guo, Z. (2004). Modeling the ENSO Modulation of Antarctic Climate in the Late 1990s with the Polar MM5*. *Journal of climate*, 17(1), 109-132.

Bromwich, D. H., Carrasco, J. F., Liu, Z., & Tzeng, R. Y. (1993). Hemispheric atmospheric variations and oceanographic impacts associated with katabatic surges across the Ross Ice Shelf, Antarctica. *Journal of Geophysical Research: Atmospheres* (1984–2012), 98(D7), 13045-13062.

Carleton, A. M. (2003). Atmospheric teleconnections involving the Southern Ocean. *Journal of Geophysical Research: Oceans* (1978–2012), 108(C4).

Clow, G. (1996) Siple Dome Shallow Ice Core Borehole Measurements. *National Snow and Ice Data Center*, Boulder, Colorado USA. http://www.nsidc.org

Cuffey, K. M., & Steig, E. J. (1998). Isotopic diffusion in polar firn: implications for interpretation of seasonal climate parameters in ice-core records, with emphasis on central Greenland. *Journal of Glaciology*, *44*(147), 273-284.

Cullather, R. I., Bromwich, D. H., & Van Woert, M. L. (1996). Interannual variations in Antarctic precipitation related to El Niño–Southern Oscillation. *Journal of Geophysical Research: Atmospheres* (1984–2012), 101(D14), 19109-19118.

Dansgaard, W. "Stable isotopes in precipitation." *Tellus* 16.4 (1964): 436-468.

Delaygue, G., Masson, V., Jouzel, J., Koster, R. D., & Healy, R. J. (2000). The origin of Antarctic precipitation: a modelling approach. *Tellus* B, 52(1), 19-36.

Diaz, H. F., Hoerling, M. P., & Eischeid, J. K. (2001). ENSO variability, teleconnections and climate change. *International Journal of Climatology*, 21(15), 1845-1862.

Ding, Q., Steig, E. J., Battisti, D. S., & Wallace, J. M. (2012). Influence of the tropics on the Southern Annular Mode. *Journal of Climate*, 25(18), 6330-6348.

Dunbar, R. B., Wellington, G. M., Colgan, M. W., & Glynn, P. W. (1994). Eastern Pacific sea surface temperature since 1600 AD: The δ18O record of climate variability in Galápagos corals. *Paleoceanography*, 9(2), 291-315.

Ekaykin, A. A., Lipenkov, V. Y., Barkov, N. I., Petit, J. R., & Masson-Delmotte, V. (2002). Spatial and temporal variability in isotope composition of recent snow in the vicinity of Vostok station, Antarctica: implications for ice-core record interpretation. *Annals of Glaciology*, 35(1), 181-186.

Epstein, S., & Mayeda, T. (1953). Variation of O 18 content of waters from natural sources. *Geochimica et cosmochimica acta*, 4(5), 213-224.

Fisher, D. A., Reeh, N., & Clausen, H. B. (1985). Stratigraphic noise in time series derived from ice cores. *Ann. Glaciol*, 7, 76-83.

Fogt, R. L., & Bromwich, D. H. (2006). Decadal variability of the ENSO teleconnection to the high-latitude South Pacific governed by coupling with the Southern Annular Mode*. *Journal of Climate*, 19(6), 979-997.

Frezzotti, M., Urbini, S., Proposito, M., Scarchilli, C., & Gandolfi, S. (2007). Spatial and temporal variability of surface mass balance near Talos Dome, East Antarctica. *Journal of Geophysical Research: Earth Surface* (2003–2012), 112(F2).

Ghil, M., Allen, M. R., Dettinger, M. D., Ide, K., Kondrashov, D., Mann, M. E., ... & Yiou, P. (2002). Advanced spectral methods for climatic time series. *Reviews of geophysics*, 40(1), 3-1.

Gregory, S., & Noone, D. (2008). Variability in the teleconnection between the El Niño–Southern Oscillation and West Antarctic climate deduced from West Antarctic ice core isotope records. *Journal of Geophysical Research: Atmospheres* (1984–2012), 113(D17).

Grinsted, A., Moore, J. C., & Jevrejeva, S. (2004). Application of the cross wavelet transform and wavelet coherence to geophysical time series. *Nonlinear processes in geophysics*, 11(5/6), 561-566.

Guo, Z., Bromwich, D. H., & Hines, K. M. (2004). Modeled Antarctic Precipitation. Part II: ENSO Modulation over West Antarctica*. *Journal of climate*, 17(3), 448-465.

Hamilton, G. S. (2002). Mass balance and accumulation rate across Siple Dome, West Antarctica. *Annals of Glaciology*, 35(1), 102-106.

Hendricks, M. B., DePaolo, D. J., & Cohen, R. C. (2000). Space and time variation of δ18O and δD in precipitation: Can paleotemperature be estimated from ice cores?. *Global Biogeochemical Cycles*, 14(3), 851-861.

Hosking, J. S., Orr, A., Marshall, G. J., Turner, J., & Phillips, T. (2013). The influence of the Amundsen–Bellingshausen Seas low on the climate of West Antarctica and its representation in coupled climate model simulations. *Journal of Climate*, 26(17), 6633-6648.

Jacobel, R.W., Dorsey, C. W., and Harner, A. M. (1994). Ice velocities near a relict flow feature on Siple Dome. *Antarctic Journal of the United States*, XXIX, 62—66.

Jouzel, J., & Merlivat, L. (1984). Deuterium and O-18 in Precipitation-Modeling of the Isotopic Effects During Snow Formation. *Journal of Geophysical Research-Atmospheres*, 89(ND 7), 1749-1757.

Jouzel, J., Alley, R. B., Cuffey, K. M., Dansgaard, W., Grootes, P., Hoffmann, G., Johnsen, S. J., Koster, R. D., Peel, D., Shuman, C. A., Stievenard, M., Stuiver, M. & White, J. (1997). Validity of the temperature reconstruction from water isotopes in ice cores. *Journal of Geophysical Research: Oceans* (1978–2012), 102(C12), 26471-26487.

Kavanaugh, J. L. & Cuffey, K. M. (2003). Space and time variation of delta O-18 and delta D in Antarctic precipitation revisited. *Global Biogeochemical Cycles*, 17, 1017, 2003.

Kreutz, K. J., Mayewski, P. A., Pittalwala, I. I., Meeker, L. D., Twickler, M. S., & Whitlow, S. I. (2000). Sea level pressure variability in the Amundsen Sea region inferred from a West Antarctic glaciochemical record. *Journal of Geophysical Research: Atmospheres* (1984–2012), 105(D3), 4047-4059.

Lamorey, G. W. (2003) Siple Shallow Core Density Data. *National Snow and Ice Data Center*, Boulder, Colorado USA, http://www.nsidc.org

Masson-Delmotte, V., Hou, S., Ekaykin A., Jouzel J., Aristarain A., R. T. Bernardo, D. Bromwich, O. Cattani, M. Delmotte, S. Falourd, M. Frezzotti, H. Gallée, L. Genoni, E. Isaksson, A. Landais, M. M. Helsen, G. Hoffmann, J. Lopez, V. Morgan, H. Motoyama, D. Noone, H. Oerter, J. R. Petit, A. Royer, R. Uemura, G. A. Schmidt, E. Schlosser, J. C. Simões, E. J. Steig, B. Stenni, M. Stievenard, M. R. van den Broeke, R. S. W. van de Wal, W. J. van de Berg, F. Vimeux, and J. W. C. White (2008). A review of Antarctic surface snow isotopic composition: Observations, atmospheric circulation, and isotopic modeling*. *Journal of Climate*, 21(13), 3359-3387.

Meyerson, E. A., Mayewski, P. A., Kreutz, K. J., Meeker, L. D., Whitlow, S. I., & Twickler, M. S. (2002). The polar expression of ENSO and sea-ice variability as recorded in a South Pole ice core. *Annals of Glaciology*, 35(1), 430-436.

Nereson, N. A., Raymond, C. F., Waddington, E. D., & Jacobel, R. W. (1998). Migration of the Siple Dome ice divide, West Antarctica. *Journal of Glaciology*, 44(148), 643-652.

Nereson, N. A., Raymond, C. F., Jacobel, R. W., & Waddington, E. D. (2000). The accumulation pattern across Siple Dome, West Antarctica, inferred from radar-detected internal layers. *Journal of Glaciology*, 46(152), 75-87.

Nicolas, J. P., & Bromwich, D. H. (2011). Climate of West Antarctica and influence of marine air intrusions*. *Journal of Climate*, 24(1), 49-67.

Noone, D., & Simmonds, I. (2002). Annular variations in moisture transport mechanisms and the abundance of δ18O in Antarctic snow. *Journal of Geophysical Research: Atmospheres* (1984–2012), 107(D24), ACL-3.

Percival, D. B., & Walden, A. T. (1993). *Spectral Analysis for Physical Applications: Multitaper and Conventional Univariate Techniques* (Cambridge. Press, New York.

Petit, J. R., White, J. W. C., Young, N. W., Jouzel, J., & Korotkevich, Y. S. (1991). Deuterium excess in recent Antarctic snow. *Journal of Geophysical Research: Atmospheres* (1984–2012), 96(D3), 5113-5122.

Schilla, A. S. (2007). *The stable isotopes and deuterium excess from the Siple Dome ice core: implications for the late Quaternary climate and elevation history of the Ross Sea Region, West Antarctica.* ProQuest.

Schneider, D. P., Steig, E. J., & Comiso, J. C. (2004). Recent climate variability in Antarctica from satellite-derived temperature data. *Journal of Climate*, 17(7), 1569-1583.

Shimizu, H. (1964). Glaciological Studies in West Antarctica, 1960–19621. *Antarctic snow and ice studies*, 37-64.

Steig, E. J. and White, J. W. C. (2003). Siple Dome highlights: Stable isotopes. *National Snow and Ice Data Center*, Boulder, Colorado USA, http://www.nsidc.org

Thompson, D. W., & Wallace, J. M. (2000). Annular modes in the extratropical circulation. Part I: month-to-month variability*. *Journal of Climate*, 13(5), 1000-1016.

Thomson, D. J. (1982). Spectrum estimation and harmonic analysis. *Proceedings of the IEEE*, 70(9), 1055-1096.

Torrence, C., & Compo, G. P. (1998). A practical guide to wavelet analysis. *Bulletin of the American Meteorological society*, 79(1), 61-78.

Trenberth, K. E., & Hoar, T. J. (1997). El Niño and climate change. *Geophysical Research Letters*, 24(23), 3057-3060.

Turner, J. (2004). The El Niño–Southern Oscillation and Antarctica. *International Journal of Climatology*, 24(1), 1-31.

Turner, J., Phillips, T., Hosking, J. S., Marshall, G. J., & Orr, A. (2013). The Amundsen Sea low. *International Journal of Climatology*, 33(7), 1818-1829.

Urban, F. E., Cole, J. E., & Overpeck, J. T. (2000). Influence of mean climate change on climate variability from a 155-year tropical Pacific coral record. *Nature*, 407(6807), 989-993.

Vaughn, B. H., White, J. W. C., Delmotte, M., Trolier, M., Cattani, O., & Stievenard, M. (1998). An automated system for hydrogen isotope analysis of water. *Chemical Geology*, 152(3), 309-319.

Zwally, H. J., & Gloersen, P. (1977). Passive microwave images of the polar regions and research applications. *Polar Record*, 18(116), 431-450.

Chapter 3

A Continuous Flow Analysis System for Measurement of Water Isotopes in Ice Cores and Firn

Abstract

Water isotopes in ice cores are used as a climate proxy for local temperature and regional atmospheric circulation (δD and $\delta^{18}O$), as well as sea surface temperature and moisture source changes (deuterium excess). Traditional measurements of water isotopes have been achieved using magnetic sector isotope ratio mass spectrometry (IRMS). However, a recent paradigm shift in water isotope analysis has displaced some IRMS measurements with laser absorption technology (LAS). The new LAS technology has been combined with continuous flow analysis (CFA) to improve data density and time commitments in ice coring projects. In this chapter, we present a semi-automated LAS continuous flow analysis (CFA) system for measuring high-resolution water isotopes of ice cores. The system utilizes a 16-position carousel contained in a freezer to deliver ~1m x 1.3cm^2 ice sticks to a temperature controlled melt head, where it is converted to a continuous liquid stream. Depth registration is achieved using a precise overhead laser distance device with

an uncertainty of ± 0.2 mm. The liquid stream is vaporized using a concentric nebulizer and furnace, and plumbed into an LAS instrument for isotopic analysis. An integrated delivery system for water isotope standards is used for calibration to the VSMOW2-VSLAP2 scale. We perform a number of tests to determine the uncertainty of the CFA method relative to traditional IRMS, including analysis of replicate South Pole firn samples, replicate Greenland ice samples, and inter-lab comparisons of the WAIS Divide Ice Core (WDC) at depths of ~212-222 meters. We report improved 1σ uncertainty (relative to IRMS) on our system for δD, δ18O, and deuterium excess of 0.55, 0.09, and 0.55 per mil, respectively.

3.1. Introduction

The origins of ice core science began with a backyard experiment performed in Copenhagen in 1952. In that pioneering study, Willi Dansgaard used a funnel and glass bottle to collect rainwater from a passing frontal system. Then, using a mass spectrometer, Dansgaard determined that oxygen isotope ratios in his rainwater samples were correlated with cloud temperature (recounted in Dansgaard, 2005[3]). These results led to the landmark paper *Stable Isotopes in Precipitation* (Dansgaard, 1964) and gave rise to an entirely new field of geochemistry. Scientists began to test icebergs for water

[3] This story was told in "Frozen Annals: Greenland Ice Cap Research", written by Willi Dansgaard. Quoting the preface: "Prior to World War II most ice cap research rested on relatively simple techniques applied by daring Polar explorers. The civilian post-war research was marked by international co-operation and logistical progress (reliable surface and air transport), as well as new analytical and drilling techniques. For example, in the 1950'es some seeds of stable isotope meteorology were sowed at the University of Copenhagen, and from the late 1960'es they developed into extensive studies of Greenland ice cores, originally in co-operation with USA CRREL (Cold Regions Research and Engineering Laboratories)."

isotope ratios, and eventually deep ice cores were drilled with the intent to reconstruct past climates.

Traditional measurements of water isotopes, such as those in the original Dansgaard experiment, have been achieved using specialized mass spectrometry set-ups, known as isotope ratio mass spectrometry (IRMS). In a typical experiment, a gas sample is ionized and accelerated through a magnetic field. The magnetic field causes the ion beam to separate and deflect along trajectories related to the mass-to-charge ratio of the varying isotopes in the sample. The trajectory corresponding to the highest mass-to-charge ratio will be curved less, while the lowest mass-to-charge ratio will be curved more. The abundance of molecules in each trajectory is measured using Faraday cups, and the relative ratios of differing isotopes in a sample can be determined.

One shortcoming of IRMS is that water vapor tends to adsorb onto the walls of the high-vacuum systems used in mass spectrometers, resulting in large memory effects. This memory effect is overcome by transferring the isotopic composition of liquid water to other less reactive molecules. For oxygen, water isotope ratios have been measured using a CO_2/H_2O equilibration method (Epstein, 1953 and Craig et al., 1963). For hydrogen isotopes, a variety of methods have been used including reduction of water with uranium and zinc (Bigelseisen et al., 1952; Vaughn et al., 1998; and Coleman et al., 1982) or equilibration using platinum (Bond, 1968; Coplen, 1991; and Huber and Leuenberger, 2003).

Recent advances in high-precision laser spectroscopy (LAS) methods are being adopted as an alternative to IRMS methods (Kerstel et al., 1999; Lis et al, 2008; Gupta, et al, 2009; and Brand et al., 2009). There are two main optical methods used for measuring

water isotopes including cavity ring-down laser spectroscopy (CRDS; manufactured by Picarro, Inc.) and off-axis integrated cavity output laser spectroscopy (OA-ICOS; manufactured by Los Gatos Research). The CRDS method (utilized in this study) requires the input of water vapor into a detection cavity, which is a highly reflective enclosure with 3-mirrors that confine and reflect laser pulses. Initially, a laser pulse is emitted until a threshold value is reached, then the laser is turned off, and the optical extinction of the laser pulse is measured. When the cavity is empty, the laser "ring-down" time (i.e. the amount of time for light to dissipate) occurs over a known period. However, when a gas species is introduced to the cavity, the ring down time decreases due to the absorption of light by varying molecules at known wavelengths. The combination of the two values – both the extinction of light in an empty cavity and the modified extinction related to molecular absorption – can be used to determine water isotope concentration values. These measurements are made in fractions of a second.

Researchers have developed input systems that deliver continuous water sample flow into LAS measurement devices. The technique, known as continuous flow analysis (CFA), is often implemented by slowly melting solid ice sticks into a continuous liquid stream, which is distributed by pumps to instruments for analysis. CFA was originally used for chemical measurements in ice cores (e.g. Rothlesberger, 2000 and Osterberg et al., 2006), and more recent work by Gkinis et al. (2010 and 2011) established a CFA framework for water isotope analysis. Specifically, Gkinis reproduced traditional IRMS water isotope measurements in Greenland ice using a Picarro L1102-*i* CRDS instrument. The resulting CFA measurements achieved comparable uncertainty to IRMS in a fraction of the time. Maselli et al. (2012) expanded on Gkinis' technique by testing multiple new-

generation Picarro devices (L2130-*i* and L2140-*i*). Maselli found that the precision of hydrogen isotope measurements was comparable to IRMS, oxygen isotope precision was slightly decreased, depth resolution was increased by one order of magnitude, and analysis time decreased by $1/10^{th}$.

Besides the aforementioned benefits (i.e. precision, resolution, and time), LAS is advantageous to ice core science in another way: the simultaneous measurements of oxygen and hydrogen isotope ratios. Using traditional IRMS methods, both oxygen and hydrogen had to be analyzed on separate systems, which introduced uncertainty into the second order parameter deuterium excess (dxs). The dxs depends largely on differential kinetic evaporation effects between oxygen and hydrogen at the moisture source location to an ice core site. Determination of dxs requires high-precision measurements and has been historically difficult to measure. But, the LAS technique removes multi-system uncertainty, eliminates chemical preparation techniques, and provides measurements of hydrogen and oxygen under the same boundary conditions – all of which are advantageous for dxs records. Additional information about hydrogen and oxygen isotopes, as well as dxs, is found the next section.

In general, LAS systems differ from traditional IRMS systems in a number of key ways: 1) A stream of water vapor is analyzed in LAS, while discrete samples are analyzed in IRMS. 2) LAS systems measure both hydrogen and oxygen isotope ratios simultaneously, while IRMS requires differing protocols and differing mass spectrometer systems for each isotope. 3) Unlike IRMS, LAS systems invariably mix liquid and vapor, requiring that the analyzed values be "unmixed" to yield the isotopic composition of the water. 4) The LAS method of measurement is faster than IRMS, resulting in higher data

density, and exhibits comparable or better precision. We explore these concepts throughout the rest of this chapter.

3.1.1. Water Isotope Geochemistry

The partitioning of stable water isotopes between phase changes and within different hydrologic reservoirs is the fundamental basis for water isotope geochemistry. Due to differences in molecular weight, heavier isotopes prefer to exist in lower energy states during phase changes. In the ocean atmosphere system, evaporation causes water molecules containing ^{1}H and ^{16}O to preferentially, but not exclusively, evaporate from the oceans relative to ^{2}H and ^{18}O, respectively. Likewise, condensation causes water containing ^{2}H and ^{18}O to preferentially precipitate from clouds, leaving ^{1}H and ^{16}O behind. The process of differential movement of stable isotopes is known as isotopic fractionation.

Isotopic fractionation of water molecules is commonly expressed in delta notation (Epstein, 1953; Mook, 2000) relative to Vienna Standard Mean Ocean Water (VSMOW):

$$\delta_{sample} = 1000\left[\left(\frac{R_{sample}}{R_{VSMOW}}\right) - 1\right] \quad (1)$$

where R is the isotopic ratio $^{18}O/^{16}O$ or D/H in the sample or VSMOW. The dD and $d^{18}O$ symbols refer to parts per thousand deviations from equilibrium conditions set by VSMOW (defined as 0.00 per mil). Both dD and $d^{18}O$ are used as proxies for local temperature and regional atmospheric circulation, dependent on the temperature gradient

from moisture source to deposition site (Dansgaard, 1964). The main physical control on this relationship is the temperature of the cloud at the time of condensation (Jouzel and Merlivat, 1984; Jouzel et al., 1997; Johnsen et al., 2001).

Deuterium excess (dxs) can be used as a proxy for conditions in the regions providing moisture to ice core sites. In general, changes in dxs result from sea surface temperature changes at the vapor source or a change in the vapor source location. The dxs is a function of both hydrogen and oxygen isotope ratios:

$$\mathrm{dxs} = \delta\mathrm{D} - 8\,\delta^{18}O \tag{2}$$

Kinetic effects associated with evaporation at the ocean surface control the dxs parameter (Dansgaard, 1964). For example, $^{1}H_2H^{16}O$ (mass of 19) will have a higher diffusivity rate than $^{1}H_2{}^{18}O$ (mass of 20), resulting in higher dxs values during deviation from equilibrium conditions. The initial isotope concentration in an air parcel will have a dxs value that is a function of SST, relative humidity and wind speed (Jouzel and Merlivat, 1984; Johnsen, et al. 1989), where SST is the primary determinant (Petit et al, 1991).

3.2. Methods

In this chapter, we present a semi-automated water isotope CRDS-CFA system with novel componentry and methodology. The system was developed at the Institute of Arctic and Alpine Research (INSTAAR) Stable Isotope Lab (SIL). The CRDS-CFA system provides steady water vapor input to a Picarro L2130-*i* CRDS instrument. We test

uncertainty on the system in a number of ways: 1) Replicate analysis of seven Greenland ice core sticks, from which we introduce a method to assign partitioned and total uncertainty for WI-CFA systems. 2) Comparison of IRMS discrete and CRDS continuous water isotope samples from depths of 212-222 meters in the West Antarctic Ice Sheet Divide Ice Core (WDC); 3) High vs. low-resolution inter-lab discrete and continuous CRDS sample comparisons over the same WDC section; and 4) Comparison of discrete and continuous CRDS samples in South Pole firn. We also discuss new methods for memory correction and diffusion length, and ultimately offer insight for future development of CRDS-CFA systems.

3.2.1. Experimental System

The CRDS-CFA system is composed of three parts: 1) The ice core melting component, 2) the liquid-to-gas conversion component, and 3) the isotopic analyzer. A full system schematic is shown in Figure 3.1. The ice core melting component can accommodate 16 sticks of ice that measure ~1m x 1.3cm^2 (each stored in 1.9 cm^2 acrylic tubes) that are loaded vertically into a rotating carousel contained in a freezer. Using a computer controlled stepper motor (Parker ViX), the carousel rotates individual ice sticks over an aluminum melt head. The melt head (51 mm^2 x 12.6 mm) is machined with 2 mm concentric square catchments that channel melt water into a small drain. To regulate temperature, the melt head is attached with thermal paste to a heater block (51 mm^2 x 45.8 mm) that is maintained at 14.6 ± 0.1 °C by internally circulating dilute propylene glycol from a temperature-controlled bath. This method is preferable to proportional-

integral-derivative (PID) controlled resistive heaters used in most systems, which introduce small temperature fluctuations that result in slightly varying melt rates. At 14.6°C, the ice melts at a rate of 2.5 cm/min.

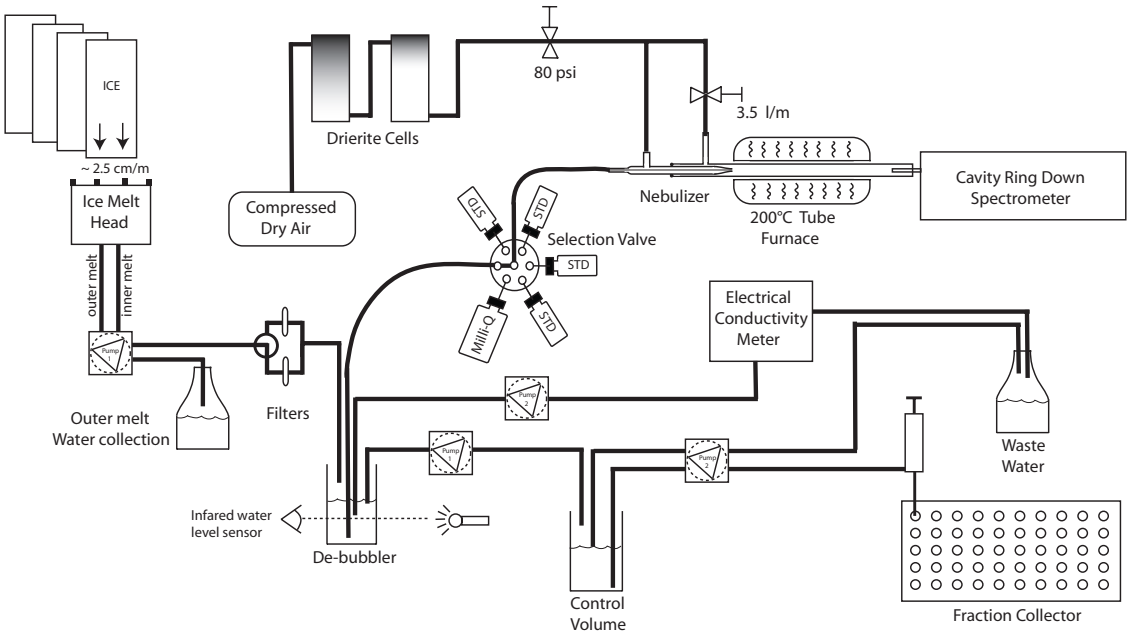

Figure 3.1. *The INSTAAR CRDS-CFA system, showing sample flow from the ice melt head through the filter block and debubbler and on to the Valco stream selection valve, nebulizer, furnace and the Picarro L-2130-i CRDS instrument.*

At the melt head interface, liquid water is drawn away using peristaltic pumps (Masterflex L/S 7534-04). The outer square catchment of the melt head is over pumped and collected for use as standard water. The inner square catchment is pumped at a rate matching that of the ice stick melt. This liquid water is pushed through an 8-micrometer

disposable filter backed by a 10-micrometer Peek frit[4] (IDEX A-411). The filtered water then enters a 2 ml glass, open-top vial where bubbles can escape (debubbler). A portion of the debubbled water is used as primary flow (i.e. for isotopic measurements), channeled through a Valco 6-port stream selection valve (Valco Instruments, Co. Inc.). To induce suction, high-pressure (80 psi) dry air is supplied to a downstream glass concentric nebulizer (Meinhard TL-HEN-150-A0.1), which creates a pressure difference that pulls the primary water out of the debubbler. The primary liquid water is aspirated from the debubbler through a 1/16" OD 0.020" ID tubing via a selector valve (VICI Cheminert 10P-0392L). As the water flows through the nebulizer, it is turned into a fine spray (i.e. a nominal droplet size of ~1.5 micrometers). The spray is directed into a 20.0 x 1.8 cm Pyrex vaporizing tube that is heated to 200 °C inside a ceramic tube furnace (Whatlow VC400N06A). Additional dry air (< 30 ppm H_2O) is added at a rate of ~3.5 L/min to dilute the water vapor and achieve a final water vapor content of ~25,000 ppm H_2O (the optimal range for the Picarro L2130-*i* is 20,000-40,000 ppm H_2O). Finally, the water vapor flows through an intake line (3.175 mm OD x 2 mm ID x 10 cm stainless steel tubing) inserted approximately 5 cm into the Pyrex vaporizing tube. This line is plumbed into a Picarro L2130-*i* analyzer by an open split interface. Any excess vapor is vented away from the instrumentation.

At the Valco 6-port stream selection valve, the primary flow can be switched off, allowing other auxiliary ports to be switched on. Each auxiliary port is connected to vials of secondary isotopic water standards, which can be analyzed isotopically and used for calibration of ice core measurements to international reporting standards. The auxiliary

[4] With filters in place, the system is tolerant of ice with ash or dust layers, which most commonly occur from past volcanic eruptions (ash) or atmospheric transport from desert regions (dust).

port water is pulled in the same fashion as the primary flow by suction induced by the nebulizer. Besides the primary flow and auxiliary Valco ports, additional water streams (secondary flow) are pumped from the debubbler to an electrical conductivity (EC) measurement cell (Amber Science 1056) and to a fraction collector (Gilson 215). The EC measurement allows for the comparison of chemical signatures at a known depth between labs. The fraction collector is used to archive water samples for discrete analysis and as a safeguard against system failures. It is programmed to fill approximately twenty-five 2 ml glass vials for every meter of ice melted.

3.2.2. A Typical Analysis Day

On a given run day, we perform a sequence of measurements related to calibration, correction, and ice samples (Figure 3.2). There are four main analytical features: 1) At the beginning and end of a melt day, secondary isotopic water standards[5] are analyzed to calibrate the ice core data against International Atomic Energy Agency (IAEA) primary standards (VSMOW2, VSLAP2, and GISP). We use four secondary standards including Boulder Standard Water (BSW), Antarctic Standard Water (ASW), Greenland Standard Water (GSW), and Polar Standard Water (PSW). Each secondary standard is analyzed twice for 20 minutes at the beginning and end of the day (4 times total), except for PSW, which is only analyzed 2 times total. Values for these standards are shown in Table 3.1. 2) To characterize isotopic mixing throughout the system, three small (20 cm x 13mm^2) sections of laboratory prepared ice are made from batches of

[5] Each secondary standard is stored in sealed stainless steel containers with a slight overpressure of inert argon gas in the headspace (described by Newman et al., 2009).

isotopically distinct waters with δD values of -240, -120, and -240 per mil (hereafter referred to as mock ice[6]). The mock ice is analyzed twice per day at the beginning and end of an ice core melt sequence. Each instance of mock ice analysis is used to determine how the CRDS-CFA system is responding to an instantaneous step change in isotopic values (in this case, a change from -240 to -120 per mil, and vice versa). Ideally, the system would instantly register the change, but mixing in the liquid and vapor phase causes a slower reaction. By quantifying the mixing effect, some data can be recovered during isotopic transitions into and out of an ice core melt sequence. 3) An ice core melt sequence occurs in the middle of an analysis day. Key variables are closely monitored during this time, including water concentration in the Picarro instrument, the melt rate, and depth registration. 4) During the ice core melt sequence, every set of four ice cores are separated by 20 cm sections of isotopically homogenous ice with a δD value of about -115 per mil (hereafter referred to as push ice). The push ice maintains a consistent thermal load on the melt head and a constant flow rate during routine maintenance tasks that include changing the filters and cleaning the melt head. As stated above, the transition from push ice to ice core requires a mixing correction (discussed later in this chapter).

[6] The mock ice is created by filling lay-flat tubing with isotopically homogenous water, freezing the water at -30 °C in chilled ethanol to minimize fractionation, and cutting the ice into small sections using a band saw.

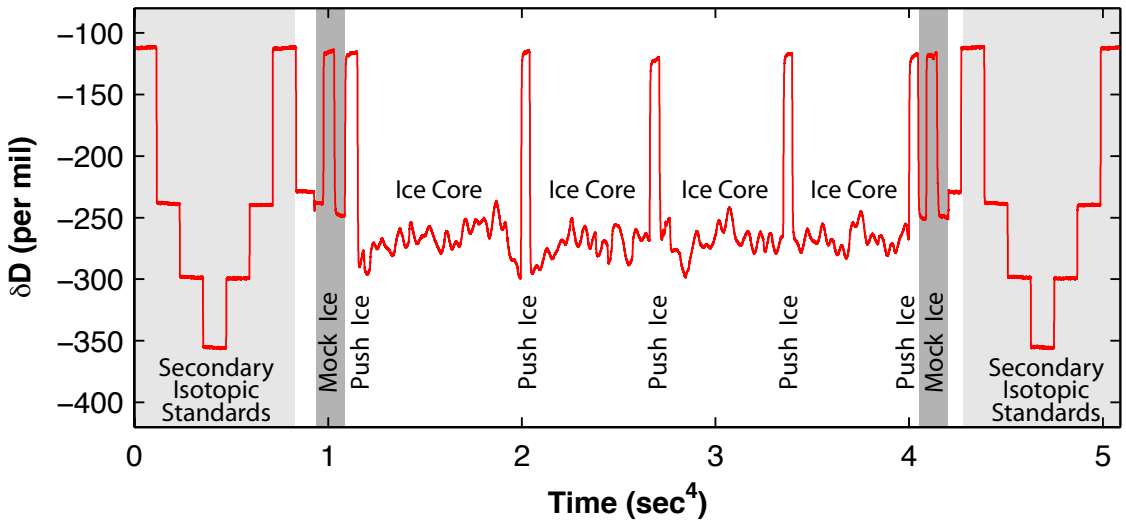

Figure 3.2. *A typical CRDS-CFA melt day consisting of the analysis of 12 meters of ice core sticks from the WDC. The light grey regions show the analysis of four calibrated secondary isotopic standards. The dark grey regions show the analysis of mock ice. The prominent white region shows the analysis of ice core sticks separated by short sections of push ice every fourth ice stick.*

Table 3.1.
Water isotope standards in units of per mil. The secondary standards (BSW, ASW, GSW, and PSW) were calibrated to primary standards (VSMOW2, VSLAP2, and GISP) in March 2010. The primary standards are reported with errors given by the IAEA. The secondary standards are reported with errors determined from the average standard deviation of multiple isotopic determinations across multiple analysis platforms (IRMS and CRDS).

Standards	δD	δD uncertainty	$\delta^{18}O$	$\delta^{18}O$ uncertainty
VSMOW2	0	0.3	0	0.02
VSLAP2	-427.5	0.3	-55.5	0.02
GISP	-189.5	1.2	-24.76	0.09
BSW	-111.8	0.2	-14.19	0.02
ASW	-239.3	0.3	-30.35	0.04
GSW	-298.7	0.2	-38.09	0.03
PSW	-355.6	0.2	-45.43	0.05

3.2.3. System Software

A graphical user interface (GUI) developed in Python is used to automate and record many of the on-line procedures related to carousel positioning, active Valco port, ice core depth registration, quality control (e.g. H_2O concentration), electrical conductivity, and commenting. This data, along with auxiliary data from the Picarro instrument, are collected from a serial port (MOXA UPORT 1610-8). All data is recorded at the same data frequency as the isotopic data generated by the Picarro L2130-*i*, and the data is exported as a raw text file generated by the Picarro and GUI. The raw data is then post-processed off-line by a separate semi-automated Python script. In the off-line analysis, we first identify and separate various analysis sections (e.g. secondary standards, mock ice, push ice, and ice cores) using integer values in a comment field. Second, depth data for the ice core sections (derived from the distance laser) is filtered for any outliers, as well as corrected for anomalous depth registration. The anomalous depth registration arises when an ice stick temporarily wedges against the acrylic tube during ice melt[7]. The top section of the ice remains stationary, while the bottom continues to melt. In the depth registration field, this appears as a flat line followed by an abrupt increase in depth (usually not longer than 15 seconds). These sections must be interpolated across to accurately characterize the depth of the accompanying isotopic measurements. Third, for every ice core section preceded by push ice, we assign an initial depth to the ice core section at the minimum derivative of the isotopic step-change. This effectively marks the mid-point of the isotopic step change and corresponds to the point

[7] On occasion, ice sticks can become temporarily stuck during melting, usually occurring in the brittle ice zone where broken ice pieces tend to wedge against the acrylic tube. To prevent wedging, we fitted a set of small vibrating devices made from DC motors with off-axis weight to the outside of the acrylic tubes. Vibrational frequency is controlled by a variable DC power supply that controls the rotation per minute of the motors.

when ice core isotopic values begin to dominate the preceding push ice signal. We tested this initial depth assignment scheme (as well as other schemes) with discrete samples of the same ice section, and the minimum derivative method was determined to work best. Finally, other computational analyses are performed related to isotopic calibration, signal processing, and data export. We further discuss these later in this chapter.

Besides data processing, the large amounts of data generated by CRDS-CFA require careful planning. The Picarro L2130-*i* generates and records isotopic data at approximately ~1.18 Hz intervals (0.85 second intervals). For a melt rate of 2.5 cm/min, this translates into sub-millimeter isotopic resolution, and roughly 2,800 data points per meter. At 12 meters of ice core per day, and recording 36 total quality control parameters, each melt day generates over 1.2 million data points. For a deep ice core of ~3,000 meters, this equates to ~300 million data points recovered in the course of 250 melt days (0.7 years). A computer with RAM upgrades and at least two-processing disks, plus a robust data back-up plan, is necessary to handle an analysis of this magnitude. In comparison, traditional IRMS produces about ~60 ice core data points per day, equating to the analysis of ~2.0 meters of ice per day at 3.0 cm resolution. For a deep ice core of ~3,000 meters, this would generate a total of 99,000 data points for a single parameter (which fits in an Excel file) and require about 4 years to complete, plus additional time commitment for cutting, packaging, melting and pipetting each ice sample. The CRDS-CFA system presented in this chapter provides a ~5-6 fold time savings and an order of magnitude improvement in data density compared to traditional IRMS methods.

3.2.4. System Performance

The protocol used for the correction of measured water isotope values to the VSMOW2-VSLAP2 scale is performed at the beginning and end of a melt day using secondary isotopic standards (i.e. BSW, ASW, GSW, and PSW). To perform the correction, we calculate "measured" secondary standard values by averaging BSW, ASW, and PSW over the last 5 minutes of each 20-minute run (four 20-minute runs are performed in a typical analysis day). These three "measured" values are then plotted versus the "known" secondary isotopic standard values previously calibrated against VSMOW2-VSLAP2. From the plot of measured vs. known values, a linear regression is used to define a calibration slope ($m_{calibrated}$) and a calibration intercept ($b_{calibrated}$). We then correct the GSW isotopic standard using the following equation:

$$\mathrm{x}_{corrected} = y_{measured} - \frac{b_{calibrated}}{m_{calibrated}} \tag{3}$$

where $y_{measured}$ is the GSW value measured on the CRDS-CFA system (averaged over the last 5 minutes of each 20 minute run), $b_{calibrated}$ is the y-intercept of the linear regression, $m_{calibrated}$ is the slope of the linear regression, and $x_{corrected}$ is the GSW value calibrated to the VSMOW2-VSLAP2 scale. This same calibration is done for all ice core isotopic values. We also define daily values for precision and accuracy of the CRDS-CFA system. The precision is determined by the standard deviation of the average of the last 5 minutes of each 20-minute secondary standard run, while the accuracy is defined as the difference of GSW from its known value. These values can then be compared over the long-term to monitor drift in the CRDS-CFA system.

The stability of the Picarro CRDS analyzer is determined by tests of Allan variance (Allan, 1966), which is a method for analyzing a series of data to determine intrinsic noise in the measurement system as a function of the length of the measurement. The length of the measurement is also known as the integration time (τ). In CRDS, the integration time refers to how much time a parcel of vapor is present in the laser cavity. The Allan variance is defined as:

$$\mathrm{AVAR}^2(\tau) = \frac{1}{2(n-1)} \sum_{i=1}^{n-1} (y(\tau)_{i+1} - y(\tau)_i)^2 \tag{4}$$

where τ is the integration time, $y(\tau)$ is the average value of the measurements in an integration bin of length τ, n is the total number of bins, and AVAR is the Allan variance. The idea of integration bins simply refers to taking a long sequence of data and dividing it into smaller successive bins of a certain averaging time τ, and then averaging the values in each bin to determine values for $y(\tau)$. To obtain an AVAR^2 vs. τ curve, the computation must be repeated many times for different values of τ (i.e. different integration bin values such as 10 sec, 20 sec, 30 sec, etc.).

We determine Allan deviation (the square root of Allan variance) by continuous injection of isotopically homogenous water into the CRDS-CFA for many hours at a time. The Allan deviation values for a 7-hour run are plotted in Figure 3.3 and selected Allan deviation values are shown in Table 3.2. The Allan deviation shows that the CRDS-CFA system short-term noise is negligible (i.e. 0.1 per mil in δD for a 10-second integration time; a small value compared to the isotopic signal seen in ice cores), that the system is most stable at integration time values of 1,000 seconds or greater, and that the

system is stable over all integration times to at least 3 hours in length. We provide an estimate of uncertainty on CRDS-CFA isotopic measurements later in this chapter.

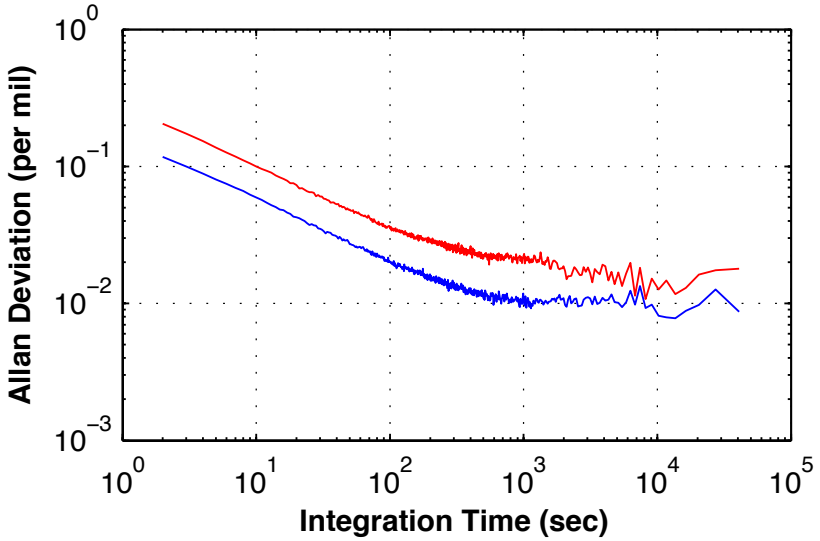

Figure 3.3. *A 7-hour analysis of Allan deviation for δD (red) and $\delta^{18}O$ (blue) on the CRDS-CFA using isotopically homogenous water vapor.*

Table 3.2.
Selected Allan deviation values in per mil for a 7-hour analysis of isotopically homogenous water on the CRDS-CFA system.

Integration Time (sec)	δD	$\delta^{18}O$
10	0.1	0.063
60	0.045	0.026
600	0.022	0.01
3600	0.017	0.009

3.2.5. Mixing Correction

During a typical analysis day, every 4th ice stick is separated by isotopically distinct push ice. Ideally, the isotopic shift between push ice and the beginning of an ice core stick would occur instantaneously. However, mixing effects in the CRDS-CFA system result in a delayed transition. Possible contributors to the mixing effect include: liquid mixing at the melt head and debubbler; liquid drag on tubing walls; vapor mixing in the nebulizer, Pyrex vaporizing tube, and laser cavity; adsorption of water molecules onto the laser cavity walls; vapor interactions with two Picarro instrument filters (Mykrolis Wafergaurd) prior to entering the laser cavity; and diffusional effects that can occur at any point in the CRDS-CFA system. We do not attempt to quantify these mixing effects, except to mention that lab tests indicate the removal of the 1st Picarro instrument filter can reduce the mixing effect by one-third to one-half. However, the removal of the filter also risks damaging the laser cavity, and we opt to leave the filter in place.

In total, the mixing of isotopic values during a step-change results in the loss ~5-7 cm of ice core data. However, the mixing effect can be partially corrected by recording the time the step-change occurs at the melt head, and then comparing the expected isotopic values (i.e. those expected from an instantaneous isotopic step change) to the actual recorded isotopic values (i.e. those of the delayed isotopic reaction). We quantify mixing coefficients (c_t) using mock ice (i.e. during a shift from -240 to -120 per mil δD). For example, at a time of 5 seconds after an instantaneous shift in mock ice at the melt head, the measured isotopic value (not including the delay in transport from the melt head to the Picarro instrument) may only be 2% of the expected value. After 40 seconds, the measured value may be 40% of the expected value, and after 100 seconds, the measured

value may be 95% of the expected value. For these three examples, the mixing coefficients would be 0.02, 0.40, and 0.95, respectively. To remove noise from the c_t calculation, we average both of the mock ice isotopic transitions measured during a typical analysis day, normalize between 0 and 1, and apply a cubic spline. The following equation describes the water isotope mixing correction:

$$\delta_{tc} = \frac{\delta_t - \delta_{t-1}(1 - c_t)}{c_t} \tag{5}$$

where δ_t is the measured isotopic value at time t, δ_{t-1} is the previously measured isotopic value at time $t-1$, c_t is the memory coefficient at time t, and δ_{tc} is the corrected isotopic value at time t. An example of an isotopic mixing correction is shown in Figure 4. Even with noise removed, we find that the mixing correction can only be applied at $c_t \geq 0.65$ due to inconsistencies in the timing of the isotopic transition related to small perturbations in flow rate, which become amplified in the mixing correction at small c_t. For $c_t \geq 0.65$, the correction saves an additional ~2.25-3.15 cm of data that would otherwise be discarded, while isotopic values at $c_t \leq 0.65$ are discarded, resulting in a loss of ~2.75-3.85 cm of data.

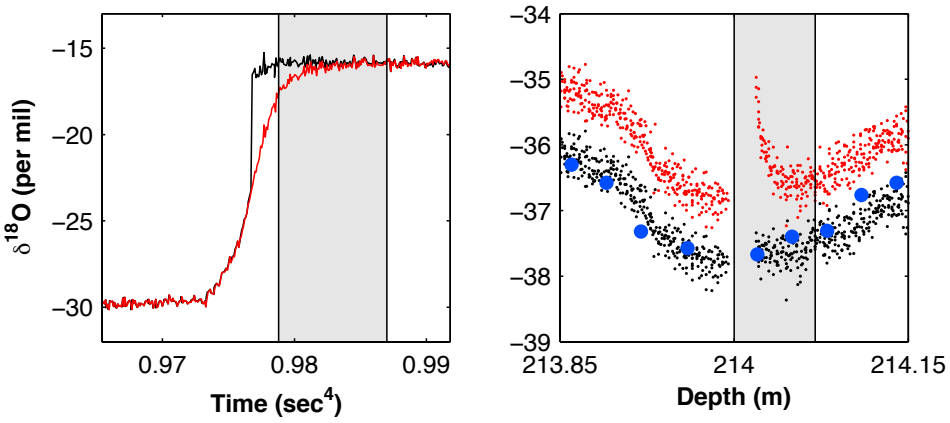

Figure 3.4. *Mixing corrections for mock ice (left) and the beginning of an ice core section (right). The ice core mixing correction is based upon a known step-function change defined by the mock ice, from which mixing coefficients are determined. Red represents raw uncorrected isotopic data with no memory correction, black represents VSMOW-VSLAP2 corrected data with the memory correction applied, blue dots represent 3 cm IRMS discrete samples, and the grey region represents the time and depth range of corrected data that would otherwise be discarded.*

3.2.6. Diffusion Length

The transfer function and impulse response function of the system can be defined using mock ice or secondary water standards. The transfer function is simply the system response to an instantaneous isotopic step-change at the melt head or Valco stream selection valve, which appears as a delayed response due to mixing and diffusion in the system. The impulse response function is the first derivative of the transfer function. The spread or deviation of the impulse response function corresponds to the amount of mixing and diffusion that has occurred in the CRDS-CFA system: more spread means more mixing and diffusion. The standard deviation of the impulse response corresponds to the

"diffusion length[8]", which defines the average movement of a water molecule in the time or depth domain relative to its original position prior to analysis in the CRDS-CFA system. For ice sticks, the diffusion length depends on a water molecule's original position in the ice before coming in contact with the melt head. For secondary isotopic standards, the diffusion length depends on a water molecules original position in a vial of water connected to the Valco stream selection valve. Figure 3.5 shows transfer functions and impulse response functions of the CRDS-CFA system for δD and $\delta^{18}O$. The derivation for these functions is discussed throughout the rest of this section.

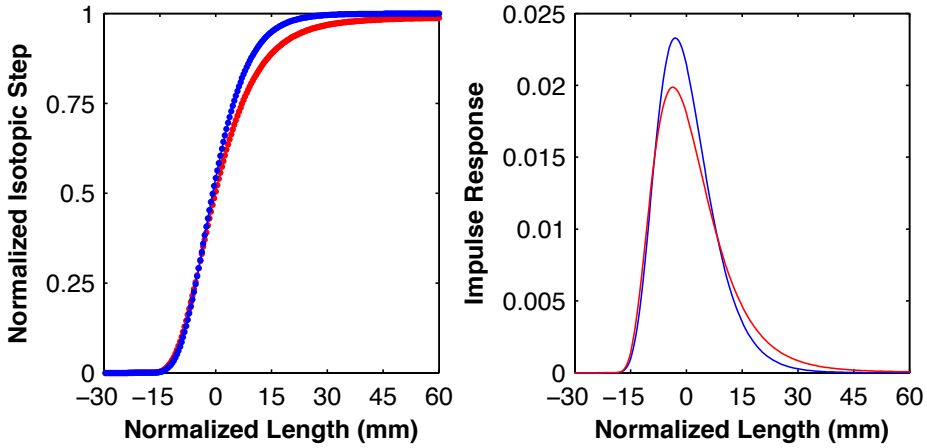

Figure 3.5. *The log-log CDF transfer functions (left) and skew normal impulse response functions (right) of the CRDS-CFA system for δD (red) and $\delta^{18}O$ (blue). The functions are derived from a normalized mock ice isotopic step change from -240 per mil to -120 per mil. The normalized length scale is calculated using an average melt rate of 2.5 cm per minute.*

[8] The diffusion length defines the combined effects of mixing and diffusion occurring in the CRDS-CFA system. To maintain consistency with other water isotope CFA publications, we retain the conventional "diffusion length" terminology when discussing both diffusion and mixing.

The difference in diffusion lengths between ice sticks and secondary isotopic standards is useful for partitioning mixing effects in different parts of the CRDS-CFA system. Ice stick diffusion lengths ($\sigma_{mock\ ice}$; determined from mock ice step changes) characterize mixing in the entire CRDS-CFA system, including the melt head, tubing, debubbler, nebulizer, Pyrex furnace tube, and laser cavity. Conversely, secondary isotopic standards diffusion lengths (σ_{SWS}; determined from secondary isotopic standards step changes) characterize mixing primarily in the vapor phase because the liquid tubing pathway from the Valco stream selector valve to the nebulizer and furnace (where liquid water is converted to vapor) is short. In previous work by Gkinis et al. (2010, 2011), a transfer function is fit to an isotopic step change using a scaled version of the cumulative distribution function (CDF) of a normal distribution described by:

$$\delta_{model}(z) = \frac{C_1'}{2}\left[1 + erf\left(\frac{z - z_o}{\sigma_{step}\sqrt{2}}\right)\right] + C_2' \tag{6}$$

where C_1', C_2', z_o, and σ_{step} are estimated by least squares optimization. The impulse response of the system is described by a Gaussian:

$$G_{cfa}(z) = \frac{1}{\sigma_{cfa}\sqrt{2\pi}} e^{-\frac{z^2}{2\sigma_{cfa}^2}} \tag{7}$$

where σ_{cfa} is the diffusion length term (1σ) estimated by least squares optimization.

We modify the Gkinis et al. (2010, 2011) approach by fitting a transfer function in the form of a log-normal CDF multiplied with a log-normal CDF (log-log fit):

$$\delta_{model}(z) = \frac{1}{2}\left[1 + erf\left(\frac{z - z_1}{\sigma_1\sqrt{2}}\right)\right] \cdot \frac{1}{2}\left[1 + erf\left(\frac{z - z_2}{\sigma_2\sqrt{2}}\right)\right] \quad (11)$$

where z_1, z_2, σ_1, and σ_2 are predetermined to maximize the fit. The σ_1 and σ_2 values should not be confused with $\sigma_{mock\ ice}$ or σ_{SWS}. This log-log fit matches CRDS-CFA isotopic step changes better than a normal CDF. Then, rather than using a derivation of the log-log fit, we simplify the calculation of the impulse response function by using a skew normal probability density function (SN-PDF; Azzalini and Valle, 1996) fitted to the first derivative of a mock ice transition. The SN-PDF is described by:

$$\delta_{model}(z) = 2\phi(x)\Phi(\alpha x) \quad (8)$$

where $\phi(x)$ is the standard normal PDF, $\Phi(x)$ is the standard normal CDF, and α is a shape parameter. The transform $x \rightarrow \frac{x-\varepsilon}{\omega}$ introduces the location parameter ε and the scale parameter ω. The σ_{cfa} term is recovered using the $\delta_{parameter}$ and variance equation:

$$\delta_{parameter} = \frac{\alpha}{\sqrt{1 + \alpha^2}} \quad (9)$$

$$\sigma_{cfa}^2 = \omega^2\left(1 - \frac{2\,\delta_{parameter}^2}{\pi}\right) \quad (10)$$

where α, ε, and ω are estimated by least squares optimization. The $\delta_{parameter}$ should not be confused with δD or $\delta^{18}O$. Using equation 5 and equation 8, diffusion length values can be determined for $\sigma_{mock\ ice}$ and σ_{SWS} transitions (Table 3.3), where the difference between the two is the amount of diffusion and mixing occurring in the liquid phase of the WI-CFA system. We find that about ~52 to 55% of the mixing and diffusion in the CRDS-CFA system occurs in the vapor phase (i.e. downstream of the Valco stream selection valve to the laser cavity), while the remainder occurs in the liquid phase of the system (i.e. downstream of the melt head to the Valco stream selection valve).

Table 3.3.
Diffusion lengths determined from mock ice step changes ($\sigma_{mock\ ice}$) and from secondary isotopic standards step changes (σ_{SWS}). The difference in $\sigma_{mock\ ice}$ and σ_{SWS} is the amount of diffusion and mixing occurring in the liquid phase of the CRDS-CFA system. Values are given in seconds (meters) for skew normal and normal PDF impulse response functions based on a melt rate of 2.5 cm/min.

	σ_{SWS}		$\sigma_{mock\ ice}$	
Fit Type	**δD**	**$\delta^{18}O$**	**δD**	**$\delta^{18}O$**
Skew	10.3 (0.004)	9.6 (0.004)	18.7 (0.008)	17.7 (0.007)
Normal	10.2 (0.004)	9.4 (0.004)	19.1 (0.008)	17.4 (0.007)

Both the log-log fit transfer function and skew normal impulse function capture asymmetric mixing and diffusion occurring in the CRDS-CFA system over time, which is not previously discussed in the literature (see Figure 3.5). We speculate that the fast isotopic response in the first half of an isotopic step change is related simply to the input of a new signal into the vapor cavity, while the slow isotopic response in the second half of an isotopic step change (i.e. the long trailing tail) is related to "sticky" water

adsorption on the walls of the laser cavity from prior water input that takes a certain amount of time to overcome. We do not attempt to investigate this further, but do suggest that new generation water isotope CFA systems test both skewed and normal diffusion length properties to ensure that mixing and diffusion are not unreasonably skewing results.

3.3. Results

3.3.1. Greenland Test Ice Replication

To test WI-CFA reproducibility, nine sticks of ice were cut from a single meter of Greenland test ice (GTI) at about 400 meters depth, obtained from the National Science Foundation National Ice Core Laboratory (Lakewood, Colorado) This ice was a byproduct of initial tests of the US. DISC (Deep Ice Sheet Coring) Drill performed in Greenland in 2006 (Johnson et al., 2007). The same drill was deployed in West Antarctica to obtain the WAIS Divide ice core. Seven of the nine GTI sticks were analyzed on the CRDS-CFA system. Four out of seven of these ice sticks were measured continuously, while three of the ice sticks were broken into parts to test mixing correction and depth registration methodology. The final two GTI sticks were discretely sampled at 1 cm and 5 cm increments, melted into vials, and analyzed on a separate Picarro L2130-*i*. A plot of all GTI analyzed for δD, $\delta^{18}O$, and dxs is shown in Appendix A, Figure 3.9.

The isotopic data for the seven 1-meter long GTI sticks analyzed on the CRDS-CFA system was measured at sub-millimeter resolution. This data was then averaged to 1 cm successive values (GTI-1cm) for each stick (i.e. seven values total at each 1 cm

increment), from which the average standard deviation across all seven GTI sticks at each centimeter increment was determined (for a total of 100 standard deviation values). We take the average of the standard deviation values to estimate the uncertainty of the CRDS-CFA system (Figure 3.6). This approach gives a combined estimate of the analytical error on the isotope ratio plus additional isotopic uncertainty introduced in the depth registration process for each ice stick. It is the total uncertainty of the system. We find total uncertainty values (1σ) for δD, $\delta^{18}O$, and dxs of 0.55 per mil, 0.09 per mil, and 0.55 per mil, respectively. For comparison, traditional IRMS measurements for δD, $\delta^{18}O$, and dxs are commonly reported with uncertainties of about 1.0 0.1, and 1.3 per mil, respectively.

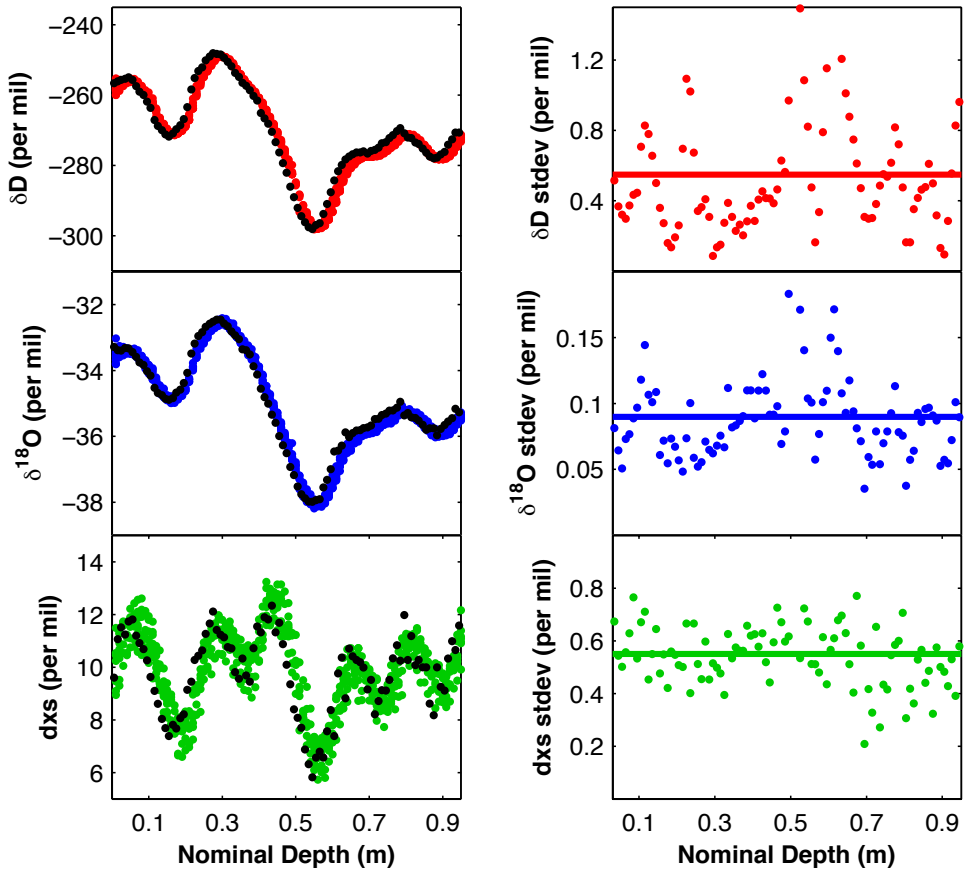

Figure 3.6. *Greenland test ice (GTI) for a nominal 1-meter section. In the left column, seven GTI sticks averaged to 1 cm increments measured on the CRDS-CFA system for* δD *(red dots),* $\delta^{18}O$ *(blue dots), and dxs (green dots) compared with discrete 1 cm samples (black dots) measured on a Picarro L2130-i. In the right column, the standard deviation of seven GTI values is taken at each 1 cm increment (red, blue, and green dots). The average standard deviation is shown by the horizontal line, which represents the total system uncertainty (1σ) for δD,* $\delta^{18}O$*, and dxs.*

Previously, we mentioned a number of possible sources of mixing or analytical uncertainty in the CRDS-CFA system: depth registration; liquid mixing at the melt head and in the debubbler; flow rate fluctuations; drag in rubber tubing; vapor mixing in the nebulizer, Pyrex furnace tubing, and laser cavity; and isotopic analysis on the Picarro

instrument. These can be subdivided into two parts: uncertainty arising on the preparation side of the system (i.e. uncertainty occurring prior to vapor entering the Picarro instrument) and uncertainty arising on the CRDS side of the system (i.e. uncertainty occurring in the laser cavity and during isotopic analysis). We can isolate the CRDS uncertainty by analyzing a continuous stream of isotopically homogenous water (IHW) inputted directly into the Picarro instrument. To determine a CRDS uncertainty of comparable resolution to the total system uncertainty (which we determined using 1 cm averages of Greenland test ice), we take averages of the IHW over 24-second consecutive intervals, which corresponds to the time needed to melt 1 cm of ice at a melt rate of 2.5 cm/min. The standard deviation of 100 consecutive 24-second averages of the IHW (the equivalent of a meter long section of ice) yields the CRDS uncertainty. The difference in the CRDS uncertainty and the total system uncertainty gives an estimate of the uncertainty arising on the preparation side of the system (Table 3.5). We find that uncertainty on the preparation side of the system for δD, $\delta^{18}O$, and dxs is ~83%, 56%, and 42% of the total system uncertainty, respectively. The high value for δD preparation uncertainty reflects the fact that the CRDS method is better resolved for δD than $\delta^{18}O$, resulting in low δD CRDS uncertainty (only ~17% of total system uncertainty).

Table 3.5.
The isotopic measurement uncertainty (1σ) of varying parts of the CRDS-CFA system given in per mil. The difference of the total system uncertainty derived from GTI (Total) and that arising from the Picarro instrument (CRDS) gives an estimate of the uncertainty introduced on the preparation side of the system (Prep). The preparation uncertainty includes all uncertainty except that arising from mixing or analysis in the Picarro instrument. Plots for the Picarro uncertainty are shown in Appendix A, Figure 3.10.

Measurement	Total	CRDS	Prep.
δD	0.55	0.09	0.46
$\delta^{18}O$	0.09	0.04	0.05
dxs	0.55	0.32	0.23

As a final analysis using GTI, the reproducibility of GTI-1cm data and discrete-1cm data taken from the same meter of Greenland ice are compared. Both are analyzed using a Picarro L2130-*i*. A scatter plot and linear regression of the two variables gives a slope, y-intercept, and R^2 value (Appendix A, Figure 3.11). The coefficient of determination values (R^2) for δD and $\delta^{18}O$ are 0.99 and 1.00, respectively, while dxs remains inherently more difficult to measure with an R^2 value of 0.88. Because this test shows the comparison of seven GTI sticks analyzed on CRDS-CFA compared with a single ice stick measured discretely on CRDS, the R^2 values represent an idealized version of system reproducibility using multiple ice sticks. For a typical ice core analysis on CRDS-CFA, however, we only have the option to measure a single ice core stick. We explore system reproducibility for this "typical single ice stick scenario" in the following section.

3.3.2. WAIS Divide Ice Core Replication

A comparison of traditional IRMS discrete measurements and CRDS-CFA measurements analyzed at the INSTAAR Stable Isotope Lab was performed on the WAIS Divide Ice Core (WDC) over depths of ~212-222 meters (Figure 3.7). The discrete samples (3 cm cuts) were measured using a uranium reduction technique for δD (Vaughn et al., 1998) and a CO_2/H_2O equilibration method for $\delta^{18}O$ (Epstein; 1953; Craig et al., 1963). We find that the amplitude of the δ signal between the IRMS and CRDS-CFA techniques is nearly identical, except for a disagreement in a single amplitude value at ~216.2 meters of ~4 per mil (δD). There is also a systematic δ offset over the entire ten-meter section, where CRDS-CFA measurements are about 2-4 per mil less on average than the IRMS measurements. We suggest that the offset was caused by fractionation within the discrete sample vials over time, which would result in decreased or negative dxs values. Indeed, the dxs values in the IRMS samples are decreased and more negative over the ten-meter section as compared to CRDS-CFA, sometimes with offsets of up to 7 per mil.

A second WDC comparison test was performed between high-resolution CRDS-CFA measurements and low-resolution discrete CRDS measurements (Figure 3.7). The low-res data were measured at the University of Washington using a Picarro 2120-*i* at ~50 cm increments (Steig et al., 2013). To determine inter-lab reproducibility, we average the high-resolution CRDS-CFA data to the exact low-resolution discrete CRDS increments (referred to as down-sampling). Over a depth of ~212-222 meters, scatter plot comparisons of the down-sampled high-res data and low-res measurements have R^2 values for δD, $\delta^{18}O$, and dxs of 0.99, 0.99, and 0.29, respectively. The maximum per mil

offset for δD, $\delta^{18}O$, and dxs values are 2.0, 0.30, and 1.95 per mil, respectively. As with the comparison of CRDS-CFA and IRMS, δD and $\delta^{18}O$ are reproducible for down-sampled high-resolution CRDS-CFA data and low-resolution discrete CRDS data. The dxs measurements are also improved, with no offset in mean values, but do not exhibit a high R^2 value. The combination of the above results lead to the following conclusions: 1) The δD and $\delta^{18}O$ data is reproducible between traditional IRMS and CRDS-CFA techniques, as well as between labs. 2) The dxs data may only be replicable over longer time scales. 3) However, the analysis of GTI shows that dxs is reproduced seven different times on the CRDS-CFA system presented in this study. And, the seven GTI sticks are strongly correlated ($R^2 = 0.88$) with a 1 cm discretely sampled GTI stick. Therefore, we are unsure why the CRDS-CFA dxs measurement comparisons with IRMS and between labs do not exactly agree.

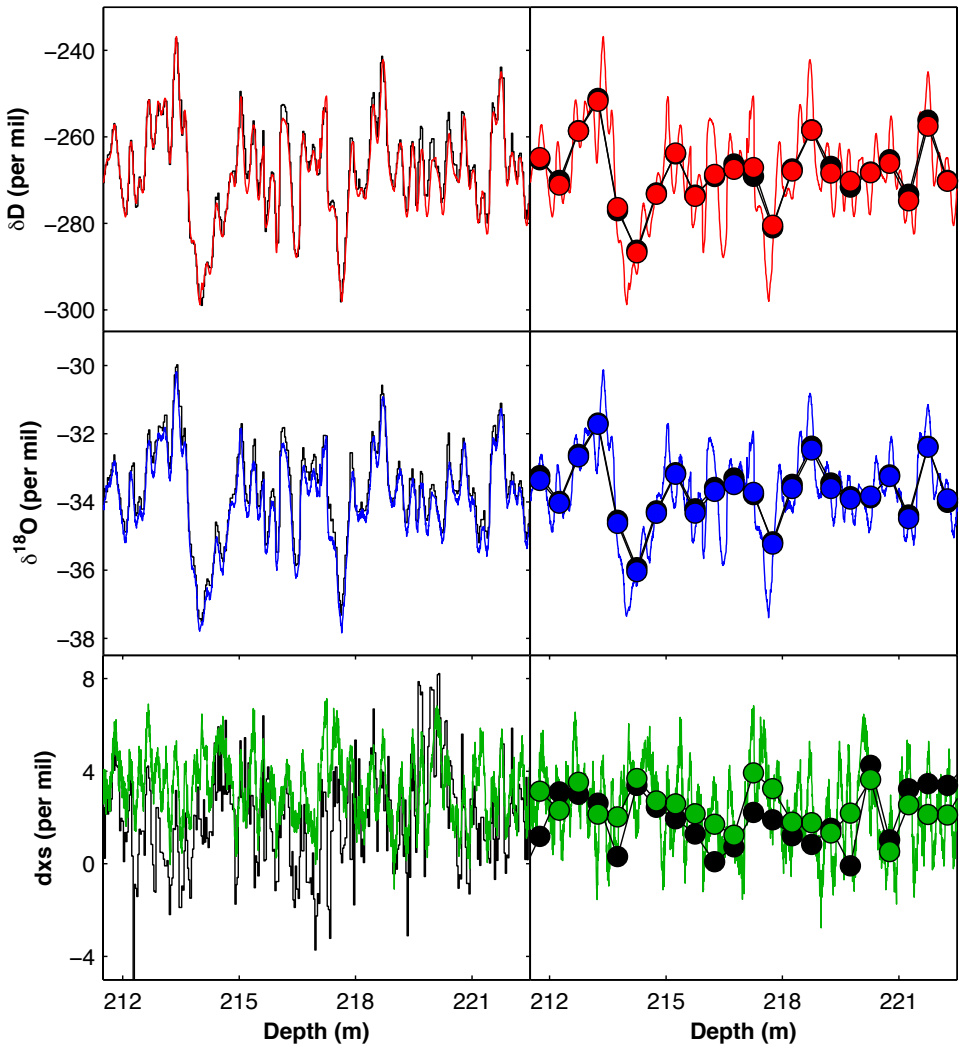

Figure 3.7. *Data from the WDC over a depth range of ~212-222 meters. In the left column, CRDS-CFA data for δD (red line), $\delta^{18}O$ (blue line), and dxs (green line) compared with traditional IRMS discrete samples (black lines). In the right column, comparison of CRDS-CFA high-res data (red, blue, and green lines), low-resolution discrete samples (black dots), and down-sampled CRDS-CFA data (red, blue, and green dots).*

3.3.3. South Pole Firn Replication

Measuring firn ice by CFA methods involves additional complexity relative to deep ice. Due to the increased porosity of firn ice, liquid water at the melt head can wick

upwards by capillary action through the pore spaces, artificially smoothing the isotopic signal and decreasing signal amplitude. This can, for example, alter frequency analysis calculations or cause the misinterpretation of the size of summer-winter signals. To test the ability of the CRDS-CFA system to measure firn samples, two identical 1-meter sections from 4, 9, and 29 meters depth in a South Pole ice core are analyzed on CRDS-CFA (hereafter referred to as South Pole Firn; SPF). The CRDS-CFA results are then compared with a third identical 1-meter SPF section discretely sampled at 1 cm increments using a Picarro L2130-*i* (Figure 3.8).

Based upon a steady-state Herron and Langway density model (Herron and Langway, 1980), the SPF sticks have estimated densities of 340, 386, and 562 kg/m^3, respectively (assuming an average accumulation rate of 0.085 m/yr, an average temperature of -50°C, and an average snow density in the top 2 meters of 300 kg/m^3). For comparison, the density of snow at the surface of the WAIS Divide ice core is ~370 kg/m^3. Because of the low-density firn sticks, the pump rate was increased to prevent wicking during this experiment, which increased the flow rate of water through the CRDS-CFA system. We observed that no wicking occurred during the melting process.

The data show that a loss in δD amplitude not surpassing 11% occurred in the CRDS-CFA data relative to the discretely sampled data, while maximum depth registration offsets were 4 cm, <0.5 cm, and <0.5cm at 4, 9, and 29 m depth, respectively. Furthermore, at 29 meters depth, CRDS-CFA δD measurements are anomalously higher than discrete measurements in the first 20 cm. At 4 meters depth, the phase of the CRDS-CFA and discrete δD signal is offset by about 3 cm over the last ~60 cm of the SPF section, which is likely related to imprecise depth registration on the CRDS-CFA related

to the increased flow rate (i.e. this SPF section required a flow rate of 4.4 cm/min instead of the normal 2.5 cm/min) and density variations across annual layers. The dxs values for the CRDS-CFA and 1 cm discrete signals have the same pattern and range of values, except for small offsets in the last ~60 cm of the 4-meter depth section and again at ~9.30 and 9.55 meters.

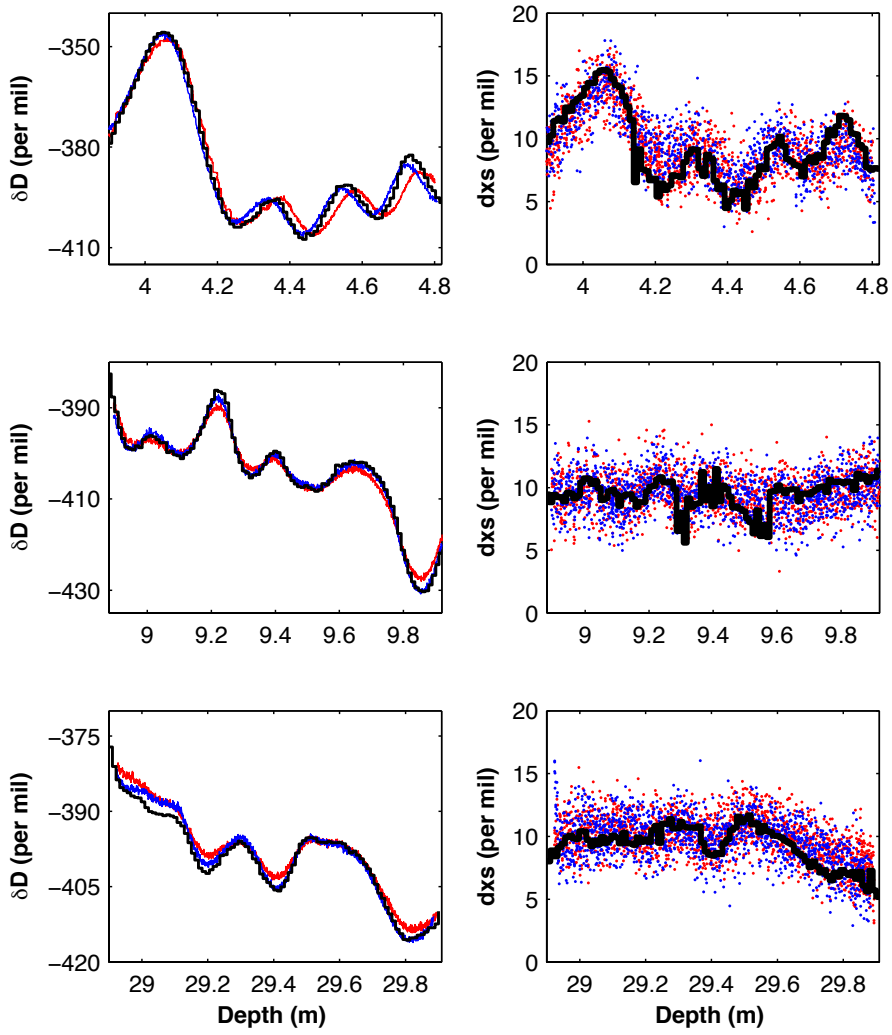

Figure 3.8. *Replicate SPF ice measurements of δD and dxs at depths of ~4, 9, and 29 m, corresponding to densities of 340, 386, and 562 kg/m^3, respectively. The red and blue data are from SPF sticks analyzed on the CRDS-CFA system and the black data are 1 cm discrete samples analyzed on a separate Picarro L2130-i.*

3.4. Discussion

In comparison to other CFA systems (e.g. Gkinis et al., 2010, 2011 and Maselli et al., 2012), the INSTAAR CRDS-CFA system has a number of important differences: 1) The entire system is operated solely for the purpose of isotopic measurements, so melt rate and performance can be optimized for water isotope analysis without complications arising from prior in-line chemical analysis using the same water stream; 2) New hardware has been implemented to control melt head temperature within ± 0.1 °C by using internally circulating dilute propylene glycol from a temperature-controlled bath; 3) The conversion of liquid water to vapor utilizes a high-efficiency glass concentric nebulizer driven by high pressure dry air, which provides water vapor concentrations consistently in the range of 20,000-25,000 ppm to the Picarro instrument; 4) The CRDS-CFA uses a reduced flow rate and achieves higher-resolution (>1Hz) measurements by utilizing an updated Picarro instrument, both of which increase isotopic data density. 5) An automated rotating carousel delivers up to 15 vertically oriented ice sticks to the melt head without interruption; 6) A custom graphical user interface (GUI) and a python-application allows for integration and export of multiple external data streams at the same sampling interval as the isotopic data measurements occurring on the Picarro instrument; and 7) The small cross sectional area of the ice stick (1.3 cm^2) in combination with adjusted pump rates appears to limit wicking in firn sticks at the melt head, yielding measurements that are similar in phase and amplitude (but not exact) to discrete measurements

3.4.2. Improvements in Methodology for Next Generation WI-CFA Systems

One method for determining uncertainty in a Cavity Ring Down Spectroscopy-Continuous Flow Analysis (CRDS-CFA) system is partitioning. We have outlined a method to partition analytical uncertainty occurring in a CRDS instrument and from preparation uncertainty associated with the rest of the CFA system. First, we find the total uncertainty of the system using replicate ice sticks, and then we isolate the analytical uncertainty by directly injecting isotopically homogenous water into the CRDS instrument. The difference in the two values (properly scaled) is the uncertainty arising from just the preparation side of the system. This allows for testing of the performance of the system in conversion of solid ice to liquid water to vapor for continuous delivery to a CRDS instrument. If the preparation uncertainty is too high, system redesign should be considered. If preparation uncertainty is tested multiple times per year, the long-term performance of the preparation system can be monitored.

We also suggest a mixing correction be applied to isotopic step-changes preceding the analysis of an ice core stick. In our methodology, a δD isotopic step-change of about ~100-180 per mil occurs from push ice-to-ice core every 4^{th} ice core stick. Due to isotopic mixing of the two signals, about ~5-7 cm of water isotope data is lost during this transition. However, defining mixing coefficients can save some of this information. This requires analyzing isotopic step changes of known values to determine a transfer function that characterizes mixing and diffusion in the system at a certain flow rate. We find that about ~2.25-3.15 cm of previously "lost information" can be recovered at a flow rate of 2.5 cm/min. For a ~3000 meter ice core, there are about 750 step changes (every 4^{th} stick), which equates to ~16.9 to 23.7 meters of isotopic data that can be saved.

In practice, the memory correction is not always achieved. For example, varying ash or dust concentrations may reduce flow rate through the filters at certain times, rendering previously determined mixing coefficients unusable for a slower flow rate. In these instances, isotopic data must be trimmed the full ~5-7 cm to remove the isotopically mixed section. We manually record instances of reduced flow rate, but improved methods can be achieved by using a flowmeter or optical sensing of ice stick movement just above the melt head. Furthermore, the sensitivity of the dxs parameter to small changes in δD and $\delta^{18}O$ requires that mixed dxs sections always be discarded.

One of the largest sources of error introduced in the WI-CFA system is depth registration, which can be summarized in three parts. First, there is a delay between ice melt at the melt-head, where depth registration is recorded, and isotopic measurement at the CRDS instrument. The actual delay is defined by flow rate through the system. Ideally, flow rate through the system is constant, but certain occurrences can cause variable flow, such as small perturbations in melt-head temperature, dust or ash load on the filter, or a constriction in the nebulizer. Therefore, depth registration may sometimes be assigned at depths slightly too shallow or slightly too deep depending on the behavior of the system at any given time. Second, initial depth registration is difficult to determine at transitions. We assign initial depth registration at the minimum derivative of an isotopic step change from push ice-to-ice core, which is an estimation of the halfway point of the isotopic change. However, the temporal location of the 50% mark is not constant, and other methodologies may work better and should be tested for accuracy by comparison to discrete samples. Third, ice wedging can occur in the acrylic tubes that hold ice sticks, resulting in inaccurate depth registration. For example, ice sometimes

wedges in the upper part of the tube, while ice continues to melt in the lower tube. Since the laser depth measurements occur overhead, depth registration will remain constant during ice wedging even as the ice continues to melt below. These occurrences are easy to detect in a depth registration file, appearing as a flat line deviation from an otherwise constantly increasing depth registration. The inaccuracy can be corrected by interpolation of depth values registered before and after the ice wedge event. However, installing video capture with optical recognition software just above the melt head can eliminate these depth registration inaccuracies. An additional possibility, discussed in Maselli et al. (2012), is to install two electrical conductivity measurement devices; one at the melt head and another just before liquid water is vaporized at the furnace. Therefore, movement of liquid water through the system can be tracked and a more reliable depth can be assigned just before water enters the CRDS instrument (this would also improve the mixing correction).

A final consideration for any CRDS-CFA water isotope system is limiting the amount of mixing and diffusion occurring in the system (i.e. the diffusion length). We found that about 45 to 48% of mixing and diffusion occurred in the liquid phase within the system, which can be improved by decreasing the volume of the debubbler and limiting the amount of tubing. The other ~52 to 55% of mixing and diffusion occur in the vapor phase, which can be improved by reducing the flow rate, decreasing the volume of glass tubing in the furnace, and modifying the CRDS instrument by reducing the volume of the cavity and/or removing the first of two filters.

3.5. Conclusion

We have presented a high-resolution continuous flow analysis (CFA) system based on cavity ring down spectroscopy technology (CRDS) that is specifically designed for water isotope analysis of ice cores. The CRDS–CFA system builds off previous water isotope CFA studies (Gkinis et al., 2010, 2011 and Maselli et al., 2012) and includes novel updates to the ice delivery mechanism, the melt head, and the water vaporizer. We also present new calculations and methodologies for determining partitioned uncertainty and partitioned diffusion lengths of the system.

The total system uncertainty for δD, $\delta^{18}O$, and dxs is 0.55 per mil, 0.09 per mil, and 0.55 per mil, respectively. Compared to traditional IRMS discrete measurement uncertainty (1.0, 0.1, and 1.3, respectively), this represents a factor of 1.8 decrease in δD uncertainty, a small decrease in $\delta^{18}O$ uncertainty, and a factor of 2.4 decrease in dxs uncertainty. We find that uncertainty on the preparation side of the system (i.e. all processes occurring outside the CRDS instrument) is ~83%, 56%, and 42% of the total system uncertainty for δD, $\delta^{18}O$, and dxs, respectively. The high value for δD preparation uncertainty reflects the fact that the CRDS method is better resolved for δD than $\delta^{18}O$. The total diffusion lengths of the system for δD and $\delta^{18}O$ are 0.8 cm and 0.7 cm, respectively. We find that about ~52 to 55% of the mixing and diffusion in the CRDS-CFA system occurs in the vapor phase, while the remainder occurs in the liquid phase of the system.

Replicates tests of seven Greenland ice sticks show that 1 cm averages of CRDS-CFA δD, $\delta^{18}O$, and dxs measurements correlate with 1 cm discrete samples with R^2 values of 0.99, 1.00, and 0.88, respectively. Inter-lab comparisons of high-resolution

CRDS-CFA measurements down-sampled to match low-resolution 50 cm discrete samples have R^2 values of 0.99, 0.99, and 0.29, respectively. The three dxs measurement techniques presented in this chapter (CRDS-CFA, IRMS discrete, CRDS discrete) appear to vary within the noise, which may result in low correlation values. However, when a set of seven replicate ice sticks are measured on CRDS-CFA, the average of the replicate dxs values converge on dxs values measured discretely on CRDS.

3.6. Appendix A: CFA System Tests

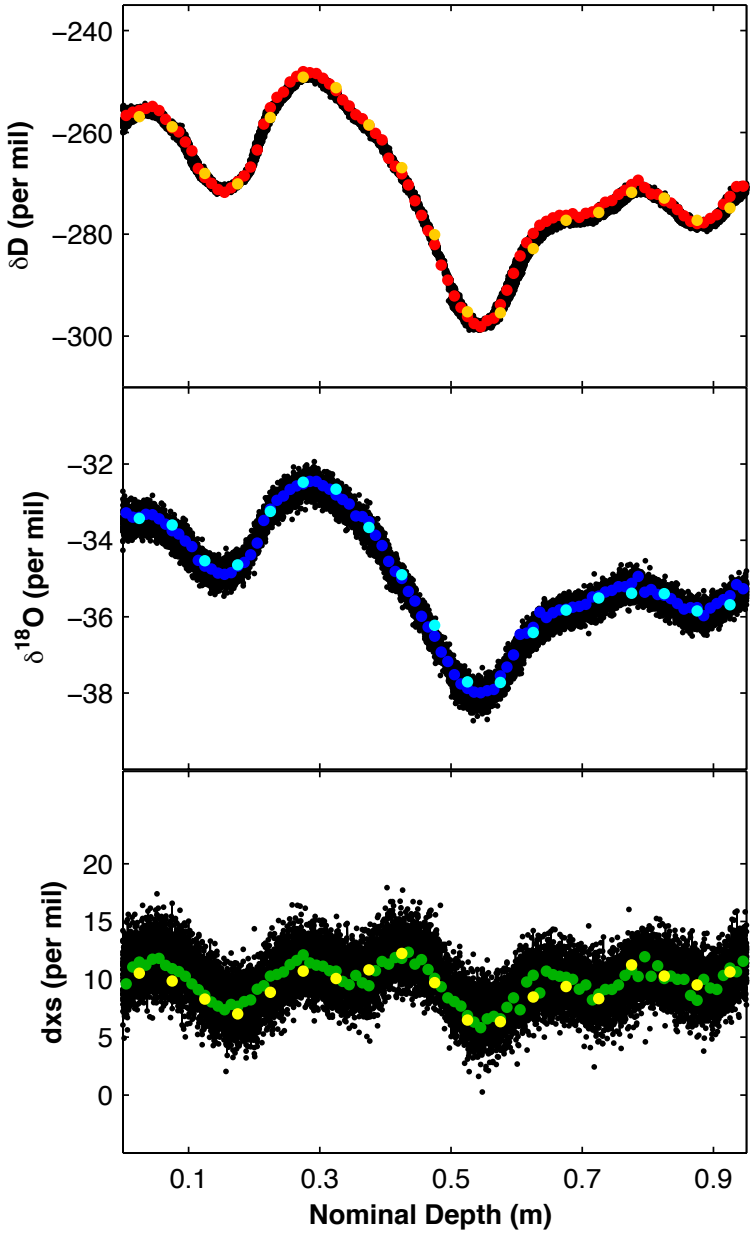

Figure 3.9. *Greenland test ice (GTI) sticks for a nominal 1-meter section at ~400 meters depth. Seven GTI sticks were measured on the WI-CFA system (black) and 2 GTI sticks were measured discretely on a separate Picarro L-2130i at 1cm and 5cm intervals (red, blue, and green colored dots).*

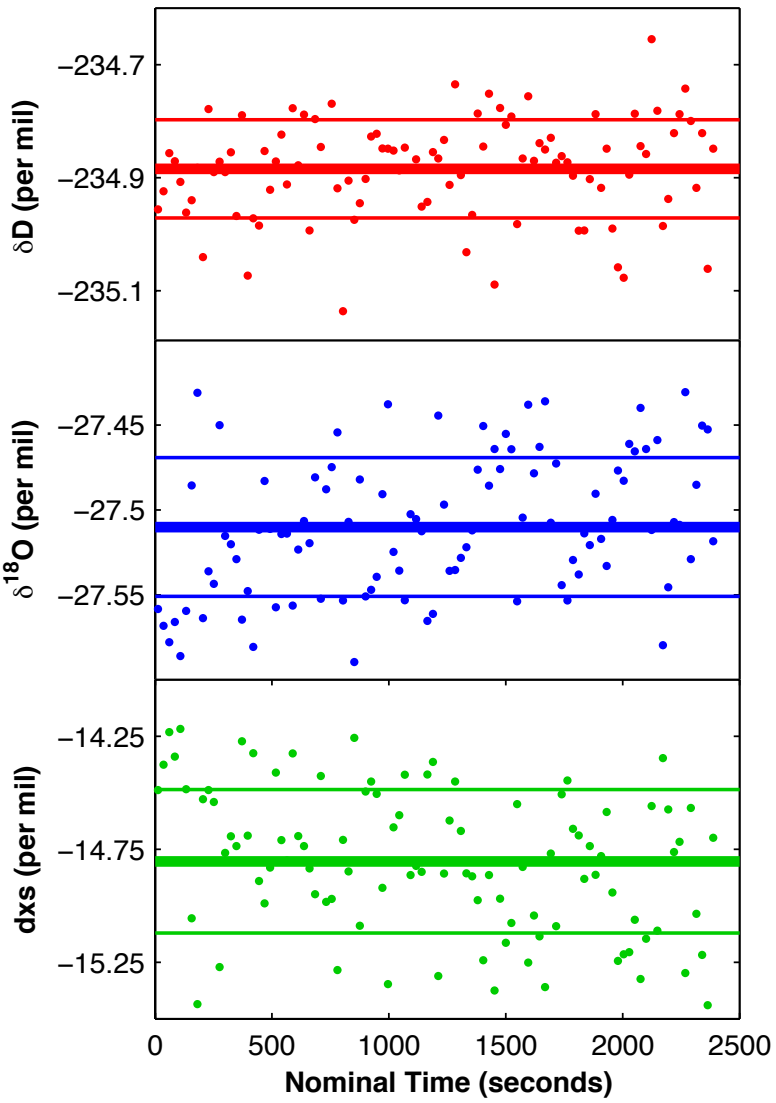

3.10. *Long-term homogenous isotopic water analysis on the Picarro L-2130i. The dots are 24 second averages of 0.85 second (1.18 Hz) measurements, corresponding to ~1 cm of ice analysis assuming a 2.5 cm/min melt rate. The thick lines are the mean, and the thinner lines show 1σ.*

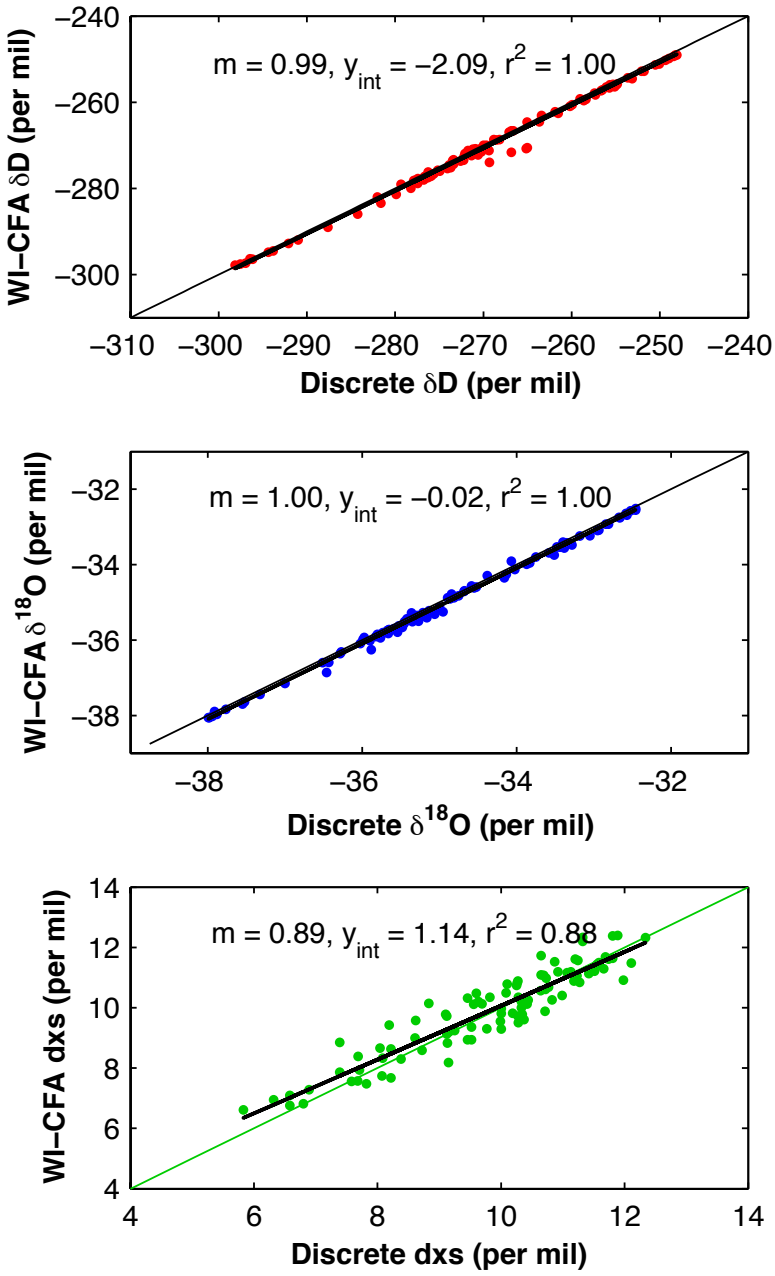

Figure 3.11. *Scatter plots of Greenland test ice (GTI) comparisons of WI-CFA vs. discrete data. Seven GTI sticks were analyzed on the WI-CFA data, down-sampled to 1 cm, and averaged. The discrete data were sampled at 1 cm and analyzed on a separate Picarro L-2130i. The black line is the best-fit linear regression.*

3.7. References

Allan, D. W. (1966). Statistics of atomic frequency standards. *Proceedings of the IEEE*, 54(2), 221-230.

Azzalini, A., & Dalla Valle, A. (1996). The multivariate skew-normal distribution. Biometrika, 83(4), 715-726.

Bigeleisen, J., Perlman, M. L., & Prosser, H. C. (1952). Conversion of hydrogenic materials to hydrogen for isotopic analysis. *Analytical Chemistry*, 24(8), 1356-1357.

Bond, G. C. (1968). Catalysis by metals. *Annu. Rep. Prog. Chem., Sect. A. Gen. Phys and Inorg. Chem.,* 65, 121-128.

Brand, W. A., Geilmann, H., Crosson, E. R., & Rella, C. W. (2009). Cavity ring‐down spectroscopy versus high‐temperature conversion isotope ratio mass spectrometry; a case study on δ^2H and $\delta^{18}O$ of pure water samples and alcohol/water mixtures. *Rapid Communications in Mass Spectrometry*, 23(12), 1879-1884.

Coleman, M. L., Shepherd, T. J., Durham, J. J., Rouse, J. E., & Moore, G. R. (1982). Reduction of water with zinc for hydrogen isotope analysis. *Analytical Chemistry*, 54(6), 993-995.

Coplen, T. B., Wildman, J. D., & Chen, J. (1991). Improvements in the gaseous hydrogen-water equilibration technique for hydrogen isotope-ratio analysis. *Analytical Chemistry*, 63(9), 910-912.

Craig, H., Gordon, L. I., & Horibe, Y. (1963). Isotopic exchange effects in the evaporation of water: 1. Low‐temperature experimental results. *Journal of Geophysical Research*, 68(17), 5079-5087.

Dansgaard, W. (1964). Stable isotopes in precipitation. *Tellus*, 16(4), 436-468.

Dansgaard, W. (2005). Frozen Annals – Greenland Icecap Research. Neils Bohr Institute, *Narayana Press*, Odder, Denmark, www.narayanapress.dk. ISBN: 87-990078-0-0. 124 p.

Epstein, S., Buchsbaum, R., Lowenstam, H. A., & Urey, H. C. (1953). Revised carbonate-water isotopic temperature scale. *Geological Society of America Bulletin*, 64(11), 1315-1326.

Gkinis, V., Popp, T.J., Blunier, T., Bigler, M., Schupbach, S., Kettner, E., Johnsen, S.J. (2011). Water isotopic ratios from a continuously melted ice core sample. *Atmos. Meas. Tech*. 4, 2531–2542.

Gkinis, V., Popp, T. J., Johnsen, S. J., & Blunier, T. (2010). A continuous stream flash evaporator for the calibration of an IR cavity ring-down spectrometer for the isotopic analysis of water. *Isotopes in environmental and health studies*, 46(4), 463-475.

Gupta, P., Noone, D., Galewsky, J., Sweeney, C., & Vaughn, B. H. (2009). Demonstration of high‐precision continuous measurements of water vapor isotopologues in laboratory and remote field deployments using wavelength‐scanned cavity ring‐down spectroscopy (WS‐CRDS) technology. *Rapid communications in mass spectrometry*, 23(16), 2534-2542.

Herron, M. M., & Langway Jr, C. C. (1980). Firn densification: an empirical model. *Journal of Glaciology*, 25, 373-385.

Huber, C., & Leuenberger, M. (2003). Fast high‐precision on‐line determination of hydrogen isotope ratios of water or ice by continuous‐flow isotope ratio mass spectrometry. *Rapid communications in mass spectrometry*, 17(12), 1319-1325.

Johnsen, S. J., Dansgaard, W., & White, J. W. C. (1989). The origin of Arctic precipitation under present and glacial conditions. *Tellus B*, *41*(4), 452-468.

Johnsen, S. J., Dahl‐Jensen, D., Gundestrup, N., Steffensen, J. P., Clausen, H. B., Miller, H., Masson-Delmotte, V., Sveinbjörnsdottir, A. E., & White, J. (2001). Oxygen isotope and palaeotemperature records from six Greenland ice‐core stations: Camp Century, Dye‐3, GRIP, GISP2, Renland and NorthGRIP. *Journal of Quaternary Science*, 16(4), 299-307.

Johnson, J. A., Mason, W. P., Shturmakov, A. J., Haman, S. T., Sendelbach, P. J., Mortensen, N. B., Laurent, J. A., & Dahnert, K. R. (2007). A new 122 mm electromechanical drill for deep ice-sheet coring (DISC): 5. Experience during Greenland field testing. *Annals of Glaciology*, 47(1), 54-60.

Jouzel, J., Alley, R. B., Cuffey, K. M., Dansgaard, W., Grootes, P., Hoffmann, G., Johnsen, S. J., Koster, R. D., Peel, D., Shuman, A., Stievenard, M., Stuiver, M., & White, J. (1997). Validity of the temperature reconstruction from water isotopes in ice cores. J*ournal of Geophysical Research: Oceans* (1978–2012), 102(C12), 26471-26487.

Jouzel, J., & Merlivat, L. (1984). Deuterium and oxygen 18 in precipitation: modeling of the isotopic effects during snow formation. *Journal of Geophysical Research: Atmospheres* (1984–2012), 89(D7), 11749-11757.

Jouzel, J., Vimeux, F., Caillon, N., Delaygue, G., Hoffmann, G., Masson‐Delmotte, V., & Parrenin, F. (2003). Magnitude of isotope/temperature scaling for interpretation of central Antarctic ice cores. *Journal of Geophysical Research: Atmospheres* (1984–2012), 108(D12).

Kerstel, E. T., Van Trigt, R., Reuss, J., & Meijer, H. A. J. (1999). Simultaneous determination of the 2H/1H, 17O/16O, and 18O/16O isotope abundance ratios in water by means of laser spectrometry. *Analytical chemistry*, 71(23), 5297-5303.

Lis, G., Wassenaar, L. I., & Hendry, M. J. (2008). High-precision laser spectroscopy D/H and 18O/16O measurements of microliter natural water samples. *Analytical Chemistry*, 80(1), 287-293.

Maselli, O. J., Fritzsche, D., Layman, L., McConnell, J. R., & Meyer, H. (2013). Comparison of water isotope-ratio determinations using two cavity ring-down instruments and classical mass spectrometry in continuous ice-core analysis. *Isotopes in environmental and health studies*, 49(3), 387-398.

Mook, W. (2000). Environmental Isotopes in the Hydrological Cycle. IHP-V Technical Documents in Hydrology No. 39. *UNESCO/IAEA*: Paris/Vienna.

Newman, B., Tanweer, A., & Kurttas, T. (2009). IAEA standard operating procedure for the liquid-water stable isotope analyser. *IAEA water resources programme.*

Osterberg, E. C., Handley, M. J., Sneed, S. B., Mayewski, P. A., & Kreutz, K. J. (2006). Continuous ice core melter system with discrete sampling for major ion, trace element, and stable isotope analyses. *Environmental science & technology*, 40(10), 3355-3361.

Petit, J. R., White, J. W. C., Young, N. W., Jouzel, J., & Korotkevich, Y. S. (1991). Deuterium excess in recent Antarctic snow. *Journal of Geophysical Research: Atmospheres* (1984–2012), 96(D3), 5113-5122.

Röthlisberger, R., Bigler, M., Hutterli, M., Sommer, S., Stauffer, B., Junghans, H. G., & Wagenbach, D. (2000). Technique for continuous high-resolution analysis of trace substances in firn and ice cores. *Environmental Science & Technology*, 34(2), 338-342.

Steig, E. J., Ding, Q., White, J. W. C., Kuttel, M., Rupper, S. B., Neumann, T. A., Neff, P. D., Gallant, A. J. E., Mayewski, P. A., Taylor, K. C., Hoffmann, G., Dixon, D. A., Schoenemann, S. W., Markle, B. R., Fudge, T. J., Schneider, D. P., Schauer, A. J., Teel, R. P., Vaughn, B. H., Burgener, L., Williams, J., & Korotkikh, E. (2013), Recent climate and ice-sheet changes in West Antarctica compared with the past 2,000 years, *Nature Geoscience*, 6(5), 372–375.

Vaughn, B. H., White, J. W. C., Delmotte, M., Trolier, M., Cattani, O., & Stievenard, M. (1998). An automated system for hydrogen isotope analysis of water. *Chemical Geology*, 152(3), 309-319.

Chapter 4

Differential Water Isotope Diffusion from the WAIS Divide Ice Core: Climatic and Glaciological Interpretations over the last 29,000 years

Abstract

Water isotope records in ice cores are used as a proxy for local temperature and regional atmospheric circulation. However, a water isotope record cannot be interpreted properly without quantifying diffusional processes. We use an unprecedented high-resolution water isotope record from the West Antarctic Ice Sheet Divide, annually dated to 29 ka bp, to evaluate the effects of diffusion. Most diffusional effects occur in the firn column, a near-surface region in ice sheets where inter-connected vapor pathways allow the movement of gases. Slower diffusional processes occur in solid ice below the firn column. We utilize two diffusion models to analyze diffusion parameters, including diffusivity and tortuosity, and discuss uncertainty in our modeling approach. We then determine diffusion lengths in both the depth and time domain, which describe the total diffusion in different sections of the ice core. We find anomalous diffusion at a number of depths that may be related to the effects of impurities in solid ice. By quantifying the total

diffusion in the ice core as a function of depth and time, including anomalous sections, we create a useful tool for interpretation of the water isotope record from both a climatic and glaciological viewpoint.

4.1. Introduction

Isotopes are atoms of the same chemical element with the same numbers of protons and electrons but differing numbers of neutrons. Isotopes of hydrogen, for example, have slightly different chemical and physical properties because of their mass differences. During physical, chemical, and biological processes, the relative ratio of varying isotopes tends to change, which is known as fractionation. Two types of processes cause isotope fractionation: equilibrium and kinetic effects. Equilibrium fractionation is related to the bond strength of chemical elements, while kinetic fractionation is related to the translational velocity of a chemical element. As a consequence of fractionation, all water in the hydrologic cycle has a unique isotopic composition related to its source of formation and the processes it has undergone.

Polar ice cores are a natural archive of isotopic fractionation occurring within the hydrologic cycle. The composition of water molecules in an ice core is mainly a function of temperature and regional atmospheric circulation. In an idealized example, water molecules evaporate from the ocean – and simultaneously fractionate – leaving more heavy water molecules in the liquid phase and preferentially (but not exclusively) selecting lighter molecules in the vapor phase. The reverse process occurs in a cloud during condensation events. Here, the heavier water molecule is preferentially selected,

while the lighter water molecule tends to remain as vapor in the cloud. As a cloud moves northward, eventually reaching polar regions, the snow falling on an ice sheet has an isotopic history related to the temperature and atmospheric pathway of the cloud (Dansgaard, 1964).

Ice cores are not a perfect recorder of Earth's surface climate, however. There are a number of physical processes that alter the water isotope signal after the deposition of snow. The majority of these processes occur in the firn, which is a porous, unconsolidated layer of snow at the surface of an ice sheet (ranging from about 50-95 meters deep). The firn is comparable to styrofoam in that air can move through inter-connected vapor pathways, allowing water molecules to exchange between the vapor and solid phase. In the vapor phase, water molecules diffuse[9] across concentration gradients and thermal gradients (Johnsen, 1977 and Grew and Ibbs, 1952). Diffusion also occurs in solid ice beneath the firn layer, but this process is orders of magnitude slower than diffusion occurring within the firn (Itagaki, 1967 and Robin, 1983). The total diffusion a parcel of ice experiences serves to decrease the amplitude of the water isotope signal and spread the signal through the strata.

Independent of diffusion, the natural flow of ice within an ice sheet alters the original configuration of snow layers. Initially, annual layers of snow sink deeper in the ice sheet as new snow is continually added on top. The density of these layers increases deeper in the firn, eventually forming ice. Layers of snow and ice are also strained,

[9] Diffusion causes the movement of molecules from high to low concentration. The diffusion process does not require energy, but rather occurs due to the random kinetic movements of molecules. Net diffusion stops when the concentration of molecules is uniform.

mainly in the vertical direction, as the ice is pulled horizontally due to ice flow[10]. The ice strain is also known as thinning, since the layers become progressively thinner over time. The thinning of ice can reach a point where annual ice layers are no longer discernable. The processes affecting a water isotope record after the initial deposition of snow can be quantified using physical models and analytical techniques like frequency (spectral) analysis. These quantification methods are discussed below.

4.1.1. Firn Ice

The firn column can be subdivided into a number of important layers. In the upper part of the firn (perhaps the top ~10 m), convective mixing of air due to surface wind stress creates a wind pumping effect, causing atmospheric air to continually mix within vapor pathways. Beneath this layer is a stagnant air column (over a depth of perhaps ~10-80 m), where gas transport occurs by diffusion and fractionation effects. Finally, at a certain depth (perhaps ~80 m), pore close off occurs, where air in the firn column ceases to be interconnected and small bubbles become trapped in solid ice. This is known as the "firn-ice transition" or "close-off depth". An idealized firn column is shown in Figure 4.1.

[10] Ice cores are generally drilled on or near ice divides where the strain of ice is mainly in the vertical direction, rather than other drilling locations that are more prone to both vertical and horizontal strain.

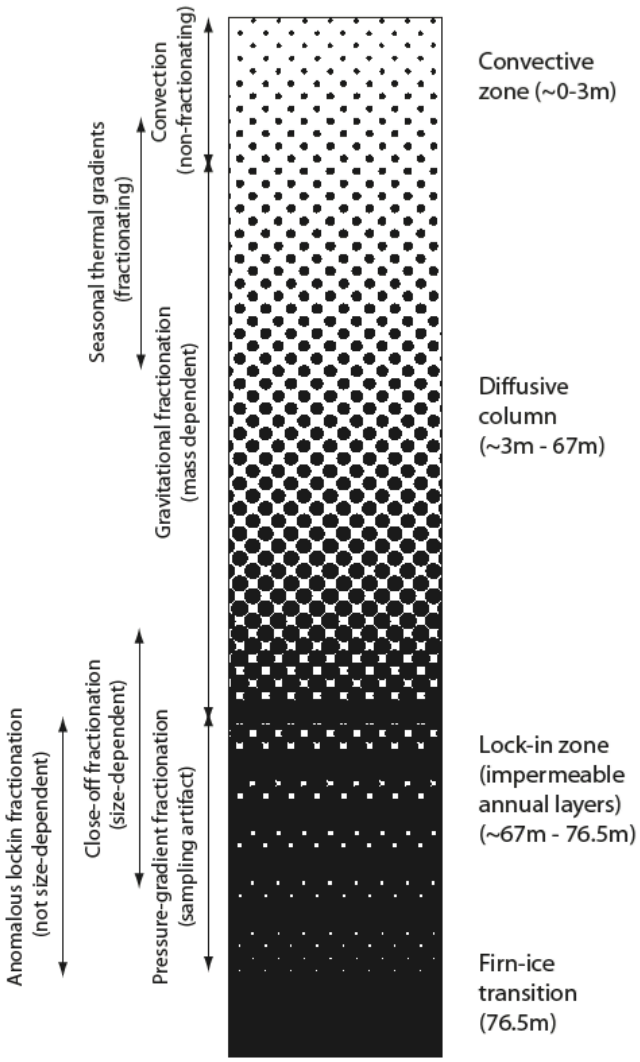

Figure 4.1. *A schematic diagram of an idealized firn column from Battle et al. (2011). The depth range of varying physical properties is shown on the left, and the approximate depths of certain features at WDC are shown on the right.*

Given a temperature, accumulation rate, and surface snow density, physical modeling can be used to calculate a firn column density profile and the depth of the firn-ice transition (Herron and Langway, 1980). For WAIS Divide, the model depth of the firn-ice transition is 73.4 m, assuming a temperature of -30° Celsius, an accumulation rate of 0.22 m/yr, and a surface snow density of 420 kg/m^3. Table 4.1 shows the

temperature, accumulation rate, and depth of the firn-ice transition (corresponding to a firn density of 830 kg/m³) for a number of ice course sites (Cuffey and Paterson, 2010).

Table 4.1.
Depth of firn-ice transition at certain ice core locations

Location	Temp. (°C)	Accum. Rate (m/yr)	Firn-Ice Transition (m)
Vostok	-57	0.022	95
GISP2	-32	0.22	77
Agassiz Ice Cap	-25	0.16	53
Byrd	-28	0.14	64

At the firn-ice transition, an important distinction must be made between the age of snow and the age of trapped air bubbles. Because the firn is porous, atmospheric air continually mixes into the firn column, making the air younger than the firn ice itself. The age difference is known as the "gas-age ice-age difference" or "Δage", which depends mostly on the snow accumulation rate (but also temperature), and can vary from several hundred years (e.g. central Greenland) to several thousand years (central Antarctica). The thickness of the firn column and Δage in Greenland and Antarctica have changed over time, and for example, were significantly larger during periods of colder climate, such as the last glacial maximum from about ~19.5 – 26.5 ka bp.

In terms of water molecules, diffusion in the firn is mainly a function of density, temperature, accumulation rate, and molecular weight. Various models have been put forth to quantify these relationships. Johnsen (1977) originally modeled residence times of water molecules in the vapor and solid phase of firn. Johnsen introduced a highly useful diffusion length term (σ), defined as the average vertical displacement of a water

molecule from its original position in the ice (disregarding the sinking of annual layers). Whillans and Grootes (1985) later modeled the firn diffusivity factor (Ω_f) for water vapor. Due to tortuosity (i.e. how twisted the pathways are within the firn), Ω_f is smaller than the diffusivity of water molecules in open, unrestricted air (Ω_a). Cuffey and Steig (1998) showed that the Whillans and Grootes model predicted the decay of seasonal isotopic amplitudes with depth at the GISP2 ice core site in central Greenland, although the physical treatment of water vapor diffusivity had to be enhanced due to lower atmospheric pressure at high-altitude and a small adjustment was made to the close off density parameter ρ_c. Johnson et al. (2000) improved on the Whillans and Grootes model by introducing a tortuosity factor (τ), which accounted for the discrepancy in ρ_c[11], and by distinguishing between the two different heavy isotopic species of water ($H_2{}^{18}O$ and $HD^{16}O$).

4.1.2. Deep Ice

Large ice sheets (e.g. Greenland and Antarctica) behave like enormous rivers of slowly moving ice, adding mass to the surface during depositional events and losing mass at the edges, such as tidewater glacier calving events that form icebergs. The ice rheology (flow of ice) is dependent on the applied stress (force per unit area) of overlying ice relative to gravity, and because the ice flows downwards and outwards towards the margins over time, the ice has both a vertical and horizontal velocity and strain component. At the ice divide, the surface slope is roughly equal to zero, resulting in ice

[11] The close off density parameter ρ_c occurs at a density of 830 kg/m^3. Cuffey and Steig (1998) had to adjust ρ_c to 730 kg/m^3 to accurately model the decay of the annual water isotope signal at GISP2. Johnsen et al. (2000) accounted for this discrepancy by introducing tortuosity τ and keeping ρ_c equal to 830 kg/m^3.

deformation occurring mainly in the horizontal direction, and a strain rate occurring mainly in the vertical direction. Due to the dominant vertical strain rate, an ice divide is the best location to drill an ice core, since annual ice layers tend to stay stacked neatly on top of each other[12] (Figure 4.2).

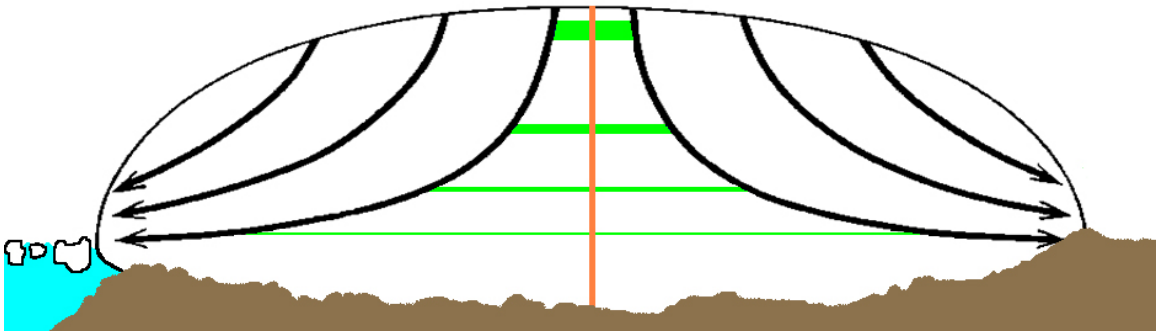

Figure 4.2. *A schematic diagram of a polar ice sheet (courtesy Centre for Ice and Climate). The black arrows show the flow of ice over time. Along the vertical red line, layers of ice tend to stay stacked horizontally. This is the best location to drill an ice core. The brown region represents bedrock.*

Theoretical ice flow models have been developed for use in ice core studies. These models depend on changes in ice flow, ice thickness, temperature, and accumulation rates. The most widely used model is the Dansgaard-Johnsen model (D-J model), which was developed for dating the Camp Century ice core (Dansgaard and Johnsen, 1969). The D-J model assumes a constant horizontal velocity (e.g. 3.3 m/yr) for ice flow from the surface to a certain depth, followed by a "kink" as horizontal velocity decreases linearly to 0 m/yr at the bedrock interface. Using the D-J model, a thinning

[12] In the lower portion of an ice sheet, old ice layers are often perturbed due to interactions between the ice and bedrock. This effect requires careful modeling and consideration before glaciological or climatic interpretations can be made.

function can be derived that quantifies the accumulated strain along the length of an ice core. The thinning function can also be thought of as the total change in the thickness of a layer divided by the original thickness of a layer (i.e. the total strain) as a function of depth. Besides thinning, the thickness of an annual layer in an ice core record depends on the accumulation rate at the time of deposition and variations in the size of the ice sheet through time (resulting in variations in overburden stress). A thicker layer, resulting from greater accumulation, will persist longer than a low accumulation layer.

An additional post-depositional process affecting the isotopic record beneath the firn column occurs from solid ice diffusion, otherwise known as self-diffusion. In one of the pioneering studies by Ramseier (1967), the self-diffusion of tritium (^{3}H) was studied in natural (Mendenhall glacier) and artificial (laboratory) grown monocrystals parallel and perpendicular to the c-axis[13]. The study found that entire H_2O molecules diffuse primarily by a vacancy mechanism (a jump to the nearest empty space in the ice matrix), and that the reaction rate is described by an Arrhenius dependence[14] for temperatures between -2.5 and -35.9 °C. The diffusion coefficient D is given by the Arrhenius equation:

$$D = D_o \, exp\left(\frac{-Q}{R\,T}\right) \tag{1}$$

in m^2/s, where D_o is the diffusion pre-exponential, Q is the effective activation energy, R is the gas constant, and T is the absolute temperature. Ramseier (1967) found a D_o of

[13] Ice crystals are arranged as layers of interconnected hexagons at the molecular level, and the c-axis is perpendicular to these hexagonal layers.
[14] The empirically derived Arrhenius equation relates a reaction rate to temperature.

0.001 m^2/sec and a Q of 0.62 ± ~0.04 eV for all cases. At -10 °C, the D value was (1.49 ± 0.06) x 10^{-15} m^2/sec, which increased by 7% and 16% perpendicular to the c-axis for natural and artificially grown ice, respectively. These results for ^3H are valid for ^{18}O within experimental error (Delibaltas et al., 1966).

In the GRIP ice core, Johnsen et al. (2000) found that the diffusion coefficient for Holocene ice at about -32 °C was ~10 times greater than for monocrystalline ice in the Ramseier study (1967). That is, there was too much diffusion (excess diffusion) in the ice core relative to the model. Nye (1998) had previously shown that the presence of a liquid vein network between ice grain boundaries in ice sheets could increase diffusion. The liquid veins result from processes that lower the freezing point of water between ice grain boundaries[15], including curvature of the ice-liquid water interface (Gibbs-Thomson effect[16]), water-soluble impurities, and intermolecular interactions between adjacent ice grains, vapor bubbles, and/or impurities. Nye's process proceeds over three steps: 1) An exchange of isotopes between solid grains and liquid veins, 2) Rapid diffusion within liquid veins along an isotope concentration gradient, and 3) An exchange of isotopes between liquid veins and solid grains at another location. Thus, the liquid veins expedite the movement of water molecules between solid grains, causing excess diffusion.

Johnsen et al. (2000) also tested a vein-driven diffusion model (similar to Nye) for GRIP ice, but could only explain a 3-fold increase in self-diffusion (rather than 10-fold). Rempel and Wettlaufer (2003) later determined that there is a range of possible self-diffusion behavior (perhaps even larger than Johnsen and Nye predict), dependent on

[15] Liquid and solid can coexist at temperatures lower than the melting temperature of the bulk, which is known as premelting. The premelting effect occurs in many solids, including solid ice.
[16] The Gibbs–Thomson effect describes a solid-liquid interface with curvature K, where the surface energy σ_{sl} contributes to the departure of the equilibrium temperature from that at bulk coexistence (definition from Rempel and Wettlaufer (2003)).

whether impurities reside in pre-melted liquid veins or in solid ice grains. If the impurities reside primarily in liquid veins, then the volume fraction of liquid water is larger, resulting in larger liquid veins and greater self-diffusion of ice. If the impurities reside primarily in the ice grains, the effect on the self-diffusion of ice may be less. Figure 4.3 shows the potential molecular pathways for water molecules in an ice core.

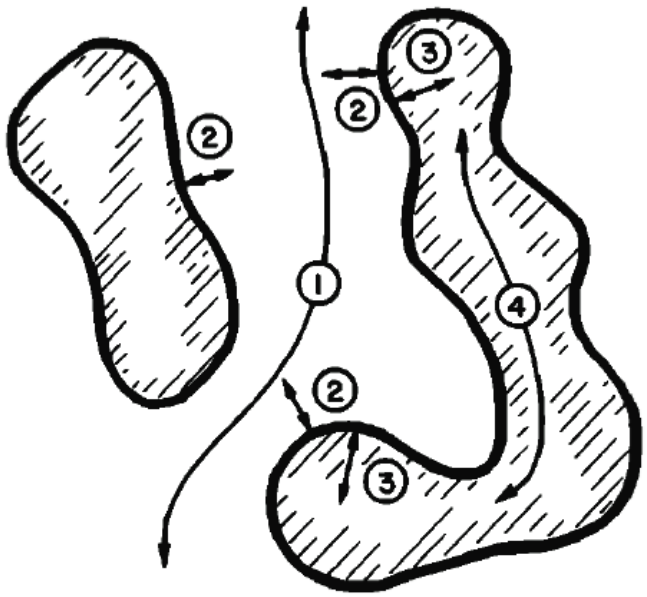

Figure 4.3. *A schematic diagram of molecular pathways for water molecule movement (Whillans and Grootes, 1985): 1) vapor-vapor, 2) vapor-ice surface, 3) ice surface-ice matrix, 4) ice matrix-ice matrix. Not shown is the diffusion and advection of liquid water in veins between ice grain boundaries.*

4.1.3. Differential Water Isotope Diffusion in a West Antarctic Ice Core

Water isotopes are recorders of processes occurring within the hydrologic cycle. In ice cores, the temperature of condensation in a cloud and atmospheric circulation mainly influences water isotopes. However, additional post-depositional processes alter

the original climatic signal, including diffusion in firn, diffusion in solid ice, and thinning. These alteration processes must be accounted for to properly understand the water isotope record.

In this study, we present a ~29 ka annually dated water isotope record from the West Antarctic Ice Sheet Divide ice core (WDC). We analyze diffusion and thinning in the ice core using various methodologies, including decay of the annual signal and diffusion lengths. We initially separate the firn from deeper ice, but eventually combine methodologies to determine total diffusion. Total diffusion lengths, which refer to the average displacement of a water molecule from its original position in the ice sheet, are presented in the depth, depth destrained, and time domain. Sections of anomalous diffusion prompt questions as to whether impurities (e.g. dust, calcium, etc.) may significantly alter the water isotope signal below the firn column. Ultimately, the diffusion length records can be used to back diffuse the water isotope signal, allowing for the reconstruction of high-frequency oscillations. This analysis has implications for interpretation of the one-year signal in Antarctica, including separation of a summer and winter signal, as well as 2-15 year signals that are thought to originate in the tropical Pacific Ocean as part of the El Niño Southern Oscillation.

4.2. Methods

4.2.1. Site Location

The West Antarctic Ice Sheet Divide (WAIS Divide) deep ice core (WDC06A, hereafter referred to as WDC) was drilled over six field seasons from 2006 – 2012. Each

field season consisted of ~40 drilling days, where a team of nine drillers worked 24 hours per day, six days per week. On December 31, 2011 the drilling crew reached a final depth of 3,405 m, resulting in the longest USA ice core drilled to date and a well-deserved New Year's Eve celebration.

The WDC drill site is located at 79°28.058' S by 112°05.189' W in the Pacific sector of West Antarctica, ~24 km from the current ice flow divide. The surface elevation is 1,766 m above sea level and the ice sheet thickness is 3,465 m. The current average annual surface temperature is -31°C and the current ice accumulation rate is 22 cm/yr. The WDC is the first southern hemisphere paleoclimate archive of comparable time resolution and maximum age as Greenland ice cores, which is useful for inter-hemispheric comparisons. Figure 4.4 shows a map of West Antarctica and the WDC drilling location.

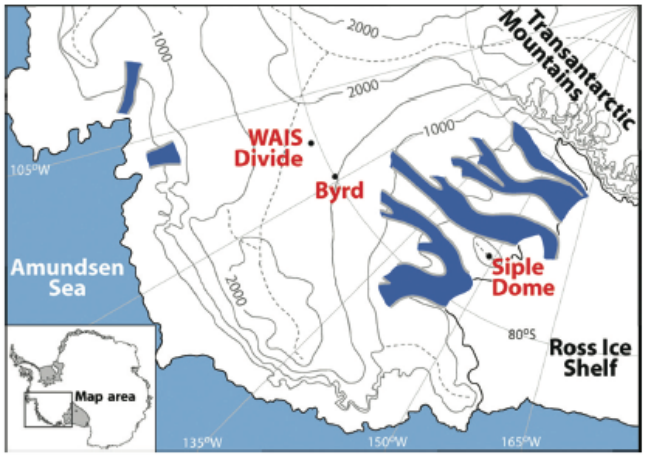

Figure 4.4. *A map of the West Antarctic region showing the drilling location of WDC (WAIS Divide ice core). The black contours show elevation above sea level (m). Figure from Souney et al. (2014) and originally modified from Morse et al. (2002).*

4.2.2. Methods of Measurement

The WDC water isotope record was analyzed on a cavity ring-down laser spectroscopy (CRDS) continuous flow analysis (CFA) system at the Institute of Arctic and Alpine Research, University of Colorado (see Chapter 3). As of 2015, this is the highest resolution water isotope record containing last glacial ice from West Antarctica. The data consists of measurements of hydrogen and oxygen isotopes in water molecules, where the ratio of heavy to light water isotopes in a water sample is commonly expressed in delta notation (Epstein, 1953; Mook, 2000) relative to Vienna Standard Mean Ocean Water (VSMOW):

$$\delta_{sample} = 1000\left[\left(\frac{R_{sample}}{R_{VSMOW}}\right) - 1\right] \quad (2)$$

where R is the isotopic ratio $^{18}O/^{16}O$ or H^2/H^1 (i.e. D/H where D is H^2, termed deuterium) in the sample or VSMOW. The δD and $\delta^{18}O$ symbols refer to parts per thousand deviations from equilibrium conditions set by VSMOW (defined as 0.00 per mil). Both δD and δ18O are used as proxies for local temperature and regional atmospheric circulation, dependent on the temperature gradient from moisture source to deposition site (Dansgaard, 1964). The main physical control on this relationship is the temperature of the cloud at the time of condensation (Jouzel and Merlivat, 1984; Jouzel et al., 1997; Johnsen et al., 2001). The WDC water isotope record is shown in Figure 4.5.

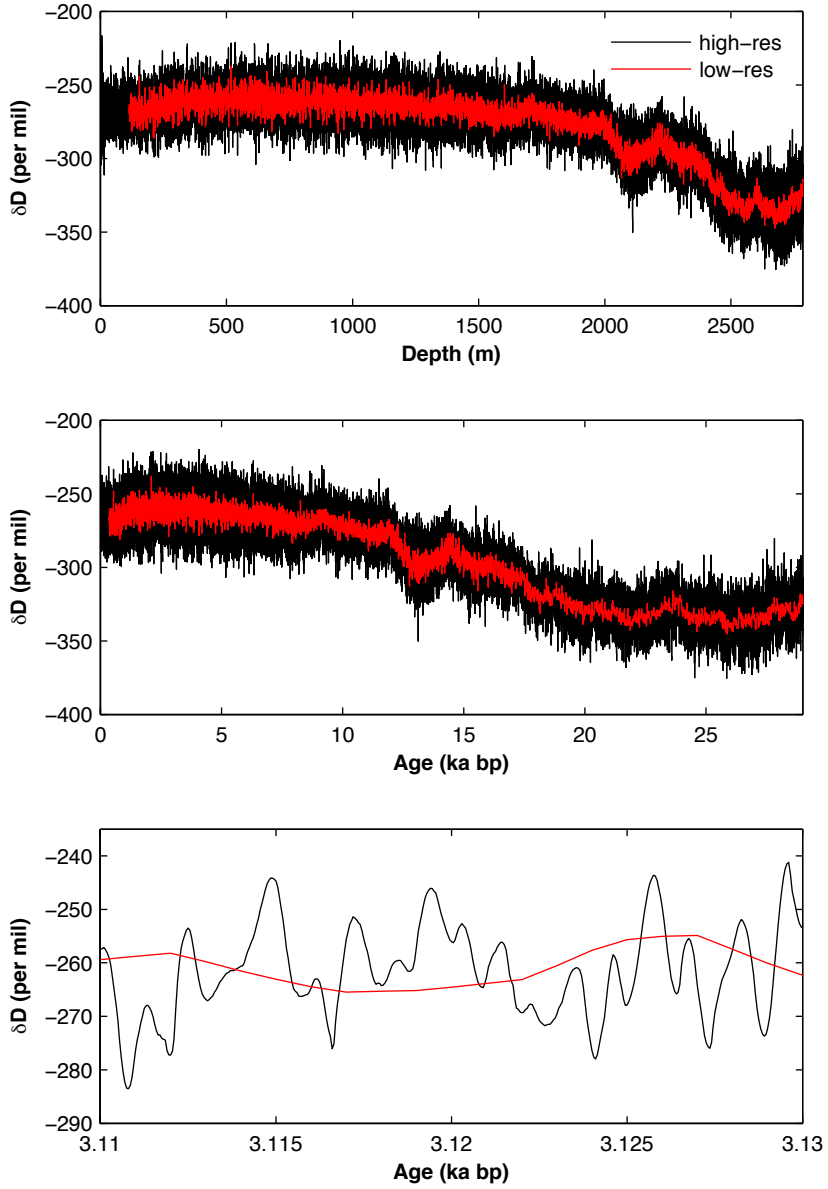

Figure 4.5. *Plots of the WDC water isotope record for depth (top), time (middle), and a zoom of 3.11-3.13 ka bp (bottom). The red lines are previously published low-resolution water isotope data from Steig et al. (2013) and WAIS Divide Project Members (2013). The black lines are the high-resolution record used in this study.*

The dating of the WDC water isotope record is based on a depth-age scale developed by the WAIS Divide Project Members (2013). The authors state:

> The WDC06A-7 timescale is based on high-resolution (<1 cm) measurements of sulphur, sodium, black carbon and electrical conductivity (ECM) above 577 m (2,358 yr before present (BP; AD 1950). Below 577 m, WDC06A-7 is based primarily on electrical measurements: di-electrical profiling was used for the brittle ice from 577 to 1,300 m (to 6,063 yr BP). Alternating-current ECM measurements were used from 1,300 to 1,955 m (to 11,589 yr BP) and both alternating-current and direct-current ECM measurements were used below 1,955 m. The interpretation was stopped at 2,800 m because the expression of annual layers becomes less consistent, suggesting that all years may not be easily recognized.

4.2.3. Methods of Modeling

It is useful to think about the water isotope record in terms of seasonal cycle amplitudes. For any given year, seasonal cycle amplitudes can be defined as the difference in the maximum summer δ value from the mean or as the difference in minimum winter δ value from the mean. In this study, we model the decay of seasonal cycle amplitudes over time to understand the effects of diffusion and thinning, including diffusion in firn (rapid loss of signal), diffusion in deep ice (much slower loss of signal, but progressively important over time), and thinning history (dependent on glaciological flow processes). For the firn, we compare WDC water isotope observations to the Cuffey and Steig diffusion model (1998; adapted from Whillans and Grootes, 1985; hereafter WGCS) and the Johnson et al. (2000; hereafter J) diffusion model, all of which are informed by a Herron and Langway (1980) firn density model. For deep ice diffusivity and thinning, we use the WGCS model. For both firn and deep ice modeling, layer tracking was implemented for temperature and thinning fraction using an external ice

flow model (pers. comm. Cuffey, 2014). Layer histories at 2 ka intervals (starting at 1 ka bp) were parametrically interpolated to 100-year intervals. This method effectively tracks layers of ice throughout their entire history in the ice sheet, providing improved paleo-reconstructions of diffusion and ice flow processes.

Based on Cuffey and Steig (1998) formulae, the fractional δ amplitude remaining in the deep ice after t years relative to the amplitude at the base of firn is given by:

$$\frac{A_D}{A_F}(t) = exp\left(\frac{-c\ \alpha^*(t)\ t}{L_o^2(t)}\right) \tag{3}$$

where A_D is the amplitude of the annual isotope cycle in deep ice at time t, A_F is the original amplitude of the annual isotope cycle at the base of firn (generally not a known quantity, except by analogy with the modern value or by inference from firn modeling), c is the constant $4\pi^2$, L_o is the ice equivalent accumulation rate (m/yr), and α^* is the time averaged effective diffusivity (m^2/sec) given by:

$$\alpha^*(t) = \frac{1}{t}\int_0^t \left(\frac{\alpha(\tau)}{(1 + \epsilon(\tau))^2}\right) d\tau \tag{4}$$

where ϵ is the strain, $1 + \epsilon(t)$ is the thinning function (reflecting the total strain of a layer at some time or depth), and $\alpha(t)$ is the isotopic diffusivity (m^2/sec), which can be related to temperature by the Arrhenius equation:

$$\alpha(t) = \alpha_o \cdot exp^{\frac{-Q}{RT}} \quad (5)$$

where α_o is a reference isotopic diffusivity (m^2/sec), Q is the effective activation energy, R is the gas constant, and T is the absolute temperature. Since the temperature range in the ice is small, this equation can be simplified to:

$$\alpha(t) = \alpha_o + \gamma(T - T_o) \quad (6)$$

where γ is a temperature sensitivity parameter and T_o is a reference temperature (243 K). Finally, a diffusion length for the deep ice component of the model (σ_{deep}) can be determined using the following equation:

$$\sigma_{deep} = \frac{1}{\pi\sqrt{2}} \cdot \lambda_{avg} \cdot ln^{\frac{1}{(\frac{A_D}{A_F})}} \quad (7)$$

where λ_{avg} is the mean annual layer thickness at the age (or depth equivalent) of interest.

Two models are used for firn ice modeling with differing treatments of water vapor diffusion in air. The J model uses differential diffusivity values ($HD^{16}O$ and $H_2{}^{18}O$) for water vapor in air and introduces a tortuosity factor to quantify the amount of curvature or twistedness of firn ice. The WGCS model uses a non-differential diffusivity of water vapor in air originally described by Whillans and Grootes (1985) and does not incorporate tortuosity. Both of these models are linked with a Herron and Langway (1980) firn density model.

In the J model, the firn diffusivity (Ω_{fi}) for $H_2{}^{18}O$ and $HD^{16}O$, where *i* represents ^{18}O or D, is given by:

$$\Omega_{fi} = \frac{m\ p\ \Omega_{ai}}{R\ T\ \alpha_i\ \tau}\left(\frac{1}{\rho} - \frac{1}{\rho_{ice}}\right) \tag{8}$$

in units of m^2/s, where *m* is the molar weight of water, T is the absolute temperature, p is the saturation pressure over ice at T, Ω_{ai} is the diffusivity of water molecules in air, R is the gas constant, α_i is the fractionation factor in water vapor over ice, τ is the tortuosity factor, ρ is the density of firn, and ρ_{ice} is the density of ice. The tortuosity factor can be defined as a function of density:

$$\frac{1}{\tau} = 1 - b\left(\frac{\rho}{\rho_{ice}}\right) \qquad for\ \rho \leq \frac{\rho_{ice}}{\sqrt{b}} \tag{9}$$

where b = 1.30 and $(1/\tau) = 0$ for $\rho \geq 804.3$ kg/m^3. The tortuosity factor quantifies how twisted the vapor pathways are in the firn, which directly affects the amount of diffusion. By accounting for tortuosity, Johnsen et al. (2000) showed that his model predicts nearly identical diffusion lengths as Cuffey and Steig (1998), without adjusting the ρ_c parameter[17].

Related to tortuosity, the WGCS and J diffusion models have differing definitions of the firn diffusivity parameter (Ω_p; not to be confused with Ω_{fi}). Cuffey and Steig used the Whillans and Grootes (1985) equation for Ω_p:

[17] Note that the ρ_c parameter was adjusted by Cuffey and Steig (1998) to 730 kg/m^3, even though firn at GISP2 reaches close-off depth at about 822 kg/m^3.

$$\Omega_p = \Omega_a \left(1 - \frac{\rho}{\rho_c}\right) \qquad for\ \rho \leq \rho_c \tag{10}$$

where Ω_a is the diffusivity of water vapor in air and ρ_c is the density of impermeable ice (pore-close off density). Johnsen et al. (2000) instead defined a new relation:

$$\Omega_{pi} = \frac{\Omega_{ai}}{\tau}\left(1 - \frac{\rho}{\rho_{ice}}\right) \tag{11}$$

where Ω_a varies for each diffusing species (defined below in equations 17 and 18). The Cuffey and Steig model uses the Geiger and Poirier (1973) definition of Ω_a:

$$\Omega_a = 0.0371 \cdot T^{1.75} \tag{12}$$

in units of m^2/yr. The Johnsen model instead uses the Hall and Pruppacher (1976) definition of Ω_a:

$$\Omega_a = 0.211 \cdot \left(\frac{T}{T_o}\right)^{1.94} \left(\frac{P}{P_o}\right) \tag{13}$$

in units of cm^2/s, where T is absolute temperature (K), T_o is 273.15 K, P is ambient pressure (atm), and P_o is 1 atm.

Due to differences in mass, heavy isotopologues of water have different diffusivity rates. Johnsen et al. (2000) utilizes empirically derived fractionation factors

between water vapor and ice for O^{18} (Majoube, 1970) and D (Merlivat and Nief, 1967) as a function of temperature in their model:

$$\alpha_{18O} = 0.9722 \cdot \exp\left(\frac{11.839}{T}\right) \tag{14}$$

$$\alpha_{D} = 0.9098 \cdot \exp\left(\frac{16288}{T^2}\right) \tag{15}$$

The fractionation factor alpha is defined as the ratio of the number of atoms of two isotopes within one chemical compound divided by the corresponding ratio in another compound. For example, the fractionation factor for O^{18} or D between water vapor and ice can also be written as follows:

$$\alpha_i = \frac{R_{ice}}{R_{water\ vapor}} \tag{16}$$

where R is the ratio $H_2{}^{18}O/H_2{}^{16}O$ or $HD^{16}O/H_2{}^{16}O$ in ice or water vapor. Finally, Merlivat and Jouzel (1979) define the diffusivities of heavy water molecules in air:

$$\Omega_{a18O} = \frac{\Omega_a}{1.0251} \tag{17}$$

$$\Omega_{aD} = \frac{\Omega_a}{1.0285} \tag{18}$$

Thus, the loss of isotopic signal (i.e. the amount of smoothing) in a δD profile is less than a $\delta^{18}O$ profile, and this differential diffusion should be observable in high-resolution ice

cores.

The diffusion length for the firn ice component of the model (σ_{firn}) can be determined using the following equation:

$$\sigma_{firn}^2 = 2 \cdot \Omega_{fi} \cdot t \tag{19}$$

and the fractional δ amplitude remaining after t years relative to the surface amplitude is described by:

$$\frac{A_F}{A_S} = exp\left(-\frac{2\pi^2}{\lambda_F^2} \cdot \sigma_{firn}^2\right) \tag{20}$$

where A_F is the amplitude of the annual isotope cycle in firn ice at time t, A_S is the original amplitude of the annual isotope cycle at the surface (generally not a known quantity, except by analogy with the modern value), and λ_F is the ice equivalent layer thickness at firn base. The value of A_F/A_S at the pore close-off depth gives the fractional reduction of δ amplitude at firn base relative to the surface.

The total fractional δ amplitude remaining after t years (A_T), combining both firn and deep ice modeling, is given by:

$$A_T = A_S \cdot \frac{A_F}{A_S} \cdot \frac{A_D}{A_F} \tag{21}$$

where varying parameters in the model must be optimized to match observations. The

total diffusion length after t years (σ_T), combining both firn and deep ice modeling, is given by:

$$\sigma_T = \sigma_{firn} + \sigma_{deep} \cdot (\frac{\lambda}{\lambda_F}) \quad (22)$$

where λ is the thickness of a layer at some age (or equivalent depth), and λ_F is the ice equivalent layer thickness at firn base.

4.2.4. Models vs. Observations

The diffusion models discussed above can be compared directly to observations by converting the WDC δD and $\delta^{18}O$ time series (dating to ~29 ka bp) into frequency space. Frequency analysis of a time series, otherwise known as spectral analysis, is a complete representation of the data set in frequency space over a certain window length. The conversion of a time series to frequency space, in the simplest representation, involves fitting oscillating functions (i.e. sine and cosine functions) to a periodic data set. This is known as a Fourier series, which is the expansion of a periodic function f(x) in terms of an infinite sum of sines and cosines. A version of the Fourier calculation is the discrete Fourier transform (DFT), which reveals periodicities and the relative strengths of any periodic components in evenly spaced time series (Arfken, 1985 and Press et al., 1989). The fast Fourier transform (FFT) is a DFT algorithm that reduces the computational expense of the transformation (Cooley and Tukey, 1965). FFT is commonly used in many disciplines such as engineering, science, geology, mathematics,

and communications. In this study, we use an FFT type technique known as MultiTaper method (MTM) spectral analysis (Thomson, 1982; Percival and Walden, 1993) used for signal reconstruction (e.g., Park, 1992). The MTM method has been widely applied in paleoclimate and geochemical studies, such as periodic analysis of the El Niño Southern Oscillation or North Atlantic Ocean sediment cores.

A certain minimum window length is necessary to accurately characterize a time series in frequency space, which depends on the sampling interval (resolution) of the time series. In paleoclimate studies of high-resolution records (i.e. records with yearly oscillations), a window of at least 100 to 200 years is necessary. For frequency analysis, we specifically use an MTM Matlab script developed by Peter Huybers at Harvard University to calculate 1-year amplitudes and diffusion lengths from WDC water isotope observations. These values can then be compared with diffusion modeling described above. Figure 4.6 shows an example of a δ time series and the subsequent conversion to the frequency domain.

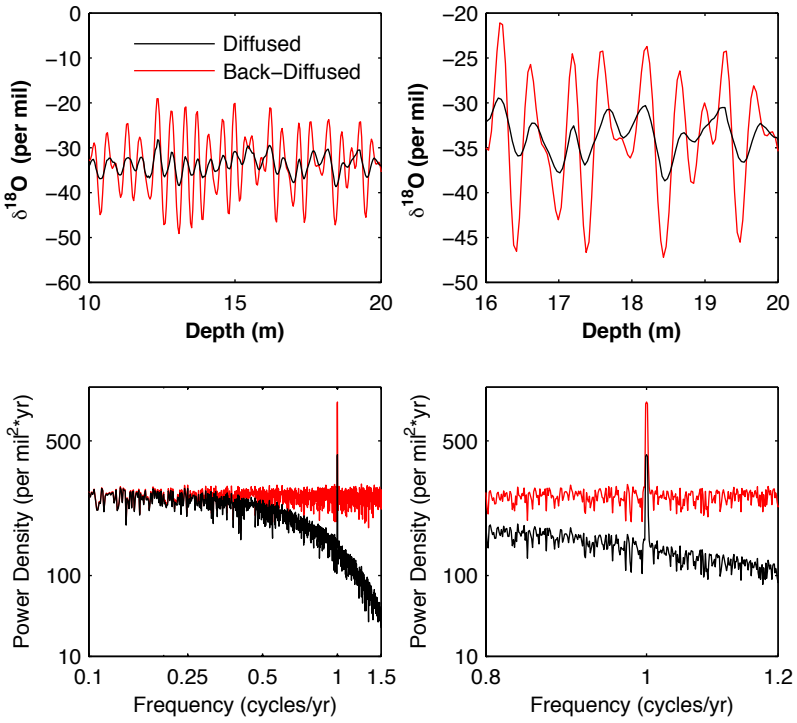

Figure 4.6. *An example of a $\delta^{18}O$ time series from the Crete ice core. (Top Left) A 10-meter section of diffused (black) and back-diffused (red) annual $\delta^{18}O$ data from the firn column. The back-diffused data is an estimate of the original signal. (Top Right) A 4-meter zoom of the $\delta^{18}O$ time series. The annual signal has diffused away at 19 m (black) relative to the original signal (red). (Bottom Left) Conversion of the same signal to the frequency domain (shown as cycles/yr) Diffusion causes a loss of signal in the higher-frequencies (i.e. about 0.5 to 1.5 cycles/yr on the plot). (Bottom Right) A zoom of the 1-year oscillation, which is evident as a sharp peak in the frequency domain. Notice that the diffused signal (black) has lost power relative to the original signal (red).*

A fundamental property of water isotope diffusion is that it spatially averages the δ signal along the ice core. For an isotope record that looks like a solitary spike at some location along the depth axis, the signal will evolve over time as an ever-widening Gaussian[18]. Gaussian functions are the Green's function[19] for the diffusion equation.

[18] A Gaussian has a bell curve shape and is used in statistics to describe normal probability distributions or in signal processing as filters.

Taking a synthetic isotopic record and convolving it with a Gaussian can model the effect of diffusion in the depth domain. Convolution of two functions *f* and *g* over a finite range [0,t] is given by:

$$[f * g](t) = \int_0^t f(\tau)\, g(t-\tau)\, d\tau \tag{23}$$

where the symbol $[f * g](t)$ denotes convolution of *f* and *g*. For an ice core, the diffusion Gaussian (i.e. $g(t-\tau)$) "slides" over the water isotope record (i.e. $f(\tau)$). The diffusion Gaussian at depth z with standard deviation σ is represented by:

$$G(z) = \frac{1}{\sigma\sqrt{2\pi}} \cdot exp^{\frac{-z^2}{2\sigma^2}} \tag{24}$$

The standard deviation of the Gaussian can be used to calculate the diffusion length (Johnsen, 1977). A useful property of a Gaussian in the depth or time domain is that conversion to the frequency domain also yields a Gaussian:

$$\Im[G(z)] = \hat{G} = exp^{\frac{-k^2\sigma^2}{2}} \tag{25}$$

where $\Im$ is the Fourier transform (denoted by the hat symbol), k is $2\pi f$, and f is frequency. Converting the relation δ (per mil) vs. depth (m) to frequency space using

[19] In certain instances, the convolution of a Green's function with a function f(x) is the solution to the inhomogeneous differential equation for f(x).

MTM spectral analysis yields the relation power density (per mil^2 * m) vs. frequency (cycles/m), where power density is the relative strength of the frequency components of the original signal. In this study, we fit a Gaussian ($\hat{G}_z$) to the WDC δ vs. depth signal in the form:

$$\hat{G}_z = K_z \cdot exp^{\frac{-f^2}{2\sigma_{stdz}^2}} \tag{26}$$

where K_z is the power density value of the white noise signal[20] and σ_{stdz} is the standard deviation in 1/meters. We determine σ_{stdz} in a precise way by calculating the linear regression of the natural log of the power density (ln(PD)) vs. frequency squared (f^2) within the range of 0.01 cycles/m and the point where systematic noise from the ice core analysis system overwhelms the physical signal. The point where noise dominates appears as a "kink" or "bend" in the linear decay of ln(PD). In this case σ_{stdz} is determined using the equation:

$$\sigma_{stdz} = \sqrt{\frac{1}{2 \cdot abs(\mathrm{m}_{ln})}} \tag{27}$$

where m_{ln} is the slope of the linear regression of ln(PD) vs. f^2. A maximum and minimum slope is fit within the standard error of the linear regression to determine an uncertainty range for σ_{stdz} (Figure 4.7).

[20] The white noise signal in WDC Holocene ice occurs across 10 yr to 2 yr periodic oscillations (i.e. 0.1 to 0.5 cycles/year). This value will be different in other ice cores, depending on the preservation of the δ signal relative to diffusion and thinning.

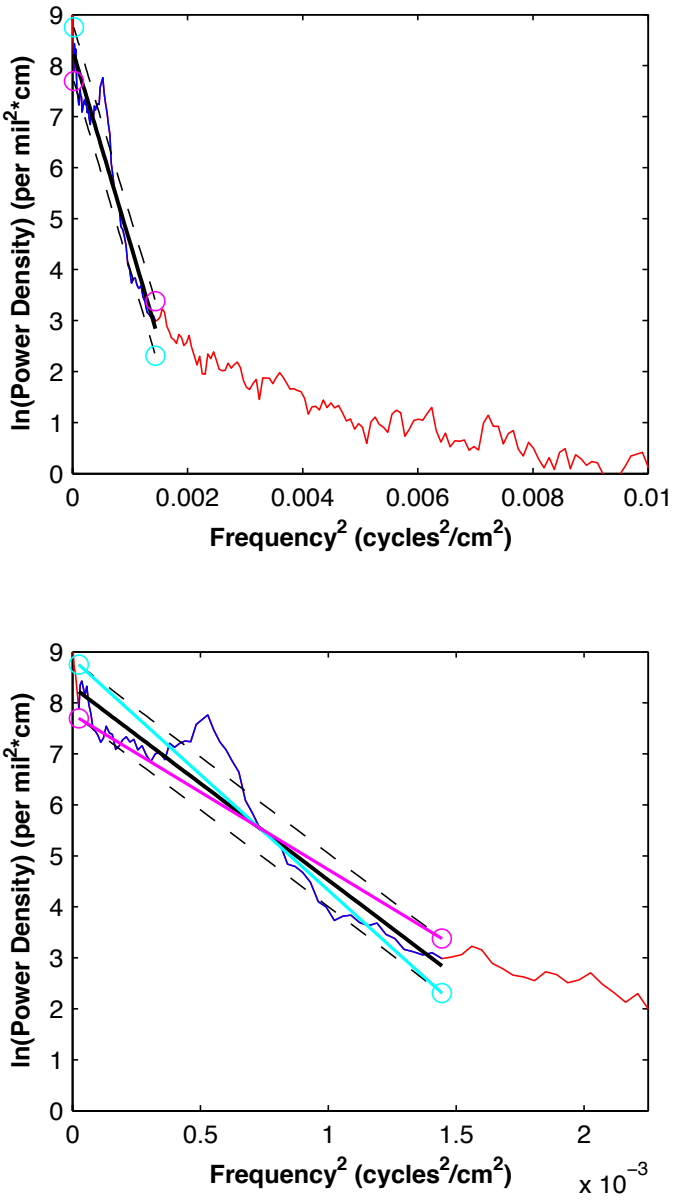

Figure 4.7. *Plots of the natural log fit determination method for standard deviation (σ_{stdz}). In the upper plot, the point where noise dominates (resulting from lab instrumentation and other sources) appears as a "kink" or "bend" in the linear decay of the natural log of power density. In the lower plot, the dark blue line shows the data used for the linear fit and the slope of the linear fit (black line) is used to determine the standard deviation. The standard error of the linear fit (dashed black lines) is used to find a maximum slope (light blue line) and minimum slope (pink line), which constrains the uncertainty of σ_{stdz}.*

The conversion of σ_{stdz} into the time domain (σ_{stdt}) is determined by:

$$\sigma_{stdt} = \sigma_{stdz} \cdot \lambda_{avg} \tag{28}$$

where λ_{avg} is the mean annual layer thickness in m/yr. With a well-dated core, this conversion from depth to time domain should introduce limited uncertainty, and requires an adjustment to the K variable. A correction of σ_{stdt} and σ_{stdz} is required to yield a diffusion length:

$$\sigma_i = \frac{1}{2\pi\sqrt{2}} \cdot \frac{1}{\sigma_{stdi}} \tag{29}$$

where σ_{stdi} is either σ_{stdz} and σ_{stdt} in (1/meters) or (1/years), respectively, while the σ_i variable now refers to diffusion length in meters (σ_z) or years (σ_t), respectively[21]. An estimate of A_T/A_S is then given by:

$$\frac{A_T}{A_S} = exp^{\frac{-2\pi^2\sigma_z^2}{\lambda_{avg}}} \tag{30}$$

Figure 4.8 shows examples of Gaussian fits for depth and time in frequency space.

[21] Johnsen et al. (2000) uses σ for diffusion length, which is also the symbol for standard deviation. Unless the subscript reads σ_{std}, we refer to diffusion lengths using the term σ.

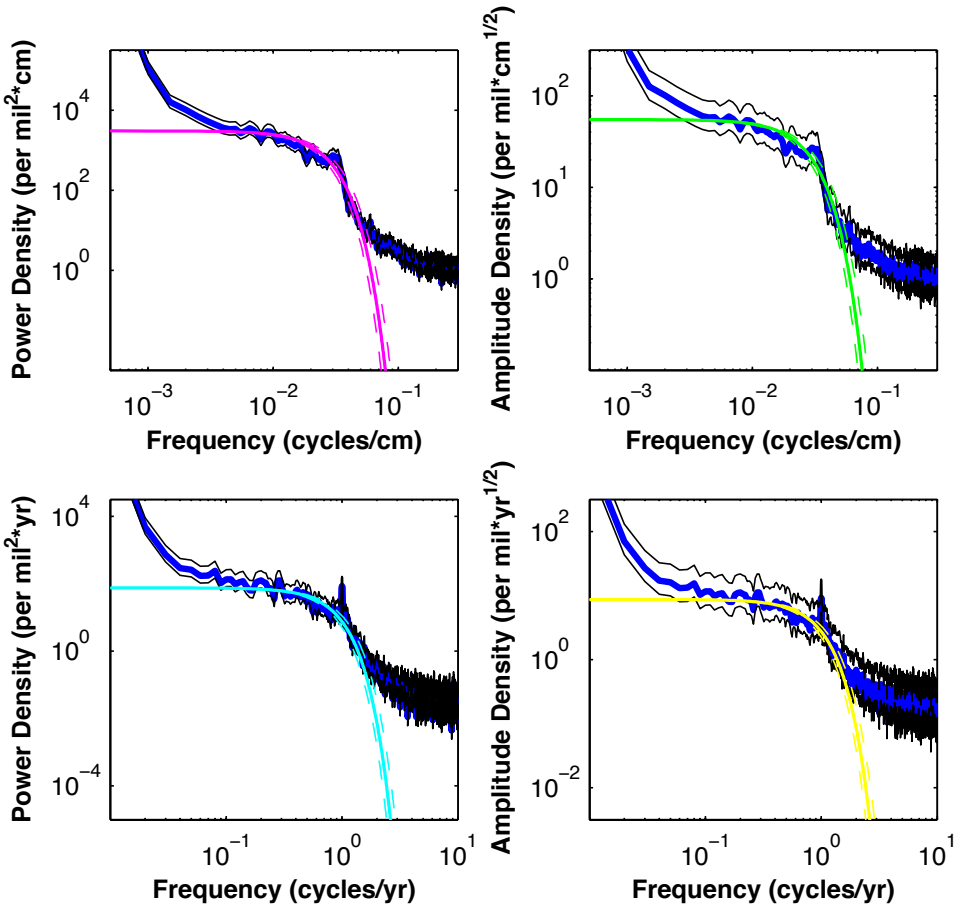

Figure 4.8. *Gaussian fits for the depth domain (upper plots) and time domain (lower plots) over the time increment 3.0–3.5 ka bp. Both power density (left plots) and amplitude density (right plots) are shown. The amplitude density is the square root of power density in units of per mil·yr$^{1/2}$. The integral of amplitude density over a certain frequency range yields units of per mil, which has the same units as the δ signal. The dark blue lines are the MTM spectral estimate, the black lines are the 95% confidence interval, and the colored lines are the Gaussian fit using a diffusion length determined from a natural log fit of power density (described above).*

4.3. Results and Discussion

4.3.1. Models vs. Observations in the Modern Firn

Observations from WDC for surface amplitude (A_S) and attenuation of the δ signal at firn base (A_F) can be compared to firn models (Cuffey and Steig, 1998, WGCS; Johnsen et al., 2000, J-D and J-18O). The actual value of A_S at WDC is difficult to determine due to natural weather variability expressed in the upper portion of the ice core. For example, in 1993 there was a large difference in the summer-to-winter δ signal, resulting in δD and $\delta^{18}O$ amplitude values of 38.5 and 4.49 per mil, respectively. The following ten years (1993-2003) had a maximum δD and $\delta^{18}O$ amplitude value occurring in 2003 of 26.4 and 3.19 per mil, respectively. Half-year δ amplitudes are shown in Figure 4.9.

We opt to determine values of A_S and A_F using three methods (Obs1, Obs2, and Obs3): Obs1) The absolute maximum δ value in the upper 10 years of the firn (A_S) and within the age range 90-100 years (A_F). Obs2) Using a 10-year smoothing window, the maximum δ value in the upper 20 years of the firn (A_S) and within the age range 80-100 years (A_F). 3) Using a 10-year smoothing window, the absolute maximum δ value in the upper 10 years of the firn (A_S) and the maximum δ value within the age range 80-100 years (A_F). For Obs1, we find δD and $\delta^{18}O$ values for A_S of 38.5 and 4.49 per mil and for A_F of 8.2 and 0.81 per mil, respectively. For Obs2, we find δD and $\delta^{18}O$ values for A_S of 22.8 and 2.74 per mil and for A_F of 4.1 and 0.45 per mil, respectively. For Obs3, we find δD and $\delta^{18}O$ values for A_S of 38.5 and 4.49 per mil and for A_F of 4.1 and 0.45 per mil, respectively. The δD ratio of A_F/A_S for Obs1, Obs2, and Obs3 are 0.21, 0.17, and 0.11,

respectively, and 0.18, 0.16, and 0.10 for $\delta^{18}O$, respectively. Firn diffusion modeling yielded A_F/A_S values (at 100 years) of 0.104, 0.170, and 0.124 for the WGCS, J-D, and J-18O models, respectively. To calculate A_F/A_s in the models, we used values for site temperature, ice-equivalent accumulation, atmospheric pressure, ice thickness, average density in the upper 1-2 meters, and tortuosity factor (J-D and J-18O model only) of -30.3°C, 0.23 m/yr, 0.76 atm, 3400 m, 405 kg/m^3, and 1.3, respectively. WDC firn diffusion model results for A_F/A_S and σ_z are shown in Figure 4.9 and Table 4.2.

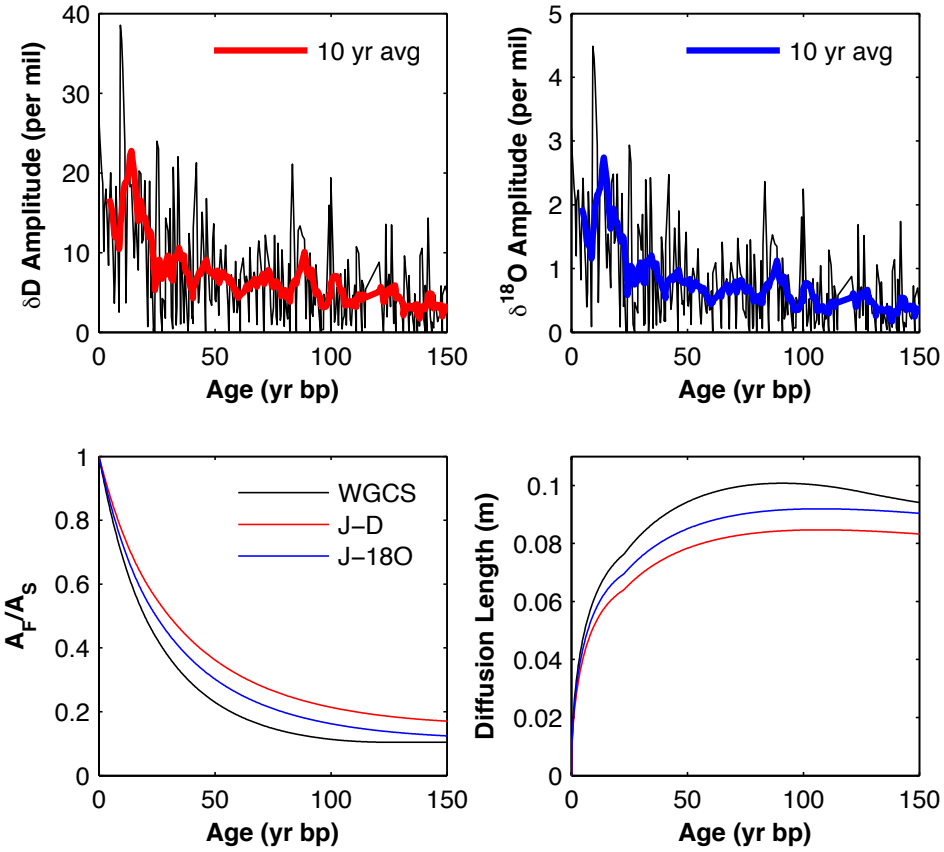

Figure 4.9. *(Upper plots) Half-year δ amplitudes for δD and $\delta^{18}O$ (black lines) with 10 year moving average (thick red and blue lines, respectively). (Lower plots) Firn diffusion model results for A_F/A_S and σ_z for WGCS, J-D, and J-18O (black, red, and blue lines, respectively). The diffusion length decreases at an age greater than 90 years in the WGCS model due to thinning effects that begin to dominate over firn diffusion. The J model diffusion length decreases at an age greater than 140 years.*

Table 4.2.
Values of δ at firn base relative to the surface (A_F/A_S) and diffusion length at firn base (σ_F) for the Cuffey and Steig (CS; 1998) and Johnsen et al. (J; 2000) diffusion models. Note that Johnsen treats the heavy water molecules $H_2{}^{18}O$ and $HD^{16}O$ separately. WDC firn observations are shown as Obs1, Obs2, and Obs3.

Type	WGCS	J	Obs1	Obs2	Obs3
A_F/A_S (δD)	0.104	0.170	0.21	0.17	0.11
A_F/A_S ($\delta^{18}O$)	0.104	0.124	0.18	0.16	0.10
σ_F (δD)	0.094	0.083	-	-	-
σ_F ($\delta^{18}O$)	0.094	0.090	-	-	-

The ambiguity in the amplitude of the δ signal in the upper firn observations makes it difficult for direct comparison to firn models. However, we find that the attenuation of the WDC $\delta^{18}O$ signal is greater than δD, as expected by empirical measurements and theoretical derivations. In the J diffusion model, we can vary the tortuosity factor (τ) between 1.19 and 1.39 to match the entire range of Obs1, 2, and 3 estimates (Johnsen et al. (2000) used a value of 1.3 for GRIP Holocene ice). However, values less than 1.3 may also be unrealistic, and the uncertainty likely arises because we cannot define A_S properly. Additional discussion of tortuosity can be found later in this chapter.

4.3.2. Annual Amplitude Reductions to 29 ka bp

Our modeling approach separates diffusion processes in the firn at any given time from processes occurring beneath the firn column in deeper layers, which is useful for visualization of differing processes occurring over the entire life of a layer in the ice core.

The firn and deep ice modeling must be combined together to get a full representation of the entire loss of signal in the ice core. We use a number of important input time series in our model, including temperature, thinning fraction, and accumulation rate. Both temperature and thinning fraction are derived from 2 ka layer histories determined using a complex ice flow model developed at UC Berkeley (pers. comm. Cuffey, 2013). The layer histories are used to track the unique movement of ice layers through the ice sheet. For example, a layer of ice 21,000 years old (glacial ice) would have a much different thinning and temperature history than a layer of ice only 3,000 years old (Holocene ice). We parametrically interpolate the 2 ka layer histories to 200 yr temperature and thinning fraction layer histories (Figure 4.10). The 200 yr interpolation corresponds to the approximate age at the base of modern firn (i.e. pore close off).

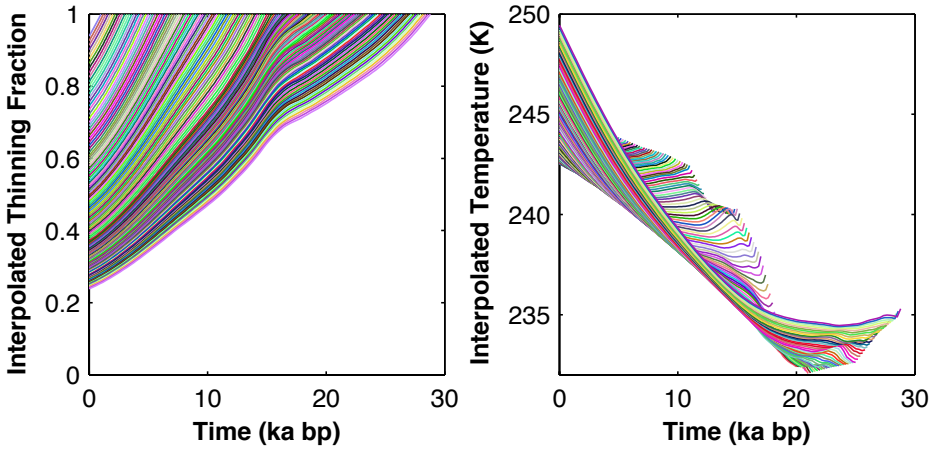

Figure 4.10. *Parametrically interpolated 200-year temperature and thinning fraction layer histories from an ice flow model (pers. comm. Cuffey, 2013). The original model output was at 2 ka intervals at 1 ka, 3ka, 5ka, etc. The plots show the unique thinning and temperature histories of ice layers of a certain age. For example, shorter lines correspond to young ice layers (i.e. ice that fell as snow as a more recent age), and the longest lines correspond to oldest ice (i.e. ice that fell as snow at a much older age).*

For diffusion processes occurring in the firn, temperature largely controls the rate of diffusion, but accumulation rate is more important for the preservation of the δ signal at most ice core sites. For example, if temperature is held constant at -32°C and strain is similar to that seen at WDC, an ice core site with an average accumulation rate of 2 cm/yr would have no annual δ signal remaining at firn base. However, an ice core site with an accumulation rate of 23 cm/yr would have most of the annual δ signal remaining, although some years with small δ amplitudes might "diffuse" into neighboring years with large δ amplitudes. If, however, temperature were to fluctuate by many degrees Celsius, then temperature would have an imprint visibly superimposed on any accumulation changes. Warmer temperatures increase the rate of diffusion, whereas colder temperatures slow the rate of diffusion. Cuffey and Steig (1998) showed that high-accumulation and low temperature ice core sites are best for preservation of an annual water isotope signal.

In Figure 4.11, the firn model values of A_F/A_S over the last 29 ka bp are shown. As expected, A_F/A_S is more similar to accumulation than temperature, largely because temperature remains relatively constant throughout the Holocene, and because the change in accumulation during the glacial transition occurs at a more recent age than temperature. So, when temperature begins to rise at ~20 ka bp, accumulation is still low enough that no annual signal remains at base of firn. Only when accumulation begins to increase at ~17.5 ka bp does an annual signal survive. Accumulation rate and modeled A_F/A_S also show corresponding increases during the mid-Holocene (~3-5 ka bp) and during the accumulation spike at ~11.6 ka bp, as well as a corresponding decrease centered at ~9.6 ka bp. The pattern of A_F/A_S reflects the importance of accumulation

relative to temperature for the preservation of the delta signal at low temperature (i.e. -32°C) ice core sites.

Deep ice δ amplitude remaining relative to firn base (A_D/A_F) is dependent mainly on thinning, accumulation rate, and diffusivity rate (Figure 4.11). Assuming the strain rate of the ice is constant only in the vertical direction[22], annual δ layers are pulled in the horizontal direction due to ice flow dynamics, thinning the annual layers over time. For a layer that was once 23 cm thick at the surface of an ice sheet, that same layer may only be 7 cm thick after 15 thousand years in the ice sheet. If accumulation varies over time, the thickness of a layer at some time will depend on the original annual accumulation rate at the surface of the ice sheet as well as thinning due to strain. Thinner layers are more affected by diffusion, causing a decrease in the amplitude of the signal. And, layers can thin so much as to completely eliminate the annual signal.

[22] Vertical strain ($\boldsymbol{\varepsilon_{zz}}$) is the change in thickness of a layer divided by the total thickness of a layer ($\Delta L/L$). An ice core is often drilled on an ice divide so that the ice experiences only vertical strain and no horizontal strain for the majority of the record.

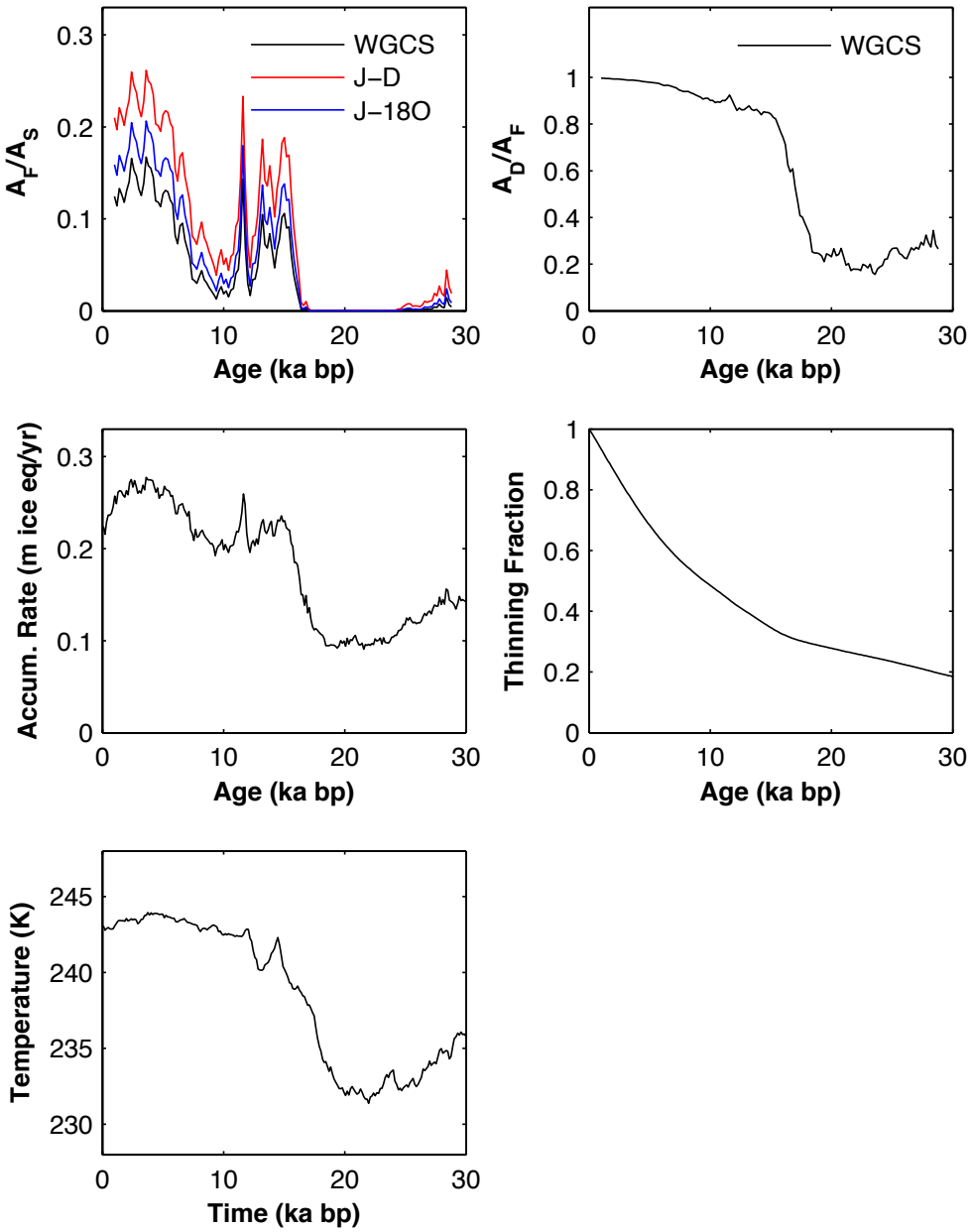

Figure 4.11. *Model realizations for the firn and deep ice compared with accumulation rate, thinning fraction, and temperature histories at WDC. We used values for site temperature, ice-equivalent accumulation, atmospheric pressure, ice thickness, average density in the upper 1-2 meters, and tortuosity factor (J-D and J-18O model only) of -30.3°C, 0.23 m/yr, 0.76 atm, 3400 m, 405 kg/m^3, and 1.3, respectively. The deep ice model isotopic diffusivity $\alpha(t)$ was set to a constant value of 5.0x10^{-6} m^2/sec.*

The total δ amplitude reduction value in an ice core can be obtained from the product of estimated surface amplitude, the modeled fractional amplitude at base of firn relative to the surface, and the modeled fractional amplitude in deep ice relative to the base of firn ($A_T = A_S \cdot \frac{A_F}{A_S} \cdot \frac{A_D}{A_F}$). The model results can then be compared to WDC observations in the frequency domain. We take 250-year windows of WDC water isotope data (units of per mil) and convert to frequency space by MTM spectral analysis. This yields power density (per mil$^2 \cdot$ yr), and the square root of the integral of the 1-year power density peak gives the total amplitude value A_T (per mil). In the models, we vary a number of values to maximize the fit including the surface amplitude A_S, the isotopic diffusivity (α), and the tortuosity (τ). Table 4.3 shows the summary of the variables used in the model to match observations. Figure 4.12 shows the comparison of A_T derived from both diffusion modeling and WDC observations.

Table 4.3.
A summary of the variables used in Figure 4.12 to determine A_T. Three model realizations allowed a single parameter to vary over time. For example, when A_S varied, α and τ were held constant at $1.0*10^{-5}$ m^2/s and 1.30, respectively. When α varied, δD A_S, $\delta^{18}O$ A_S, and τ were held constant at 25 per mil, 3.3 per mil, and 1.30, respectively. When τ varied, δD A_S, $\delta^{18}O$ A_S, and α were held constant at 25 per mil, 3.3 per mil and $1.0*10^{-5}$ m^2/s, respectively. Values for A_S are shown for δD ($\delta^{18}O$).

Age Range (ka bp)	A_S (per mil)	α (m^2/s)	τ
1 to 3	17 (2.3)	$2.0*10^{-4}$	1.10
3 to 5	21 (2.8)	$8.0*10^{-5}$	1.10
5 to 7	24 (3.2)	$1.0*10^{-5}$	1.10
7 to 9	28 (3.7)	$1.0*10^{-5}$	1.10
9 to 11	28 (3.7)	$1.0*10^{-5}$	1.45
11 to 13	18 (2.4)	$3.0*10^{-5}$	1.30
13 to 15	12 (1.6)	$3.5*10^{-5}$	1.00

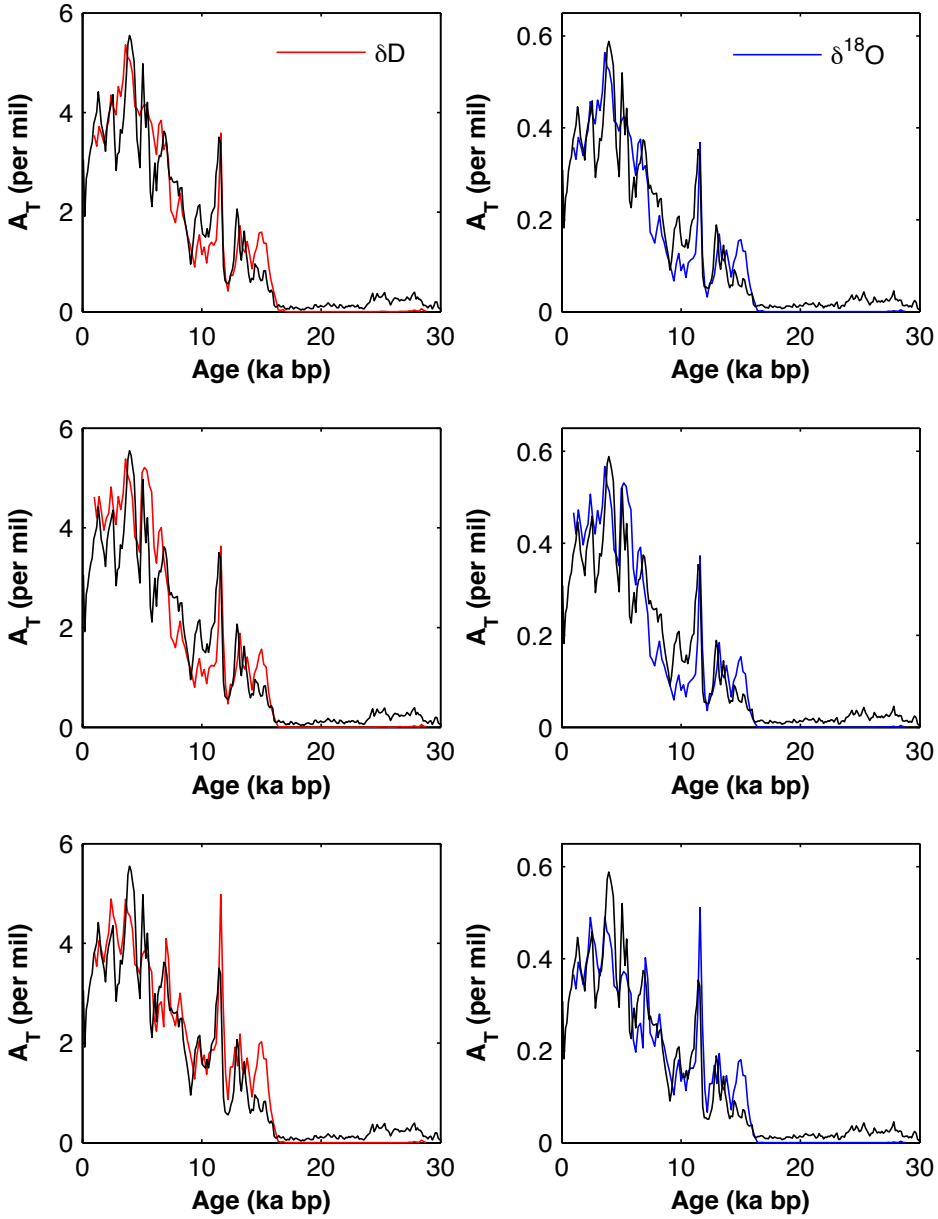

Figure 4.12. *Model realizations of A_T for δD (red) and $\delta^{18}O$ (blue). The upper plots vary A_S (surface amplitude) only, while holding isotopic diffusivity (α) and tortuosity (τ) constant at $1.0*10^{-5}$ m^2/s and 1.3, respectively. The middle plots vary α only, while holding δD A_S, $\delta^{18}O$ A_S, and τ constant at 25 per mil, 3.3 per mil, and 1.3, respectively. The lower plots vary τ only, while holding δD A_S, $\delta^{18}O$ A_S, and α constant at 25 per mil, 3.3 per mil, and $1.0*10^{-5}$ m^2/s, respectively. Some combination of variability in all three parameters (A_S, α, and τ) would optimize the fit. Varying the temperature sensitivity γ does not significantly alter these results. Table 4.3 shows a summary of the values used in this analysis.*

The results of the three model realizations used to determine A_T give possible ranges of values for A_S (surface amplitude), isotopic diffusivity (α), and tortuosity (τ). For any given model run, only one of three parameters was allowed to vary, while the other were held constant. A constant value for A_S of 25 per mil and 3.3 per mil for δD and $\delta^{18}O$, respectively, was chosen based upon modern firn surface amplitude estimates shown in Figure 4.9. A constant value for α of $1.0*10^{-5}$ m^2/s was chosen based upon the published diffusivities at Siple Station given by Swander et al. (1988). A constant value for τ of 1.3 was chosen based upon the published tortuosity value at GRIP given by Johnsen et al. (2000). Using these values, and allowing 1 of 3 parameters to vary during a model run, we find a possible range of values for δD A_S, $\delta^{18}O$ A_S, α, and τ of 12 to 28 per mil, 1.6 to 3.7 per mil, $2.0*10^{-4}$ to $1.0*10^{-5}$ m^2/s, and 1.00 to 1.45, respectively. Varying the temperature sensitivity (γ) did not significantly alter these results.

4.3.3. Diffusion Lengths to 29 ka bp

An alternative method for modeling reduction in δ amplitudes at WDC is by analysis of diffusion lengths[23] using the full spectrum of frequency information from the water isotope record, rather than the annual peak. To determine diffusion lengths in the frequency domain, we fit a Gaussian filter to frequency observations in the range 0.1-1.2 cycles/yr (i.e. 10 yr to sub-annual oscillations) over 500 year intervals. There are three advantages to this technique: 1) Using the entire frequency spectrum allows for diffusion modeling over the entire annually dated portion of WDC to 29 ka bp, whereas modeling

[23] The diffusion length term (σ) is the average vertical displacement of a water molecule from its original position in the ice (disregarding the sinking of annual layers).

the annual peak only yields information to ~15 ka bp before the yearly oscillation decays away. 2) Modeling diffusion length removes the surface amplitude A_S parameter, which is difficult to estimate in the modern firn and is generally unknown in the past. 3) Diffusion lengths can be used for back diffusion to estimate the original δ signal (discussed in Chapter 5 of this dissertation). We specifically look at diffusion lengths in terms of depth (m), depth destrained (m), and time (yr).

In terms of physical processes, diffusion of water molecules in an ice sheet spreads the δ signal through the strata, which causes diffusion length to increase. Initially, most diffusion occurs in the firn column. For example, the estimated WDC diffusion length in the CSWG model increases from 0 cm at the surface to 8 cm within ~200 years (Figure 4.9, Table 4.2). Solid ice diffusion occurs much slower, which gradually effects diffusion length over time. In young ice, the effects of solid ice diffusion are small compared to the firn. In old ice (perhaps 40 to 50 ka bp), solid ice diffusion can be as large or larger than the original diffusion occurring in the firn. So, the firn dominates diffusion length at first, but as a layer of ice moves through the ice sheet, solid diffusion slowly increases until it becomes quite important.

Diffusion length can be reported from both depth and time based δ records, but with important differences. When determining diffusion length as a function of depth beneath the firn, layers of ice are compressing (i.e. thinning or being strained) faster than the isotopes are diffusing due to solid diffusion, so the diffusion length (m) decreases over time. The effects of thinning can be removed by dividing the diffusion length (m) by

the thinning function[24]. The destrained diffusion length is then affected mainly by temperature and accumulation rate. When determining diffusion length as a function of age beneath the firn, diffusion length must increase due to solid diffusion if the accumulation rate is constant. In this case, thinning has already been accounted for by the dating of annual layers, but the spreading of water molecules is still occurring over the same distance. With a constant accumulation rate, solid diffusion would cause diffusion length (yr) to increase, since the water molecules will become more displaced over time relative to the age markers. If the accumulation rate varies over time (e.g. at WDC), then the annual layer thicknesses vary and diffusion length (yr) must vary too. Temperature fluctuations also affect diffusion length (yr) and are most visible during large transitions. For any diffusion length calculation (depth, depth destrained, or time), impurities in the ice (i.e. dust, etc.) can affect diffusion rates and alter the δ signal (Rempel et al., 2001; 2002), but more research is needed to understand this anomaly. Diffusion length as a function of depth, age, and depth destrained are shown in Figure 4.13.

[24] The thinning function gives the total strain (i.e. the total change in length in the vertical direction of a layer relative to the original thickness of the layer) as a function of depth.

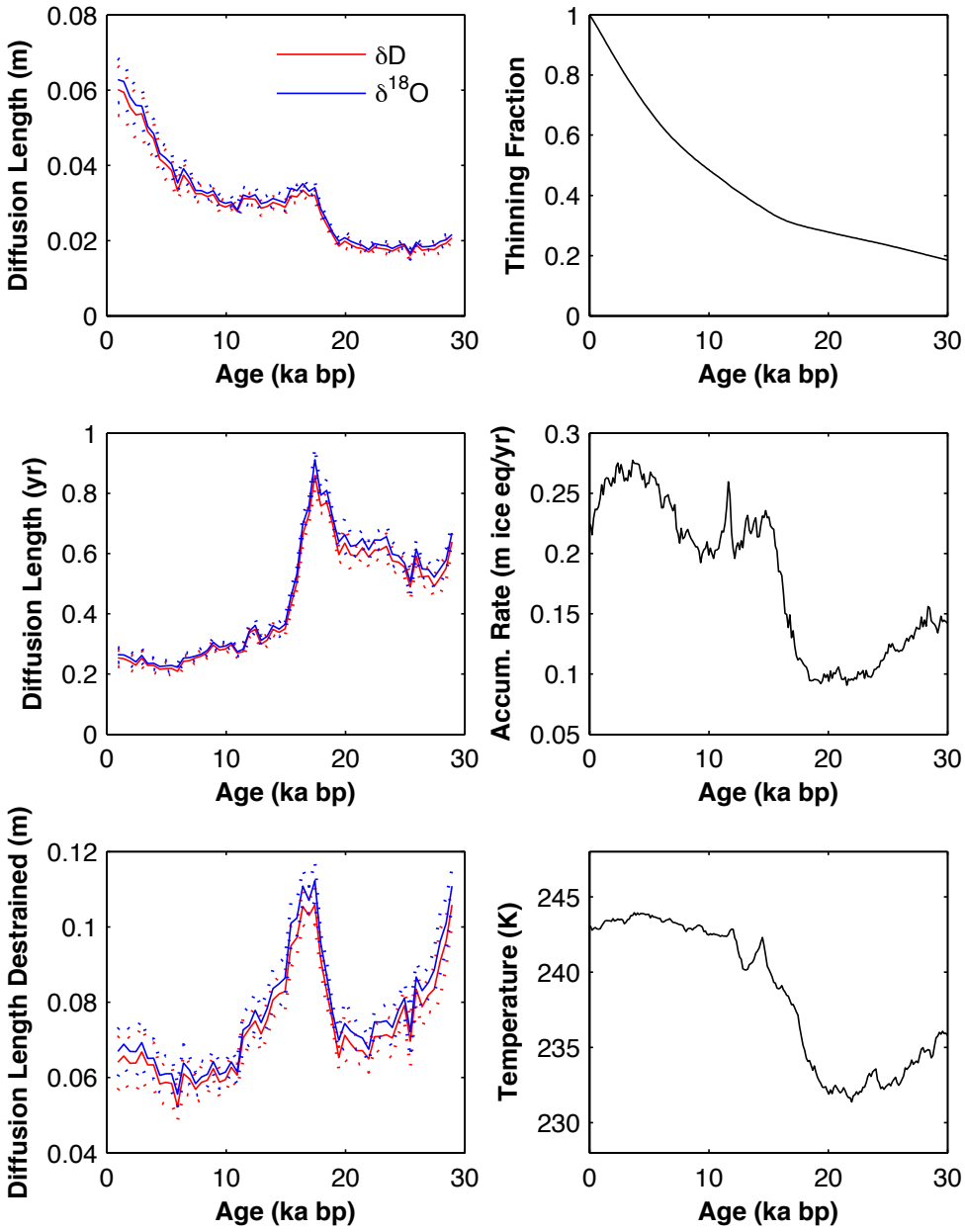

Figure 4.13. (*Left Column) Diffusion lengths for δD (red) and $\delta^{18}O$ (blue) as a function of depth (m; top), time (yr; middle), and depth destrained (m; bottom). The uncertainty of the diffusion length fit is shown by the dotted lines. (Right Column) Plots of thinning fraction (top), accumulation rate (m ice eq/yr; middle), and temperature (K; bottom).*

The overall shape of diffusion length as a function of depth is very similar to the thinning history of the ice. From ~0-7 ka bp, the ice thins fastest, followed by decreases in the thinning rate from ~7-16 ka bp, and again from ~16-30 ka bp. In comparison, diffusion length (m) decreases relatively rapidly from ~0-5 ka bp (6.0 to 3.5 cm), and then more slowly decreases overall from ~5-29 ka bp (3.5 to 1.8 cm), with almost no change occurring from ~19-29 ka bp (2.0 to 1.8 cm). There is a relatively rapid increase in diffusion from 19.0 to 17.5 ka bp (1.8 to 3.3 cm) related to the increase in temperature (and increased rate of diffusion) during the glacial-interglacial transition. In general, diffusion length as a function of depth is directly related to thinning, with some effects from temperature evident.

Diffusion length as a function of years decreases slightly from ~0-5.5 ka bp (0.3 to 0.2 yr), and then increases from ~5.5-15.0 ka bp (0.2 to 0.3 yr). A minimum diffusion length (yr) value occurs during the mid-Holocene at a time when the accumulation rate is higher than anytime in the last 29 ka. From ~17-15 ka bp, diffusion length (yr) decreases rapidly (0.9 to 0.3 yr), coherent with an increase in accumulation during the glacial-interglacial transition. From ~20-17 ka bp, diffusion length (yr) increases abruptly (0.6 to 0.9 yr) due to the temperature change during the glacial-interglacial transition. The temperature affect on diffusion length (yr) is superimposed on a more dominant accumulation signal. From ~29-20 ka bp, the diffusion length varies over the range 0.5 to 0.6 years. In general, diffusion length as a function of time is inversely related to accumulation rate, with temperature effects evident as well.

Destrained diffusion length as a function of depth decreases relatively rapidly from ~29-19.5 ka bp (11 to 7 cm), but neither temperature nor accumulation can explain

this change. From ~19.5-17 ka bp, destrained diffusion length increases rapidly (7 to 11 cm) related to the increase in temperature during the glacial-interglacial transition. Then, destrained diffusion length decreases relatively rapidly from ~17-11 ka bp (11 to 6 cm). Again, neither temperature nor accumulation can explain this change. From ~11-1 ka bp, destrained diffusion length (m) varies between 5.3 and 6.6 cm. In general, destrained diffusion length as a function of depth is affected by the glacial-interglacial temperature change, as well as other anomalous processes.

One possible explanation for the mystery intervals seen in destrained diffusion length (m) is changes in the deposition of impurities like dust and calcium. Impurities can affect the densification process in the firn (Alley, 1987 and Hörhold et al., 2012) as well as affect paleoclimate records and cause anomalous diffusion in the deep ice (Rempel and Wettlaufer, 2003). In Figure 4.14, we show a comparison of destrained diffusion length and calcium (Ca^{2+}) over the interval 6-27 ka bp. The Ca^{2+} concentration is highest during the glacial period from 27-19 ka bp, varying between 6 to 25 ppb. The highest values occur from 27-25 ka bp. From 19-15 ka bp, calcium decreases by an order of magnitude, likely due to climatic changes during the glacial-interglacial transition. From 15-6 ka, Ca^{2+} varies between 0.1 to 1 ppb. Information from 0-6 ka bp is not available. In general, Ca^{2+} decreases by a factor of 2 from 27 to 20 ka bp, and decreases by an order of magnitude from 20 to 10 ka bp.

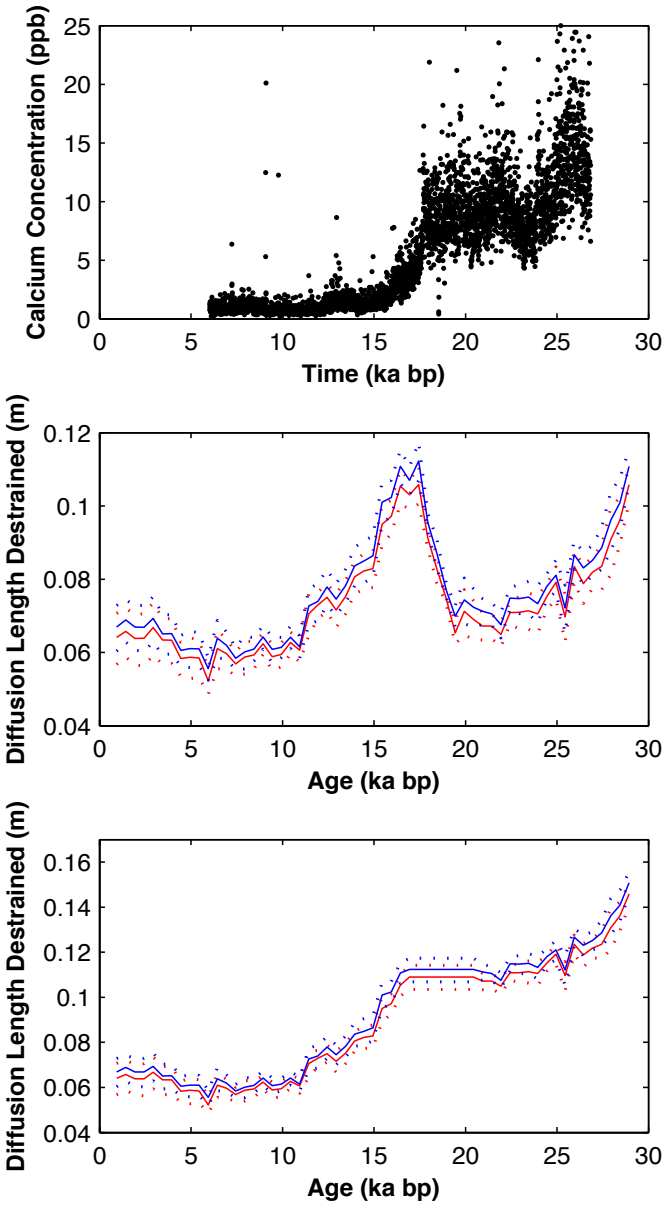

Figure 4.14. *(Top) Comparison of calcium concentration (ppb; impurity proxy), (middle) destrained diffusion length (m) for δD (red) and $\delta^{18}O$ (blue), and (bottom) estimated destrained diffusion length with temperature effects removed during the glacial-interglacial transition. Specifically, the temperature increase from ~19-17 ka bp resulted in a destrained diffusion length increase of ~4cm. Destrained diffusion lengths greater than 19ka were increased 4cm, and the resulting plot looks similar to calcium concentrations at WDC. Temperatures on either side of the glacial-interglacial transition ire relatively constant and excluded for the purposes of this thought experiment.*

In the following two paragraphs, we discuss possible impurity driven mechanisms for the anomalous destrained diffusion lengths. In the modern WDC firn, diffusion length is almost entirely determined by vapor phase diffusion from 3-67 meters depth (Figure 4.1). The density of the firn column, microstructure, and temperature controls vapor phase diffusion. The firn column density is controlled mainly by temperature and accumulation rate, and recent research has shown impurity effects can have a significant impact on firn densification processes as well. For example, Hörhold et al. (2012) found that Ca^{2+} concentrations increased densification over a wide range of concentrations. However, if higher impurity concentrations speed up the densification process, this would reduce diffusion lengths since water molecules have less time to move through the interconnected vapor pathways in the firn. The destrained diffusion lengths show the exact opposite: higher destrained diffusion lengths correspond to higher Ca^{2+} concentrations. The presence of impurities in the firn cannot be affecting destrained diffusion length.

In ice deeper than the firn, impurities concentrate on grain boundaries and within intergranular veins. More impurities can produce wider grain boundaries and bigger veins. If deep ice diffusion occurs mainly in unfrozen liquid veins that separate the ice grain boundaries (termed premelting[25]; Dash and Wettlaufer, 1995; Wettlaufer, 1999; Dash et al., 2006), then diffusion should be enhanced where there are more impurities because water molecules diffuse faster in the liquid phase than in the solid phase. The impurity effect could also be temperature dependent, only switching on when the impurity concentration exceeds a certain threshold. As a thought experiment, the effects

[25] The term premelting refers to the phenomenon that quasi-liquid films can exist on or between polycrystalline ice surfaces below the melting point of water.

of temperature can be removed from destrained diffusion length (m) by increasing the diffusion length at ages greater than 20 ka bp by 4 cm, which is equal to the change in diffusion length during the glacial-interglacial temperature change from 19-17 ka bp (Figure 4.14). When the effects of temperature are removed, the destrained diffusion length looks very similar to Ca^{2+}. There appears to be a delay of ~1 ka from the initiation of the Ca^{2+} decrease at 17 ka and the destrained diffusion length decrease at 16 ka bp. However, this period of time is uncertain due to large changes in accumulation and temperature at the glacial-interglacial transition, and more research would be needed to form any conclusions. Specifically, an impurity driven solid diffusion model would be needed to determine the effects of impurities residing primarily in liquid veins or primarily within the ice grains themselves, as described by Rempel and Wettlaufer (2003). Based on our results, we suggest that impurities are having a substantial effect on deep ice diffusion at WDC.

The change in total diffusion length ($\sigma_T = \sigma_{firn} + \sigma_{deep} * \frac{\lambda}{\lambda_F}$) over time can be investigated using three diffusion models (WGCS, J-D, J-18O). Model realizations of δD diffusion lengths for three diffusivities and variable tortuosity are showing in Figure 4.15. All three diffusion models over estimate σ_T by 2 cm at 1 ka bp. This discrepancy can be resolved in the J-D and J-18O model by adjusting the tortuosity τ (the WGCS model does not incorporate tortuosity). To achieve a fit of WDC diffusion lengths at 1 ka bp requires a τ value of 1.7. Then, using a constant τ of 1.7, a range of diffusivity values can then be determined. An elevated diffusivity of $9.0*10^{-6}$ m^2/s is necessary to explain the data ranging from ~11-19 ka bp. From ~19-25 ka bp, a diffusivity of $5.0*10^{-7}$ m^2/s is need to explain the data. From ~3-11 ka bp, diffusivity cannot be lowered enough to match the

data (i.e. before achieving zero diffusivity), and requires additional adjustment to the tortuosity parameter. If an average diffusivity of $5.0*10^{-6}$ m^2/s is chosen, adjustments to τ ranging from 1.3 to 2.2 accurately capture the change in observed diffusion lengths over time. The range of diffusivity and tortuosity values can be used as first order approximations of the values needed to match observations. Adjustments to the temperature sensitivity of diffusivity in the deep ice do not significantly change these results.

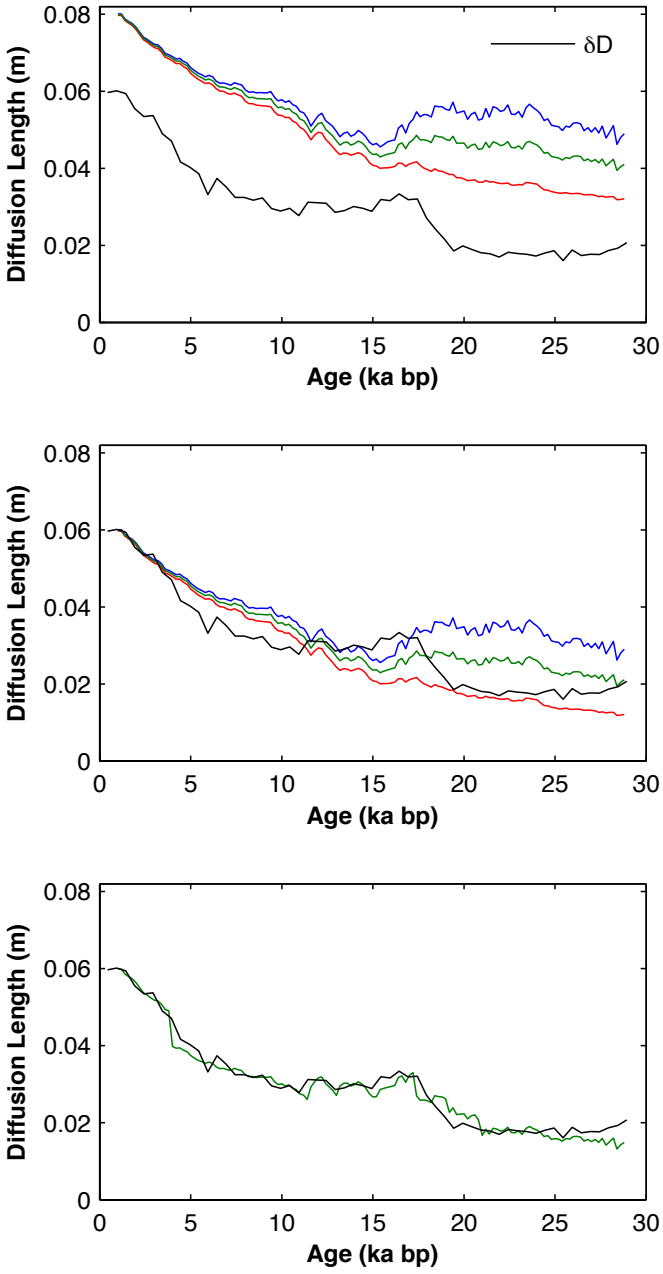

Figure 1.2. *Plots of model vs. observations for δD total diffusion length. (Top) The Johnsen et al. (2000) deuterium model using a tortuosity value of 1.3 and three diffusivity values: $9.0*10^{-6}$ m^2/s (blue), $5.0*10^{-6}$ m^2/s (green), and $5.0*10^{-7}$ m^2/s (red). (Middle) Using the same diffusivity values as the top plot, tortuosity is adjusted to 1.7 to fit the model to data at 1 ka bp. (Bottom) Using a constant diffusivity of $5.0*10^{-6}$ m^2/s (green) and tortuosity values ranging from 1.3-2.2 maximizes the model fit to observations. The effects of impurities are not included in the model.*

A number of studies have documented varying values of diffusivity and tortuosity in polar ice sheet locations. Most gas diffusion models have historically used a tortuosity and porosity relation published by Schwander (1988) at Siple Station. Schwander found a linear relation between tortuosity values ranging from 2.0 to 7.0 for porosity ranging from 0.5 to 0.2, respectively. But, recent research has shown this approach to be inadequate. Fabre et al. (2000) showed that tortuosity profiles are site dependent and related to the microstructure of the ice. At WDC and other ice core site, the total porosity of firn decreases with depth as firn densifies, reflecting the amount of space not filled by ice. But, the relationship is more complicated, as both an open porosity and closed porosity can be defined. Open porosity is the amount of interconnected air space (between solid ice) available for gas transport that is connected in some way to the atmosphere, while closed porosity is the amount of air space completely surrounded by ice. Depending how much of the total porosity is comprised of open or closed porosity, and ice grain size, will have an effect on diffusion and the depth of the lock-in zone (Gregory et al., 2014). At WDC, from 55 to 75 meters depth, the total porosity ranges from about 6-16%, which in the Schwander (1988) would correspond to a tortuosity of at least 7.0. However, in both δ amplitude reduction and diffusion length modeling discussed in this paper, we find values of tortuosity ranging from 1.10-1.45 and 1.30-1.22, respectively. For diffusivity, Schwander (1988) found values of $1.0*10^{-6}$ to $9.0*10^{-6}$ m^2/sec for porosity of 0.2 to 0.5, respectively. Fabre et al. (2000) and Freitag et al. (2002) found similar results for porosities greater than 0.2. In this study, δ amplitude reduction and diffusion length modeling result in diffusivity values ranging from $2.0*10^{-4}$ to $1.0*10^{-5}$ m^2/s and $5.0*10^{-6}$ m^2/s to $5.0*10^{-7}$ m^2/s.

The modeled values for tortuosity and diffusivity must be taken in context. The adjustment of other boundary conditions like surface amplitude (A_S) and the relative unknown combination of all values relative to each other greatly increases the complexity of ice core δ modeling. We are also unsure how self-diffusion of water in deep ice is affected by impurities: we think it may be substantial. These uncertainties require a more complex model, which is beyond the scope of this research, and also have implications for inverse modeling, which requires certain parameters to be constant throughout the ice core (i.e. diffusivity). Without steady state behavior, inverse reconstruction of an alternative accumulation history, for example, is not possible.

4.3.4. Differential Diffusion Length

Due to differences in mass and a higher vapor-ice fractionation factor for $HD^{16}O$, there are less diffusing $HD^{16}O$ water vapor molecules relative to $H_2{}^{18}O$. This causes the diffusion length for $\delta^{18}O$ to be greater than δD. As a result, the δD signal is smoothed less in an ice core record, and the amplitude of the δD signal grows during firnification relative to the $\delta^{18}O$ signal. The water isotope data from WDC consistently shows this effect. In each of the sub plots in Figure 4.16, the diffusion length for $\delta^{18}O$ is greater than δD over the last 29 ka. Johnsen et al. (2000) showed that the ratio of diffusion length in the firn is temperature dependent:

$$\frac{\sigma_{f18}}{\sigma_{fD}} = \sqrt{\frac{\alpha_D}{\alpha_{18}}} \tag{31}$$

where α_i is the fractionation factor for deuterium or oxygen-18 in water vapor over ice. The fractionation factors are dependent only on temperature (Equations 14 and 15). For modern firn at WDC, the Johnsen et al. (2000) model (J model) value for σ_{f18}/σ_{fD} is 1.09, which is a ~9% greater diffusion length for $\delta^{18}O$ than δD. Observations at WDC for the last 29 ka show σ_{f18}/σ_{fD} values ranging from 1.02 to 1.07, with an average value of 1.05 (Figure 4.15). For the most recent 1 ka, the observations are under predicting the amount of differential diffusion by ~4% relative to the J model. There does not appear to be a strict temperature dependence of the ratio over time either, which is especially evident during the glacial-interglacial transition temperature change from 19 to 17.5 ka bp. This suggests that post-firnification diffusion processes may be affecting the amount of differential diffusion, such as impurity effects on solid ice diffusion.

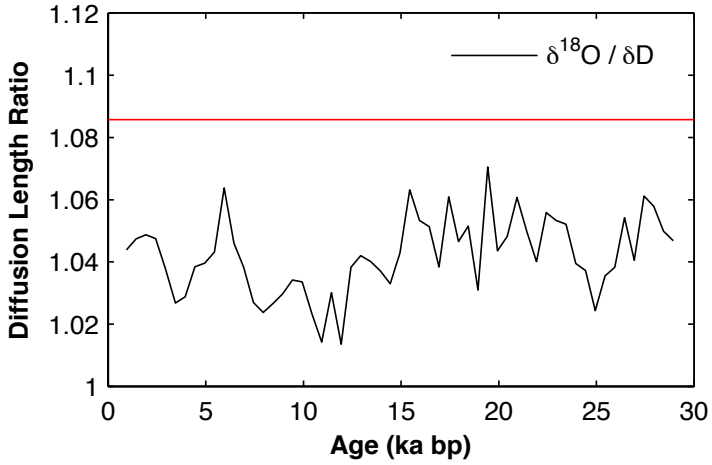

Figure 4.16. *Plot of differential diffusion length ratio for WDC ($\delta^{18}O/\delta D$; black line). The red line is the modern modeled diffusion length ratio at base of firn using the Johnsen et al. (2000) model. The model predicts ~9% greater diffusion length for $\delta^{18}O$ than δD, whereas observations on average are about ~4% smaller. There does not appear to be a strict temperature dependence on the ratio, which is evident in the lack of response during the glacial-interglacial temperature increase from 19-17.5 ka bp.*

4.4. Conclusions

Water isotopes records in polar ice cores are natural archives of past climatic change. Post-depositional processes alter the original isotope signal. The strongest signal attenuation occurs in the firn column due to diffusion. A much slower diffusion process occurs in deep ice below the firn. The effects of diffusion can be quantified by solving for diffusion length, which represents the average displacement of a water molecule in the vertical direction, using a Gaussian filter in the frequency domain. We have presented diffusion lengths for the West Antarctic Ice Sheet Divide ice core (WDC) as a function of depth, depth destrained, and time. Each of these diffusion length types shows varying effects from changes in temperature, accumulation rate, and thinning. An anomalous diffusion process is also evident that may be related to the effects of impurities on the self-diffusion of ice. The differential diffusion of $H_2{}^{18}O$ and $HD^{16}O$ is consistent throughout the ice core: the δD signal is smoothed less. However, the differential diffusion of δD relative to $\delta^{18}O$ is 4% less than empirically derived model values for firn at 1 ka bp, suggesting post-firnification processes have a noticeable influence on the water isotope record.

Classic water isotope diffusion models are used to understand the diffusion processes at WDC. We find values for tortuosity and diffusivity for the last 29 ka that are similar to other polar-centric studies, but cannot determine exact values because neither parameter can be fully constrained relative to the other. Further complexity arises from the apparent effects of impurities in solid ice, which is not accounted for in our models. These difficulties point to the benefit of a more complex, coupled water isotope diffusion

model that approximates the firn microstructure (porosity and tortuosity) of unique ice core sites and the self-diffusion of ice in the presence of impurities.

Beyond modeling considerations, the total diffusion length values can be used for reconstruction of past climatic processes. For example, diffusion lengths are useful for back diffusion of spectral power and reconstruction of the original amplitude of oscillations in the water isotope signal. The correction of water isotope signals occurring in the 2-7 year range, which is a known oscillation band of the El Niño Southern Oscillation, would be useful to constrain models, provide context for other paleoclimate records, and provide insight into climate changes occurring on human relevant timescales. Along similar lines, the 1-year signal could be reconstructed to determine how West Antarctic annual climate has responded to long-term insolation changes and varied over shorter time-scales. The seasonality of the isotope signal associated with summer and winter maximum amplitudes could also be examined.

4.5. References

Albert, M. R., Shultz, E. F., & Perron, F. E. (2000). Snow and firn permeability at Siple Dome, Antarctica. *Annals of Glaciology*, 31(1), 353-356.

Albert, M. R., & Shultz, E. F. (2002). Snow and firn properties and air–snow transport processes at Summit, Greenland. *Atmospheric Environment*, *36*(15), 2789-2797.

Alley, R. B. (1987). Firn densification by grain-boundary sliding: a first model. Le *Journal de Physique Colloques*, 48(C1), C1-249.

Arfken, G. (1985). Discrete Orthogonality--Discrete Fourier Transform. (1985). *§14.6 in Mathematical Methods for Physicists*, 3rd ed. Orlando, FL: Academic Press, pp. 787-792.

Battle, M. O., Severinghaus, J. P., Sofen, E. D., Plotkin, D., Orsi, A. J., Aydin, M., Montzka, S. A., Sowers, T., & Tans, P. P. (2011). Controls on the movement and composition of firn air at the West Antarctic Ice Sheet Divide. *Atmospheric Chemistry and Physics*, 11(21), 11007-11021.

Cooley, J. W. and Tukey, O. W. (1965). An Algorithm for the Machine Calculation of Complex Fourier Series. *Math. Comput.* 19, 297-301.

Cuffey, K. M., & Steig, E. J. (1998). Isotopic diffusion in polar firn: implications for interpretation of seasonal climate parameters in ice-core records, with emphasis on central Greenland. *Journal of Glaciology*, *44*(147), 273-284.

Cuffey, K. M., & Paterson, W. S. B. (2010). *The physics of glaciers*. Academic Press.

Cuffey, K. M., personal communication, Layer tracking from a temperature-strain model for the WAIS Divide ice core. November, 2013.

Dansgaard, W., & Johnsen, S. J. (1969). A flow model and a time scale for the ice core from Camp Century, Greenland. *Journal of Glaciology*, *8*, 215-223.

Dash, J. G., Fu, H., & Wettlaufer, J. S. (1995). The premelting of ice and its environmental consequences. *Reports on Progress in Physics*, 58(1), 115.

Dash, J. G., Rempel, A. W., & Wettlaufer, J. S. (2006). The physics of premelted ice and its geophysical consequences. *Reviews of modern physics*, 78(3), 695.

Delibaltas, P., Dengel, O., Helmreich, D., Riehl, N., & Simon, H. (1966). Diffusion von18O in Eis-Einkristallen. *Physik der kondensierten Materie*, 5(3), 166-170.

Fabre, A., Barnola, J. M., Arnaud, L., & Chappellaz, J. (2000). Determination of gas diffusivity in polar firn: comparison between experimental measurements and

inverse modeling. *Geophysical research letters*, 27(4), 557-560.

Freitag, J., Wilhelms, F., & Kipfstuhl, S. (2004). Microstructure-dependent densification of polar firn derived from X-ray microtomography. *Journal of Glaciology*, 50(169), 243-250.

Geiger, G. H., & Poirier, D. R. (1973). Transport phenomena in metallurgy. Addison-Wesley Publishing Co., Reading, Mass. 1973, 616 p.

Gregory, S. A., Albert, M. R., & Baker, I. (2014). Impact of physical properties and accumulation rate on pore close-off in layered firn. *The Cryosphere*, 8(1), 91-105.

Grew, K. E., & Ibbs, T. L. (1952). Thermal diffusion in gases. *Cambridge University Press.*

Hall, W. D., & Pruppacher, H. R. (1976). The survival of ice particles falling from cirrus clouds in subsaturated air. *Journal of the Atmospheric Sciences*, *33*(10), 1995-2006.

Herron, M. M., & Langway Jr, C. C. (1980). Firn densification: an empirical model. *Journal of Glaciology*, *25*, 373-385.

Hörhold, M. W., Laepple, T., Freitag, J., Bigler, M., Fischer, H., & Kipfstuhl, S. (2012). On the impact of impurities on the densification of polar firn. *Earth and Planetary Science Letters,* 325, 93-99.

Itagaki, K. (1967). Self-diffusion in single crystal ice. *Journal of the Physical Society of Japan*, *22*(2), 427-431.

Johnsen, S. J. (1977). Stable isotope homogenization of polar firn and ice. *Isotopes and impurities in snow and ice*, 210-219.

Johnsen, S. J., Clausen, H. B., Cuffey, K. M., Hoffmann, G., Schwander, J., & Creyts, T. (2000). Diffusion of stable isotopes in polar firn and ice: the isotope effect in firn diffusion. *Physics of ice core records*, 159, 121-140.

Majoube, M. (1970). Fractionation factor of 18O between water vapour and ice.

Merlivat, L., & Nief, G. (1967). Isotopic fractionation of solid-vapor and liquid-vapor changes of state of water at temperatures below 0◦ C. *Tellus*, *19*, 122-127.

Merlivat, L., & Jouzel, J. (1979). Global climatic interpretation of the deuterium–oxygen 18 relationship for precipitation. *Journal of Geophysical Research: Oceans (1978–2012)*, *84*(C8), 5029-5033.

Morse, D. L., Blankenship, D. D., Waddington, E. D., & Neumann, T. A. (2002). A site for deep ice coring in West Antarctica: results from aerogeophysical surveys and thermo-kinematic modeling. *Annals of Glaciology*, 35(1), 36-44.

Nye, J. F. (1998). Diffusion of isotopes in the annual layers of ice sheets. *Journal of Glaciology*, *44*(148), 467-468.

Park, J. (1992). *Envelope estimation for quasi-periodic geophysical signals in noise: A multitaper approach, in Statistics in the Environmental and Earth Sciences*, edited by A.T. Walden and P. Guttorp, 189-219, Edward Arnold, London.

Percival, D. B., & Walden, A. T. (1993). *Spectral analysis for physical applications: multitaper and conventional univariate techniques*, 583 pp.

Press, W. H.; Flannery, B. P.; Teukolsky, S. A.; and Vetterling, W. T. (1989). Fourier Transform of Discretely Sampled Data. *§12.1 in Numerical Recipes in FORTRAN: The Art of Scientific Computing*, 2nd ed. Cambridge, England: Cambridge University Press, pp. 494-498.

Ramseier, R. O. (1967). Self‐Diffusion of Tritium in Natural and Synthetic Ice Monocrystals. *Journal of Applied Physics*, *38*(6), 2553-2556.

Rempel, A. W., Waddington, E. D., Wettlaufer, J. S., & Worster, M. G. (2001). Possible displacement of the climate signal in ancient ice by premelting and anomalous diffusion. Nature, 411(6837), 568-571.

Rempel, A. W., Wettlaufer, J. S., & Waddington, E. D. (2002). Anomalous diffusion of multiple impurity species: predicted implications for the ice core climate records. Journal of Geophysical Research: Solid Earth (1978–2012), 107(B12), ECV-3.

Rempel, A. W., & Wettlaufer, J. S. (2003). Isotopic diffusion in polycrystalline ice. *Journal of Glaciology*, *49*(166), 397-406.

Robin, G. (1983). The climatic record from ice cores. *The climatic record in polar ice sheets*, 180-195.

Schwander, J., Stauffer, B., & Sigg, A. (1988). Air mixing in firn and the age of the air at pore close-off. *Ann. Glaciol*, 10, 141-145.

Severinghaus, J. P., Bender, M. L., Keeling, R. F., & Broecker, W. S. (1996). Fractionation of soil gases by diffusion of water vapor, gravitational settling, and thermal diffusion. *Geochimica et Cosmochimica Acta*, 60(6), 1005-1018.

Souney, J. M., Twickler, M. S., Hargreaves, G. M., Bencivengo, B. M., Kippenhan, M. J., Johnson, J. A., Cravens, E. D., Neff, P. D., Nunn, R. M., Orsi, A. J., Popp, T. J., Rhoades, J. F., Vaughn, B. H., Voight, D. E., Wong, G. J., & Taylor12, K. C. (2014). Core handling and processing for the WAIS Divide ice-core project. *Annals of Glaciology*, 55, 68.

Steig, E. J., Ding, Q., White, J. W. C., Kuttel, M., Rupper, S. B., Neumann, T. A., Neff, P. D., Gallant, A. J. E., Mayewski, P. A., Taylor, K. C., Hoffmann, G., Dixon, D. A., Schoenemann, S. W., Markle, B. R., Fudge, T. J., Schneider, D. P., Schauer, A. J., Teel, R. P., Vaughn, B. H., Burgener, L., Williams, J., & Korotkikh, E. (2013), Recent climate and ice-sheet changes in West Antarctica compared with the past 2,000 years, *Nature Geoscience*, 6(5), 372–375.

Thomson, D. J. (1982). Spectrum estimation and harmonic analysis. *Proceedings of the IEEE*, 70(9), 1055-1096.

WAIS Divide Project Members. (2013). Onset of deglacial warming in West Antarctica driven by local orbital forcing. *Nature*, 500(7463), 440-444.

Wettlaufer, J. S. (1999). Impurity effects in the premelting of ice. *Physical Review Letters*, 82(12), 2516.

Whillans, I. M., & Grootes, P. M. (1985). Isotopic diffusion in cold snow and firn. *Journal of Geophysical Research: Atmospheres (1984–2012)*, *90*(D2), 3910-3918.

Chapter 5

Reconstruction of High and Low Frequency Oscillations in the WAIS Divide Ice Core over the last 68,000 years

Abstract

Ultra-high resolution water isotope measurements from the WAIS Divide Ice Core (WDC) have been analyzed using a continuous flow system (CFA) to 68 ka bp. Frequency analysis of the CFA water isotope signal (δD) shows 1-year spectral power persists throughout the Holocene and part way into the glacial period. Earlier annual signals have been lost by diffusion in the firn and ice. However, a 2-year spectral signal persists throughout the ice core showing that oscillations with periods of 2 years or greater are preserved in the ice. We use the exceptional preservation of the water isotope signal to analyze the amplitude of high and low frequency signals. We find distinct differences in high-frequency oscillations between the Holocene and Glacial period, as well as a decoupled trend between 1-year oscillations and short-term oscillations (4-15 years) throughout the Holocene. While the 1-year signal primarily represents local near-surface atmospheric temperature dependent on the seasonal cycle and weather events

(white noise), short-term oscillations are more heavily dependent on regional atmospheric circulation patterns including the Southern Annular Mode, the El Niño Southern Oscillation, and other undefined internal noise. An additional complexity is introduced due to diffusion of the water isotope signal occurring mainly in the firn, which produces red noise. We correct for diffusion over a sliding window to estimate original power spectra of the water isotope data. The corrected high-frequency oscillations have a partial dependence on teleconnection signals as far away as the tropics. At low-frequencies, we find a combination of ~2.4, 2.2, and 2.0 oscillations that persists for the entire 68 kyr water isotope record. These oscillations also prominently appear in radiocarbon tree ring records of solar variability. We investigate solar trigger mechanisms of abrupt climate change, but can find no recurring connection.

5.1. Introduction

The Earth is capable of both long-term and short-term changes. Long-term changes arise from subtle variations in Earth's orbit and orientation relative to the sun (Milankovitch, 1941). In terms of a typical human lifespan (i.e. less than 100 years), these long-term changes have little consequence, except to set the background climate. Conversely, short-term changes occur at timescales much less than 100 years and matter greatly to humans. The strongest short-term changes on Earth are annual shifts in weather and temperature, related to the transition between summer and winter. At timescales greater than 1 year, the strongest short-term changes (omitting abrupt climate change) are evident in climate oscillations such as the El Niño-Southern Oscillation (ENSO), the

Pacific Decadal Oscillation (PDO), the North Atlantic Oscillation (NAO), and the Southern Annular Mode (SAM). These oscillations change on decadal and sub-decadal time scales.

The most dominant and far-reaching climate oscillation (>1 year) is ENSO, which consists of three phases. El Niño (the warm phase) is a large-scale ocean-atmosphere climate phenomenon linked to periodic warming in sea surface temperatures across the central and east central equatorial Pacific Ocean. El Niño events cause trade winds that normally blow from east to west over the Pacific Ocean to diminish, warm surface water migration from the western Pacific into the eastern Pacific, increased rainfall in northwest South America and much of the southern United States, and drought conditions in Indonesia and Australia. La Niña (the cold phase) is linked to a periodic cooling in sea surface temperatures across the central and east central equatorial Pacific Ocean. La Niña events are characterized by unusually strong easterly trade winds over the equatorial Pacific Ocean, strong upwelling of cold bottom waters off the west coast of South America, decreased rainfall in the eastern Pacific, and heavy rainfall in India, Southeast Asia, Australia, and southeastern Africa.

ENSO has global socioeconomic implications. For centuries, fishermen in Peru have documented changes in ocean circulation and sea surface temperature that directly impact fish landings (Lagos and Buzier, 1992). In North America, ENSO influences the seasonal frequency and intensity of storm tracks (Eichler and Higgins, 2006), which can influence winter snowpack and water availability. Similar climate anomalies are also seen in Europe (Fraedrich and Müller, 1992). In Australia, severe drought is directly related to ENSO (Chiew et al., 1998). And even as far away as the African Sahel (a band of semi-

arid land south of the Sahara), rainfall patterns have been directly linked to ENSO (Ward, 1998), which can influence tropical disease outbreaks and food supply. Figure 5.1 shows an example of global ENSO climate effects during December to February, a time period when ENSO events begin to form in the tropical Pacific Ocean.

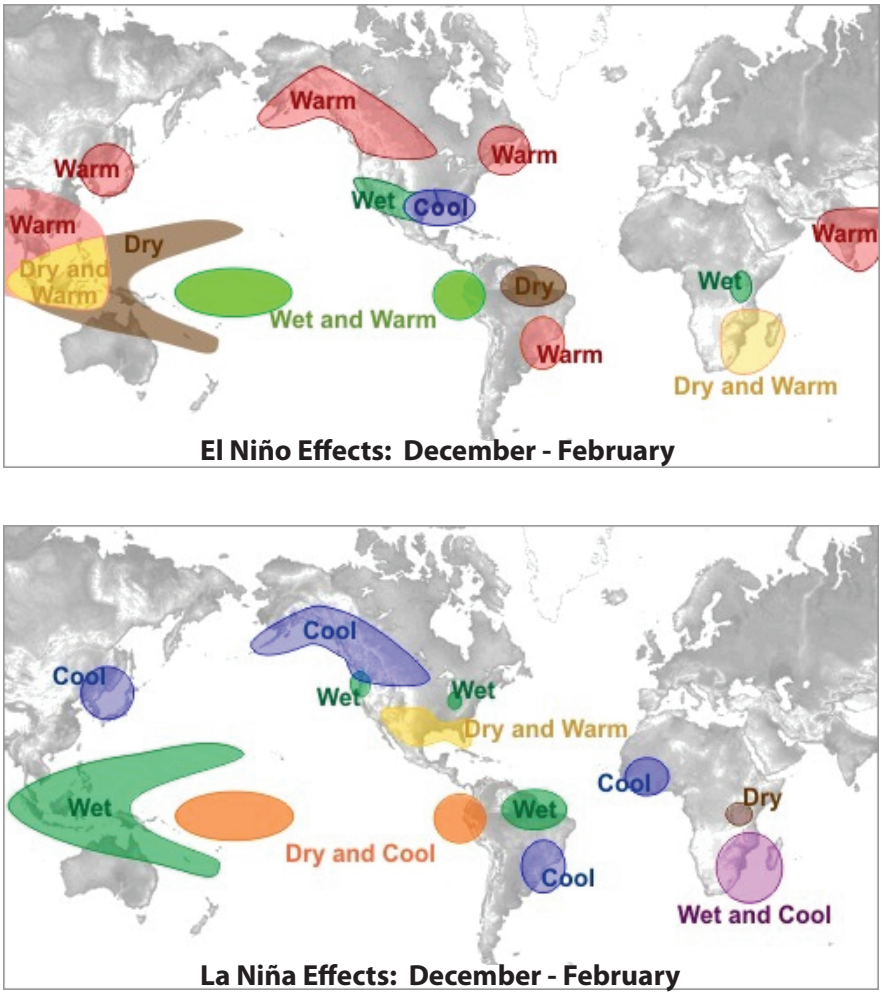

Figure 5.1. *A map illustrating the effects of El Niño and La Niña from December to February. The impacts are global, with some regions experiencing temperature anomalies, and other regions experiencing precipitation anomalies, or both. The effects of Antarctic ENSO teleconnections are not shown. (image source: noaa.gov)*

5.1.1. Paleo-ENSO

ENSO can be studied in a paleo-context using biological, physical, and chemical measurement proxies. The most common proxy types include tropical corals, lake sediments, ocean sediments, varying marine creatures like mollusks, and ice cores. Each of these proxies has benefits and drawbacks, depending whether the record is continuous, whether the measurements are located in an ENSO center-of-action, or whether the measurement is high-resolution. Based on these criteria, tropical coral proxies are arguably the most useful paleo-ENSO tools because they are located within the ENSO center-of-action and preserve an annual signal at high-resolution. The largest drawback, however, is that coral records are non-continuous and only consist of discrete time sections that must be used to infer longer climate patterns. In the following paragraphs, we use a number of ENSO proxy records, with a focus on tropical corals, to summarize paleo-ENSO variability and strength.

In a study by Tudhope et al. (2001), annually banded corals from Papua New Guinea were analyzed for oxygen isotope ratios (a proxy for temperature). Discrete coral sections used in the study were dated to ~2.5, 2.7, 6.5, 38.3, 39.4, 38 to 40, 41.9, 85, 111.9, 118 to 128, and 130 ka bp. The data show that ENSO oscillations have existed in the western tropical Pacific for the last 130 ka. Coral segments from the last interglacial (Eemian period, 115-130 ka bp) show a possible weaker ENSO than today. At ~6.5 and ~112 ka bp, ENSO variance and amplitude were lowest. The highest amplitude events occurred from ~2 to 3 ka bp. At all other time periods, ENSO amplitude was at an intermediate level, including the entire glacial period (11.7-110 ka bp). The authors suggest that a combination of ENSO dampening during glacial conditions and ENSO

modulation by precessional variations[26] is driving the signal.

The most widely studied ENSO time period is the Holocene (0-11.7 ka bp). Similar to the Tudhope et al. (2001) study, a recurring finding is that ENSO was weaker in the early-to-mid Holocene, summarized as follows: 1) Inorganic laminae from lake sediments in Ecuador (proxy for precipitation and debris flow related to ENSO) show 15 year or greater oscillations from 7 to 15 ka bp, and smaller oscillations of 2-8.5 years from 0 to 7 ka bp (Rodbell et al., 1999); 2) Mollusks from archaeological sites on the north and central coasts of Peru (proxy for sea surface temperature in ENSO regions) show that ENSO was less frequent from ~5.8 to 3.2-2.8 ka bp compared to today (Sandweiss et al., 2001); 3) Pollen data from tropical northern Australia (proxy for precipitation related to ENSO) shows a maximum from ~5.0 to 4.0 ka bp, followed by a decline between ~4.0 to 3.5 ka bp (Shulmeister and Lees, 1995); 4) The oxygen isotopic composition of foraminifera from deep-sea sediments (proxy for deep ocean temperature in ENSO regions) show mid-Holocene reductions in ENSO variance of 50%, implying reduction in ENSO sea surface temperature amplitudes (Koutavas et al., 2006); and 5) Grain size and carbon/nitrogen (C/N) ratios in sediment cores from El Junco Crater Lake in the Galápagos Islands (proxy for lake level and precipitation related to ENSO) show decreased precipitation intensity from ~4.2 to 9.0 ka bp, implying reduced ENSO duration and frequency (Conroy et al, 2008).

Varying Global Circulation Models have also been used for paleo-ENSO research. Simulations for the last glacial-interglacial cycle using the NCAR Climate

[26] Precessional variations refer to a change in the orientation of Earth's tilted axis relative to Earth's orbit around the sun, which oscillates at timescales from 19 – 23 ka. Precession would, for example, cause the location of the equinoxes (when the length of night and day are roughly equal) to slowly shift positions within Earth's orbit, thus slowly shifting to different days of the year.

System Model (CSM; a global, coupled ocean-atmosphere-sea ice model) show greater Niño3[27] variability with reduced precipitation in the western Pacific during the last glacial maximum (LGM) and weaker ENSO variability in the mid-Holocene due to decreased insolation (Otto-Bliesner et al., 2003). Weaker ENSO in the mid-Holocene is commonly explained by two model-based mechanisms: 1) Feedbacks from the enhancement of the South Asian monsoon due to higher sub-Arctic summer insolation, which strengthen the Pacific trade winds, increase upwelling in the equatorial Pacific, decrease equatorial Pacific ocean temperatures, and ultimately dampen El Niño events (originally discussed by Kutzbach and Otto-Bleisner, 1982). 2) Feedbacks from higher Southern Hemisphere winter insolation warms South Pacific surface waters, which are subducted northward towards the equator, where the newly introduced warm subsurface waters deepen the thermocline[28] and decrease the zonal (west-to-east) thermocline gradient, which may reduce upwelling water and associated affects on sea surface temperature, therefore suppressing ENSO events (originally discussed by Zebiak and Cane, 1987). Liu et al. (2000) reproduced both of the aforementioned mechanisms using the Fast Ocean-Atmosphere Model (FOAM), a similar but lower resolution model as the CSM. Zheng et al. (2008) found similar results related to the Asian summer monsoon using the Paleoclimate Modeling Intercomparison Project (PMIP2) model.

A study of coral isotope records from the central Pacific has challenged the idea of weak ENSO in the mid-Holocene (Cobb et al., 2013). The study uses oxygen ratios in non-continuous coral sections from Palmyra Island, Fanning Island, and Christmas Island (collectively part of the Line Islands) over the last 7 ka. Cobb et al. (2013) found highly

[27] The Niño3 region refers to average sea surface temperatures from 5°S-5°N and 150°W-90°W.
[28] The thermocline is a layer of water where temperature changes more rapidly with depth than it does in the layers above or below.

variable ENSO activity throughout the mid-to-late Holocene, but with no systematic trend in ENSO variance, even in the 20th century. The Cobb study contradicts the notion that insolation induced a dampened ENSO system in the mid-Holocene. The authors suggest that some paleo-ENSO proxies that show weak mid-Holocene ENSO may be detecting a precipitation signal that is not directly coupled to sea surface temperature changes.

An additional finding from coral isotope studies is that ENSO has been highly variable over the last millennium. Cobb et al. (2003) used oxygen ratios in non-continuous coral sections from Palmyra Island over the last 1.1 ka to assess ENSO variance. They found that ENSO was highly variable and the amplitude and frequency of the coral isotope signal changes significantly in as little as a decade. Urban et al. (2000) also documented significant ENSO variability in a 155-year continuous bi-monthly coral isotope record from Maiana Atoll in the central tropical Pacific. The authors describe the variability as follows:

> A gradual transition in the early twentieth century and [an] abrupt change in 1976, both towards warmer and wetter conditions, co-occur with changes in variability. In the mid–late nineteenth century, cooler and drier background conditions coincided with prominent decadal variability; in the early twentieth century, shorter-period (approx. 2.9 years) variability intensified. After 1920, variability weakens and becomes focused at interannual timescales; with the shift in 1976, variability with a period of about 4 years becomes prominent.

The majority of paleo-ENSO research portrays a highly variable system, summarized as follows: 1) ENSO has operated in the Earth climate system since the last interglacial period 130 ka bp; 2) Coral isotopes in the western tropical Pacific suggest dampened ENSO in the glacial, whereas the CSM GCM shows greater ENSO variability

with reduced precipitation in the glacial; 3) Many studies, such as coral, lake sediment, ocean sediment, and archaeological proxies, as well as model results, show a weak ENSO in the mid-Holocene relative to today; 4) A tropical Pacific coral record conflicts with these findings, showing ENSO has been highly variable with no systematic trend since 7 ka bp; 5) The amplitude and frequency of ENSO can change abruptly, sometimes in as little as a decade; 6) In the last 155 years, ENSO has operated at both sub-decadal and decadal time periods, rather than the classical interpretation of ENSO as a 2-7 year oscillator; and 7) Proxy and modeling discrepancies are common and require more research.

5.1.2. ENSO in Antarctica

Tropical ENSO signals can be transmitted to higher latitudes through atmospheric teleconnection[29] mechanisms. In a pioneering theoretical study, Hoskins and Karoly (1981) used a linear steady-state five-layer baroclinic[30] model to study the response of a spherical atmosphere to thermal (and other) forcing. The study showed that areas of deep convection[31] near the equator can generate Rossby wave trains, which are large-scale waves (like the jet stream) that occur in the ocean-atmosphere system. Rossby waves are capable of transmitting climate signals over long distances. For example, in the Southern Hemisphere, atmospheric Rossby waves can form in the Pacific Ocean between repeating high and low pressure anomalies. Air masses tend to flow between the pressure anomaly

[29] Teleconnection mechanisms refer to climate anomalies that are transmitted over large distances - typically thousands of kilometers – such that the climate signals at one location (i.e. the tropics) are correlated with those in a distant location (i.e. Antarctica).
[30] The density in a baroclinic atmosphere depends on both temperature and pressure, where distinct air masses exist, with low pressure, high pressure, and frontal boundaries, among other properties.
[31] Deep convection generally refers to the vertical movement of air masses above a certain geopotential height (i.e. the height above mean sea level needed to reach a certain pressure, usually 500 hPa).

boundaries, connecting tropical climate with higher latitudes via a convoluted "sine function" type wave train. Figure 5.2 shows pressure anomalies during the initial stages of an ENSO event.

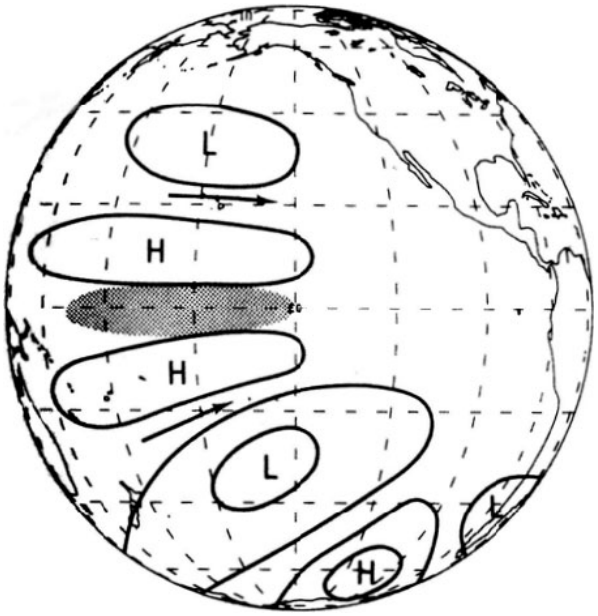

Figure 5.2. *A schematic diagram of repeating high and low pressure anomalies occurring across the Pacific Ocean during the initial stages of an ENSO event (Turner, 2004). In the south Pacific Ocean, the pressure pattern arcs to the southeast, interacting directly with the Pacific Sector of West Antarctica. Rossby waves form between the high and low-pressure boundaries, creating teleconnection mechanisms for tropical climate variability in high-latitudes.*

Many studies have shown that the teleconnection of tropical ENSO signals to high-southern latitude regions is not straightforward. Some of these mechanisms are listed here: 1) Deep tropical convection usually occurs when sea surface temperatures reach 26°C to 29.5-30°C (Zhang, 1993), but even within this temperature range, the formation of Rossby wave trains does not always occur (Graham and Barnett, 1987); 2) At mid-latitudes, Rossby waves form complex interactions with westerlies (i.e. winds

occurring at ~35°-65° south). Karoly (1989) found that westerlies weakened during some, but not all, ENSO warm events, while Harangozo (2000) showed that westerlies are regulated by Rossby waves, but not consistently between ENSO warm events; 3) In a study of teleconnections between low, mid, and high-latitudes, Bals-Elsholz et al. (2001) found a weak correlation between the sub-tropical jet (~30° south) and split polar jet (~60° south) with the Southern Oscillation Index[32] (SOI), and no correlation between the polar front jet (~60° south) and SOI; and 4) Cullather et al. (1996) showed that from 1980 to 1990, the moisture flux into Antarctica was stronger and in phase with the SOI during ENSO cold events, but anti-correlated from 1992 to 1994 (roughly 40% of the moisture flux into Antarctica occurred along the West Antarctic coast). In summary, teleconnection research shows that an ENSO signal can propagate to higher latitudes, but with varying responses that result in an inconsistent teleconnection mechanism. Rather than a direct link to the tropics, weather systems in the high-southern latitudes should be thought of as an integrator of the processes occurring in the tropics, sub-tropics, and polar regions.

5.1.3. ENSO in Ice Cores

Previous studies have shown that teleconnected ENSO climate signals are pervasive, yet non-stationary, across the Antarctic continent (reviewed by Turner, 2004). In one study, an atmospheric general circulation model fitted with water tracer capabilities showed that present day Antarctic precipitation originates primarily in the

[32] The Southern Oscillation Index (SOI) is a standardized index of the observed sea level pressure differences between Tahiti, French Polynesia and Darwin, Australia. The SOI is a direct proxy for ENSO.

sub-tropics and mid-latitudes (Delaygue et al., 2000). Delaygue also showed that a given region of Antarctica derives the majority of its moisture from the nearest ocean basin, especially in coastal locations. In another study, Guo et al. (2004) used meteorological analyses and reanalyses to show that the correlation between decadal oscillations in West Antarctic precipitation and SOI is stronger in the 1990s than the 1980s. Later, Schneider and Steig (2004) analyzed Antarctic climate variability using monthly surface temperatures (specifically, satellite thermal infrared observations and passive microwave brightness temperatures) from 1982 to 1999. They found that Antarctic temperature anomalies are mainly controlled by atmospheric circulation. A principal component analysis of the temperature field compared with 500 hPa geopotential height anomalies revealed the following: 1) The leading principle component of temperature strongly correlates with the Southern Annular Mode[33] (SAM), 2) The second principle component of temperature reflects the influences of both the zonal wavenumber-3 and Pacific–South American[34] (PSA) patterns, and 3) The third principle component of temperature explains winter warming trends. ENSO variability appears in the second principle component at interannual time scales, but is a weak predictor of Antarctic temperatures.

Additional studies show that a positive correlation exists between ENSO and SAM during times of strong teleconnection (Fogt and Bromwich, 2006), such that the SAM index expresses both high-latitude and tropical climate variability (Ding et al.,

[33] The Southern Annular Mode (SAM) is a standardized index of the leading principal component of 850 hPa geopotential height anomalies poleward of 20°S (Thompson and Wallace, 2000), providing a short record of opposing pressure anomalies centered in the Antarctic near 40-50°S.

[34] The Pacific–South American pattern (PSA) refers to two pervasive modes of atmospheric variability in the Southern Hemisphere, appearing at multi-seasonal to decadal timescales as the primary empirical orthogonal functions of 500 hPa height anomalies (PSA1) or the 200 hPa stream function (i.e. related to the streamlines of a fluid flow; PSA2; Mo and Higgins, 1998 and Mo and Paegle, 2001). The PSA exhibits wavenumber 3 patterns in the mid-to-high latitudes, where wavenumber is the number of complete waves that are found around a latitude circle.

2012). Hosking et al. (2013) showed that ~25% of variance expressed in the SAM index is related to ENSO variations. In turn, the SAM influences the depth of the Amundsen Sea Low Pressure Area[35] (ASL), and both the location and depth of the ASL affects the climatology of the Ross Sea region and the interior of West Antarctica by influencing storm tracks (Turner et al., 2013). The exact location, phasing, and climate forcing of the ASL in relation to ENSO has been the topic of numerous studies. Turner et al. (2013) showed that the ASL is significantly deeper during La Niña as compared to El Niño, but the zonal (west-east) location of the ASL is not statistically different during either ENSO phase. Bertler et al. (2006) showed that the ASL causes near-surface temperature anomalies in the eastern Ross Sea, resulting in a net cooling during El Niño events and a net warming during La Niña events. Fogt and Bromwich (2006) found that positive SAM index years are more likely during strong La Niña years, while Bromwich et al. (1993) found a connection between katabatic surges over inland West Antarctica and across the Ross Ice Shelf during El Niño events.

To study the teleconnection mechanisms listed above (and other physical processes), an in-depth project documenting of the relation between ice cores and West Antarctic climate was undertaken as part of the International Trans-Antarctic Scientific Expedition (ITASE, Steig et al., 2005). Twenty-three shallow ice cores (with depths ranging from ~50-300 meters) were obtained between the boundaries of the Antarctic Peninsula, South Pole, Ross Sea ice drainage, and Amundsen Sea ice drainage. The absolute dating error for each ice core was less than or equal to 2 years, while relative dating accuracy is less than one year. In a study of six ITASE ice cores for high-

[35] The Amundsen Sea Low Pressure Area (ASL) is a low-pressure system located in the Pacific sector of the Southern Ocean between 170°-290° E and 75°-60°.

resolution surface mass balance (Genthon et al., 2005), SOI and the Antarctic Oscillation Index (AOI; an index nearly identical to the SAM) patterns are evident, accounting for 16% and 25% of the total variability in the western most ice core, respectively, with variability decreasing to 0% in the eastern most ice core. In a study of thirteen ITASE ice cores for accumulation (Kaspari et al., 2004), precipitation at inland, high-latitude ice core sites corresponds best with mid-latitudes processes, similar to other studies showing a dominant sub-tropical moisture source origin (Petit et al., 1991; Ciais et al., 1995; and Reijmer et al., 2002). In a study of three ITASE ice cores for stable water isotopes (Schneider et al., 2005), the signal was highly correlated with local site temperature, which had a partial dependence on the SAM.

5.1.4. High-Frequency Paleoclimate Interpretations in West Antarctica

ENSO has been a prominent part of the Earth climate system for at least the last 130 ka. The behavior of ENSO has been non-stationary, sometimes changing abruptly, and often alternating between different oscillatory modes at decadal and sub-decadal time scales. Tropical coral isotope records have offered a glimpse of this behavior, and indeed are the best source of information for ENSO reconstruction, but the records are non-continuous and missing over many important time periods. The use of ice core records from the south Pacific sector of West Antarctica can fill these voids, albeit showing an integrated climate signal spanning from the tropics to poles. Based on the totality of current research, inland ice core records from West Antarctica appear to be strongly influenced by local temperature, with an atmospheric circulation component that includes

the influences of the ENSO, SAM, ASL, and PSA, among other smaller climate oscillations and natural noise inherent to the climate system.

5.1.5. Low Frequency Climate Change

During the last glacial period, twenty-five abrupt warming events in Greenland re-occurred at roughly 1,500 – 4,000 year spacing. These abrupt climate changes are known as Dansgaard-Oeschger events (D-O events), named after the ice core scientists Willi Dansgaard and Hans Oeschger who studied them. Although the exact trigger mechanism of D-O events is still unexplained, the possible origins are either solar activity (Bond et al., 2001; Clement et al., 2001; Rahmstorf, 2003; Braun et al., 2005; Rial and Saha, 2009) or mechanisms internal to the Earth system (van Kreveld et al., 2000; Clark et al., 2001). Broecker (2003) and Clement et al. (2001) summarize North Atlantic and tropical abrupt climate change triggers (either solar or Earthly in origin), respectively. One theory suggests freshwater input to the North Atlantic triggers changes in the mode of the thermohaline overturning circulation (TOC), which alters northern/southern hemisphere heat budgets (termed the bipolar see saw by Broecker, 1998) and eventually causes global climate change. The other theory suggests that shifts in the tropical ocean-atmosphere system, such as in the regions where ENSO occurs, trigger widespread climate change. For either theory, a semi-cyclical causation mechanism must explain D-O and H events, such that immediate atmospheric impacts propagate globally.

Certain high-resolution ice core records from Antarctica have revealed small warmings known as Antarctic Isotope Maxima (AIM) related to D-O events. For

example, the EPICA Dronning Maud Land (EDML) ice core (Atlantic sector of East Antarctica) has shown a direct relationship between AIM and D-O events (EPICA Community Members, 2006). The EPICA Dome C (EDC) ice core (Indo-Pacific sector of East Antarctica) has shown similar results as EDML. In both EPICA ice cores, Antarctica begins to cool when Greenland abruptly warms, and AIM events appear more symmetrical and dampened than D-O events seen in Greenland. In a study of the WAIS Divide ice core (WDC), the phasing of D-O and AIM events has recently been resolved. Buizert et al. (2015) showed that abrupt Greenland warming events lead Antarctic cooling onsets by 221 ± 92 years, while Greenland cooling (interstadial terminations) leads Antarctic warming onsets by 196 ± 95 years. The multi-century long delay shows that the ocean is the central mechanism of signal propagation via the bipolar see saw.

Steffensen et al. (2008) suggests a possible sequence of events that can cause abrupt warmings in Greenland and associated changes in Antarctica. The authors analyzed a Greenland ice core for high-resolution water isotopes (δD , $\delta^{18}O$, and deuterium excess), annual layer thickness, insoluble dust, soluble sodium (Na^{+}), and soluble calcium (Ca^{2+}) for the last two abrupt warmings occurring in the glacial period. Based on these proxies, the proposed sequence of global events is linked to the tropics and the location of the Intertropical Convergence Zone (ITCZ), explained by the authors:

> During Greenland cold phases, the thermohaline circulation (THC) was reduced, northern sea ice extended far south, and the Intertropical Convergence Zone (ITCZ) was shifted southward, resulting in dry conditions at the low-latitude dust-source regions. Meanwhile, southern high latitudes and tropical oceans accumulated heat and underwent gradual warming as reflected in the bipolar seesaw pattern because of a reduction in the North Atlantic overturning circulation. We suggest that this Southern Hemisphere/tropical warming induced first a northward shift of the ITCZ and, when a threshold was reached, an abrupt intensification of the Pacific monsoon. The wetter conditions at the Asian dust-

> source areas then caused decreased uplift and increased washout of atmospheric dust, leading to the first sign of change in Greenland: decreasing dust and Ca2+concentrations. This reorganization of the tropical atmospheric circulation was followed by a complete reorganization of the mid- to high-latitude atmospheric circulation almost from one year to the next.

One of the main suggestions of Steffensen et al. (2008) was that the tropical-ocean atmosphere system caused the North Atlantic atmosphere system to change within 1 to 3 years, which forced abrupt warmings. Whether this is the case or not, it provides a framework for thinking about abrupt climate change, and certain hypotheses to test against. Yet, a major drawback to determining the cause of abrupt climate change is that the absolute timing of climate change in different proxies may be unattainable (e.g. Broecker, 2003) or that climate change is expressed differently in different locations (e.g. Hemming, 2004). The clues to search for are timing, abruptness, persistence, and perhaps a cyclical underlying cause that interacts non-linearly in the climate system.

5.2. Methods

In this study, we present a ~68 ka water isotope record from the West Antarctic Ice Sheet Divide ice core (WDC), which has annual dating to ~29 ka bp. Using diffusion lengths that characterize the total decay of high-frequency oscillations (see Chapter 4), we reconstruct decadal and sub-decadal periodicities at 2-15 year timescales over the last 29 ka bp. This reconstruction shows the expression of ENSO-scale oscillations in Antarctica, which are related to Pacific Ocean and Southern Ocean climate dynamics. We also analyze low frequency oscillations, finding prominent, non-stationary oscillation patterns between 15 to 125 years as well as quais-stationary millennial signals. The

millennial signal may result from solar forcing and provide clues to the initiation of Dansgaard-Oeschger events. Overall, the results of this study can be used to understand climate change at human time scales, calibrate global circulation models, and challenge our understanding of the Earth climate system through the most recent glacial-interglacial cycle.

In Chapters 3 and 4, methodologies for the measurement of the WDC water isotope signal and diffusion lengths were outlined, as well as brief explanations of the ice core drilling location and the water isotope record to ~29 ka bp. Some of this information is repeated or summarized below as a precursor to additional methods presented in this chapter.

5.2.1. Site Location

The West Antarctic Ice Sheet Divide (WAIS Divide) deep ice core (WDC) was drilled over six field seasons from 2006 – 2012. The WDC drill site is located at 79°28.058' S by 112°05.189' W in the Pacific sector of West Antarctica, ~24 km from the current ice flow divide. The surface elevation is 1,766 m above sea level and the ice sheet thickness is 3,465 m. The current average annual surface temperature is -31°C and the current ice accumulation rate is 22 cm/yr. Figure 5.3 shows a map of West Antarctica and the WDC drilling location.

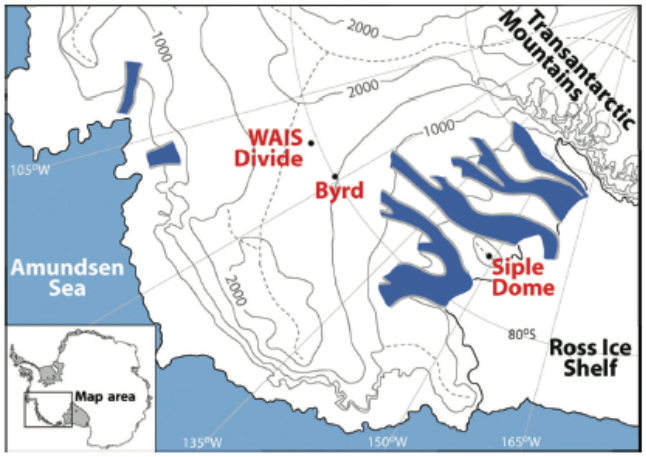

Figure 5.3. *A map of the West Antarctic region showing the drilling location of WDC (WAIS Divide ice core). The black contours show elevation above sea level (m). Figure from Souney et al. (2014) and originally modified from Morse et al. (2002).*

5.2.2. Methods of Measurement

The WDC water isotope record was analyzed on a cavity ring-down laser spectroscopy (CRDS) continuous flow analysis (CFA) system at the Institute of Arctic and Alpine Research, University of Colorado (see Chapter 3). As of 2015, this is the highest resolution water isotope record containing last glacial ice from West Antarctica. The data consists of measurements of hydrogen and oxygen isotopes in water molecules, where the ratio of heavy to light water isotopes in a water sample is commonly expressed in delta notation (Epstein, 1953; Mook, 2000) relative to Vienna Standard Mean Ocean Water (VSMOW):

$$\delta_{sample} = 1000\left[\left(\frac{R_{sample}}{R_{VSMOW}}\right) - 1\right] \quad (1)$$

where R is the isotopic ratio $^{18}O/^{16}O$ or H^2/H^1 (i.e. D/H where D is H^2, termed deuterium) in the sample or VSMOW. The δD and $\delta^{18}O$ symbols refer to parts per thousand deviations from equilibrium conditions set by VSMOW (defined as 0.00 per mil). Both δD and δ18O are used as proxies for local temperature and regional atmospheric circulation, dependent on the temperature gradient from moisture source to deposition site (Dansgaard, 1964). The main physical control on this relationship is the temperature of the cloud at the time of condensation (Jouzel and Merlivat, 1984; Jouzel et al., 1997; Johnsen et al., 2001). The WDC water isotope record is shown in Figure 5.4.

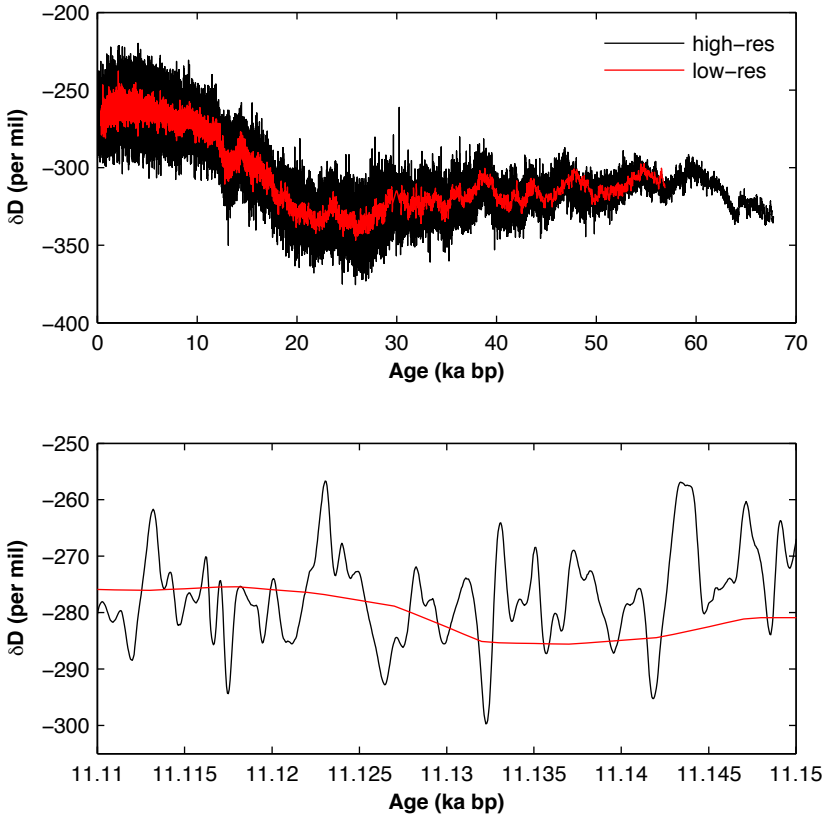

Figure 5.4. *Plots of the WDC water isotope record. The red lines are previously published low-resolution water isotope data from Steig et al. (2013) and WAIS Divide Project Members (2013). The black lines are the high-resolution record used in this study.*

The dating of the WDC water isotope record from 0-31 ka bp is based on a depth-age scale developed by the WAIS Divide Project Members (2013) and Sigl et al. (in prep, 2015). The project members state:

> The WDC06A-7 timescale is based on high-resolution (<1 cm) measurements of sulphur, sodium, black carbon and electrical conductivity (ECM) above 577 m (2,358 yr before present (BP; AD 1950). Below 577 m, WDC06A-7 is based primarily on electrical measurements: di-electrical profiling was used for the brittle ice from 577 to 1,300 m (to 6,063 yr BP). Alternating-current ECM measurements were used from 1,300 to 1,955 m (to 11,589 yr BP) and both alternating-current and direct-current ECM measurements were used below 1,955 m. The interpretation was stopped at 2,800 m because the expression of annual layers becomes less consistent, suggesting that all years may not be easily recognized.

From 31-68 ka bp, the dating is based on methane synchronization to Northern Hemisphere records of abrupt climate change (Buizert et al., 2015).

5.2.3. Back-Diffusion

Water isotope records in ice cores are subject to diffusional processes that attenuate high-frequency oscillations. The majority of diffusional processes occur in the firn column, although solid ice diffusion is increasingly important over long time periods. The amount of diffusion can be characterized by fitting a Gaussian to the water isotope data in the frequency domain over a certain window of time (e.g. a 500-year window is sufficient for determining diffusion lengths for the WDC). In Chapter 4, WDC water isotope data were fitted with a Gaussian in the form:

$$\hat{G}_z = K_z \cdot exp^{\frac{-f^2}{2\sigma_{stdz}^2}} \quad (2)$$

where the Fourier transform is denoted by the hat symbol, f is the frequency, K_z is the power density value of the white noise signal, and σ_{stdz} is the standard deviation (which is analagous to the inverse of diffusion length σ_z multiplied by a constant). The diffusion length term (σ_z) is the average vertical displacement of a water molecule from its original position in the ice (disregarding the sinking of annual layers). The σ_z variable can be used to deconvolve and back diffuse the water isotope data.

Taking a synthetic isotopic record and convolving it with a Gaussian can model the effect of diffusion. Convolution of two functions f and g over a finite range [0,t] is given by:

$$[f * g](t) = \int_0^t f(\tau)\, g(t-\tau)\, d\tau \quad (3)$$

where the symbol $[f * g](t)$ denotes convolution of f and g. For an ice core, the diffusion Gaussian (i.e. $g(t-\tau)$) "slides" over the water isotope record (i.e. $f(\tau)$). The calculation of the convolution of one function with a Gaussian function can be determined by converting both into the frequency domain using Fourier transform and multiplying the resulting spectra together. To deconvolve the two functions would require a division of the spectra.

In the depth domain, a δ profile that has been altered by diffusion can be written:

$$\delta_d(z') = \int_{-\infty}^{\infty} \delta_o(z' - z) \cdot \frac{1}{\sigma\sqrt{2\pi}} exp^{\frac{-(z)^2}{2\sigma_z^2}} dz \quad (4)$$

where z is depth (m), z' is the depth offset due to sinking annual layers in the ice sheet (m), δ_d is the diffused water isotope signal (per mil), δ_o is the original signal (per mil), and σ_z is the diffusion length (m). In the frequency domain, equation 4 can be written as:

$$\widehat{\delta_d} = \widehat{\delta_o * G} \quad (5)$$

where the Fourier transform is denoted by the hat symbol, the star ($*$) symbol means convolution, and G is equal to:

$$G = \frac{1}{\sigma_z\sqrt{2\pi}} \cdot exp^{\frac{-(z)^2}{2\sigma_z^2}} \quad (6)$$

The original delta signal can then be determined by:

$$\widehat{\delta_o} = \frac{\widehat{\delta_d}}{\widehat{G}} \quad (7)$$

The fourier transform (converting from the depth domain to the frequency domain) of δ and *G* is given by:

$$\widehat{\delta} = \int_{-\infty}^{\infty} \delta(z) \cdot e^{-ikz} dz \tag{8}$$

$$\widehat{G} = \int_{-\infty}^{\infty} \frac{1}{\sigma_z \sqrt{2\pi}} \cdot exp^{\frac{-(z)^2}{2\sigma_z^2}} \cdot e^{-ikz} dz = e^{\frac{-k^2\sigma_z^2}{2}} \tag{9}$$

where k is the wavenumber (cycles/m) and *i* is the imaginary unit in the complex number system. To restore δ_o requires a transformation away from the Fourier space:

$$\widehat{\delta_o} = e^{\frac{k^2\sigma_z^2}{2}} * \widehat{\delta_d} \tag{10}$$

$$\delta_o(z) = \frac{1}{2\pi} \int_{-k_w}^{k_w} e^{\frac{k^2\sigma_z^2}{2}} \cdot \widehat{\delta_d} \cdot dk \tag{11}$$

where k_w is the wavenumber cutoff. In ice core analysis, laboratory measurements introduce noise into the δ_d signal, such that k_w must be used to prevent the unnatural noise from affecting the δ_o deconvolution. At WDC, noise in the δ_d signal requires a k_w of ~0.52-1.50 cycles/year (Figure 5.5).

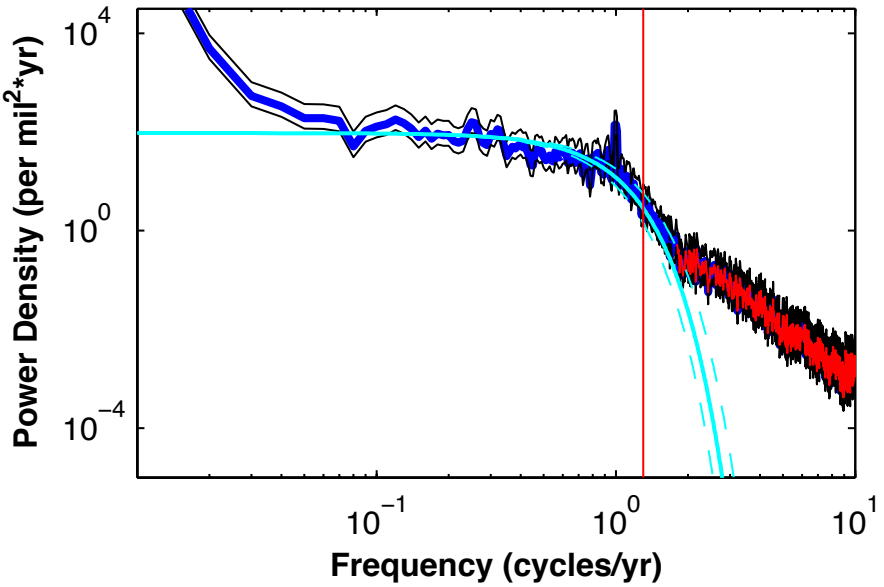

Figure 5.5. *A plot of WDC water isotope power density over a 500-year window from 3.0 to 3.5 ka bp. The dark blue line is the MTM spectrum, the black lines are the 95% confidence interval, and the light blue lines are the Gaussian fit using a diffusion length determined from a natural log fit of power density (described in Chapter 4). The red portion of the spectral estimate corresponds to the power density value where analytic noise overwhelms the climatic signal. The vertical red line corresponds to the wavenumber cutoff (k_w), which should be located well clear of the noise for deconvolution of the δ signal.*

We use a deconvolution program developed at the Centre for Ice and Climate, Neils Bohr Institute, University of Copenhagen, which was originally discussed by Johnsen (1977), to back diffuse the water isotope record for the last 10 ka. To accurately estimate δ_o requires pre-determined diffusion lengths. In Chapter 4, time-domain diffusion lengths were determined for 500-year windows of δD and $\delta^{18}O$ data by fitting a Gaussian to the water isotope data. Throughout the rest of this chapter, we opt to use the δD record for analysis of high-frequency oscillations (there is no difference in results for either δD or $\delta^{18}O$). The uncertainty of the δD diffusion lengths was used to determine a range of deconvolutions throughout the Holocene (Figure 5.6). The uncertainty is small

enough that using a best-fit diffusion length is suitable for the long-term trend analyses performed in this chapter.

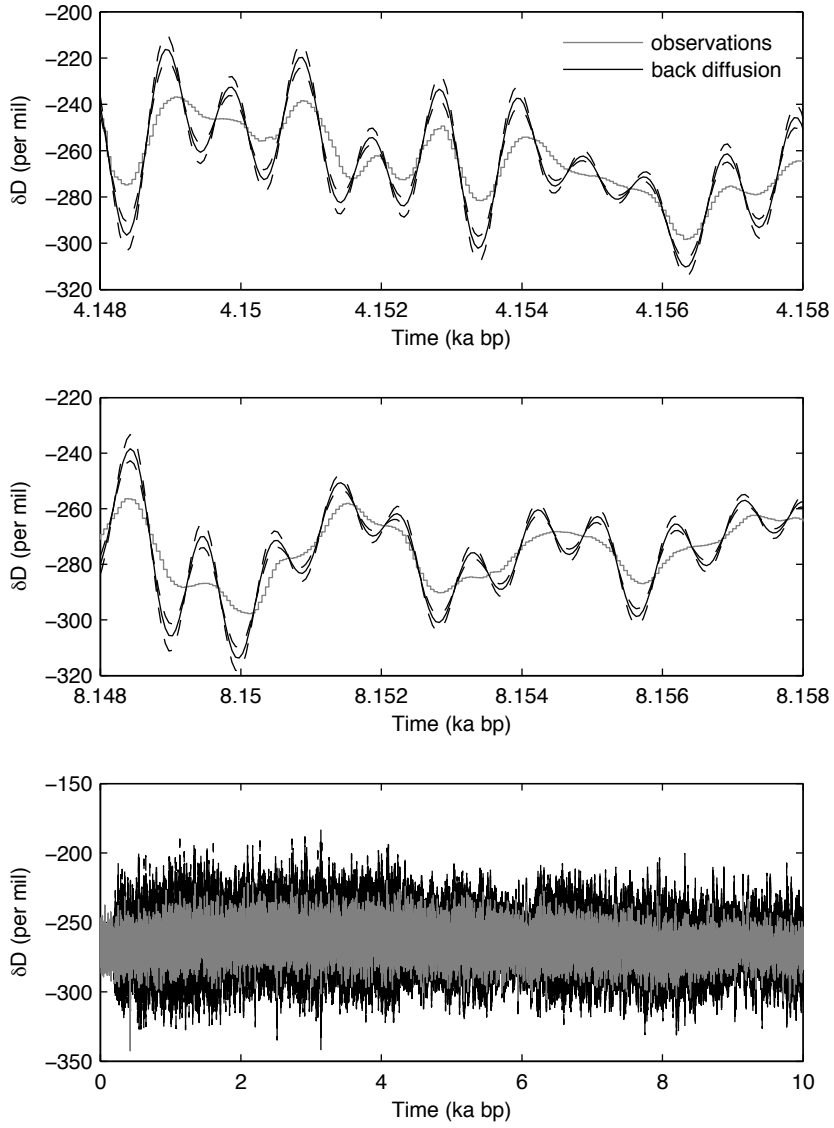

Figure 5.6. *Deconvolution of the water isotope signal for the last 10 thousand years. The light grey line is the original signal (observations), which has been attenuated due to diffusional processes. The dark line is the reconstructed signal (back-diffusion). The dashed black lines represent the uncertainty of the deconvolution due to uncertainty in the diffusion length estimates (described in Chapter 4).*

Back diffusion of the firn must be calculated separate of deeper ice. Usually, a spectral window of at least 100-200 years is necessary to calculate a diffusion length (500-year windows minimize uncertainty). In the firn, however, the diffusion length changes exponentially over short timescales, preventing an accurate analysis. Therefore, we use a firn diffusion model for δD (Johnsen et al., 2000; see Chapter 4 for additional information) to estimate a diffusion length for the most recent 250 years. Then, we use an iterative method of back diffusion for yearly sections of ice with the corresponding modeled diffusion length. Each yearly section is concatenated into a single back diffused firn record (Figure 5.7).

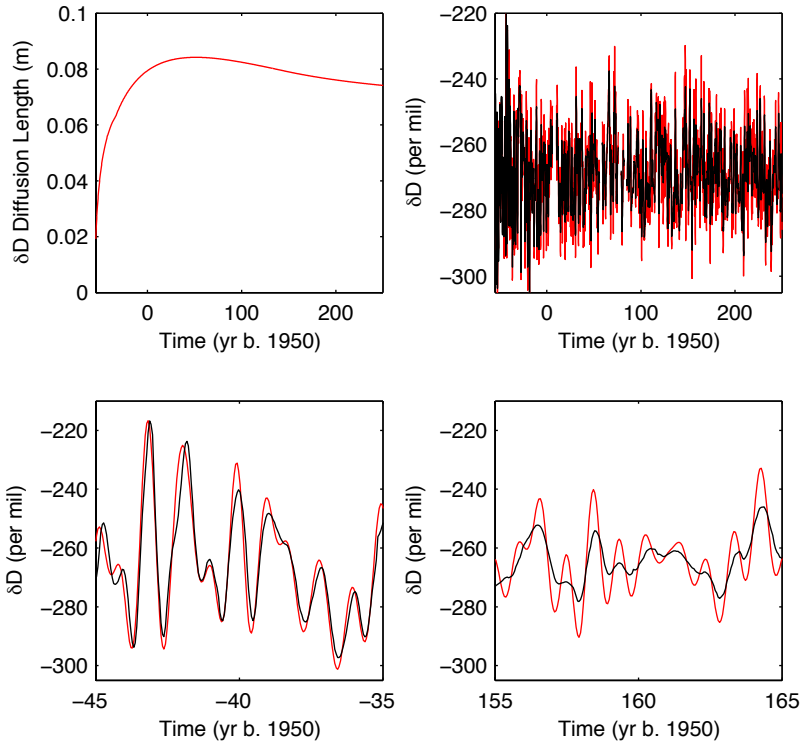

Figure 5.7. *Back-diffusion of water isotopes in the firn column. (Top Left) Modeled δD diffusion lengths (Johnsen et al., 2000) using current WDC parameters (temperature=-30.3°C, accumulation=0.23 m/yr, atmospheric pressure = 0.76 atm, ice thickness = 3,400 m). (Top Right) The back-diffused δ record. (Bottom Left and Bottom Right) Zooms of the back-diffused δ record. Notice that the δ values at 160 yr b.1950 require a larger correction than those closer to the surface at -40 yr b.1950.*

The deconvolution of the yearly signal in firn or deep ice corrects for the loss of annual signals due to diffusion. Using the back diffused record, we can isolate maximum summer and minimum winter isotope values for the last 10 ka. This is useful for analysis of long-term trends in summer, winter, and seasonal δ values. The maximum summer and minimum winter δ values are determined using a peak detection algorithm in Matlab, termed 'findpeaks'. Figure 5.8 shows the results of the peak detection algorithm.

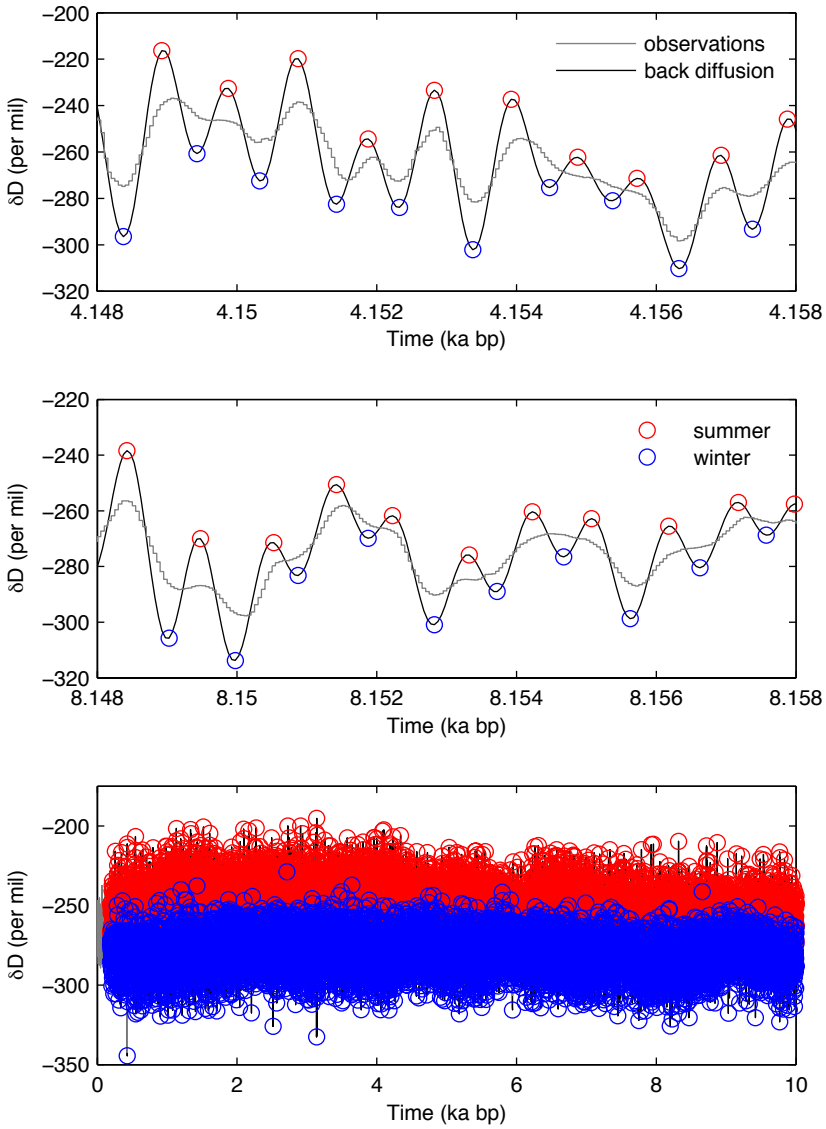

Figure 5.8. *Detection of maximum summer (red) and minimum winter (blue) δ values in the deconvoluted water isotope record.*

In addition to deconvolution of the yearly water isotope signal, we also back diffuse ENSO-scale frequencies (2-15 years) over the last 29 ka. But, instead of converting back to the time domain using reverse Fourier transform, we only back-

diffuse power density in the frequency domain. The back-diffused power density gives an estimate of the original strength of the frequency signal, defined by:

$$P_o(f) = \frac{P_d}{e^{-4\pi^2 f^2 \sigma_t^2}} \tag{11}$$

where P is the power density (per mil^2·yr), f is frequency (1/yr), and σ_t is the time-domain diffusion length (yr). Taking the integral of the power density, followed by the square root, yields amplitude density in units of per mil. Determining amplitude density is useful as the units relate directly to water isotope signal in the time domain (i.e. both have units of per mil). However, it is difficult to determine the exact amplitude of any signal in the frequency domain due to uncertainties in the Fourier transform. We generally avoid this uncertainty by using identical methodology for back diffusion over the last 29 ka. Effectively, we are comparing patterns in the relative amplitude density values, which will give the same results no matter what method is used, as long as the method is the same. As a result, most of the uncertainty in power density back diffusion arises from the determination of diffusion lengths.

Using the back-diffused power, we find relative power values (i.e. relative strength) over the last 29 ka for varying intervals related to ENSO-scale frequencies. Since the frequency values in a Fourier transform are not evenly spaced, we determine the average relative power for each interval by calculating the integral of the power density divided by the frequency range. Figure 5.9 shows back diffusion in the frequency domain for varying time periods.

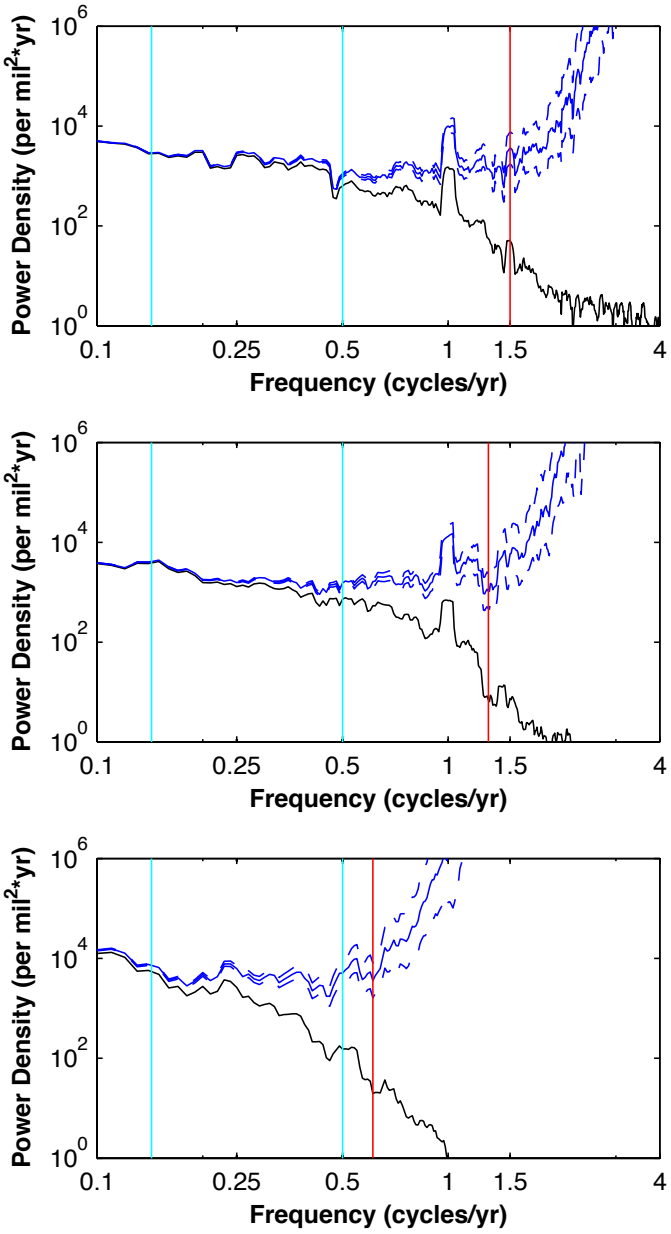

Figure 5.9. *Original (black) and back-diffused (blue) power density at 500-year windows for 5.0 to 5.5 ka bp (top), 11.0 to 11.5 ka bp (middle), and 20.0 to 20.5 ka bp (bottom). The dashed blue lines represent uncertainty from the determination of diffusion lengths. ENSO-scale power density (2-7 years) is bounded by the light blue vertical lines. The analytic noise boundary is shown by the red line. The back-diffused power density to the right of the red line will appear as blue noise and should be discarded. Otherwise, the back-diffusion should result in white noise (a flat spectrum) for ENSO scale power density, which can be used to estimate the original δ amplitude at a given frequency value.*

The significance of spectral peaks is determined by two methods. The first method is derived from Multi-Tape Method (MTM) spectral analysis for climate time series described by Mann and Lees (1996). This method is useful for climate studies because red noise[36] and narrowband[37] assumptions are used. The Mann and Lees method is available in the kSpectra toolkit. The second method utilizes wavelet analysis that changes one-dimensional time series into time-frequency space, creating a two-dimensional image of amplitude variability through time (Torrence and Compo, 1998). Additional discussion and results from the significance tests are shown later in this chapter.

5.3. Results and Discussion

5.3.1. Climate Oscillation Forcing at WDC

Ice core δ records should not be thought of as a singular climate proxy, but rather as a combination of climatic forcing originating from different locations at different times. Determining which components affect the δ record can be difficult. Shallow ice core records in West Antarctica, for example, show δ variability is strongly related to local temperature, with additional teleconnection influences from the SAM (Schneider et al., 2005). One shortcoming in understanding ice core climate forcing is that reliable meteorological records only extend into the recent past: the SAM, SOI, and Niño34 are reliable to 1950. Less reliable reanalysis information for SOI and Niño34 extends to the

[36] In climate studies, red noise often refers to a spectrum that has lower power density at higher frequencies. In this context, an ice core power density spectrum would be "red".
[37] In spectral analysis, a narrowband signal often refers to a relatively small bandwidth (width between the frequencies in question).

late 1800's. Surface temperature from meteorological stations is even less informative, only extending until 2006 at the WAIS Divide drilling site.

Despite the lack of necessary historical climate information, we attempt to form an idea of water isotope forcing mechanisms using linear regression and multiple linear regression statistical analyses. Linear regressions of SAM, SOI, and Niño34 compared with δD at monthly resolution from 1951–2003 show a weak, statistically significant correlation (R^2 = -0.17, $p < 0.05$) between δD and Niño34. Comparison of the data sets at yearly and bi-yearly resolution yields no statistically significant correlations. In addition to yearly signals, we isolate three-month timeframes in the data to compare seasonal correlations. A moderate, statistically significant correlation is evident in December-January-February (DJF) and January-February-March (JFM; Figure 5.10) between δD and SAM (R^2 = 0.31 and 0.37, respectively; $p < 0.05$). All other seasonal combinations are weakly correlated with no statistically significance. The fact that SAM is correlated with δD only in austral summer makes intuitive sense – this is the same time period that ENSO conditions appear in the tropical Pacific – and research has shown that ~25% of variance expressed in the SAM index is related to ENSO variations (Hosking et al., 2013). All linear regression results are shown in Table 5.1.

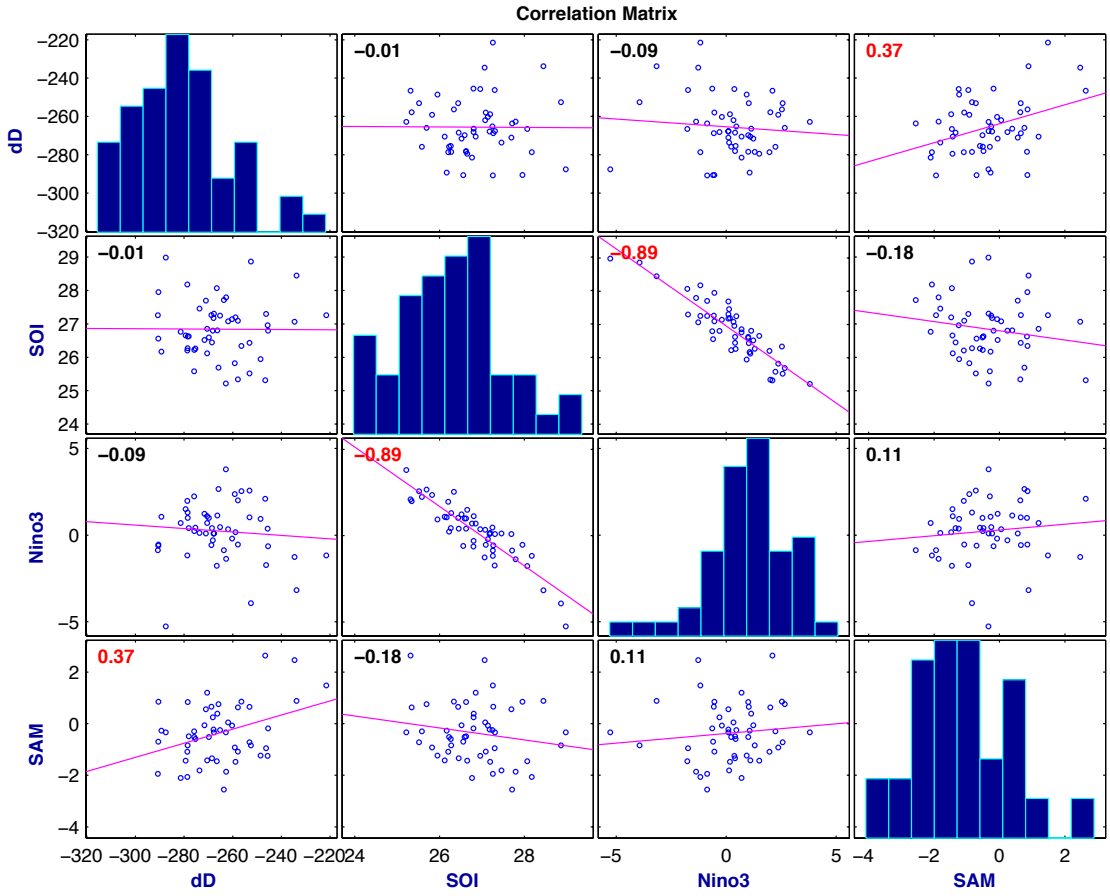

Figure 5.10. *A correlation matrix comparing linear regressions of δD, SOI, Niño34, and SAM for December-January-February averages from 1951-2003. The coefficient of determination R^2 is shown in the upper left of each plot. If R^2 is significant ($p < 0.05$), the value is shown in red. Histograms of each variable are shown on the diagonal.*

Table 5.1.
Linear regression results for δD compared with SAM, SOI, Niño34, and the solar sunspot cycle from 1951-2003. Three month averages are given in chronological order (JFM = January-February-March, FMA = February-March-April, and so on).

Scale	Niño34	SOI	SAM
Monthly	-0.17*	-0.01	0.07
Yearly	-0.14	-0.02	0.15
Bi-Yearly	0.01	-0.21	0.04
JFM	-0.09	-0.01	0.37*
FMA	-0.09	0.05	0.26
MAM	-0.04	0.07	0.05
AMJ	-0.02	0.02	-0.16
MJJ	0.09	-0.08	-0.12
JJA	0.09	-0.12	0.14
JAS	0.1	-0.11	0.23
ASO	0.06	-0.08	0.09
SON	0.1	-0.08	0.06
OND	0.06	-0.08	0.12
NDJ	-0.09	-0.02	0.21
DJF	-0.05	-0.05	0.31*

A multiple linear regression model is similar to singular linear regression except that multiple independent predictors (x_1, x_2, etc.) can be used to model the dependent variable (y). In this analysis, we use the following independent predictors from 1951-2003: SAM, SOI, Niño34, and the solar sunspot cycle (SILSO, 2015). The use of local surface temperature would greatly improve the model, but a WAIS Divide historical record older than 2006 is not available. An additional drawback of this method is that the independent variables are correlated amongst themselves, known as multi-colinearity. The SAM, SOI, and Niño34 all exhibit multi-colinearity, which can cause these independent variables to predict the same variance in the dependent variable. We include interaction terms in our analysis to partially address the multi-colinearity problem.

Examples of interaction terms include SAM*SOI, SAM*Niño34, SAM*SOI*Niño34, and so on. Finally, each additional predictor added to a multiple linear regression model will almost always increase the R^2 value since the model now has more data with which to fit the dependent variable. We use an adjusted R^2 value, which statistically estimates which combination of predictors in different models is more meaningful than others.

In the monthly multiple-linear regression model, we determine that a combination of all predictors (SAM, SOI, Niño34, and the solar sunspot cycle) yields the highest adjusted R^2 value (0.094, $p < 0.0001$). The best predictors of monthly δD (significance < 0.05) are Niño34 and SOI*Niño34*Sunspot. In the seasonal JFM multiple-linear regression model, the best model again includes all predictors, yielding an adjusted R^2 value of 0.204 ($p < 0.07$). Here, the best predictors (significance < 0.05) are Niño34, Sunspot, and Niño34*Sunspot. Removing 'Sunspot' from the seasonal JFM model gives an R^2 value of 0.126 ($p < 0.08$), which is less reliable than including the 'Sunspot'. With 'Sunspot' removed, the best predictors (significance < 0.10) are SAM and Niño34*SAM. These results suggest that sunspot activity may play a role in the WDC δD record, but must be interpreted with caution due to the multi-colinearity of the other predictors, as well as the unavailable local temperature record. Multi-linear regression results are shown in Table 5.2.

Table 5.2.
Multiple linear regression models for δD from 1951-2003 using the following independent predictors: SAM, SOI, Niño34, and the solar sunspot cycle.

Model: δD with SOI, Niño34, SAM, Sunspot Monthly Data	
Adjusted R-squared	0.094
p-value model	4.37E-10
Significant Predictors < 0.05	
Niño34	0.00045
SOI * Niño34* Sunspot	0.049

Model: δD with SOI, Niño34, SAM, Sunspot JFM Data	
Adjusted R-squared	0.204
p-value model	6.59E-02
Significant Predictors < 0.05	
Niño34	0.013
Sunspot	0.015
Niño34* Sunspot	0.015

Model: δD with SOI, Niño34, SAM JFM Data	
Adjusted R-squared	0.126
p-value model	7.33E-02
Significant Predictors < 0.10	
SAM	0.068
Niño34* SAM	0.073

Besides regression modeling, we compare δD to SAM, SOI, Niño34, and a central tropical Pacific coral stack (McGregor et al., 2013) using a 4th order Butterworth band-pass filter for 2-7 year oscillations (corresponding to the dominant ENSO frequency band in the 20th century). None of the band pass comparisons of SAM, SOI, Niño34, and the coral stack show phase continuity with δD for longer than about one decade. For example, δD and SOI are in phase from about 1992 to 2002 and from about 1952 to

1964, while other time periods are out of phase. Similar results are seen for each of the other comparisons (Figure 5.11). These results are not surprising since teleconnection mechanisms from the tropics to high-southern latitudes are non-stationary and highly dynamic.

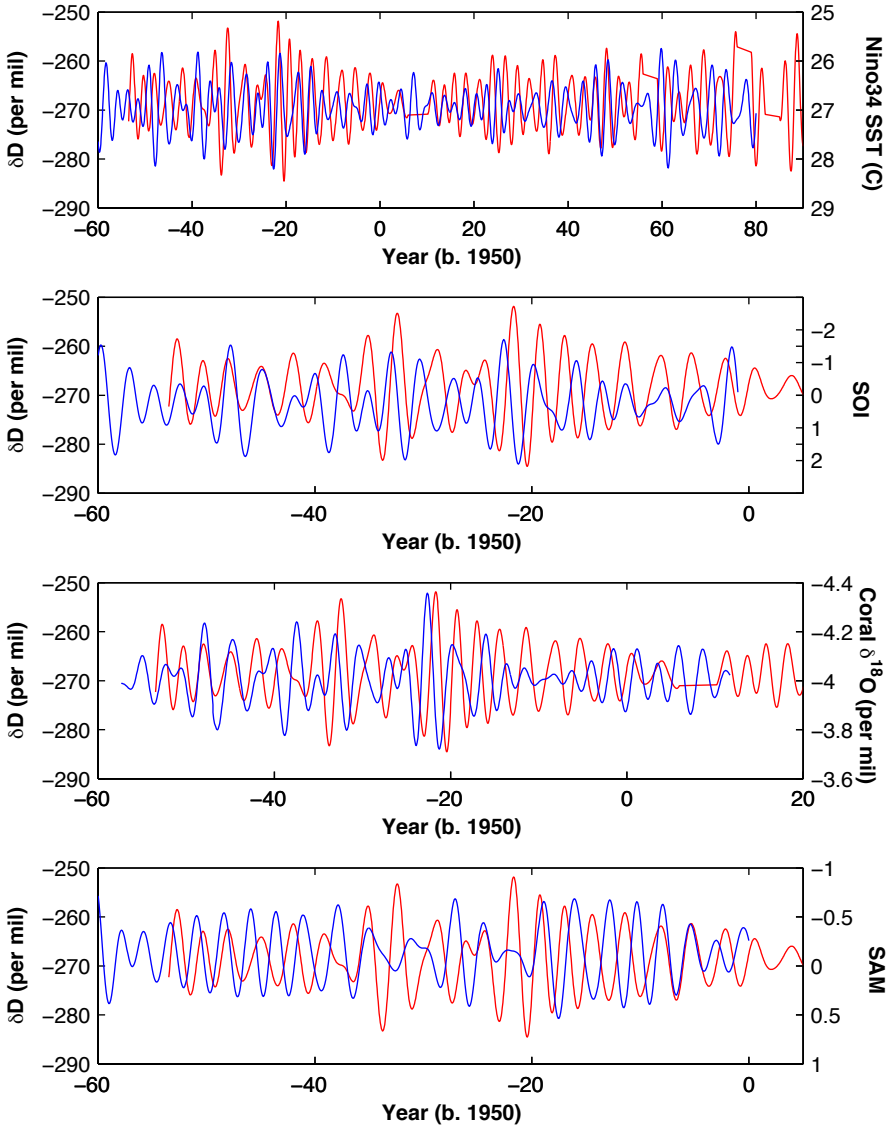

Figure 5.11. *Bandpass data between 2 and 7 years using a 4th order Butterworth filter. The δD record is shown in red. The Niño34, SOI, coral stack, and SAM are shown in blue. There is no long-term stationary behavior in any of the comparisons.*

5.3.2. Decay of High-Frequency Oscillations

In an ice core record, the decay of high-frequency signals due to strain and diffusion can be quantified in the frequency domain. In Figure 5.12, we isolate 1, 2, 3, 4, 5, 6, 7, 10, and 15-year peaks for 250-year spectral windows (at 125-year time steps) over the last 29 ka. The amplitudes are relative to each other in that they were calculated in exactly the same way using MTM spectral analysis, but are not exactly reliable in terms of absolute amplitude values due to uncertainty in the spectral estimations. The one-year signal at WDC has non-zero amplitude until about ~16 ka bp, although there is a slight indication of a remnant one year signal, especially from 24 to 29 ka bp. The decay of the one-year signal is largely influenced by accumulation rate (but also somewhat by temperature; see Chapter 4 for more information). Both the one-year signal and accumulation are highest in the mid-Holocene and lowest during the Last Glacial Maximum.

The two-year signal has nearly constant amplitude over the Holocene and declines nearly to zero at around 17 ka bp. A local two-year amplitude maximum occurs at 27 ka bp. Unlike the one-year signal, the two-year signal never fully disappears from the record. The three and four-year signals have slightly higher amplitude than the two-year signal and are nearly constant over the last 30 ka bp, except for a drop in amplitude centered at 17 ka bp. The five, six, and seven-year amplitudes are also nearly constant over the last 30 ka bp, with a small increase in amplitude from roughly 10 to 30 ka bp. The relative value of the five, six, and seven-year amplitudes are not much different than the three and four-year amplitudes. The ten and fifteen-year oscillations have the highest amplitude, with ten-year amplitude being slightly higher than seven-year amplitude, and

the fifteen-year amplitude being ~33% larger than the ten-year signal. Both the ten and fifteen year signals show a more pronounced increase in amplitude from 10 to 30 ka bp. This analysis shows that ENSO-scale oscillations (2-15 years) have persisted throughout the WDC water isotope record from 0-29 ka bp, while the one-year signal largely disappeared at 16 ka bp.

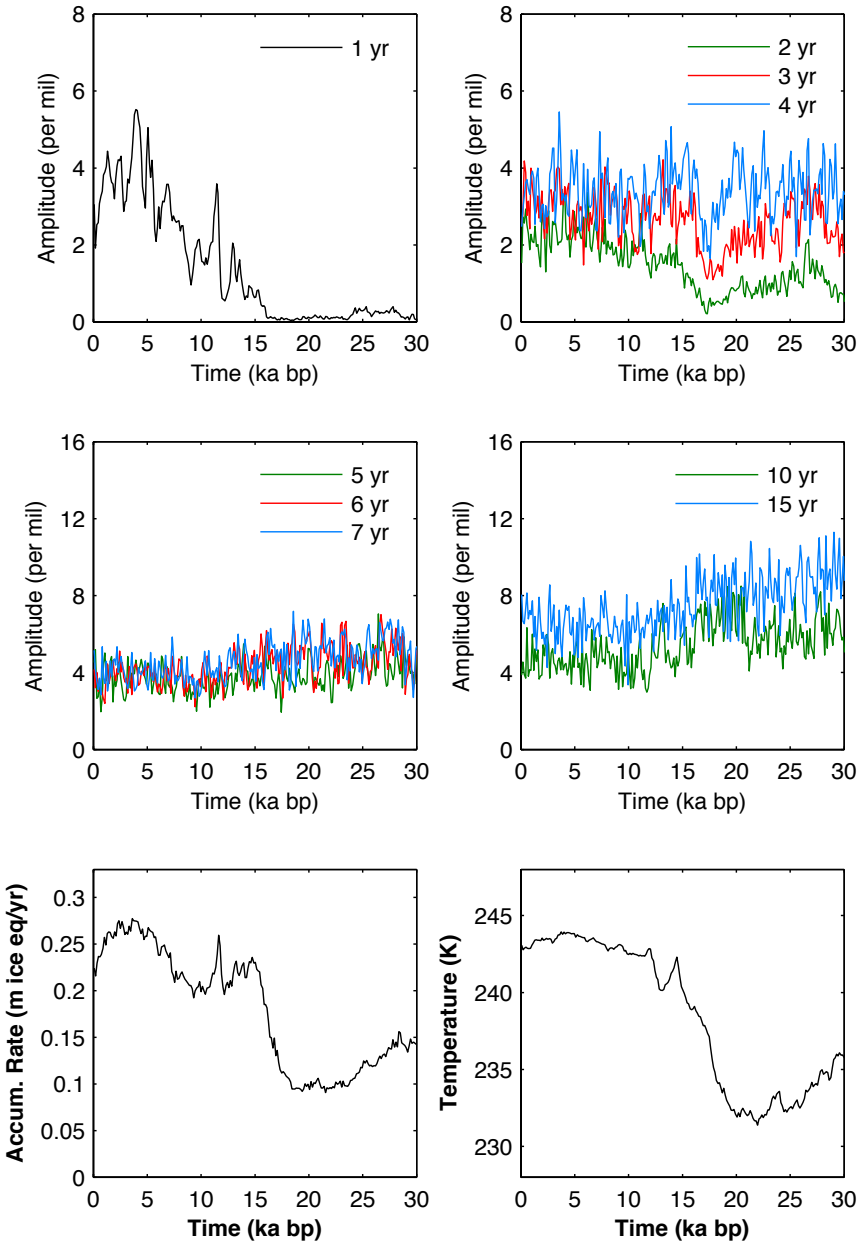

Figure 5.12. *ENSO-scale relative amplitudes for the last 29 ka. (Top Left) The 1-year signal decays effectively to zero by 16 ka bp, sharing similarities with accumulation and temperature due to their effect on the rate of diffusion. (Top Right) The decay of 2, 3, and 4-year signals never reach a value of zero. (Middle plots) The decay of 5, 6, 7, 10, and 15-year signals are essentially unaffected by diffusion, and show elevated values in the glacial period. (Bottom plots) Accumulation and temperature records for WAIS Divide.*

5.3.3. Significance of High-Frequency Oscillations

A test of significance must be done in the frequency domain to determine the likelihood that a spectral peak is caused by something other than random chance. Often, a significance test is set at 95% or 99%, meaning that random chance could cause the results only 5% or 1% of the time, respectively. When testing the significance of spectral peaks in a climate time series, a number of considerations must be taken, including signal noise and autocorrelation. Almost all climate time series exhibit a red noise background. For example, the thermal inertia of the oceans creates a memory effect on atmospheric weather forcing (Hasselmann, 1976). Similarly, diffusion occurring in the firn column of an ice sheet causes 'communication' between nearby ice layers, allowing water molecules to move and exchange between vapor and solid phases at different locations. Fisher et al. (1985) describes the full range of signal noise characteristics in an ice core: 1) Precipitated snow on the surface of the ice sheet has white noise characteristics due to the random nature of weather events; 2) Wind processes cause snow drift (e.g. via surface snow particles or larger dune like snow waves known as sastrugi); and 3) Diffusion in the firn column ultimately shifts the water isotope record to red noise.

Autocorrelation refers to the correlation of a time series with its own past and future values. A positive autocorrelation suggests that positive or negative excursions from a mean value are followed by similar changes away from the mean. For example, if the temperature today is unusually warm, a positive autocorrelation suggests that tomorrow will be unusually warm as well. Similarly, in ice core δ records, a data point is correlated with a certain amount of values before it. This autocorrelation must be accounted for in tests of statistical significance, and is usually prescribed as an AR(1)

process, where a single data point depends on the data point just before it.

MTM spectral significance with AR(1) and red noise assumptions is determined for the WDC water isotope record using 5 ka windows (Mann and Lees, 1996; Figure 5.13). For the last 10 ka bp, spectral peaks between ~0.8 to 10 years are significant. For the period 10 to 29 ka bp, spectral peaks between ~0.8 and ~50 to 100 years are significant. In each 5 ka window, ENSO-scale oscillations surpass the 99% confidence interval, showing that these high-frequency oscillations have been an integral part of the West Antarctic climate system for at least the last 29 ka.

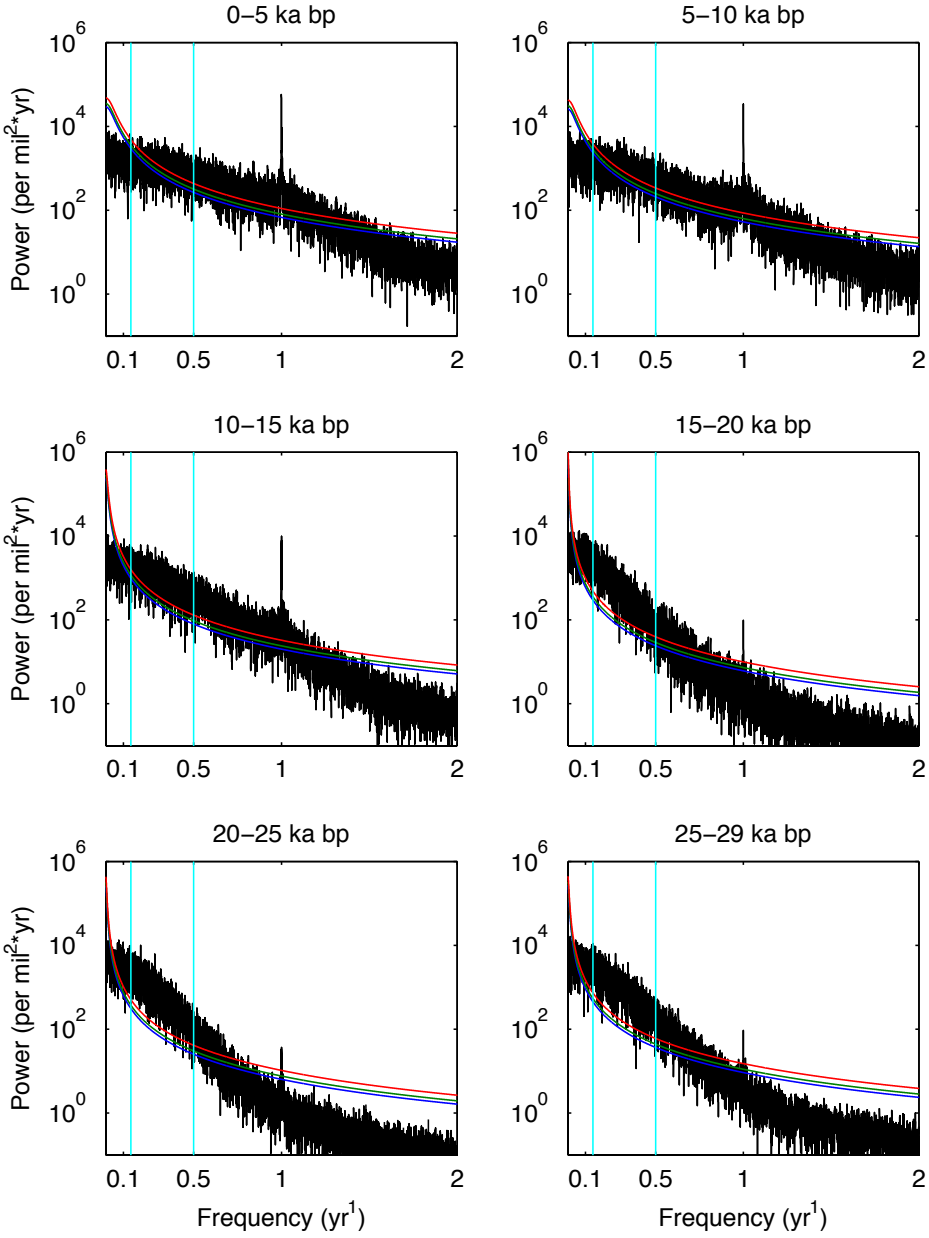

Figure 5.13. *MTM spectral analysis using the Mann and Lees (1996) method for spectral significance using red noise, AR(1), and narrowband signal assumptions. The black line is the MTM spectrum. The red, green, and blue lines represent statistical significance at 99%, 95%, and 90%, respectively. ENSO-scale power (2-7 years) is bounded by the light blue vertical lines. All ENSO-scale power is significant for the last 29 ka. Notice that the detection of a 1 yr signal from 20-25 ka bp is significantly dampened compared to 0-5 ka bp or 5-10 ka bp.*

A similar significance test using Continuous Wavelet Transform (CWT; Torrence and Compo, 1998) shows similar results. The wavelet approach differs in methodology from Mann and Lees in that a wavelet function must be chosen with a varying properties, including: orthogonal or nonorthogonal calculations (the latter is best for time series analysis), complex or real wavelet computations (a complex wavelet yields information about both amplitude and phase, while a real wavelet can only be used to isolate peaks and discontinuities), the width of the wavelet function (which inversely affects the resolution in the time vs. frequency domain), and the shape of the wavelet function (which is selected depending on whether the time series has sharp jumps). We use a Morlet function suited to ENSO-scale climate oscillations (described by Torrence and Compo, 1998) that is nonorthogonal and complex with suitable width and shape parameters. The autocorrelation is set to 0.72, meaning that 72% of the information in one data point is explained by the previous data point.

Plots of 1 ka wavelets for the time periods 5 to 6, 11 to 12, and 20 to 21 ka bp are shown in Figure 5.14. The wavelets highlight the non-stationarity of ~2 to 15 year oscillations. For example, a ~100-year time interval within a 1 ka wavelet may show significant spectral peaks centered on 5 years, while an adjacent 100-year interval may show significant spectral peaks centered on 10 years. This behavior is prominent throughout the entire 29 ka record. We note that while high frequencies (2-15 years) are non-stationary, combinations of high frequencies are almost continuously statistically significant throughout the record. Lower frequency observations (>15 years) tend to be more persistent within a certain oscillation range. For example, a statistically significant ~100 to 125 year oscillation persists from roughly 5.0 to 5.7 ka, a ~45 to 75 year

oscillation persists from 11.0 to 11.6 ka bp, and a ~20 to 32 year oscillation generally persists from 20.0 to 21.0 ka bp.

In summary, two types of statistical significance tests have been presented for oscillations occurring in the WDC water isotope record. Both methods show that ENSO-scale oscillations in the 2-15 year range are significant over the last 29 ka bp. For low frequency oscillations (>15 years) the two methods diverge in the Holocene – the MTM method suggests low frequency oscillations are not significant, while wavelet shows the opposite. Low frequency oscillations are significant in the glacial (10 to 20 ka bp) for both methods. Additional discussion of high and low frequency oscillations is found later in this chapter.

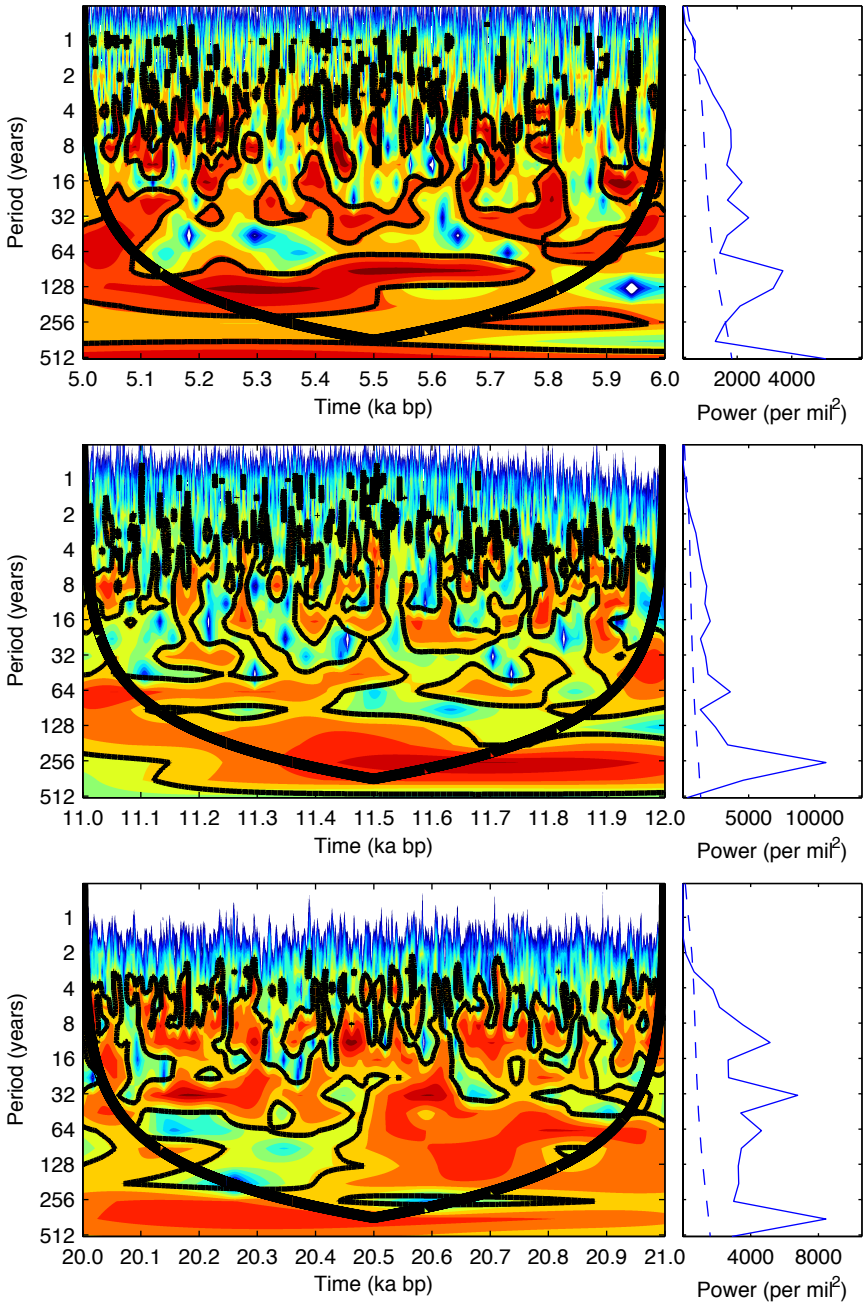

Figure 5.14. *Continuous Wavelet Transform (CWT) for 5 to 6 ka bp (top), 11 to 12 ka bp (middle), and 20 to 21 (bottom) based on a Morlet function, AR(0.72) process, and a red noise background (Torrence and Compo, 1998). Red represents the highest power and blue represents the least power. Solid black lines (or black regions) enclose periods at 95% significance levels. Any results below the thick black line (cone of influence) should be interpreted with caution. Relative power distribution is shown on the right plot as a solid blue line. The dashed blue line is the 95% significance level.*

5.3.4. Annual Signals in the Holocene

Remnants of a one-year signal exist throughout the Holocene and part way into the last glacial period (16 ka bp). Diffusional processes that have altered the original water isotope signal - mainly from diffusion in the firn column - are visibly evident, including: 1) Smaller annual signals have merged into larger nearby annual signals, creating multi-year bumps with shoulders on one or both sides, and 2) Series of smaller annual signals have merged into multi-year bumps (see Figures 5.7 and 5.8). Despite the diffusion, one-year power density in the frequency domain is highly statistically significant. A deconvolution method can be applied to the data set to estimate the original annual signal. This method entails division of a water isotope spectrum by a Gaussian filter using a pre-determined diffusion length. A discussion of diffusion lengths derived over 500-year windows can be found in Chapter 4.

We opt to only back diffuse data in the Holocene since the diffusion lengths are generally constant throughout this time period, and there are no significant abrupt changes in the water isotope data. The result of the deconvolution yields summer and winter water isotope values for the last 10 ka. This information is used to assess long-term trends in peak summer δ values, peak winter δ values, and the seasonal difference. We isolate long-term trends in the records using a 200-point smoothing window. Uncertainty in the diffusion lengths does not affect the long-term interpretation of the data, since small variations in diffusion length will propagate as equal changes in the δ values over any 500-year window. Changes at the edges of each 500-year window (i.e. at multiples of 190 and 690 years) and at sub-500 year resolution may have some small additional uncertainty. Plots of back-diffused annual data are shown in Figure 5.8.

Smoothed summer δ values trend with max summer insolation at 60°S (W/m^2) [38] (Berger, 1978; Figure 5.15). In the early Holocene at 10 ka bp, summer δ values are lowest, then rise to a maximum value around 4 ka bp, and finally decline towards the present. Smoothed winter δ values do not trend with insolation. Maximum winter δ values occur at 4.8, 5.9, 9.2 ka bp, while minimum winter δ values occur at 1.0 and 7.9 ka bp. The difference in summer and winter δ values within any given annual cycle (i.e. the annual amplitude of the signal) also trends with insolation, but not as strongly as summer values. For all three records (summer, winter, difference), significant millennial scale variations are evident, and there appear to be six millennial scale cycles over the last 10 ka. The cause of this millennial variability is unknown, but also prominently appears in Greenland ice cores during the glacial period.

[38] As a side note, the reason that the Northern and Southern Hemisphere appear to deglaciate at the same time, despite opposing maximum summer insolation forcing due to precession, are due to important differences between maximum and integrated summer insolation. In the Northern Hemisphere, where large ice sheet dynamics dominate, the max summer insolation at 65°N causes the growth and recession of ice sheets (Milankovitch, 1941 and Roe, 2006). But, the dynamics in the Southern Hemisphere, where Southern Ocean and Antarctic interactions dominate, an integration of the entire summer season insolation is more relevant (Huybers and Denton, 2008). Max summer insolation in the north and integrated summer insolation in the south are directly related and explain why inter-hemispheric deglaciation occurs at the same time. In the ice core record at WDC, the water isotopes appear to respond to max summer insolation at 60°S.

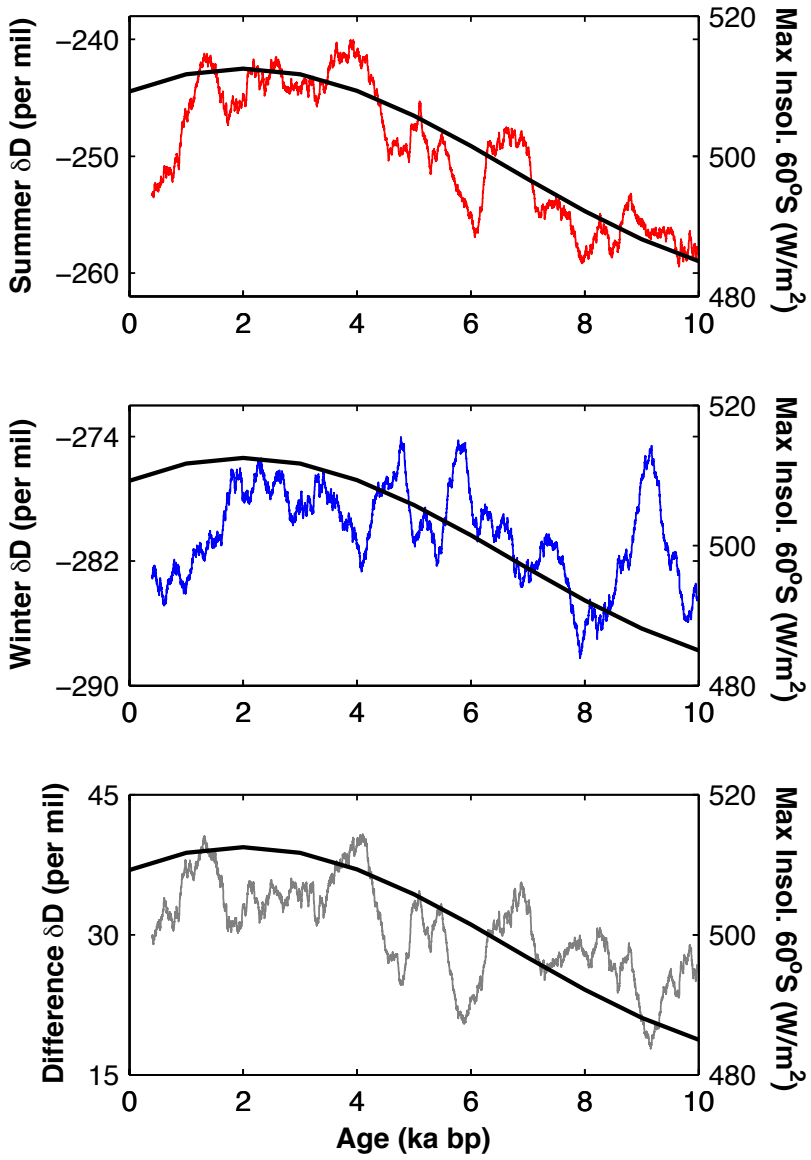

Figure 5.15. *Plots of max summer (top, red), minimum winter (middle, blue), and summer-winter (seasonal) differences (bottom, grey) in δD. The data is smoothed using a 200-point window. The black line shows maximum summer insolation at 60°S. The summer and seasonal data appear to trend with insolation, while the winter data is less correlated. Note that millennial trends are evident throughout the last 10 ka for the summer, winter, and seasonal data.*

5.3.5. ENSO-scale Oscillations to 29 ka

Remnants of WDC high-frequency oscillations between 2-15 years persist for at least the last 29 ka. Due to diffusion, the two-year signal is most attenuated, reaching a power density minimum value at around 17 ka bp (generally in-line with the accumulation rate minimum). The three and four signals also decline at 17 ka bp, while five to fifteen year oscillations show no attenuation effects. We analyze varying periodic bands in the two to fifteen year range, both in terms of the original signal and back-diffusion, to determine estimates of high-frequency paleo-oscillations. Unlike the one-year deconvolution, we do not perform a reverse Fourier transform into the time domain for back diffusion, instead keeping the data in the frequency domain. This method is sufficient to compare long-term patterns in the strength of ENSO-scale oscillations.

Without a diffusion correction, the average 2-7 year signal has nearly constant power throughout the last 29 ka, never deviating from Holocene-like amplitudes. Conversely, the 4-15 year signal, which is not significantly affected by diffusion, shows higher amplitudes in the glacial than the Holocene. When a diffusion correction is applied, the 2-7 year signal becomes elevated in the glacial period, similar to the observed 4-15 year signal. The majority of the diffusion correction is due to attenuation of 2-4 year signals by diffusional processes (Figure 5.16).

The back diffused 2-7 year relative amplitudes are nearly constant throughout the Holocene, and then increase in two steps moving backward in time from ~10.0 to 13.0 ka bp and ~16.0 to 17.5 ka bp. The relative amplitudes from 20.0 to 29.0 ka bp are ~35 percent higher than from 1.0 to 10.0 ka bp, while the spike in amplitude at ~17.5 ka bp is ~300 percent higher than any amplitude value occurring in the Holocene. A similar

pattern is evident in back diffused 4-15 year relative amplitudes. The difference in relative amplitudes moving from the Holocene to the glacial period is about 45%. Here, the increase from Holocene to glacial occurs in two steps moving backward in time from ~10.0 to 13.0 ka bp and an abrupt transition at ~16.5 ka bp. Like the 2-7 year relative amplitudes, the 4-15 year signal shows no trend in the Holocene (except for a small <10% increase centered at 7.5 ka bp). Similar results are seen for 7-10 year and 10-15 year bands.

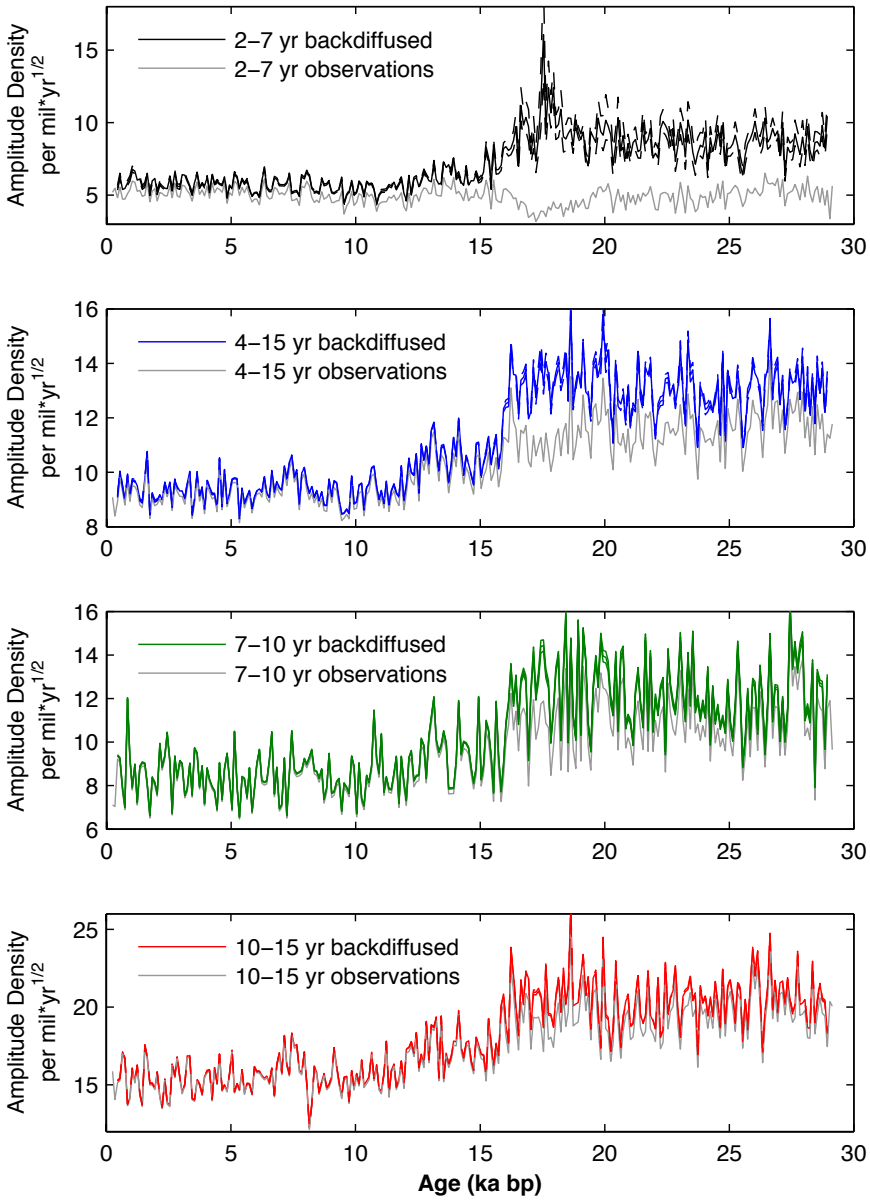

Figure 5.16. *Plots of back-diffused amplitude density vs. age for 2-7 year averages (black), 4-15 year averages (blue), 7-10 year averages (green), and 10-15 year averages (red). The grey line in each plot represents the original observations. The 2-7 year signal requires the largest diffusion correction.*

5.3.6. ENSO Modeling Over the Last Glacial-Interglacial Period

We utilize two global circulation models to analyze the potential causes of ENSO-scale variance over the most recent glacial-interglacial cycle, including 1) The TraCE-21ka (Simulation of Transient Climate Evolution over the last 21,000 years) model, developed by the National Center for Atmospheric Research (NCAR). The model provides 4-dimensional data sets of coupled ocean-sea ice-land processes. We use surface temperature (T_S) at monthly resolution to approximate shallow sea surface temperatures and land surface temperatures at varying locations in the South Pacific region (see Zheng et al., 2007 for additional ENSO modeling explanations); and 2) A modified HadCM3 model that takes into account the effects of orbital forcing, greenhouse gas concentrations, and ice sheet sizes on tropical Pacific climate (Roberts and Valdez in prep., 2015):

In the TraCE-21ka model, we analyze an array of locations in the south Pacific Ocean including the intersections of latitudes at 2°S (tropics), 20°S (sub-tropics), 40°S (mid-latitudes), 60°S (Southern Ocean), and 80°S (inland Antarctica) with longitudes of 180°E, 200°E, 220°E, and 240°E. We use T_S to determine spectral power density estimates of ENSO-scale variations (2-7 years) at each of the latitude-longitude intersections (Figure 5.17). Each latitude band behaves in a similar fashion, so we group latitude transects into bins. In the tropics bin, the model shows no apparent change between Holocene and glacial 2-7 year T_S power density. The sub-tropics and mid-latitude bins behave similarly with almost no variation over the last 21 ka, and have lower 2-7 year T_S power density than the tropics bin. The Southern Ocean bin shows lower 2-7 year T_S power density in the Holocene and elevated power density in the glacial, which is

very similar to the WDC water isotope record. This suggests that processes occurring in the Southern Ocean, rather than the tropics, dominate water isotope variations at WAIS Divide. The inland West Antarctica bin exhibits the opposite pattern as the Southern Ocean, showing higher 2-7 year T_S power density in the Holocene and lower power density moving into the glacial. This is counterintuitive, as ice core water isotopes in inland West Antarctica depend strongly on temperature, but cannot be related directly since atmospheric circulation is also important. Overall, it is unclear what is forcing these results, and how the results relate to water isotopes. One possible explanation is that stronger temperature gradients from tropics to poles increases high-latitude weather variability. More research would be needed to reach any conclusions.

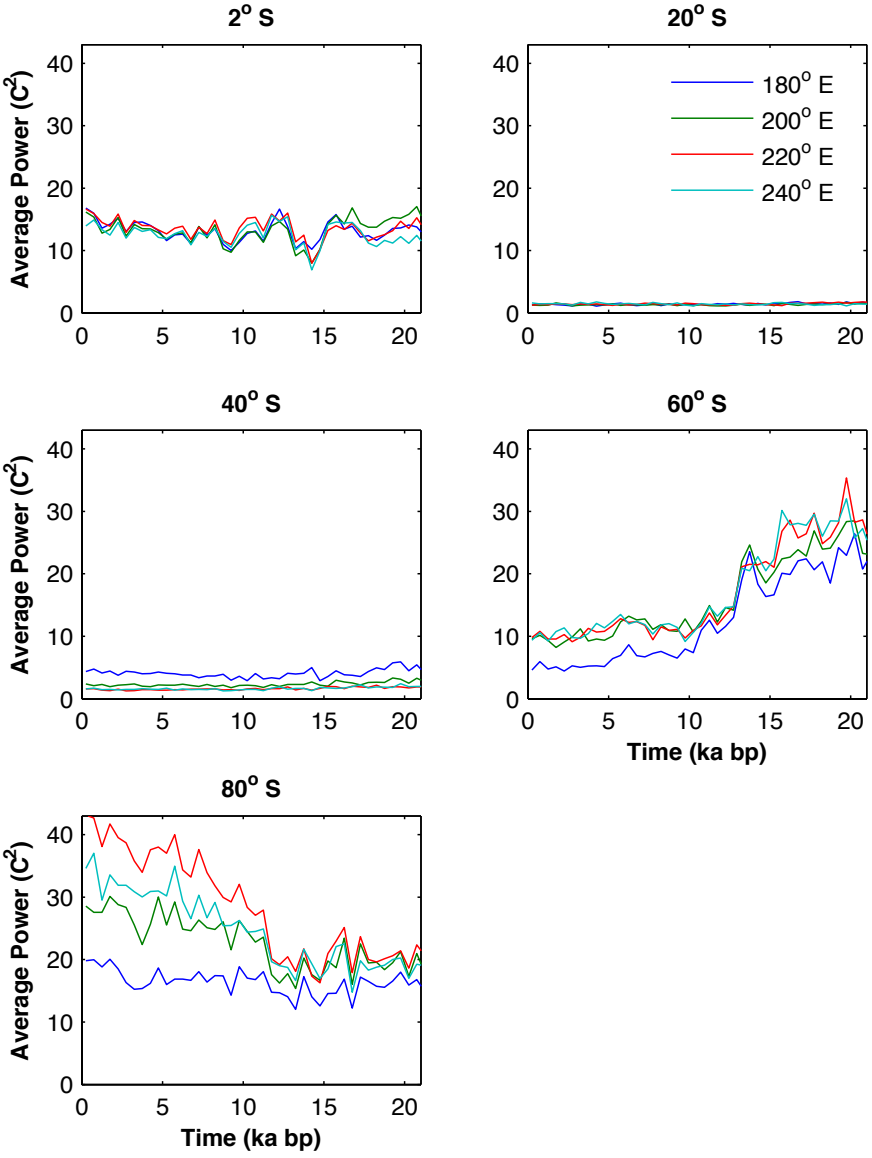

Figure 5.17. *Plots of 2-7 year average power (°C^2) for TraCE-21ka model values of T_S (surface temperature) for latitudes of 2°S (tropics), 20°S (sub-tropics), 40°S (mid-latitudes), 60°S (Southern Ocean), and 80°S (inland Antarctica) and longitudes of 180°E, 200°E, 220°E, and 240°E (west-east south Pacific transects). The 60°S pattern is most similar to the WDC water isotope record.*

The modified HadCM3 model tells a different story than the TraCE-21ka model. When orbital forcing, greenhouse gas concentration, and ice sheet sizes are all included, tropical Pacific ENSO variability in the Niño3 region is strengthened during the last glacial period, especially during the Last Glacial Maximum (LGM; Figure 5.18). This is very similar to the WDC water isotope record. One possible mechanism for stronger ENSO in the glacial, and especially the LGM, is that sea level was lower by up to 120 meters[39], which would have exposed continental shelf areas, changing oceanic and atmospheric circulation patterns. Specifically, glacial sea level values would have resulted in more exposed land area in the western tropical Pacific, which at present has many shallow seaways, than the eastern tropical Pacific, which has sharply declining continental shelves. The exposed land surface and decline in tropical Pacific surface ocean area may have significantly altered the boundary conditions for ENSO events, creating stronger oscillations. An examination of high-latitude responses to enhanced glacial ENSO is not analyzed in this model.

[39] During the LGM, the ice sheets were large, which displaced about 120 meters of water from the oceans onto land surfaces.

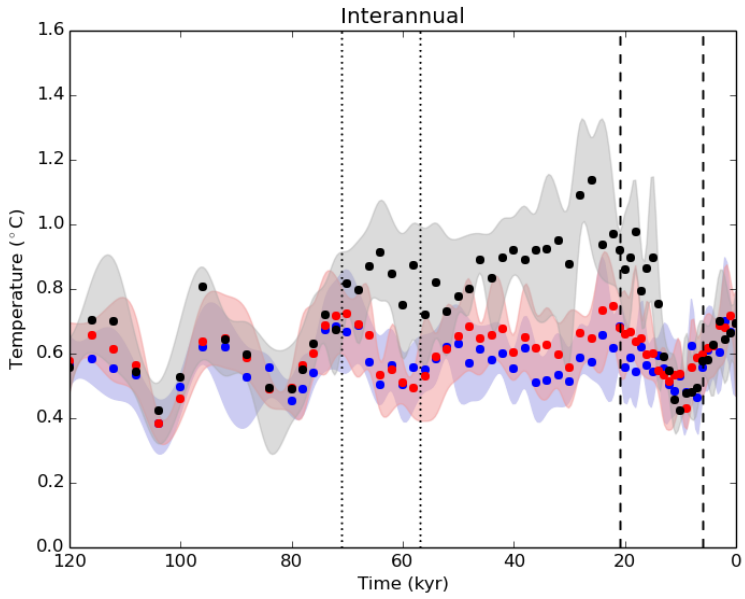

Figure 5.18. *Plot of 3-7 year variability in Niño3 temperature over the last 120 ka for orbital forcing (red), orbital + greenhouse gas forcing (blue), and orbital + greenhouse gas + ice sheet forcing (grey). The dots represent the standard deviation of the surface temperature anomalies, while the shading indicates uncertainty. The size of the ice sheets appear to cause increased strength in ENSO in the glacial period, with a max strength near the LGM at 21 ka bp. Figure courtesy of Roberts and Valdez (in prep., 2015).*

5.3.7. Low Frequency Oscillations to 68 ka

The analysis of high-frequency oscillations is often the central focus of climate time series analysis. However, there is also important climate information contained in low-frequency oscillations. We use second order Butterworth filters, in conjunction with wavelet analysis, to isolate low-frequency oscillations in the WDC water isotope record. First, we use a high-pass filter to remove any oscillations greater than a certain value (4,000 and 2,000 years). The high-pass filter centers all remaining frequencies on a zero mean value. We choose the high-pass values to remove large-scale glacial-interglacial oscillations that can dominate power in spectral analysis. We then low-pass filter the

remaining data to remove ENSO-scale oscillations at 15 years and below. Band-pass plots of 15-2,000 year filtered data are shown in Figure 5.19. Plots pertaining to the 15-4,000 year filtered data are shown in Figure 5.20.

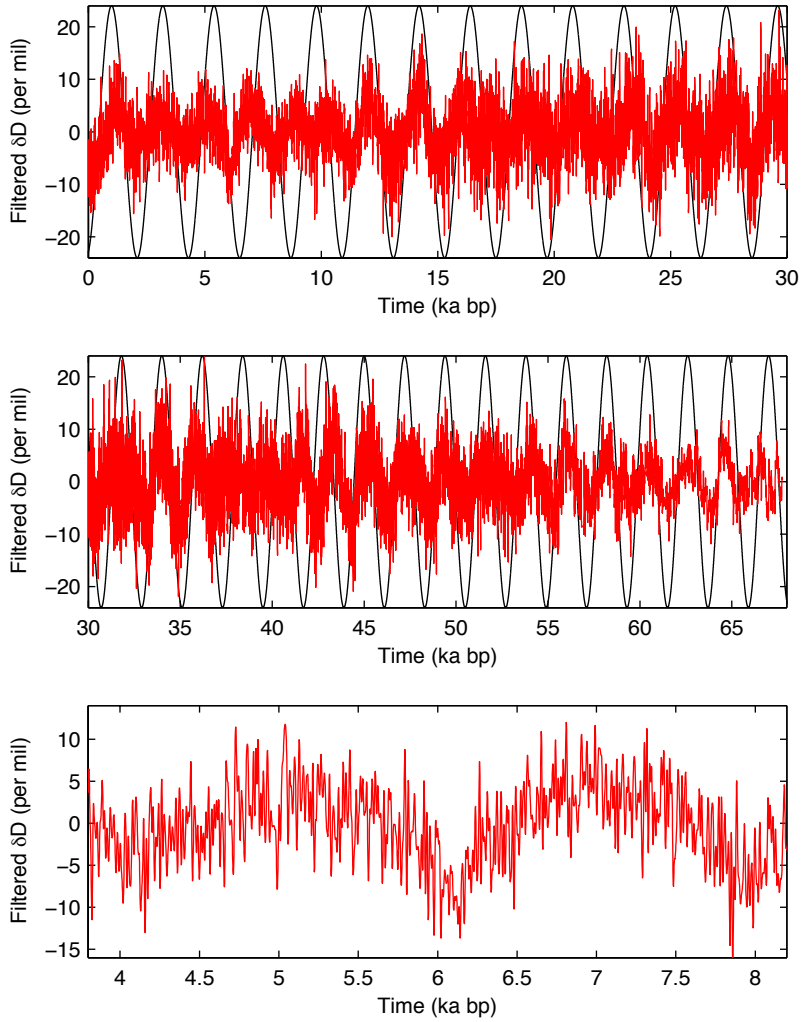

Figure 5.19. *Plots of band-passed data between 15 and 2,000 years using a 2nd order Butterworth filter. An oscillator of 2,200 years is affixed to the data, which generally estimates the periodic signal, although not for all time periods. The millennial pattern seen in this plot is also visible in wavelet analysis (Figure 5.20).*

For variability contained within 15 to 4,000 years over the last 68 ka, wavelet analysis shows 95% statistically significant oscillations between 1,000 to 8,000 years (Figure 5.20). The highest oscillations may be the result of amplitude modulation by smaller millennial scale variability. For example, variability in the amplitude of each ~2,000 year oscillation (i.e. two successive high amplitude signals, followed by two successive low amplitude signals) can result in larger wavelet derivatives (i.e. 2,000 year amplitude variability can also create 4,000 year variability, and so on). In the wavelet, the strongest power is centered at ~1,500-3,00 years. Millennial oscillations can also be seen in Figure 5.19, where ~14 millennial scale cycles are evident over the last 29 ka, showing that a ~2.14 ka average oscillation is embedded within that data set (this value cannot be considered exact, as the spacing of the peaks is not constant). Overall, the millennial signal is stationary, and there is some indication of significant variability as low as 500 years throughout the record.

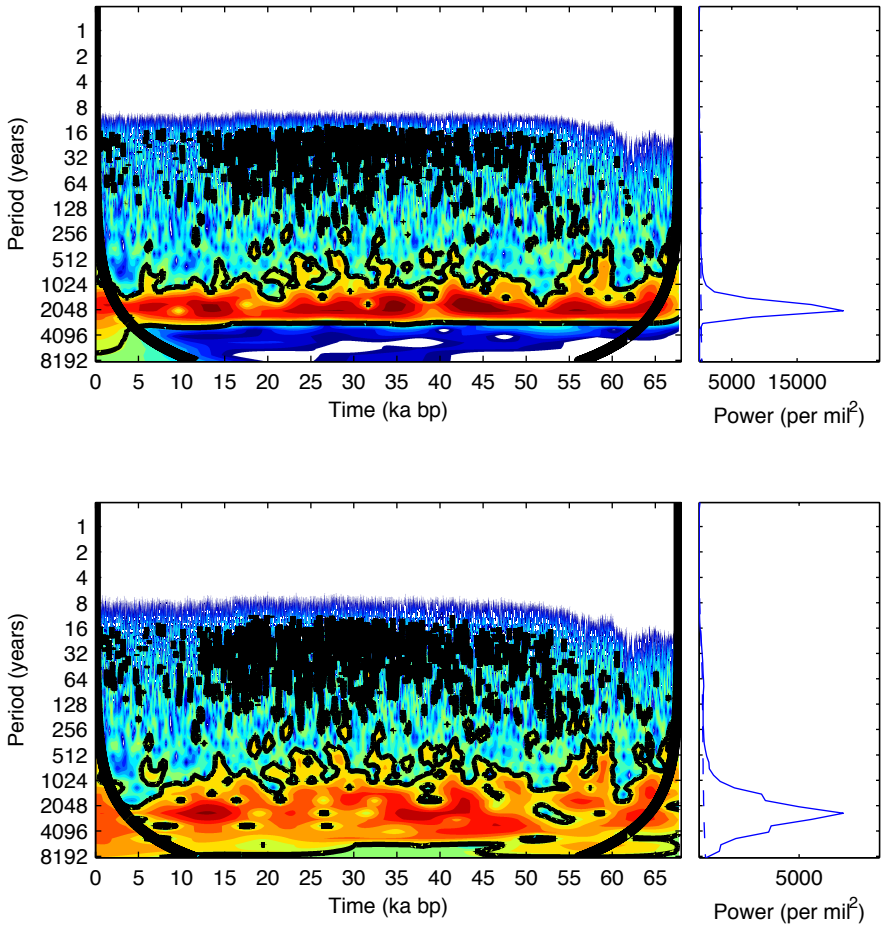

Figure 5.20. *Wavelet plots of band passed data using a 2nd order Butterworth filter for oscillations between (top) 15 and 2,000 years and (bottom) 15 and 4,000 years. Millennial variations appear prominently for the last 68 ka bp, while the occurrence of 15-125 year oscillations is more prominent in the glacial from ~12-55 ka bp. There are few instances of significant power between 125-500 years. For additional information about wavelet plot interpretation, see Figure 5.14*

At sub-millennial timescales, the occurrence of 15-125 year oscillations is more prominent in the glacial than the Holocene, while there are very few occurrences of statistically significant oscillations from 125-500 years for the last 68 ka bp. The increase in 15-125 year wavelet power occurs around 12-13 ka bp, and fades away around 55 ka bp, which may be related to thermal diffusion of ice near the bed or the size of the ice

sheets. The increase at 12-13 ka bp is similar to the glacial increase in ENSO-scale frequencies (2-15 years) discussed previously in this chapter. It is probable that some frequencies greater than 15 years may be amplitude modulated by smaller oscillations, or they may have alternative sources such as solar forcing or oceanic inertia.

5.3.8. Sources of Low Frequency Variability in the Climate System

At sub-Milankovitch time scales, there appears to be a connection between solar sunspots and climate. In a pioneering study, Eddy (1976) used telescopic observations to show that an extended decline in solar activity, known as the Maunder Minimum, is likely related to a period of cooling known as the Little Ice Age (~1550-1850 AD). The results of Eddy and the effect of sunspots on climate have been recreated in terrestrial climate models. Shindell et al. (2001) showed that the climate response to solar irradiance[40] (i.e. sunspots) during the Maunder Minimum causes colder temperatures on the Northern Hemisphere continents of 1° to 2°C during winter, while altering global average temperature by only 0.3 to 0.4 °C. Ineson et al. (2011) used data from the Solar Radiation and Climate Experiment (SORCE) satellite mission (NASA) and an ocean-atmosphere climate model to show that solar irradiance can alter the jet stream, causing mild winters in some Northern Hemisphere places and cold winters in others. These models show that changes in solar activity can affect certain places on Earth more than others (i.e. the Little Ice Age is seen most prominently in the European Alps), in line with proxy evidence (reviewed by Matthews and Briffa, 2005).

[40] Solar irradiance is the amount of solar energy hitting the top of Earth's atmosphere in units of W/m^2.

Solar activity can be reconstructed beyond historical records by studying radiocarbon formed in the upper atmosphere, which is recorded in the wood of trees (for example: Eddy, 1977; Stuiver, 1978, Castagnoli and Lal, 1980; and Suess, 1980). When cosmic rays enter the atmosphere, varying reactions occur that eventually transforms ^{14}N into ^{14}C, described by the following equation:

$$^{1}n + {}^{14}N \rightarrow {}^{14}C + {}^{1}p \tag{12}$$

Once formed, ^{14}C combines with O_2 to form $^{14}CO_2$, which is then incorporated into plants and trees through photosynthesis.

The production of ^{14}C by cosmic-ray neutrons is modulated by sunspot activity (Lingenfelter, 1963 and O'Brien, 1979), where more sunspots result in less atmospheric ^{14}C, and vice versa. Spectral analyses of ^{14}C variations in tree rings, as well as from historical telescope records, reveals a number of important solar oscillations. The most studied oscillation is the 11-year cycle, known as the Schwabe Cycle (Schwabe, 1849). A double sunspot cycle of 22 years is known as the Hale Cycle, resulting from variations in amplitude of the 11-year cycle (Hale, 1924). An 88-year (but more accurately a 70-100 year) oscillation is known as the Gleissberg cycle, which is likely amplitude modulated by the 11-year cycle (Gleissberg, 1945). A ~200-year cycle also appears, known as the de Vries or Suess cycle (Suess, 1980). The strongest spectral peak occurs at ~2,400 years, known as the Halstatt Cycle (Houtermans, 1971; Suess, 1980; Hood and Jirikowic, 1990; Charvátová, 2000; Vasiliev and Dergachev, 2002; and Charvátová and Hejda, 2013). It has been theorized that the ~2,400 peak results from the modulation of the motion of the

sun around the center of mass of the solar system by the giant planets (Jupiter, Saturn, Uranus, and Neptune; Charvátová, 2000). There is also evidence of ~6,000-year periodicity in reconstructed sunspot numbers (Xapsos and Burke, 2009)[41]. For a review of the atmospheric ^{14}C spectrum, including terrestrial and solar components, see Damon and Sonett (1991).

Solanki et al. (2004) created a sunspot record based on tree ring dated radiocarbon concentrations and physics-based models for the last 11,400 years[42]. Figure 5.21 shows spectral analysis of the Solanki ^{14}C record. The spectral peaks with the highest power, relative to a locally white noise spectrum, include 6,826, 2,275, 2,048, 976, 525, 353, 225, 209, 151, 123, 105, 88, and 85 years. Peaks less than 85 years do not appear to be significant because the ^{14}C record is averaged to 10-year resolution. Reconstructing the ^{14}C record with only significant spectral peaks yields a record with a consistent underlying ~2,200 year frequency.

[41] It should be noted that the ~6,000 year oscillation may not be solar in origin, but rather arise from changes in Earth's magnetic field.
[42] Another useful proxy for solar activity is ^{10}Be, which is independent of the carbon cycle.

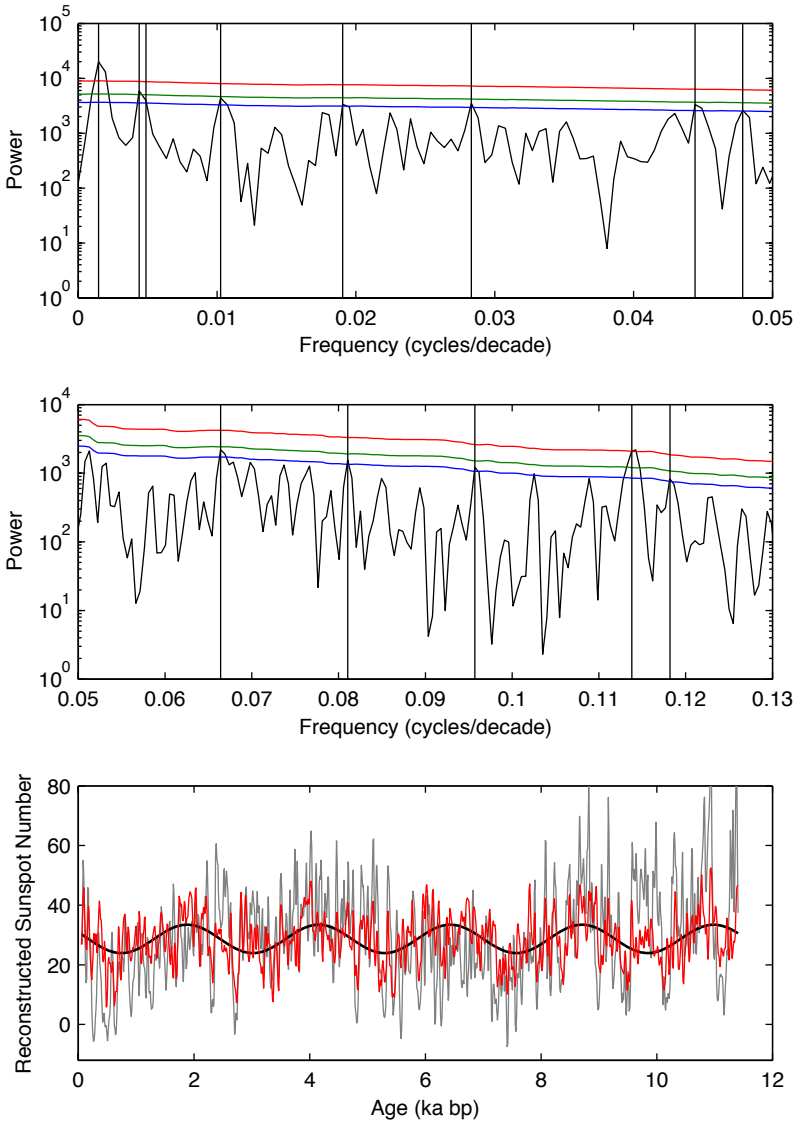

Figure 5.21. *MTM spectral analysis (Mann and Lees, 1996) of the Solanki et al. (2004) sunspot record for the last 11.4 ka bp. The top two panels show significant spectral periodicities against a locally white noise spectrum at 90% significance (blue), 95% significance (green), and 99% significance (red). In the top plot, significant peaks from left to right (vertical black lines) are 6,826, 2,275, 2,048, 976, 525, 353, 225, and 209 years. In the middle plot, significant peaks from left to right are 151, 123, 105, 88, and 85 years. In the lower plot, the original ^{14}C record is shown in grey, the reconstructed signal using all significant periodicities listed above is shown in red, and a reconstruction using only the 2,275-year oscillation is shown in black.*

5.3.9. Solar Influence

The WDC δD record can be resampled to 10-year spacing and analyzed spectrally to determine frequency component similarities to ^{14}C and other records (Figure 5.22). Using a white noise spectrum, the δD record shows significant spectral peaks at 2,926, 2,643, 2,410, 2,214, 2,048, 1,517, 1,255, 1,045, and 960-years. The 2,410-year periodicity has been found in radiocarbon records (Houtermans, 1971; Suess, 1980; and Hood and Jirikowic, 1990) and predicted from astrophysical behavior (Charvátová, 2000 and Charvátová and Hejda, 2013). The 2,214, 2,048, and 960-year periodicities appear in the Solanki et al. (2004) ^{14}C record. The 1,517-year periodicity has been seen in sediment records from the Northern Hemisphere. Specifically, Bond et al. (2001) found a ~1,500-year cycle, comprised of smaller centennial scale oscillations, in ice rafted debris from North Atlantic ocean sentiments during the Holocene. Bond suggested solar forcing was the cause of these cycles, despite the fact that no ~1,500 year solar cycle is evident in the ^{14}C record. However, Clemens (2005) suggested that heterodyne[43] frequencies may cause the ~1,500 year cycle. Using small variations (<2%) of certain ^{14}C oscillations (352 and 286 years), Clemens showed that combining frequencies (1/285–1/352 = 1/1497) matches North Atlantic sediment records. Table 5.3 shows heterodyne frequencies created from significant ^{14}C oscillations determined in this study. Combining significant oscillations results in (1/209.0–1/225.1 = 1/2922) , (1/84.6–1/87.9 = 1/2253), and

[43] A heterodyne frequency occurs when two different frequencies are combined to produce two new frequencies through the sum and difference of the original frequencies. Combined frequency behavior also appears in Milankovitch-scale climate forcing. Primary orbital variations occur at 23 kyr (precession), 41 kyr (obliquity), and 100 kyr (eccentricity). However, some tropical Pacific and Indian Ocean climate records show a 30 kyr oscillation (Clemens and Prell, 1991; Pisias and Mix, 1997; Beaufort et al., 2001; Beaufort et al., 2003), which could result from the heterodynes (1/100+1/41 = 1/29) and (1/100+1/23 = 1/30).

(1/209.0–1/232.7 = 1/2052), all of which are very similar to the WDC δD record.

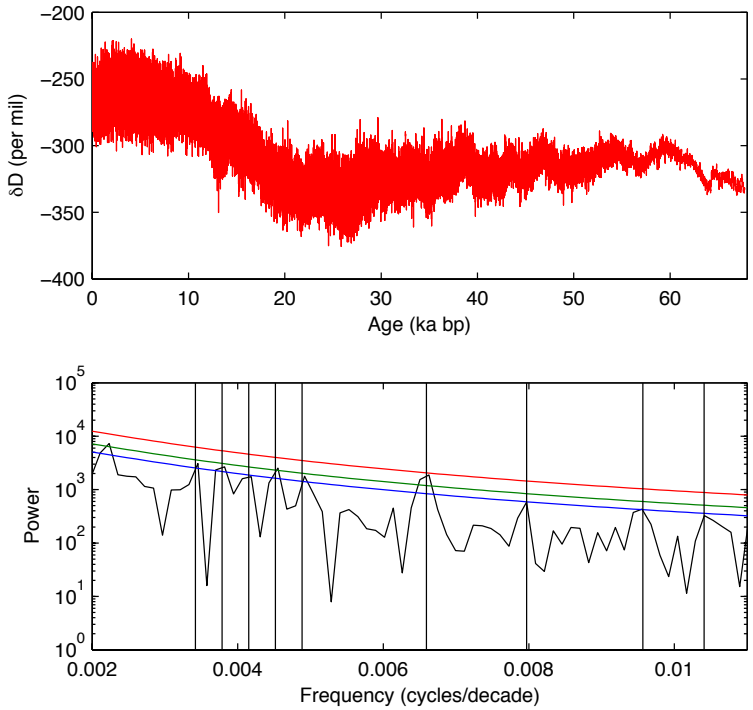

Figure 5.22. *In the top plot, the WDC δD record is shown in red. The bottom plot shows MTM spectral analysis (Mann and Lees, 1996) of the WDC δD record. Compared against a white noise background, statistically significant spectral periodicities less than 3,000 years include 2,926, 2,643, 2,410, 2,214, 2,048, 1,517, 1,255, 1,045, and 960 years. The ~2,214, 2,048, and 960-year oscillations also appear prominently in MTM spectral analysis of the Solanki et al. (2004) sunspot record. The 1,517-year oscillation is seen in North Atlantic sediments (Bond et al., 2001), which is also thought to be of solar origin.*

Table 5.3.
Heterodyne periodicities (i.e. 1/84.6–1/87.9 = 1/2253) resulting from MTM spectral analysis (Mann and Lees, 1996) of the Solanki et al. (2004) sunspot record for the last 11,400 years. Statistically significant oscillations of ~2,922, ~2,253, and ~2,052 years are seen in the WDC water isotope record as well.

	84.6	**87.9**	**104.5**	**123.4**	**150.6**	**209.0**	**225.1**	**232.7**	**353.1**	**525.2**
84.6		2253	444	269	193	142	136	133	111	101
87.9	2253		553	306	211	152	144	141	117	106
104.5	444	553		682	341	209	195	190	148	130
123.4	269	306	682		683	301	273	263	190	161
150.6	193	211	341	683		539	455	427	263	211
209.0	142	152	209	301	539		2922	2052	512	347
225.1	136	144	195	273	455	2922		6892	621	394
232.7	133	141	190	263	427	2052	6892		682	418
353.1	111	117	148	190	263	512	621	682		1078
525.2	101	106	130	161	211	347	394	418	1078	

MTM spectral analysis (Mann and Lees, 1996) of the ^{14}C sunspot record (Solanki et al., 2004) and the WDC δD record shows common and statistically significant periodicities of ~2,200 and ~2,050 years. The small errors in spectral peak locations (<2%) between ^{14}C and δD are likely caused by dating uncertainty in the two records and in uncertainty of the spectral estimation process. A third common periodicity occurs between δD and a heterodyne frequency from the ^{14}C record of ~2,900 years (i.e. a combination of 209 and 225 year oscillations). A fourth common periodicity occurs between δD and North Atlantic sediment records of ~1,500 years, which is also thought to be a solar heterodyne frequency. In Figure 5.23, we show that a combination of statistically significant periodicities found in the WDC δD record (2,410, 2,214, and 2,048 years) can be used to recreate the sunspot record for the last 11.4 ka (hereafter referred to as δD_{sun}). In Figures 5.23 and 5.24, we compare a 15-4,000 year band-passed

δD record (hereafter referred to as δD_{bp4k}) and spectrally reconstructed δD_{sun} record to the NGRIP ice core in central Greenland, specifically comparing the timing of the initiation of D-O events. The δD_{bp4k} signal can be interpreted as a signal with the effects of high-frequencies ENSO-scale oscillations and long-term glacial-interglacial changes removed.

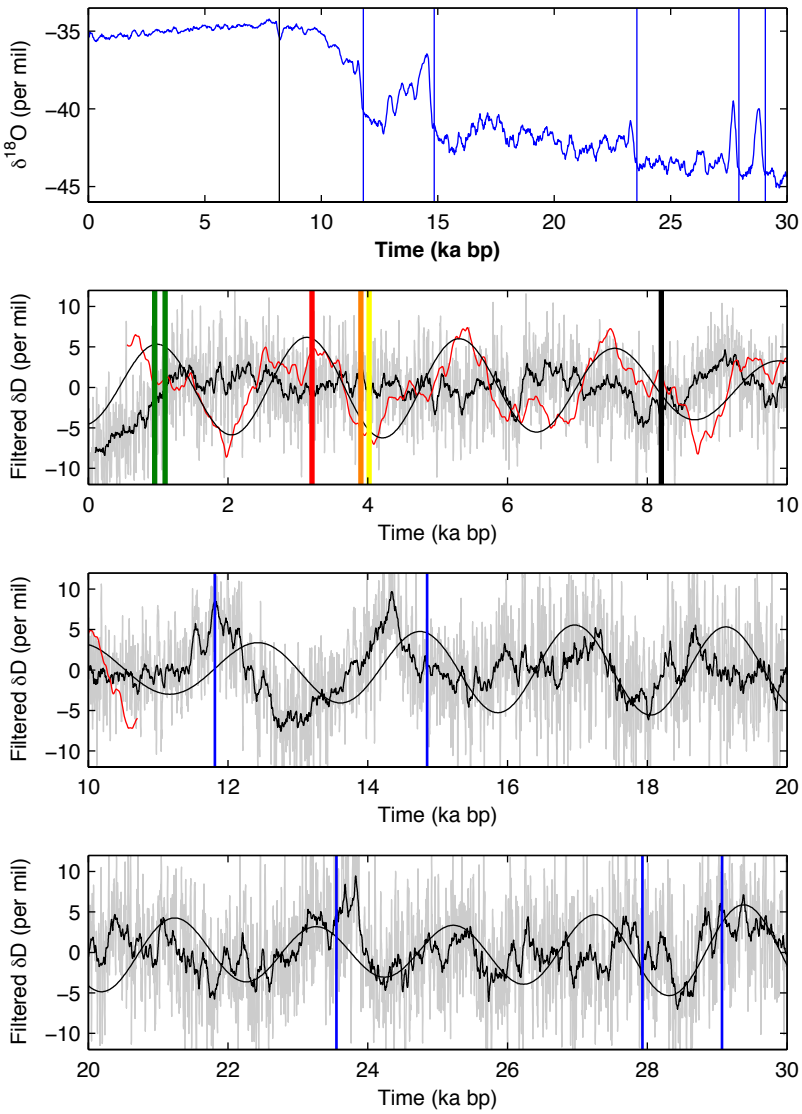

Figure 5.23. *Comparison of Greenland and Antarctic ice core records for the last 30 ka bp. (Top) The NGRIP $\delta^{18}O$ record with 10-point smooth. The vertical blue lines mark the initiation of D-O events. The vertical black line marks the 8.2 ka event. (2^{nd}, 3^{rd}, and 4^{th} from top) Band-passed WDC δD data between 15 and 4,000 years using a 2^{nd} order Butterworth filter (grey) and with 200-point smoothing applied (black). The ~2,200 year oscillation is not readily seen in this 15 and 4,000 year band-passed data, as opposed to the 15-2,000 year band-passed data shown in Figure 5.19. The red line is the inverted reconstructed ^{14}C sunspot record (Solanki et al, 2004; shown in the bottom plot of Figure 5.21). The smooth black line is an MTM reconstruction of the δD signal using 2,410, 2,214, and 2,048-year oscillations. Vertical colored lines represent collapse or decline of the Akkadian (yellow), Harrapan (orange), Bronze Age (red), and Mayan (green) civilizations (which appear to align with maxima and minima in the ^{14}C sunspot record). The vertical blue lines mark the initiation of D-O events in the NGRIP record. The vertical black line marks the 8.2 ka event.*

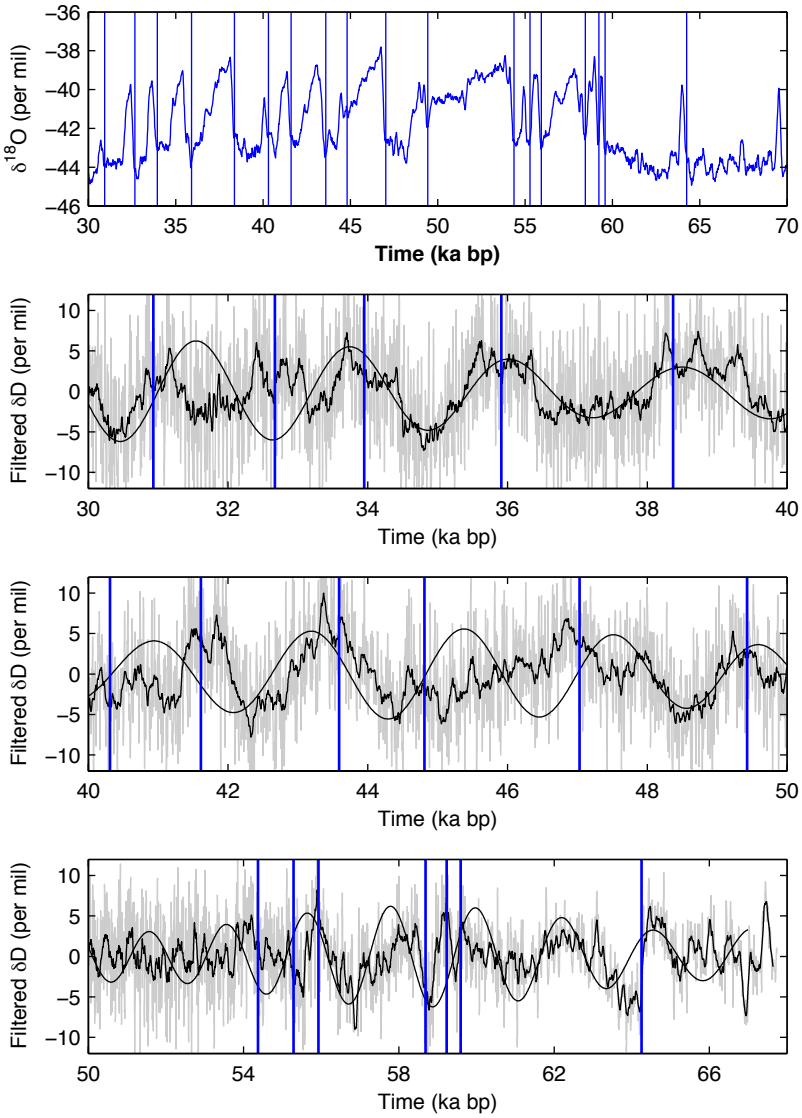

Figure 5.24. *Comparison of Greenland and Antarctic ice core records for between 30-68 ka bp. (Top) The NGRIP $\delta^{18}O$ record with 10-point smooth. The vertical blue lines mark the initiation of D-O events. (2^{nd}, 3^{rd}, and 4^{th} from top) Band-passed WDC δD data between 15 and 4,000 years using a 2^{nd} order Butterworth filter (grey) and with 200-point smoothing applied (black). The smooth black line is an MTM reconstruction of the δD signal using 2,410, 2,214, and 2,048-year oscillations. The vertical blue lines mark the initiation of D-O events in the NGRIP record.*

For the last 68 ka bp, δD_{sun} sometimes approximates δD_{bp4k}, and other times are uncorrelated. For example, δD_{sun} and δD_{bp4k} tend to match from ~33-40 and ~56-63 ka bp, as well as shorter time periods like 48-50 ka bp. When the initiation of D-O events is considered (i.e. when Greenland begins to warm abruptly, as expressed in the NGRIP record; hereafter D-O_{init}), there is no general pattern relative to δD_{sun}. Certain D-O_{init} occur at or near δD_{sun} maxima, including events at 14.85, 23.55, 29.07, 33.95, 35.91, 38.37, 43.59, 49.43, 55.29, 55.93, 59.59, and 64.25 ka bp (12/23 total). A few D-O_{init} events occur at or near a δD_{sun} minima, including 32.67, 54.37, 58.69, and 59.23 ka bp (4/23 total). The rest of the D-O_{init} fall somewhere in the middle (7/23 total). In the Holocene, the 8.2 ka event[44] occurs at a mid-point of δD_{sun}. There can be a number of interpretations of these results: 1) There is considerable uncertainty in extending the reconstructed δD_{sun} record backwards in time, simply because the sun may not always behave the same way, or there may be larger spikes in solar activity than δD_{sun} would suggest, which could cause unknown threshold events. Therefore, we should not expect to find a connection between δD_{sun} and D-O_{init}, even though a connection could exist. 2) Although there may be uncertainty, the reconstruction of δD_{sun} matches the sunspot record for the last 11.4 ka bp, and may generally capture solar variability further back in time. Using δD_{sun}, 53% of D-O_{init} events fall near δD_{sun} maxima, 30% occur somewhere near a mid-point between max and min, and 17% occur near δD_{sun} minima. Based on these results, there appears to be no direct mechanism for D-O events related to solar activity. 3) Although speculative, it is possible that solar activity does result in abrupt

[44] The 8.2 ka event was a centuries long cooling imprinted most strongly in Northern Hemisphere climate proxies. The event was likely caused by a meltwater pulse into the North Atlantic that altered the TOC.

climate changes, perhaps through a series of feedbacks that cause a shift in the jet stream. In this case, we may be incorrectly estimating $\delta D_{sun,}$ and a solution to the problem may not be possible.

5.3.10. Expression of D-O Events in Antarctica

During the glacial, the initiation of an abrupt warming in Greenland corresponds to the beginning of Antarctica cooling (EPICA Community Members, 2006). This interhemispheric connection is related to the allocation of heat between hemispheres (bipolar see saw; Broecker, 1998). In the WDC δD record, filtered δD_{bp4k} maxima correspond to D-O_{init}. Essentially, the δD_{bp4k} maxima correspond to Antarctic Isotope Maxima (AIM) events (i.e. the point just before cooling initiates in Antarctica). However, there are a number of locations where δD_{bp4k} maxima have no companion D-O event, including 17.33, 18.70, 25.43, 26.30, and 62.23 ka bp. This gives rise to the question: Why do D-O events only occur at certain peaks, but not at others? It could be possible that D-O events are triggered by an oscillator (such as solar variability or oceanic processes), but that the trigger might not always work. Modeling and investigations of other proxies in the ice core record may provide clues as to why these companionless δD_{bp4k} maxima occur.

A similar method for viewing low frequency variability in the WDC record is to use a series of filters. The boxcar is essentially an averaging window of a certain length that preserves variability at the edges. We use a 4,000 year boxcar filter to determine a long-term δD average, and then subtract that average from the original δD record. This

centers variability on a zero mean line. We then filter again using three boxcar filters of 80 years in length (equivalent to a pseudo-Gaussian or haystack smooth). This boxcar approach isolates the dominant millennial scale variability in the δD record, which is different than band-pass filtering or spectral reconstruction, which isolates only certain frequencies.

Using the boxcar method (hereafter δD_{boxcar}), maximum and minimum values can be identified throughout the record, except for the last 6 ka bp and from 65-68 ka bp; these sections are too difficult to pick. We plot the difference in δD_{boxcar} maxima or minima in Figure 5.25. The variability in the difference between maximum and minimum values is in the range of 500 years to 4,500 years. The mean value for both is 2,200 years. This is the same value as that seen in 15-2,000 year band-pass filtering and spectral analysis. Most maximum δD_{boxcar} maxima correspond to a D-O_{init} event. Except, similar to the results seen in δD_{bp4k}, there are instances of peak Antarctic warming at ~20.38 and ~18.66 ka bp, as well as less pronounced peak warming at ~17.24 and 15.95 ka bp, that have no companion D-O_{init} event. There are other max δD_{boxcar} events with no corresponding D-O_{init} (e.g. ~51.08 ka bp), but the peaks are too small, so we do not include them. For comparison, δD_{bp4k} exhibited peak variability with no coincident D-O_{init} event at ~17.33, 18.70, 25.43, 26.30, and 62.23 ka bp. Common values between these two methods (i.e. ~17.3 and 18.7) would be a useful starting point to investigate other proxy records (i.e. dust, deuterium excess, etc.) to determine why D-O events did not occur. This may hold important clues as to why D-O events occur at other times.

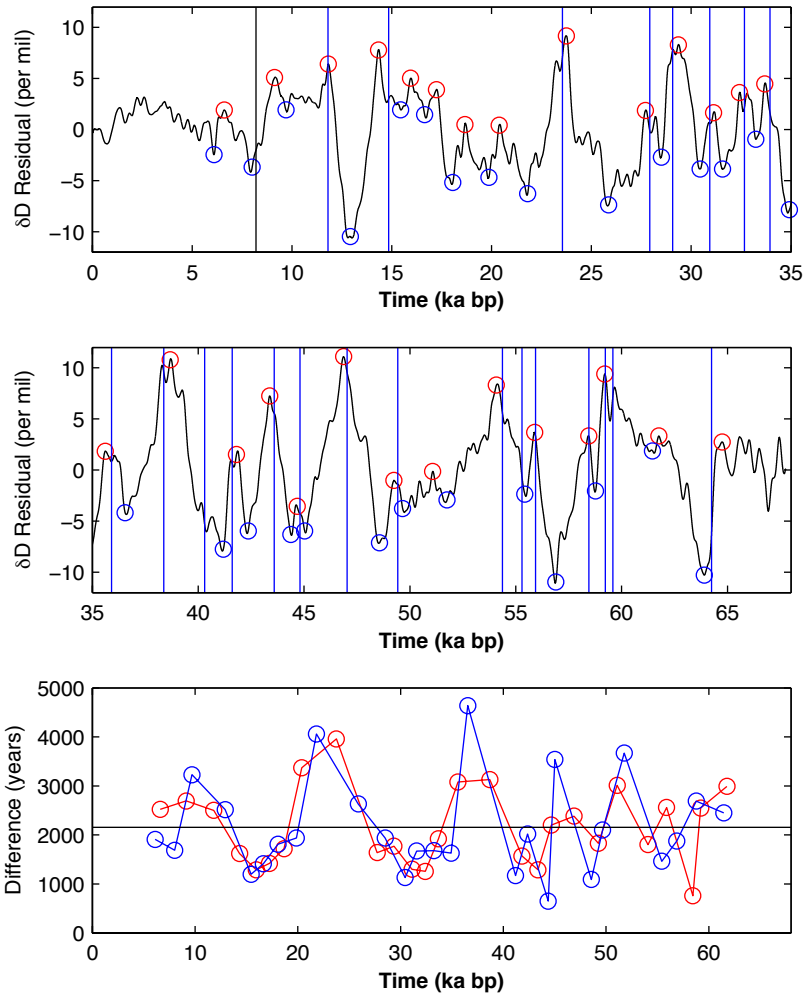

Figure 5.25. *(Top) Filtered WDC δD data using a boxcar smoothing approach from 0-35 ka bp. First, a 4,000 year boxcar filter is applied to the δD data to determine a long-term average, which is then subtracted from the original δD record. This centers variability in the δD record on a zero mean line and removes the glacial-interglacial variability. Then, the residual data is filtered again using three boxcar filters of 80 years in length (equivalent to a pseudo-Gaussian or haystack smooth). The vertical blue lines mark the initiation of D-O events in the NGRIP record. The black line at 8.2 ka bp is the 8.2 ka event. Red circles are local maxima, and blue circles are local minima. (Middle) Same as the top plot, except from 35-68 ka bp. (Bottom) The difference in adjacent maxima (red) or minima (blue) values in the boxcar filtered WDC data, plotted in time at the most recent of the two values. The black line is the mean value of the differences, which is 2,153 years for both the maxima and minima.*

5.3.11. Civilization Collapse

Recent collapse of civilizations tends to occur at maxima or minima in the ^{14}C sunspot reconstruction, which we have also shown to be reproducible in WDC water isotopes. (Figure 5.23). Cullen et al. (2000) document an abrupt increase in wind-blown dust related to Mesopotamian aridity around 4,025 ± 125 yr bp in a marine sediment core from the Gulf of Oman. The dust event lasted for ~300 years, and coincided with the collapse of the Akkadian empire at 4,170 ± 150 yr bp. Glosan et al. (2012) document a decline in monsoon and westerly source precipitation in northern and eastern India (the Indo-Gangetic Plain) beginning 5.0 yr bp, eventually reaching a low point at 4.0 ka bp. A significant decline in the Harrapan civilization began at 3.9 ka bp, coincided with the low point in precipitation. Kaniewski, et al. (2013) document the onset of a ~300 year drought at 3.2 ka bp using pollen records from coastal Cyprus and coastal Syria. The drought coincided with socio-economic difficulties, mainly in agricultural, that may have led to the decline of the Hittite, Egyptian, Canaanite and Mycenean civilizations (Bronze Age Civilizations). Finally, Hodell et al. (2005) document drought conditions from ~770–870 AD (early phase) and ~920–1100 AD (late phase) in Mexico using sediment cores from Lake Chichancanab. The droughts coincide with the collapse of the Mayan civilization.

Each of these civilization collapses may (or may not) result from solar activity that fundamentally changes atmospheric circulation patterns on Earth. In the Holocene, these changes (of solar origin or otherwise) are most evident in drought proxies and archeological evidence, but do not appear in Greenland ice core records. In the glacial period, abrupt climate change is plainly evident in Greenland ice cores, and appears in varying patterns in many other global climate proxy records. Is it possible that the same

mechanisms that forced glacial abrupt climate change continue to operate in the Holocene? The boundary conditions are certainly different – the glacial period had much larger ice sheets and a generally more 'extreme' climate (e.g. Dansgaard et al., 1993) – whereas the Holocene is regarded as a 'calm' time period. Some studies have already suggested that an underlying mechanism spans the glacial-interglacial time periods (Bond et al, 2001), but there are still more questions than answers. Somewhere in the data, the answer is probably waiting.

In the preceding five sections, we have investigated a potential solar trigger mechanism for D-O events in Greenland that coincide with a reconstruction of ~2.4, 2.2, and 2.0 kyr oscillations in the WAIS Divide ice core water isotope record. Two of the oscillations (~2.2 and 2.0 kyr) match atmospheric radiocarbon (^{14}C) records (Solanki et al., 2004), while the third oscillation has been suggested to originate from solar inertial motion related to the large planets in our solar system (~2.4 kyr; Charvátová, 2000 and Charvátová and Hejda, 2013). It is plausible that changes in sunspots can dramatically affect climate (similar to that seen during the Little Ice Age in relation to the Maunder Minimum), causing abrupt shifts in atmospheric circulation (possibly related to the jet stream). An abrupt change such as this would be in agreement with Steffensen et al. (2008) who concluded that atmospheric circulation changes (based on dxs measurements) are the probable initiation mechanism of D-O events, rather than changes in sea ice or ocean circulation. However, because the Earth system has powerful forcing and/or feedback mechanisms of its own, a solar trigger could fail or be delayed in certain instances. Or, abrupt change may be related solely to reverberations in the climate system from internal noise. Modeling and additional proxy comparisons are necessary to advance

or reject causes for abrupt climate change. We have outlined one possible avenue for future research: Why do some instances of peak millennial warming in Antarctica not correspond to D-O events in Greenland ice cores?

5.4. Conclusions

Water isotopes in ice cores are proxies for local temperature and regional atmospheric circulation. High-frequency signals in the ice core must be interpreted with caution because diffusional processes have altered the original signal. In the WAIS Divide ice core (WDC), diffusion has mainly affected high-frequency oscillations at four years and less. The one-year signal is essentially lost around 16 ka bp. The two-year signal is nearly lost around 17 ka bp, while three and four-year signals show some attenuation at 17 ka bp as well. Oscillations greater than or equal to five-years show no significant attenuation due to diffusion.

In terms of atmospheric circulation, the Pacific Sector of West Antarctica (where WDC is located) is partially affected by tropical El Niño-Southern Oscillation (ENSO) teleconnections. More so, West Antarctica is affected by the Southern Annular Mode, which itself is modulated by ENSO. The ENSO teleconnection and SAM influence is not straightforward and non-stationary. We find that December-January-February and January-February-March averages of the water isotope record are moderately correlated with SAM, while the yearly record at monthly resolution is weakly correlated with Niño34 sea surface temperatures. Ultimately, the water isotope record appears to be partially influenced by ENSO, more strongly related to the SAM, and dominated by local

and regional processes that are difficult to define. Therefore, the WDC water isotope record should be thought of as an integrator of south Pacific climate patterns, and as the Antarctic expression of ENSO-scale oscillations.

To interpret high-frequency oscillations in the WDC water isotope record (δ), we use two back-diffusion techniques: 1) Deconvolution of the annual water isotope signal during the Holocene, and 2) Correction of 2 to 15 year spectral power over the last 29 ka bp. In the Holocene, the annual maximum summer and seasonal δ signals trend with maximum summer insolation at around 50-60° south. Millennial variability is superimposed on these trends. Conversely, ENSO-scale variability (2 to 15 years) shows no Holocene trend, while variability in the glacial is elevated and noisier. Two GCM studies offer conflicting theories as to the source of this variability: either in the tropical Pacific Ocean or the Southern Ocean.

Low-frequency oscillations (15 to 125 years) are also stronger in the glacial period. The cause of these 15 to 125 year oscillations is likely related to variations in solar forcing at timescales of 11, 22, and ~88-year oscillations, or by long-term inertia of the oceans. At longer timescales, we observe significant millennial variability that persists over the last 68 ka. We show that a combination of ~2.4, 2.2, and 2.0 kyr oscillations that appear significantly in the WDC δD record can be used to reconstruct solar variability seen in a radiocarbon tree ring record for the last 11.4 ka bp. When the δD solar reconstruction is extended to 68 ka bp, it appears that the initiation of some D-O events in Greenland ice cores correspond to maxima in the solar curve. But, this method is highly uncertain and we cannot reliably attribute abrupt climate change to a solar trigger. However, we do find instances of millennial-scale warming in Antarctica that

have no companion D-O events. These instances may hold clues as to why D-O events form, and why they are absent in certain parts of the record.

The results of this study highlight both high and low frequency climate variability in West Antarctic for the last 68 ka bp. High-frequency information can be used as a climate change index to test future changes in West Antarctica occurring on human timescales. Low frequency information can be used as a metric for tests of Global Circulation Models (GCMs), which will increase predictive outcomes for future climate interpretation. Along similar lines, modelers and paleoclimate researchers should also begin to consider the origin of D-O events and possible discontinuities between Greenland and Antarctic ice core records.

5.5. References

Bals-Elsholz, T. M., Atallah, E. H., Bosart, L. F., Wasula, T. A., Cempa, M. J., & Lupo, A. R. (2001). The wintertime Southern Hemisphere split jet: Structure, variability, and evolution. *Journal of climate*, 14(21), 4191-4215.

Beaufort, L., de Garidel-Thoron, T., Mix, A. C., & Pisias, N. G. (2001). ENSO-like forcing on oceanic primary production during the late Pleistocene. *Science*, 293(5539), 2440-2444.

Beaufort, L., de Garidel-Thoron, T., Linsley, B., Oppo, D., & Buchet, N. (2003). Biomass burning and oceanic primary production estimates in the Sulu Sea area over the last 380 kyr and the East Asian monsoon dynamics. *Marine Geology*, 201(1), 53-65.

Berger, A. (1978). Long-term variations of daily insolation and Quaternary climatic changes. Journal of the Atmospheric Sciences, 35(12), 2362-2367.

Bertler, N. A., Naish, T. R., Oerter, H., Kipfstuhl, S., Barrett, P. J., Mayewski, P. A., & Kreutz, K. (2006). The effects of joint ENSO–Antarctic oscillation forcing on the McMurdo Dry Valleys, Antarctica. *Antarctic Science*, 18(04), 507-514.

Bond, G., Kromer, B., Beer, J., Muscheler, R., Evans, M. N., Showers, W., Hoffman,S., Lotti-Bond, R., Hajdas, G., & Bonani, G. (2001). Persistent solar influence on North Atlantic climate during the Holocene. *Science*, 294(5549), 2130-2136.

Braun, H., Christl, M., Rahmstorf, S., Ganopolski, A., Mangini, A., Kubatzki, C., Roth, K., & Kromer, B. (2005). Possible solar origin of the 1,470-year glacial climate cycle demonstrated in a coupled model. *Nature*, 438(7065), 208-211.

Broecker, W. S. "Paleocean circulation during the last deglaciation: a bipolar seesaw?." *Paleoceanography* 13.2 (1998): 119-121.

Broecker, W. S. "Does the trigger for abrupt climate change reside in the ocean or in the atmosphere?." *Science* 300.5625 (2003): 1519-1522.

Bromwich, D. H., Carrasco, J. F., Liu, Z., & Tzeng, R. Y. (1993). Hemispheric atmospheric variations and oceanographic impacts associated with katabatic surges across the Ross Ice Shelf, Antarctica. *Journal of Geophysical Research: Atmospheres* (1984–2012), 98(D7), 13045-13062.

Buizert, C., Cuffey, K. M., Severinghaus, J.P., Baggenstos, D., Fudge, T.J., Steig, E.J., Markle, B.R., Winstrup, M., Brook, E.J., Rhodes, R. H., Sowers, T.A., Clow, G. D., Cheng, H., Edwards, L.R., Sigl, M., McConnell, J. R., Taylor, K. C. (2014). The WAIS-Divide deep ice core WD2014 chronology–Part 2: Methane synchronization (68–31 ka BP) and the gas age-ice age difference. *Climate of the Past Discussions,* 10(4), 3537-3584.

Buizert, Christo, et al. (2015). Precise interhemispheric phasing of abrupt climate change during the last ice age. *Nature*. Manuscript in press.

Castagnoli, G., & Lal, D. (1980). Solar modulation effects in terrestrial production of carbon-14. *Radiocarbon*, 22(2), 133-158.

Charvátová, I. (2000). Can origin of the 2400-year cycle of solar activity be caused by solar inertial motion?. In *Annales Geophysicae* (Vol. 18, No. 4, pp. 399-405). Springer-Verlag.

Charvátová, I., & Hejda, P. (2013). Responses of the basic cycle of 178.7 and 2402 yr in solar-terrestrial phenomena during Holocene. *Pattern Recogn. Phys.*

Chiew, F. H., Piechota, T. C., Dracup, J. A., & McMahon, T. A. (1998). El Niño/Southern Oscillation and Australian rainfall, streamflow and drought: Links and potential for forecasting. *Journal of Hydrology*, 204(1), 138-149.

Ciais, P., White, J. W. C., Jouzel, J., & Petit, J. R. (1995). The origin of present‐day Antarctic precipitation from surface snow deuterium excess data. *Journal of Geophysical Research: Atmospheres* (1984–2012), 100(D9), 18917-18927.

Clark, P. U., Marshall, S. J., Clarke, G. K., Hostetler, S. W., Licciardi, J. M., & Teller, J. T. (2001). Freshwater forcing of abrupt climate change during the last glaciation. *Science*, 293(5528), 283-287.

Clemens, S. C., & Prell, W. L. (1991). One million year record of summer monsoon winds and continental aridity from the Owen Ridge (Site 722), Northwest Arabian Sea. In *Proceedings of the ocean drilling program, Scientific results* (Vol. 117, pp. 365-388).

Clemens, S. C. (2005). Millennial-band climate spectrum resolved and linked to centennial-scale solar cycles. *Quaternary Science Reviews*, 24(5), 521-531.

Clement, A. C., Cane, M. A., & Seager, R. (2001). An Orbitally Driven Tropical Source for Abrupt Climate Change*. *Journal of Climate*, 14(11), 2369-2375.

Cobb, K. M., Charles, C. D., Cheng, H., & Edwards, R. L. (2003). El Niño/Southern Oscillation and tropical Pacific climate during the last millennium. *Nature*, 424(6946), 271-276.

Cobb, K. M., Westphal, N., Sayani, H. R., Watson, J. T., Di Lorenzo, E., Cheng, H., Edwards, R. L., & Charles, C. D. (2013). Highly variable El Niño–Southern Oscillation throughout the Holocene. *Science*, 339(6115), 67-70.

Conroy, J. L., Overpeck, J. T., Cole, J. E., Shanahan, T. M., & Steinitz-Kannan, M. (2008). Holocene changes in eastern tropical Pacific climate inferred from a Galápagos lake sediment record. *Quaternary Science Reviews*, 27(11), 1166-1180.

Cullather, R. I., Bromwich, D. H., & Van Woert, M. L. (1996). Interannual variations in Antarctic precipitation related to El Niño‐Southern Oscillation. *Journal of Geophysical Research: Atmospheres* (1984–2012), 101(D14), 19109-19118.

Cullen, H. M., Hemming, S., Hemming, G., Brown, F. H., Guilderson, T., & Sirocko, F. (2000). Climate change and the collapse of the Akkadian empire: Evidence from the deep sea. *Geology*, 28(4), 379-382.

Damon, P. E., & Sonett, C. P. (1991). Solar and terrestrial components of the atmospheric C-14 variation spectrum. In *The Sun in Time* (Vol. 1, pp. 360-388).

Dansgaard, W., Johnsen, S. J., Clausen, H. B., Dahl-Jensen, D., Gundestrup, N. S., Hammer, C. U., Hvidberg, C. S., Steffensen, J. P., & Bond, G. (1993). Evidence for general instability of past climate from a 250-kyr ice-core record. *Nature*, 364(6434), 218-220.

Delaygue, G., Masson, V., Jouzel, J., Koster, R. D., & Healy, R. J. (2000). The origin of Antarctic precipitation: a modelling approach. *Tellus* B, 52(1), 19-36.

Ding, Q., Steig, E. J., Battisti, D. S., & Wallace, J. M. (2012). Influence of the tropics on the Southern Annular Mode. *Journal of Climate*, 25(18), 6330-6348.

Eddy, J. A. (1976). The maunder minimum. *Science*, 192, 1189.

Eddy, J. A. (1977). Climate and the changing sun. *Climatic Change*, 1(2), 173-190.

Eichler, T., & Higgins, W. (2006). Climatology and ENSO-related variability of North American extratropical cyclone activity. *Journal of climate*, 19(10), 2076-2093.

EPICA Community Members (2006). One-to-one coupling of glacial climate variability in Greenland and Antarctica. *Nature*, 444(7116), 195-198.

Fisher, D. A., Reeh, N., & Clausen, H. B. (1985). Stratigraphic noise in time series derived from ice cores. *Ann. Glaciol*, 7, 76-83.

Fogt, R. L., & Bromwich, D. H. (2006). Decadal variability of the ENSO teleconnection to the high-latitude South Pacific governed by coupling with the Southern Annular Mode*. *Journal of Climate*, 19(6), 979-997.

Fraedrich, K., & Müller, K. (1992). Climate anomalies in Europe associated with ENSO extremes. *International Journal of Climatology*, 12(1), 25-31.

Genthon, C., Kaspari, S., & Mayewski, P. A. (2005). Interannual variability of the surface mass balance of West Antarctica from ITASE cores and ERA40 reanalyses, 1958–2000. *Climate Dynamics*, 24(7-8), 759-770.

Giosan, L., Clift, P. D., Macklin, M. G., Fuller, D. Q., Constantinescu, S., Durcan, J. A., Stevens, T., Dullerc, G. A. T., Tabrezg A. R., Gangalh, K., Adhikarii, R., Alizaib, A., Filipe, F., VanLaningham, S. & Syvitski, J. P. (2012). Fluvial landscapes of the Harappan civilization. *Proceedings of the National Academy of Sciences*, 109(26), E1688-E1694.

Gleissberg, W. (1945). Evidence for a long solar cycle. *The Observatory*, 66, 123-125.

Graham, N. E., & Barnett, T. P. (1987). Sea surface temperature, surface wind divergence, and convection over tropical oceans. *Science*, 238(4827), 657-659.

Guo, Z., Bromwich, D. H., & Hines, K. M. (2004). Modeled Antarctic Precipitation. Part II: ENSO Modulation over West Antarctica*. *Journal of climate*, 17(3), 448-465.

Hale, G. E. (1924). The law of sun-spot polarity. *Proceedings of the National Academy of Sciences of the United States of America*, 10(1), 53.

Harangozo, S. A. (2000). A search for ENSO teleconnections in the west Antarctic Peninsula climate in austral winter. *International Journal of Climatology*, 20(6), 663-679.

Hasselmann, K. (1976). Stochastic climate models part I. Theory. *Tellus*, 28(6), 473-485.

Hemming, S. R. (2004). Heinrich events: Massive late Pleistocene detritus layers of the North Atlantic and their global climate imprint. *Reviews of Geophysics*, 42(1).

Hodell, D. A., Brenner, M., & Curtis, J. H. (2005). Terminal Classic drought in the northern Maya lowlands inferred from multiple sediment cores in Lake Chichancanab (Mexico). *Quaternary Science Reviews*, 24(12), 1413-1427.

Hood, L. L., & Jirikowic, J. L. (1990). A probable approx. 2400 year solar quasi-cycle in atmospheric delta C-14. *NASA Conference Paper* on the NASA Technical Reports Server.

Hoskins, B. J., & Karoly, D. J. (1981). The steady linear response of a spherical atmosphere to thermal and orographic forcing. *Journal of the Atmospheric Sciences*, 38(6), 1179-1196.

Hosking, J. S., Orr, A., Marshall, G. J., Turner, J., & Phillips, T. (2013). The influence of the Amundsen–Bellingshausen Seas low on the climate of West Antarctica and its representation in coupled climate model simulations. *Journal of Climate*, 26(17), 6633-6648.

Houtermans, J. C. (1971). Geophysical interpretations of bristlecone pine radiocarbon measurements using a method of Fourier analysis of unequally spaced data. *Ph.D. Thesis*, Univ. of Bern, 1971.

Huybers, P. (2006). Early Pleistocene glacial cycles and the integrated summer insolation forcing. *Science*, 313(5786), 508-511.

Huybers, P., & Denton, G. (2008). Antarctic temperature at orbital timescales controlled by local summer duration. *Nature Geoscience*, 1(11), 787-792.

Ineson, S., Scaife, A. A., Knight, J. R., Manners, J. C., Dunstone, N. J., Gray, L. J., & Haigh, J. D. (2011). Solar forcing of winter climate variability in the Northern Hemisphere. *Nature Geoscience*, 4(11), 753-757.

Johnsen, S. J. (1977). Stable isotope homogenization of polar firn and ice. *Isotopes and impurities in snow and ice*, 210-219.

Johnsen, S. J., Clausen, H. B., Cuffey, K. M., Hoffmann, G., Schwander, J., & Creyts, T. (2000). Diffusion of stable isotopes in polar firn and ice: the isotope effect in firn diffusion. *Physics of ice core records*, 159, 121-140.

Jones, T. R., White, J. W. C., & Popp, T. (2014). Siple Dome shallow ice cores: a study in coastal dome microclimatology. *Climate of the Past*, 10(3), 1253-1267.

Kaniewski, D., Van Campo, E., Guiot, J., Le Burel, S., Otto, T., & Baeteman, C. (2013). Environmental roots of the Late Bronze Age crisis. *PloS one*, 8(8), e71004.

Karoly, D. J. (1989). Southern hemisphere circulation features associated with El Niño-Southern Oscillation events. *Journal of Climate*, 2(11), 1239-1252.

Kaspari, S., Mayewski, P. A., Dixon, D. A., Spikes, V. B., Sneed, S. B., Handley, M. J., & Hamilton, G. S. (2004). Climate variability in West Antarctica derived from annual accumulation-rate records from ITASE firn/ice cores. *Annals of Glaciology*, 39(1), 585-594.

Koutavas, A., Olive, G. C., & Lynch-Stieglitz, J. (2006). Mid-Holocene El Niño–Southern Oscillation (ENSO) attenuation revealed by individual foraminifera in eastern tropical Pacific sediments. *Geology*, 34(12), 993-996.

Kreveld, S. V., Sarnthein, M., Erlenkeuser, H., Grootes, P., Jung, S., Nadeau, M. J., Pflaumann, U., & Voelker, A. (2000). Potential links between surging ice sheets, circulation changes, and the Dansgaard–Oeschger Cycles in the Irminger Sea, 60–18 Kyr. *Paleoceanography*, 15(4), 425-442.

Kutzbach J.E. & Otto-Bleisner, B. L. (1982). The sensitivity of the African- Asian monsoonal climate to orbital parameter changes for 9000 years in a low resolution general circulation model. *J. Atmos. Sci.,* 39, 1177-1188.

Lagos, P., & Buzier, J. (1992). El Niño and Peru: a nation's response to interannual climate variability. S.K. Majumdar (Ed.), *Natural and Technological Disasters: Causes, Effects, and Preventive Measures*, Pennsylvania Academy of Sciences (1992), p. 561

Lingenfelter, R. E. (1963). Production of carbon 14 by cosmic-ray neutrons. *Reviews of Geophysics*, 1(1), 35-55.

Liu, Z., Kutzbach, J., & Wu, L. (2000). Modeling climate shift of El Niño variability in the Holocene. *Geophysical Research Letters*, 27(15), 2265-2268.

Liu, Z., Otto-Bleisner, B. L., He, F., Brady, E. C., Tomas, R., Clark, P. U., Carlson, A. E., Lynch-Stieglitz, J., Curry, W., Brook, B. E., Erickson, D., Jacob, R., Kutzbach, J., & Cheng, J. (2009). Transient simulation of last deglaciation with a new mechanism for Bølling-Allerød warming. *Science*, 325(5938), 310-314.

Mann, M. E., & Lees, J. M. (1996). Robust estimation of background noise and signal detection in climatic time series. *Climatic change*, 33(3), 409-445.

Matthews, J. A., & Briffa, K. R. (2005). The 'Little Ice Age': Re-evaluation of an evolving concept. *Geografiska Annaler: Series A, Physical Geography*, 87(1), 17-36.

McGregor, H.V., M.J. Fischer, M.K. Gagan, D. Fink, S.J. Phipps, H. Wong, and C.D. Woodroffe. (2013). A weak El Niño-Southern Oscillation with delayed seasonal growth around 4,300 years ago. *Nature Geoscience* 6.11 (2013): 949-953.

Milankovitch, M. *Kanon der Erdebestrahlung und seine anwendung auf das eiszeitenproblem*. *Königlich Serbische Akademie*, 1941.

Mo, K. C., & Higgins, R. W. (1998). The Pacific-South American modes and tropical convection during the Southern Hemisphere winter. *Monthly Weather Review*, 126(6), 1581-1596.

Mo, K. C., & Paegle, J. N. (2001). The Pacific–South American modes and their downstream effects. *International Journal of Climatology*, 21(10), 1211-1229.

Morse, D. L., Blankenship, D. D., Waddington, E. D., & Neumann, T. A. (2002). A site for deep ice coring in West Antarctica: results from aerogeophysical surveys and thermo-kinematic modeling. *Annals of Glaciology*, 35(1), 36-44.

O'Brien, K. (1979). Secular variations in the production of cosmogenic isotopes in the Earth's atmosphere. *Journal of Geophysical Research: Space Physics* (1978–2012), 84(A2), 423-431.

Otto‐Bliesner, B. L., Brady, E. C., Shin, S. I., Liu, Z., & Shields, C. (2003). Modeling El Niño and its tropical teleconnections during the last glacial‐interglacial cycle. *Geophysical Research Letters*, 30(23).

Petit, J. R., White, J. W. C., Young, N. W., Jouzel, J., & Korotkevich, Y. S. (1991). Deuterium excess in recent Antarctic snow. *Journal of Geophysical Research: Atmospheres* (1984–2012), 96(D3), 5113-5122.

Pisias, N. G., & Mix, A. C. (1997). Spatial and temporal oceanographic variability of the eastern equatorial Pacific during the late Pleistocene: Evidence from radiolaria microfossils. *Paleoceanography*, 12(3), 381-393.

Rahmstorf, S. (2003). Timing of abrupt climate change: A precise clock. *Geophysical Research Letters*, 30(10).

Reijmer, C. H., Van den Broeke, M. R., & Scheele, M. P. (2002). Air Parcel Trajectories and Snowfall Related to Five Deep Drilling Locations in Antarctica Based on the ERA-15 Dataset*. *Journal of Climate*, 15(14), 1957-1968.

Rial, J. A., & Saha, R. (2011). Modeling abrupt climate change as the interaction between sea ice extent and mean ocean temperature under orbital insolation forcing. *Abrupt Climate Change: Mechanisms, Patterns, and Impacts*, 57-74.

Schwabe, M. (1849). Solar sunspot cycle of 11 years. *Astron. Nachr*, 21, 234.

Rodbell, D. T., Seltzer, G. O., Anderson, D. M., Abbott, M. B., Enfield, D. B., & Newman, J. H. (1999). An~ 15,000-year record of El Niño-driven alluviation in southwestern Ecuador. *Science*, 283(5401), 516-520.

Roe, G. (2006). In defense of Milankovitch. *Geophysical Research Letters*, 33(24).

Sandweiss, D. H., Maasch, K. A., Burger, R. L., Richardson, J. B., Rollins, H. B., & Clement, A. (2001). Variation in Holocene El Niño frequencies: Climate records and cultural consequences in ancient Peru. *Geology*, 29(7), 603-606.

Schneider, D. P., Steig, E. J., & Van Ommen, T. (2005). High-resolution ice-core stable-isotopic records from Antarctica: towards interannual climate reconstruction. *Annals of Glaciology*, 41(1), 63-70.

Shindell, D. T., Schmidt, G. A., Mann, M. E., Rind, D., & Waple, A. (2001). Solar forcing of regional climate change during the Maunder Minimum. *Science*, 294(5549), 2149-2152.

Shulmeister, J., & Lees, B. G. (1995). Pollen evidence from tropical Australia for the onset of an ENSO-dominated climate at c. 4000 BP. *The Holocene*, 5(1), 10-18.

Sigl, M., Cole-Dai, J. , Ferris, D., Fudge, T.J., McConnell, J.R., Welten, K., Winstrup, M., Woodruff, T.E., Brook, E.J., Buizert, C., Dunbar, N., Iverson, N., Koffman, B., Maselli, O.J., McGwire, K., Muscheler, R., Pasteris, D.R., Sowers Sowers, T.A. and Taylor, K. C., The WAIS-Divide deep ice core WD2014 chronology - Part 1: Annual layer counting (31-0 ka BP). *Climate of the Past Discussions* (in preparation)

SILSO, World Data Center (2015). Sunspot Number and Long-term Solar Observations, Royal Observatory of Belgium, on-line Sunspot Number catalogue: http://www.sidc.be/SILSO/, '1951-2003'

Solanki, S. K., Usoskin, I. G., Kromer, B., Schüssler, M., & Beer, J. (2004). Unusual activity of the Sun during recent decades compared to the previous 11,000 years. *Nature*, 431(7012), 1084-1087.

Souney, J. M., Twickler, M. S., Hargreaves, G. M., Bencivengo, B. M., Kippenhan, M. J., Johnson, J. A., Cravens, E. D., Neff, P. D., Nunn, R. M., Orsi, A. J., Popp, T. J., Rhoades, J. F., Vaughn, B. H., Voight, D. E., Wong, G. J., & Taylor12, K. C. (2014). Core handling and processing for the WAIS Divide ice-core project. *Annals of Glaciology*, 55, 68.

Steffensen, J. P., Andersen, K. K., Bigler, M., Clausen, H. B., Dahl-Jensen, D., Fischer, H., Goto-Azuma, K., Hansson, M., Johnsen, S. J., Jouzel, J., Masson-Delmotte, V., Popp, T., Rasmussen, S. O., Rothlisberger, R., Ruth, U., Stauffer, B., Siggaard-Andersen, M. L., Sveinbjornsdottir, A. E., Svensson, A., & White, J. W. (2008). High-resolution Greenland ice core data show abrupt climate change happens in few years. *Science*, 321(5889), 680-684.

Steig, E. J., Mayewski, P. A., Dixon, D. A., Kaspari, S. D., Frey, M. M., Schneider, D. P., Arcone, S. A., Hamilton, G. S., Spikes, V. B. Albert, M., Meese, D., Gow, A.J., Shuman, C. A., White, J. W. C., Sneed, S., Flaherty, J., & Wumkes, M. (2005). High-resolution ice cores from US ITASE (West Antarctica): Development and validation of chronologies and determination of precision and accuracy. *Annals of Glaciology*, 41(1), 77-84.

Steig, E. J., Ding, Q., White, J. W. C., Kuttel, M., Rupper, S. B., Neumann, T. A., Neff, P. D., Gallant, A. J. E., Mayewski, P. A., Taylor, K. C., Hoffmann, G., Dixon, D. A., Schoenemann, S. W., Markle, B. R., Fudge, T. J., Schneider, D. P., Schauer, A. J., Teel, R. P., Vaughn, B. H., Burgener, L., Williams, J., & Korotkikh, E. (2013), Recent climate and ice-sheet changes in West Antarctica compared with the past 2,000 years, *Nature Geoscience*, 6(5), 372–375.

Stuiver, M. (1978). Radiocarbon timescale tested against magnetic and other dating methods. *Nature*, 273(5660), 271-274.

Suess, H. E. (1980). The radiocarbon record in tree rings of the last 8000 years. *Radiocarbon*, 22(2), 200-209.

Thompson, D. W., & Wallace, J. M. (2000). Annular modes in the extratropical circulation. Part I: month-to-month variability*. *Journal of Climate*, 13(5), 1000-1016.

Torrence, C., & Compo, G. P. (1998). A practical guide to wavelet analysis. *Bulletin of the American Meteorological society*, 79(1), 61-78.

Tudhope, A. W., Chilcott, C. P., McCulloch, M. T., Cook, E. R., Chappell, J., Ellam, R. M., Lea, D. W., Lough, J. M., & Shimmield, G. B. (2001). Variability in the El Niño-Southern Oscillation through a glacial-interglacial cycle. *Science*, 291(5508), 1511-1517.

Turner, J. (2004). The El Niño–Southern Oscillation and Antarctica. *International Journal of Climatology*, 24(1), 1-31.

Turner, J., Phillips, T., Hosking, J. S., Marshall, G. J., & Orr, A. (2013). The Amundsen Sea low. *International Journal of Climatology*, 33(7), 1818-1829.

Urban, F. E., Cole, J. E., & Overpeck, J. T. (2000). Influence of mean climate change on climate variability from a 155-year tropical Pacific coral record. *Nature*, 407(6807), 989-993.

Vasiliev, S. S., & Dergachev, V. A. (2002). The~ 2400-year cycle in atmospheric radiocarbon concentration: bispectrum of 14 C data over the last 8000 years. In *Annales Geophysicae* (Vol. 20, No. 1, pp. 115-120).

WAIS Divide Project Members. (2013). Onset of deglacial warming in West Antarctica driven by local orbital forcing. *Nature*, 500(7463), 440-444.

Ward, M. N. (1998). Diagnosis and short-lead time prediction of summer rainfall in tropical North Africa at interannual and multidecadal timescales. *Journal of Climate*, 11(12), 3167-3191.

William, H. G. R., & Valdesa, P. J. (2015). On the tropical Pacific climate during the last 120 thousand years. *BRIDGE, School of Geographical Sciences, University of Bristol.* Bristol, England.

Xapsos, M. A., & Burke, E. A. (2009). Evidence of 6000-year periodicity in reconstructed sunspot numbers. *Solar Physics,* 257(2), 363-369.

Zebiak S. & Cane, M. A. (1987). Model ENSO. *Mon. Wea. Rev*., 115, 2262- 2278

Zhang, C. (1993). Large-scale variability of atmospheric deep convection in relation to sea surface temperature in the tropics. *Journal of Climate*, 6(10), 1898-1913.

Zheng, W., Braconnot, P., Guilyardi, E., Merkel, U., & Yu, Y. (2008). ENSO at 6ka and 21ka from ocean–atmosphere coupled model simulations. *Climate Dynamics*, 30(7-8), 745-762.

Chapter 6

Conclusions and Future Research

6.1. Conclusions

The WAIS divide ice core (WDC) has been a highly successful project in a long history of ice coring campaigns. The greatest benefit to the project has been new technologies that are pushing the limits of climate proxy data resolution. And, because new technology has increased the speed of measurement and allowed for simultaneous chemical analyses on a single sample of ice, the amount of data that has been recovered in a short time period is unprecedented. The result is an ice-coring project that will remain highly relevant for decades to come, and produce many unique scientific discoveries that redefine our understanding of the natural world.

To date, the WAIS Divide CFA water isotope record is the highest-resolution and longest-continuous ice core record that includes data from the Last Glacial Period. It provides a snapshot of West Antarctic climate - as well as information about regional and global climate - for the last 68,000 years. We have undertaken a number of diffusion corrections to make the water isotope record interpretable at timescales ranging from years to millennia. Overall, we hope that the information presented in this dissertation

significantly contributes to the scientific process of continual discovery. More so, we hope that it brings us closer to solving certain outstanding climatic mysteries: variability in the El Niño Southern oscillation and the cause of abrupt climate change.

6.2. Dissertation Summary

In this dissertation, five chapters have been presented discussing high-resolution water isotope records from West Antarctic ice cores. Chapter 1 is an overview of climate change at both human and longer-time scales, as well as the physical and chemical basis for water isotope analysis in polar ice cores. Chapter 2 discusses the recent climatology of Siple Dome, West Antarctica using a north-to-south transect of shallow ice cores. The Dome exhibits a strong microclimate effect that increases the complexity of local, regional, and teleconnected climate signal interpretation. Chapter 3 presents a continuous flow analysis (CFA) system for measurement of water isotopes in ice cores. The CFA system was used to analyze the entire WAIS Divide ice core (WDC) from surface to bedrock. Chapter 4 presents an analysis of diffusional processes that have occurred in the water isotope record in combination with glaciological modeling. Specifically, the effects of accumulation, temperature, strain, and impurities on water isotope diffusion are tested; ultimately resulting in a diffusion length record that characterizes the attenuation of high-frequency oscillations in the water isotope record. In Chapter 5, diffusion lengths are used to deconvolve the annual water isotope record and back diffuse ENSO-scale oscillations (2-15 years) dating to 29 ka bp. We then interpret low frequency oscillations (>15 years) in the water isotope record dating to 68 ka bp. At millennial timescales, a

significant solar signal is imprinted in the water isotope record, prompting an investigation of solar variability as a trigger mechanism for abrupt climate change. There appears to be regularity in the millennial-scale oscillations not previously discussed in Greenland ice cores, and this may hold important clues about Dansgaard-Oeschger events.

6.2.1. Accomplishments

A number of scientific publications have resulted from my work as a PhD student. The research presented in Chapter 2 resulted in a first-author publication in the peer-reviewed journal *Climate of the Past*:

Jones, T. R., White, J. W. C., & Popp, T. (2014). Siple Dome shallow ice cores: a study in coastal dome microclimatology. *Climate of the Past*, 10(3), 1253-1267.

Additional research and collaboration outside of this dissertation has also resulted in two co-authored papers, both in *Nature*:

Dahl-Jensen, D., Albert, M. R., Aldahan, A., Azuma, N., Balslev-Clausen, D., Baumgartner, M., ... & Kjaer, H. A. (2013). Eemian interglacial reconstructed from a Greenland folded ice core. *Nature*, 493(7433), 489-494.

Buizert, Christo, et al. (2015). Precise interhemispheric phasing of abrupt climate change during the last ice age. *Nature*. Manuscript in press.

Additionally, Chapters 3, 4, and 5 are being prepared for publication and may undergo

changes before submission to peer-reviewed journals.

Beyond publications, I participated in two ice core field seasons for the North Greenland Eemian Ice Drilling (NEEM) project, two summers at the National Ice Core Lab (NICL) processing the West Antarctic Ice Sheet Ice Core (WDC), and one summer analyzing the WDC water isotope record at the Institute of Arctic and Alpine Research. In the classroom, I spent two semesters teaching at the University of Colorado as an instructor-of-record. First, I co-taught "*Climate Change: Science and Expression through Video-Production and Presentation"*, followed by a class of my own design titled, "*Environmental Monitoring in an Era of Global Change: Historical, physical, and societal perspectives."* The culmination of my teaching experience has resulted in a Certificate in College Teaching (CCT) from the Graduate Teacher Program (GTP). Through coursework, I have also received a Certificate in Hydrological Sciences.

6.3. Future Research

6.3.1. Diffusion of Water Isotopes

There are a number of logical extensions of the research contained in this dissertation. In Chapter 4, we concluded that solid diffusion has played a discernible role in the attenuation of the water isotope signal at WAIS Divide. The exact mechanism for the excess diffusion in solid ice is unclear, but the effects of impurities likely play an important role. When we compared destrained diffusion lengths[45] with the calcium (Ca^{+}) record, the two records appear correlated (i.e. when Ca^{+} is high, there is more diffusion,

[45] Destrained diffusion lengths show the average movement of a water molecule from its original position in the vertical direction, with the effects of strain removed.

and vice versa). Previous research has shown impurities like Ca^{+} concentrate on grain boundaries and within intergranular veins in deep ice. More impurities can produce wider grain boundaries and bigger veins, enhancing diffusion (Dash and Wettlaufer, 1995; Wettlaufer, 1999; Dash et al., 2006). The impurity effect may also be temperature dependent. A useful follow up study to the results in Chapter 4 is to implement an impurity enabled diffusion model, as described by Rempel and Wettlaufer (2003).

Along similar lines, we would like to explore differences in the behavior of $\delta^{18}O$ and δD. Specifically, Johnsen et al. (2000) showed that the differential diffusion lengths of $\delta^{18}O$ and δD should be temperature dependent in the firn column. Our results show that differential diffusion is 4% less than Johnsen predicts at the base of firn, and the results spanning the last 29 ka bp do not appear to approximate the temperature record. This requires further refinement of our methods to test other possible contributing factors to differential diffusion values, such as the effects of solid ice diffusion driven by impurities. Research along these lines is being performed in Copenhagen, Denmark at the Centre for Ice and Climate and may be a useful avenue for future collaborations.

6.3.2. ENSO-scale Climate Modeling

In Chapter 5, we concluded that ENSO-scale oscillations (2-15 years) in the WDC water isotope record show no trend in the Holocene and elevated amplitude in the glacial. We showed two Global Circulation Models (GCMs) with conflicting explanatory mechanisms. One GCM suggests that enhanced high frequencies in the glacial originate in the Southern Ocean (south Pacific sector). A second GCM suggests that the pattern

originates in the tropics and is directly related to the size of the ice sheets. Neither model considers non-linear teleconnection mechanisms from tropics to poles nor is water isotope enabled. To understand the paleo-ENSO system, it would be useful to determine how and why high-frequency water isotope amplitudes are elevated in West Antarctica during the glacial. It may be that both Antarctica and the tropical Pacific have increased ENSO-scale activity, or only one of the locations shows enhanced activity. Explorations of this subject will require further collaboration with modelers at the National Center for Atmospheric Research (NCAR) and the University of Bristol.

One drawback to the interpretation of models is that climate models and water isotopes in ice cores speak a different language. Climate models output parameters like temperature and wind stress – simple and straightforward. Conversely, water isotopes are dependent on many processes like local temperature, regional atmospheric circulation, and diffusion – complex and often non-linear. The climate-modeling group at the University of Southern California (USC) is looking to bridge the "language" barrier between modeling and geologic proxies by developing forward models that incorporate physical, chemical, and biological processes to generate modeled geologic proxies. Basically, the researchers are attempting to translate coding language into a geologic language to improve modeling results. Results from the WDC ice core can provide a testing framework for forward modeling.

6.3.3. Solar Variability

Solar activity has been recorded for centuries. In the 17th and 18th centuries, sunspot numbers were recorded from visual observations using rudimentary telescopes. As time has passed, improved technology has aided the detection of sunspots, culminating with 21st-century technology using satellite instrumentation. Some solar cycles are plainly evident, like the 11-year solar cycle. But, other longer cycles have only become evident in radiocarbon (^{14}C) proxy records in tree rings, which are modulated by solar activity. An 11,400 year ^{14}C record from Solanki et al. (2004), for example, reveals significant centennial and millennial scale solar variability.

A number of studies have discussed millennial solar variability. A ~2,400-year primary solar cycle has been seen in multiple tree ring records. A ~2,200, ~2,000, and ~1,500-year cycle also appear, likely occurring as heterodyne frequencies from the combination of lesser oscillations. These same frequencies appear significantly in the WDC water isotope record, and in Chapter 5, we use the frequencies to reconstruct the Solanki et al. (2000) radiocarbon record for the last 11,400 years. These solar variations sometimes appear to have a connection to abrupt climate change in Greenland, but other times show no correlation.

The cause of the ~2,400-year period has been suggested to be related to the modulation of the motion of the sun around the center of mass of the solar system by the giant planets (Jupiter, Saturn, Uranus, and Neptune; Charvátová, 2000). Since the cycle is at least partially predictable, it would be useful to work with an astrophysicist to determine if a longer-term reconstruction of solar variability can be accomplished. Furthermore, an algorithm for testing which combinations of frequencies found in the

WDC water isotope record best reconstruct millennial-scale variability in the ^{14}C record may improve our results for comparison to abrupt climate change.

6.3.4. Abrupt Climate Change

In Chapter 5, we identified peak millennial warming events in Antarctica (Antarctic Isotope Maxima events; AIM events) that correspond to the initiation of abrupt warming events (Dansgaard-Oeschger events; D-O events) in Greenland. However, there are some peak warming events in Antarctic that have no companion D-O event. We speculate that these occurrences may hold clues as to why certain D-O events are triggered, and why others fail to trigger. A useful line of research into these "non-conforming" events would be to test the timing and magnitude of other ice core proxy records: deuterium excess, annual layer thicknesses, insoluble dust, soluble sodium (Na^{+}), and soluble calcium (Ca^{2+}). For example, if an elevated dust signal leads the initiation of all AIM events, but does not lead the non-conforming events, then the origin of the dust signal (usually mid-latitude deserts) might point to sub-polar processes as the pre-cursor to D-O events. This research would require collaboration with other Principal Investigators (PIs) on the WAIS Divide Project, specifically at the Desert Research Institute (DRI), the University of Washington, Oregon State University, and others.

6.3.5. Deuterium Excess

An important aspect of water isotope records is the second order parameter deuterium excess (dxs). In ice cores, dxs is a proxy for sea surface temperature (SST) at the moisture source to an ice core site. Variations in Antarctic dxs can be interpreted as a change in SST at the source location or a change in the actual source location. Analyzing high-frequency changes in the dxs data set would provide a useful compliment to high-frequency δD data. In Chapter 5, we concluded that frequencies in the 2-15 year range (ENSO-scale oscillations) are enhanced in the glacial period compared to the Holocene. However, it is not clear if the enhanced signal is a result of polar or tropical climatic processes. Dxs can be used to improve our understanding of this problem. If, for example, dxs shows similar elevated ENSO-scale amplitudes in the glacial as $\delta^{18}O$ and δD, then we might be able to conclude that mid-to-high latitude oceanic variability is the main forcing. Conversely, if dxs amplitudes are not elevated in the glacial, we might be able to conclude that δD forcing is a low latitude signal or a very localized signal. Or, the dxs signal could express a change in the moisture source location, which can complicate the interpretation. These results would depend on the assumed source of moisture to the WAIS Divide ice core, which is thought to be derived mostly from mid-to-high latitude locations.

A similar line of reasoning holds with low-frequency oscillations. Does dxs exhibit millennial-scale solar variability, and if so, how does it compare with the δD signal? Are there leads or lags in the ocean-atmosphere system that can be identified between the variable behavior of δD and dxs? What do the differences in signals mean for the interpretation of abrupt climate change? This analysis would add another

constraint to investigations concerning the trigger mechanism of Dansgaard-Oeschger events in Greenland.

Currently, the dxs record is undergoing post-processing to correct for spectral shifts in the Cavity Ring-Down Spectroscopy (CRDS) Picarro instrument during analysis. These shifts are correctable, but take time to identify. In terms of the dxs signal, we showed in Chapter 3 that the uncertainty of dxs on the Continuous Flow Analysis (CFA) system was 0.55 per mil over a dynamic range of ~7 per mil. The uncertainty of dxs is reported from the measurement of seven Greenland test ice sticks. For comparison, traditional IRMS measurements of dxs are typically reported with uncertainties of ~1.28 per mil. Based on these results, we feel confident the WDC dxs record will be a highly useful paleoclimate proxy.

6.4. Final Remarks

The entirety of my PhD has been a grand adventure. At times, the learning curve has been steep, but I have had the support of colleagues and friends along the way. For those who helped me, I will always be grateful.

I think there is one quote that sums up the entirety of my research best:

"If there is magic on this planet, it is contained in water."
--- Loren Eiseley

I have been lucky to document and study the hydrological cycle.

6.5. References

Alley, R. B., Marotzke, J., Nordhaus, W. D., Overpeck, J. T., Peteet, D. M., Pielke, R. A., Pierrehumbert, R. T., Rhines, P. B., Stocker, T. F., Talley, L. D., & Wallace, J. M. (2003). Abrupt climate change. *Science*, 299(5615), 2005-2010.

Charvátová, I. (2000). Can origin of the 2400-year cycle of solar activity be caused by solar inertial motion?. In *Annales Geophysicae* (Vol. 18, No. 4, pp. 399-405). Springer-Verlag.

Dash, J. G., Fu, H., & Wettlaufer, J. S. (1995). The premelting of ice and its environmental consequences. *Reports on Progress in Physics*, 58(1), 115.

Dash, J. G., Rempel, A. W., & Wettlaufer, J. S. (2006). The physics of premelted ice and its geophysical consequences. *Reviews of modern physics*, 78(3), 695.

Johnsen, S. J., Clausen, H. B., Cuffey, K. M., Hoffmann, G., Schwander, J., & Creyts, T. (2000). Diffusion of stable isotopes in polar firn and ice: the isotope effect in firn diffusion. *Physics of ice core records*, 159, 121-140.

Rempel, A. W., & Wettlaufer, J. S. (2003). Isotopic diffusion in polycrystalline ice. *Journal of Glaciology*, *49*(166), 397-406.

Solanki, S. K., Usoskin, I. G., Kromer, B., Schüssler, M., & Beer, J. (2004). Unusual activity of the Sun during recent decades compared to the previous 11,000 years. *Nature*, 431(7012), 1084-1087.

Wettlaufer, J. S. (1999). Impurity effects in the premelting of ice. *Physical Review Letters*, 82(12), 2516.

Complete Bibliography

Albert, M. R., Shultz, E. F., & Perron, F. E. (2000). Snow and firn permeability at Siple Dome, Antarctica. *Annals of Glaciology*, 31(1), 353-356.

Albert, M. R., & Shultz, E. F. (2002). Snow and firn properties and air–snow transport processes at Summit, Greenland. *Atmospheric Environment*, *36*(15), 2789-2797.

Allan, D. W. (1966). Statistics of atomic frequency standards. *Proceedings of the IEEE*, 54(2), 221-230.

Alley, R. B. (1987). Firn densification by grain-boundary sliding: a first model. Le *Journal de Physique Colloques*, 48(C1), C1-249.

Alley, R. B. (2000). The Younger Dryas cold interval as viewed from central Greenland. *Quaternary Science Reviews*, 19(1), 213-226.

Alley, R. B., Marotzke, J., Nordhaus, W. D., Overpeck, J. T., Peteet, D. M., Pielke, R. A., Pierrehumbert, R. T., Rhines, P. B., Stocker, T. F., Talley, L. D., & Wallace, J. M. (2003). Abrupt climate change. *Science*, 299(5615), 2005-2010.

Alley, R. (2003) Visible Stratigraphic Dating, Siple Dome and Upstream C Cores. *National Snow and Ice Data Center*, Boulder, Colorado USA, http://www.nsidc.org

Altabet, M. A., Higginson, M. J., & Murray, D. W. (2002). The effect of millennial-scale changes in Arabian Sea denitrification on atmospheric CO_2. *Nature*, *415*(6868), 159-162.

Antón, S. C. (2003). Natural history of Homo erectus. *American journal of physical anthropology*, 122(S37), 126-170.

Arfken, G. (1985). Discrete Orthogonality--Discrete Fourier Transform. (1985). *§14.6 in Mathematical Methods for Physicists*, 3rd ed. Orlando, FL: Academic Press, pp. 787-792.

Axtell, R. L., Epstein, J. M., Dean, J. S., Gumerman, G. J., Swedlund, A. C., Harburger, J., Chakravarty, S., Hammond, R., Parker, J., & Parker, M. (2002). Population growth and collapse in a multiagent model of the Kayenta Anasazi in Long House Valley. *Proceedings of the National Academy of Sciences of the United States of America,* 99(Suppl 3), 7275-7279.

Azzalini, A., & Dalla Valle, A. (1996). The multivariate skew-normal distribution. Biometrika, 83(4), 715-726.

Bals-Elsholz, T. M., Atallah, E. H., Bosart, L. F., Wasula, T. A., Cempa, M. J., & Lupo, A. R. (2001). The wintertime Southern Hemisphere split jet: Structure, variability, and evolution. *Journal of climate*, 14(21), 4191-4215.

Battle, M. O., Severinghaus, J. P., Sofen, E. D., Plotkin, D., Orsi, A. J., Aydin, M., Montzka, S. A., Sowers, T., & Tans, P. P. (2011). Controls on the movement and composition of firn air at the West Antarctic Ice Sheet Divide. *Atmospheric Chemistry and Physics*, 11(21), 11007-11021.

Beaufort, L., de Garidel-Thoron, T., Mix, A. C., & Pisias, N. G. (2001). ENSO-like forcing on oceanic primary production during the late Pleistocene. *Science*, 293(5539), 2440-2444.

Beaufort, L., de Garidel-Thoron, T., Linsley, B., Oppo, D., & Buchet, N. (2003). Biomass burning and oceanic primary production estimates in the Sulu Sea area over the last 380 kyr and the East Asian monsoon dynamics. *Marine Geology*, 201(1), 53-65.

Berger, A. (1978). Long-term variations of daily insolation and Quaternary climatic changes. Journal of the Atmospheric Sciences, 35(12), 2362-2367.

Bertler, N. A., Barrett, P. J., Mayewski, P. A., Fogt, R. L., Kreutz, K. J., & Shulmeister, J. (2004). El Niño suppresses Antarctic warming. *Geophysical Research Letters*, 31(15).

Bertler, N. A. N., Naish, T. R., Mayewski, P. A., & Barrett, P. J. (2006). Opposing oceanic and atmospheric ENSO influences on the Ross Sea Region, Antarctica. *Advances in Geosciences*, 6, 83-86.

Bertler, N. A., Naish, T. R., Oerter, H., Kipfstuhl, S., Barrett, P. J., Mayewski, P. A., & Kreutz, K. (2006). The effects of joint ENSO–Antarctic oscillation forcing on the McMurdo Dry Valleys, Antarctica. *Antarctic Science*, 18(04), 507-514.

Bigeleisen, J., Perlman, M. L., & Prosser, H. C. (1952). Conversion of hydrogenic materials to hydrogen for isotopic analysis. *Analytical Chemistry*, 24(8), 1356-1357.

Blunier, T., Chappellaz, J., Schwander, J., Dällenbach, A., Stauffer, B., Stocker, T. F., Raynaud, D., Jouzel, J., Clausen, H. B., Hammer, C. U., & Johnsen S. J. (1998). Asynchrony of Antarctic and Greenland climate change during the last glacial period. *Nature*, 394(6695), 739-743.

Blunier, T., & Brook, E. J. (2001). Timing of millennial-scale climate change in Antarctica and Greenland during the last glacial period. *Science*, *291*(5501), 109-112.

Bond, G. C. (1968). Catalysis by metals. *Annu. Rep. Prog. Chem., Sect. A. Gen. Phys and Inorg. Chem.,* 65, 121-128.

Bond, G. C., and R. Lotti (1995), Iceberg discharges into the North Atlantic on millennial time scales during the last glaciation, *Science*, 267, 1005–1010.

Bond, G., Kromer, B., Beer, J., Muscheler, R., Evans, M. N., Showers, W., Hoffman,S., Lotti-Bond, R., Hajdas, G., & Bonani, G. (2001). Persistent solar influence on North Atlantic climate during the Holocene. *Science*, 294(5549), 2130-2136.

Brand, W. A., Geilmann, H., Crosson, E. R., & Rella, C. W. (2009). Cavity ring‐down spectroscopy versus high‐temperature conversion isotope ratio mass spectrometry; a case study on δ^2H and $\delta^{18}O$ of pure water samples and alcohol/water mixtures. *Rapid Communications in Mass Spectrometry*, 23(12), 1879-1884.

Braun, H., Christl, M., Rahmstorf, S., Ganopolski, A., Mangini, A., Kubatzki, C., Roth, K., & Kromer, B. (2005). Possible solar origin of the 1,470-year glacial climate cycle demonstrated in a coupled model. *Nature*, 438(7065), 208-211.

Broecker, W. S. (1998). Paleocean circulation during the last deglaciation: a bipolar seesaw?. *Paleoceanography*, 13(2), 119-121.

Broecker, W. S. (2003). Does the trigger for abrupt climate change reside in the ocean or in the atmosphere?. *Science*, 300(5625), 1519-1522.

Broecker, W. S. (2006). Abrupt climate change revisited. Global and Planetary Change, 54(3), 211-215.

Bromwich, D. H. (1988). Snowfall in high southern latitudes. *Reviews of Geophysics,* 26(1), 149-168.

Bromwich, D. H., Rogers, A. N., Kållberg, P., Cullather, R. I., White, J. W., & Kreutz, K. J. (2000). ECMWF Analyses and Reanalyses Depiction of ENSO Signal in Antarctic Precipitation*. *Journal of Climate*, 13(8), 1406-1420.

Bromwich, D. H., Monaghan, A. J., & Guo, Z. (2004). Modeling the ENSO Modulation of Antarctic Climate in the Late 1990s with the Polar MM5*. *Journal of climate*, 17(1), 109-132.

Bromwich, D. H., Carrasco, J. F., Liu, Z., & Tzeng, R. Y. (1993). Hemispheric atmospheric variations and oceanographic impacts associated with katabatic surges across the Ross Ice Shelf, Antarctica. *Journal of Geophysical Research: Atmospheres* (1984–2012), 98(D7), 13045-13062.

Buizert, C., Cuffey, K. M., Severinghaus, J.P., Baggenstos, D., Fudge, T.J., Steig, E.J., Markle, B.R., Winstrup, M., Brook, E.J., Rhodes, R. H., Sowers, T.A., Clow, G. D., Cheng, H., Edwards, L.R., Sigl, M., McConnell, J. R., Taylor, K. C. (2014). The WAIS-Divide deep ice core WD2014 chronology–Part 2: Methane synchronization (68–31 ka BP) and the gas age-ice age difference. *Climate of the Past Discussions,* 10(4), 3537-3584.

Buizert, Christo, et al. (2015). Precise interhemispheric phasing of abrupt climate change during the last ice age. *Nature*. Manuscript in press.

Cacho, I., Grimalt, J. O., Pelejero, C., Canals, M., Sierro, F. J., Flores, J. A., & Shackleton, N. (1999). Dansgaard‐Oeschger and Heinrich event imprints in Alboran Sea paleotemperatures. *Paleoceanography*, 14(6), 698-705.

Carleton, A. M. (2003). Atmospheric teleconnections involving the Southern Ocean. *Journal of Geophysical Research: Oceans* (1978–2012), 108(C4).

Castagnoli, G., & Lal, D. (1980). Solar modulation effects in terrestrial production of carbon-14. *Radiocarbon*, 22(2), 133-158.

Charvátová, I. (2000). Can origin of the 2400-year cycle of solar activity be caused by solar inertial motion?. In *Annales Geophysicae* (Vol. 18, No. 4, pp. 399-405). Springer-Verlag.

Charvátová, I., & Hejda, P. (2013). Responses of the basic cycle of 178.7 and 2402 yr in solar-terrestrial phenomena during Holocene. *Pattern Recogn. Phys.*

Chiang, J. C., Biasutti, M., & Battisti, D. S. (2003). Sensitivity of the Atlantic intertropical convergence zone to last glacial maximum boundary conditions. *Paleoceanography*, 18(4).

Chiew, F. H., Piechota, T. C., Dracup, J. A., & McMahon, T. A. (1998). El Niño/Southern Oscillation and Australian rainfall, streamflow and drought: Links and potential for forecasting. *Journal of Hydrology*, 204(1), 138-149.

Ciais, P., White, J. W. C., Jouzel, J., & Petit, J. R. (1995). The origin of present‐day Antarctic precipitation from surface snow deuterium excess data. *Journal of Geophysical Research: Atmospheres* (1984–2012), 100(D9), 18917-18927.

Clark, I. & Fritz, P. (1997). *Environmental isotopes in Hydrogeology*. Lewis Publishers. New York.

Clark, P. U., Marshall, S. J., Clarke, G. K., Hostetler, S. W., Licciardi, J. M., & Teller, J. T. (2001). Freshwater forcing of abrupt climate change during the last glaciation. *Science*, 293(5528), 283-287.

Clemens, S. C., & Prell, W. L. (1991). One million year record of summer monsoon winds and continental aridity from the Owen Ridge (Site 722), Northwest Arabian Sea. In *Proceedings of the ocean drilling program, Scientific results* (Vol. 117, pp. 365-388).

Clemens, S. C. (2005). Millennial-band climate spectrum resolved and linked to centennial-scale solar cycles. *Quaternary Science Reviews*, 24(5), 521-531.

Clement, A. C., Cane, M. A., & Seager, R. (2001). An Orbitally Driven Tropical Source for Abrupt Climate Change*. *Journal of Climate*, *14*(11), 2369-2375.

Clow, G. (1996) Siple Dome Shallow Ice Core Borehole Measurements. *National Snow and Ice Data Center*, Boulder, Colorado USA. http://www.nsidc.org

Cobb, K. M., Charles, C. D., Cheng, H., & Edwards, R. L. (2003). El Niño/Southern Oscillation and tropical Pacific climate during the last millennium. *Nature*, 424(6946), 271-276.

Cobb, K. M., Westphal, N., Sayani, H. R., Watson, J. T., Di Lorenzo, E., Cheng, H., Edwards, R. L., & Charles, C. D. (2013). Highly variable El Niño–Southern Oscillation throughout the Holocene. *Science*, 339(6115), 67-70.

Coleman, M. L., Shepherd, T. J., Durham, J. J., Rouse, J. E., & Moore, G. R. (1982). Reduction of water with zinc for hydrogen isotope analysis. *Analytical Chemistry*, 54(6), 993-995.

Conroy, J. L., Overpeck, J. T., Cole, J. E., Shanahan, T. M., & Steinitz-Kannan, M. (2008). Holocene changes in eastern tropical Pacific climate inferred from a Galápagos lake sediment record. *Quaternary Science Reviews*, 27(11), 1166-1180.

Cooley, J. W. and Tukey, O. W. (1965). An Algorithm for the Machine Calculation of Complex Fourier Series. *Math. Comput.* 19, 297-301.

Coplen, T. B., Wildman, J. D., & Chen, J. (1991). Improvements in the gaseous hydrogen-water equilibration technique for hydrogen isotope-ratio analysis. *Analytical Chemistry*, 63(9), 910-912.

Craig, H. (1961). Isotopic variations in meteoric waters. *Science*, (133), 1702-3.

Craig, H., Gordon, L. I., & Horibe, Y. (1963). Isotopic exchange effects in the evaporation of water: 1. Low-temperature experimental results. *Journal of Geophysical Research*, 68(17), 5079-5087.

Cuffey, K. M., & Steig, E. J. (1998). Isotopic diffusion in polar firn: implications for interpretation of seasonal climate parameters in ice-core records, with emphasis on central Greenland. *Journal of Glaciology*, *44*(147), 273-284.

Cuffey, K. M., & Paterson, W. S. B. (2010). *The physics of glaciers*. Academic Press.

Cuffey, K. M., personal communication, Layer tracking from a temperature-strain model for the WAIS Divide ice core. November, 2013.

Cullather, R. I., Bromwich, D. H., & Van Woert, M. L. (1996). Interannual variations in Antarctic precipitation related to El Niño–Southern Oscillation. *Journal of Geophysical Research: Atmospheres* (1984–2012), 101(D14), 19109-19118.

Cullen, H. M., Hemming, S., Hemming, G., Brown, F. H., Guilderson, T., & Sirocko, F. (2000). Climate change and the collapse of the Akkadian empire: Evidence from the deep sea. *Geology*, 28(4), 379-382.

Damon, P. E., & Sonett, C. P. (1991). Solar and terrestrial components of the atmospheric C-14 variation spectrum. In *The Sun in Time* (Vol. 1, pp. 360-388).

Dansgaard, W. (1964). Stable isotopes in precipitation. *Tellus*, 16(4), 436-468.

Dansgaard, W., & Johnsen, S. J. (1969). A flow model and a time scale for the ice core from Camp Century, Greenland. *Journal of Glaciology*, *8*, 215-223.

Dansgaard, W., Johnsen, S. J., Clausen, H. B., Dahl-Jensen, D., Gundestrup, N. S., Hammer, C. U., Hvidberg, C. S., Steffensen, J. P., & Bond, G. (1993). Evidence for general instability of past climate from a 250-kyr ice-core record. *Nature*, 364(6434), 218-220.

Dansgaard, W. (2005). Frozen Annals – Greenland Icecap Research. Neils Bohr Institute, *Narayana Press*, Odder, Denmark, www.narayanapress.dk. ISBN: 87-990078-0-0. 124 p.

Dash, J. G., Fu, H., & Wettlaufer, J. S. (1995). The premelting of ice and its environmental consequences. *Reports on Progress in Physics*, 58(1), 115.

Dash, J. G., Rempel, A. W., & Wettlaufer, J. S. (2006). The physics of premelted ice and its geophysical consequences. *Reviews of modern physics*, 78(3), 695.

Delaygue, G., Masson, V., Jouzel, J., Koster, R. D., & Healy, R. J. (2000). The origin of Antarctic precipitation: a modelling approach. *Tellus* B, 52(1), 19-36.

Delibaltas, P., Dengel, O., Helmreich, D., Riehl, N., & Simon, H. (1966). Diffusion von18O in Eis-Einkristallen. *Physik der kondensierten Materie*, 5(3), 166-170.

de Menocal, P. B. 2001. Cultural responses to climate change during the late Holocene. *Science* 292:667–73.

Diaz, H. F., Hoerling, M. P., & Eischeid, J. K. (2001). ENSO variability, teleconnections and climate change. *International Journal of Climatology*, 21(15), 1845-1862.

Ding, Q., Steig, E. J., Battisti, D. S., & Wallace, J. M. (2012). Influence of the tropics on the Southern Annular Mode. *Journal of Climate*, 25(18), 6330-6348.

Dunbar, R. B., Wellington, G. M., Colgan, M. W., & Glynn, P. W. (1994). Eastern Pacific sea surface temperature since 1600 AD: The δ18O record of climate variability in Galápagos corals. *Paleoceanography*, 9(2), 291-315.

Eberle, J. J., Fricke, H. C., Humphrey, J. D., Hackett, L., Newbrey, M. G., & Hutchison, J. H. (2010). Seasonal variability in Arctic temperatures during early Eocene time. *Earth and Planetary Science Letters*, 296(3), 481-486.

Eddy, J. A. (1976). The maunder minimum. *Science*, 192, 1189.

Eddy, J. A. (1977). Climate and the changing sun. *Climatic Change*, 1(2), 173-190.

Eichler, T., & Higgins, W. (2006). Climatology and ENSO-related variability of North American extratropical cyclone activity. *Journal of climate*, 19(10), 2076-2093.

Ekaykin, A. A., Lipenkov, V. Y., Barkov, N. I., Petit, J. R., & Masson-Delmotte, V. (2002). Spatial and temporal variability in isotope composition of recent snow in the vicinity of Vostok station, Antarctica: implications for ice-core record interpretation. *Annals of Glaciology*, 35(1), 181-186.

EPICA Community Members (2006). One-to-one coupling of glacial climate variability in Greenland and Antarctica. *Nature*, 444(7116), 195-198.

Epstein, S., & Mayeda, T. (1953). Variation of O 18 content of waters from natural sources. *Geochimica et cosmochimica acta*, 4(5), 213-224.

Epstein, S., Buchsbaum, R., Lowenstam, H. A., & Urey, H. C. (1953). Revised carbonate-water isotopic temperature scale. *Geological Society of America Bulletin*, 64(11), 1315-1326.

Fabre, A., Barnola, J. M., Arnaud, L., & Chappellaz, J. (2000). Determination of gas diffusivity in polar firn: comparison between experimental measurements and inverse modeling. *Geophysical research letters*, 27(4), 557-560.

Fisher, D. A., Reeh, N., & Clausen, H. B. (1985). Stratigraphic noise in time series derived from ice cores. *Ann. Glaciol*, 7, 76-83.

Fogt, R. L., & Bromwich, D. H. (2006). Decadal variability of the ENSO teleconnection to the high-latitude South Pacific governed by coupling with the Southern Annular Mode*. *Journal of Climate*, 19(6), 979-997.

Fraedrich, K., & Müller, K. (1992). Climate anomalies in Europe associated with ENSO extremes. *International Journal of Climatology*, 12(1), 25-31.

Freitag, J., Wilhelms, F., & Kipfstuhl, S. (2004). Microstructure-dependent densification of polar firn derived from X-ray microtomography. *Journal of Glaciology*, 50(169), 243-250.

Frezzotti, M., Urbini, S., Proposito, M., Scarchilli, C., & Gandolfi, S. (2007). Spatial and temporal variability of surface mass balance near Talos Dome, East Antarctica. *Journal of Geophysical Research: Earth Surface* (2003–2012), 112(F2).

Geiger, G. H., & Poirier, D. R. (1973). Transport phenomena in metallurgy. Addison-Wesley Publishing Co., Reading, Mass. 1973, 616 p.

Genthon, C., Kaspari, S., & Mayewski, P. A. (2005). Interannual variability of the surface mass balance of West Antarctica from ITASE cores and ERA40 reanalyses, 1958–2000. *Climate Dynamics*, 24(7-8), 759-770.

Ghil, M., Allen, M. R., Dettinger, M. D., Ide, K., Kondrashov, D., Mann, M. E., ... & Yiou, P. (2002). Advanced spectral methods for climatic time series. *Reviews of geophysics*, 40(1), 3-1.

Gill, R. B. *The great Maya droughts: water, life, and death*. UNM Press, 2001.

Giosan, L., Clift, P. D., Macklin, M. G., Fuller, D. Q., Constantinescu, S., Durcan, J. A., Stevens, T., Dullerc, G. A. T., Tabrezg A. R., Gangalh, K., Adhikarii, R., Alizaib, A., Filipe, F., VanLaningham, S. & Syvitski, J. P. (2012). Fluvial landscapes of the Harappan civilization. *Proceedings of the National Academy of Sciences*, 109(26), E1688-E1694.

Gkinis, V., Popp, T.J., Blunier, T., Bigler, M., Schupbach, S., Kettner, E., Johnsen, S.J. (2011). Water isotopic ratios from a continuously melted ice core sample. *Atmos. Meas. Tech*. 4, 2531–2542.

Gkinis, V., Popp, T. J., Johnsen, S. J., & Blunier, T. (2010). A continuous stream flash evaporator for the calibration of an IR cavity ring-down spectrometer for the isotopic analysis of water. *Isotopes in environmental and health studies*, 46(4), 463-475.

Gleissberg, W. (1945). Evidence for a long solar cycle. *The Observatory*, 66, 123-125.

Graham, N. E., & Barnett, T. P. (1987). Sea surface temperature, surface wind divergence, and convection over tropical oceans. *Science*, 238(4827), 657-659.

Gregory, S., & Noone, D. (2008). Variability in the teleconnection between the El Niño–Southern Oscillation and West Antarctic climate deduced from West Antarctic ice core isotope records. *Journal of Geophysical Research: Atmospheres* (1984–2012), 113(D17).

Gregory, S. A., Albert, M. R., & Baker, I. (2014). Impact of physical properties and accumulation rate on pore close-off in layered firn. *The Cryosphere*, 8(1), 91-105.

Grew, K. E., & Ibbs, T. L. (1952). Thermal diffusion in gases. *Cambridge University Press*.

Grimm, E. C., Jacobson Jr, G. L., Watts, W. A., Hansen, B. C., & Maasch, K. A. (1993). A 50,000-Year Record of Climate Oscillations from Florida and its Temporal Correlation. *Science*, 261(5118), 198-200.

Grinsted, A., Moore, J. C., & Jevrejeva, S. (2004). Application of the cross wavelet transform and wavelet coherence to geophysical time series. *Nonlinear processes in geophysics*, 11(5/6), 561-566.

Guo, Z., Bromwich, D. H., & Hines, K. M. (2004). Modeled Antarctic Precipitation. Part II: ENSO Modulation over West Antarctica*. *Journal of climate*, 17(3), 448-465.

Gupta, P., Noone, D., Galewsky, J., Sweeney, C., & Vaughn, B. H. (2009). Demonstration of high‐precision continuous measurements of water vapor isotopologues in laboratory and remote field deployments using wavelength‐scanned cavity ring‐down spectroscopy (WS‐CRDS) technology. *Rapid communications in mass spectrometry*, 23(16), 2534-2542.

Hale, G. E. (1924). The law of sun-spot polarity. *Proceedings of the National Academy of Sciences of the United States of America*, 10(1), 53.

Hall, W. D., & Pruppacher, H. R. (1976). The survival of ice particles falling from cirrus clouds in subsaturated air. *Journal of the Atmospheric Sciences*, *33*(10), 1995-2006.

Hamilton, G. S. (2002). Mass balance and accumulation rate across Siple Dome, West Antarctica. *Annals of Glaciology*, 35(1), 102-106.

Harangozo, S. A. (2000). A search for ENSO teleconnections in the west Antarctic Peninsula climate in austral winter. *International Journal of Climatology*, 20(6), 663-679.

Hasselmann, K. (1976). Stochastic climate models part I. Theory. *Tellus*, 28(6), 473-485.

Hemming, S. R. (2004). Heinrich events: Massive late Pleistocene detritus layers of the North Atlantic and their global climate imprint. *Reviews of Geophysics*, 42(1).

Hendricks, M. B., D. J. DePaolo, and R. C. Cohen (2000), Space and time variation of δ18O and δD in precipitation: Can paleotemperature be estimated from ice cores?, *Global Biogeochem. Cycles,* 14(3), 851–861

Herron, M. M., & Langway Jr, C. C. (1980). Firn densification: an empirical model. *Journal of Glaciology*, 25, 373-385.

Hodell, D. A., Curtis, J. H., & Brenner, M. (1995). Possible role of climate in the collapse of Classic Maya civilization. *Nature*, *375*(6530), 391-394.

Hodell, D. A., Brenner, M., & Curtis, J. H. (2005). Terminal Classic drought in the northern Maya lowlands inferred from multiple sediment cores in Lake Chichancanab (Mexico). *Quaternary Science Reviews*, 24(12), 1413-1427.

Hoffman, P. F., & Schrag, D. P. (2000). Snowball earth. *Scientific American*, *282*(1), 68-75.

Hood, L. L., & Jirikowic, J. L. (1990). A probable approx. 2400 year solar quasi-cycle in atmospheric delta C-14. *NASA Conference Paper* on the NASA Technical Reports Server.

Hosking, J. S., Orr, A., Marshall, G. J., Turner, J., & Phillips, T. (2013). The influence of the Amundsen–Bellingshausen Seas low on the climate of West Antarctica and its representation in coupled climate model simulations. *Journal of Climate*, 26(17), 6633-6648.

Hoskins, B. J., & Karoly, D. J. (1981). The steady linear response of a spherical atmosphere to thermal and orographic forcing. *Journal of the Atmospheric Sciences*, 38(6), 1179-1196.

Hörhold, M. W., Laepple, T., Freitag, J., Bigler, M., Fischer, H., & Kipfstuhl, S. (2012). On the impact of impurities on the densification of polar firn. *Earth and Planetary Science Letters,* 325, 93-99.

Houtermans, J. C. (1971). Geophysical interpretations of bristlecone pine radiocarbon measurements using a method of Fourier analysis of unequally spaced data. *Ph.D. Thesis*, Univ. of Bern, 1971.

Huybers, P. (2006). Early Pleistocene glacial cycles and the integrated summer insolation forcing. *Science*, 313(5786), 508-511.

Huybers, P., & Denton, G. (2008). Antarctic temperature at orbital timescales controlled by local summer duration. *Nature Geoscience*, 1(11), 787-792.

Huber, C., & Leuenberger, M. (2003). Fast high‐precision on‐line determination of hydrogen isotope ratios of water or ice by continuous‐flow isotope ratio mass spectrometry. *Rapid communications in mass spectrometry*, 17(12), 1319-1325.

Ineson, S., Scaife, A. A., Knight, J. R., Manners, J. C., Dunstone, N. J., Gray, L. J., & Haigh, J. D. (2011). Solar forcing of winter climate variability in the Northern Hemisphere. *Nature Geoscience*, 4(11), 753-757.

IPCC, 2013: Climate Change 2013: *The Physical Science Basis. Contribution of Working Group I to the Fifth Assessment Report of the Intergovernmental Panel on Climate Change* [Stocker, T.F., D. Qin, G.-K. Plattner, M. Tignor, S.K. Allen, J. Boschung, A. Nauels, Y. Xia, V. Bex and P.M. Midgley (eds.)]. Cambridge University Press, Cambridge, United Kingdom and New York, NY, USA, 1535 pp.

Itagaki, K. (1967). Self-diffusion in single crystal ice. *Journal of the Physical Society of Japan*, *22*(2), 427-431.

Jacobel, R.W., Dorsey, C. W., and Harner, A. M. (1994). Ice velocities near a relict flow feature on Siple Dome. *Antarctic Journal of the United States*, XXIX, 62—66.

Johnsen, S. J., Dansgaard, W., & White, J. W. C. (1989). The origin of Arctic precipitation under present and glacial conditions. *Tellus B*, *41*(4), 452-468.

Johnsen, S. J. (1977). Stable isotope homogenization of polar firn and ice. *Isotopes and impurities in snow and ice*, 210-219.

Johnsen, S. J., Clausen, H. B., Cuffey, K. M., Hoffmann, G., Schwander, J., & Creyts, T. (2000). Diffusion of stable isotopes in polar firn and ice: the isotope effect in firn diffusion. *Physics of ice core records*, 159, 121-140.

Johnsen, S. J., Dahl‐Jensen, D., Gundestrup, N., Steffensen, J. P., Clausen, H. B., Miller, H., Masson-Delmotte, V., Sveinbjörnsdottir, A. E., & White, J. (2001). Oxygen isotope and palaeotemperature records from six Greenland ice‐core stations: Camp Century, Dye‐3, GRIP, GISP2, Renland and NorthGRIP. *Journal of Quaternary Science*, 16(4), 299-307.

Johnson, J. A., Mason, W. P., Shturmakov, A. J., Haman, S. T., Sendelbach, P. J., Mortensen, N. B., Laurent, J. A., & Dahnert, K. R. (2007). A new 122 mm electromechanical drill for deep ice-sheet coring (DISC): 5. Experience during Greenland field testing. *Annals of Glaciology*, 47(1), 54-60.

Jones, T. R., White, J. W. C., & Popp, T. (2014). Siple Dome shallow ice cores: a study in coastal dome microclimatology. *Climate of the Past*, 10(3), 1253-1267.

Joughin, I., Smith, B. E., & Medley, B. (2014). Marine Ice Sheet Collapse Potentially Under Way for the Thwaites Glacier Basin, West Antarctica. *Science*, *344*(6185), 735-738.

Jouzel, J., & Merlivat, L. (1984). Deuterium and oxygen 18 in precipitation: Modeling of the isotopic effects during snow formation. *Journal of Geophysical Research: Atmospheres (1984–2012)*, *89*(D7), 11749-11757.

Jouzel, J., Vimeux, F., Caillon, N., Delaygue, G., Hoffmann, G., Masson‐Delmotte, V., & Parrenin, F. (2003). Magnitude of isotope/temperature scaling for interpretation of central Antarctic ice cores. *Journal of Geophysical Research: Atmospheres* (1984–2012), 108(D12).

Jouzel, J., Alley, R. B., Cuffey, K. M., Dansgaard, W., Grootes, P., Hoffmann, G., Johnsen, S. J., Koster, R. D., Peel, D., Shuman, A., Stievenard, M., Stuiver, M., & White, J. (1997). Validity of the temperature reconstruction from water isotopes in ice cores. J*ournal of Geophysical Research: Oceans* (1978–2012), 102(C12), 26471-26487.

Jouzel, J., Vimeux, F., Caillon, N., Delaygue, G., Hoffmann, G., Masson‐Delmotte, V., & Parrenin, F. (2003). Magnitude of isotope/temperature scaling for interpretation of central Antarctic ice cores. *Journal of Geophysical Research: Atmospheres* (1984–2012), 108(D12).

Kaniewski, D., Van Campo, E., Guiot, J., Le Burel, S., Otto, T., & Baeteman, C. (2013). Environmental roots of the Late Bronze Age crisis. *PloS one*, 8(8), e71004.

Karoly, D. J. (1989). Southern hemisphere circulation features associated with El Niño-Southern Oscillation events. *Journal of Climate*, 2(11), 1239-1252.

Kaspari, S., Mayewski, P. A., Dixon, D. A., Spikes, V. B., Sneed, S. B., Handley, M. J., & Hamilton, G. S. (2004). Climate variability in West Antarctica derived from annual accumulation-rate records from ITASE firn/ice cores. *Annals of Glaciology*, 39(1), 585-594.

Kavanaugh, J. L., & Cuffey, K. M. (2003). Space and time variation of δ18O and δD in Antarctic precipitation revisited. *Global Biogeochemical Cycles*, *17*(1).

Kerstel, E. T., Van Trigt, R., Reuss, J., & Meijer, H. A. J. (1999). Simultaneous determination of the 2H/1H, 17O/16O, and 18O/16O isotope abundance ratios in water by means of laser spectrometry. *Analytical chemistry*, 71(23), 5297-5303.

Koutavas, A., Olive, G. C., & Lynch-Stieglitz, J. (2006). Mid-Holocene El Niño–Southern Oscillation (ENSO) attenuation revealed by individual foraminifera in eastern tropical Pacific sediments. *Geology*, 34(12), 993-996.

Kreutz, K. J., Mayewski, P. A., Pittalwala, I. I., Meeker, L. D., Twickler, M. S., & Whitlow, S. I. (2000). Sea level pressure variability in the Amundsen Sea region inferred from a West Antarctic glaciochemical record. *Journal of Geophysical Research: Atmospheres* (1984–2012), 105(D3), 4047-4059.

Kreveld, S. V., Sarnthein, M., Erlenkeuser, H., Grootes, P., Jung, S., Nadeau, M. J., Pflaumann, U., & Voelker, A. (2000). Potential links between surging ice sheets, circulation changes, and the Dansgaard‐Oeschger Cycles in the Irminger Sea, 60–18 Kyr. *Paleoceanography*, 15(4), 425-442.

Kutzbach J.E. & Otto-Bleisner, B. L. (1982). The sensitivity of the African- Asian monsoonal climate to orbital parameter changes for 9000 years in a low resolution general circulation model. *J. Atmos. Sci.,* 39, 1177-1188.

Lagos, P., & Buzier, J. (1992). El Niño and Peru: a nation's response to interannual climate variability. S.K. Majumdar (Ed.), *Natural and Technological Disasters: Causes, Effects, and Preventive Measures*, Pennsylvania Academy of Sciences (1992), p. 561

Lamorey, G. W. (2003) Siple Shallow Core Density Data. *National Snow and Ice Data Center*, Boulder, Colorado USA, http://www.nsidc.org

Landais, A., Barnola, J. M., Masson‐Delmotte, V., Jouzel, J., Chappellaz, J., Caillon, N., Huber, C., Leuenberger, M., & Johnsen, S. J. (2004). A continuous record of temperature evolution over a sequence of Dansgaard‐Oeschger events during Marine Isotopic Stage 4 (76 to 62 kyr BP). *Geophysical Research Letters*, 31(22).

Lingenfelter, R. E. (1963). Production of carbon 14 by cosmic‐ray neutrons. *Reviews of Geophysics*, 1(1), 35-55.

Lis, G., Wassenaar, L. I., & Hendry, M. J. (2008). High-precision laser spectroscopy D/H and 18O/16O measurements of microliter natural water samples. *Analytical Chemistry*, 80(1), 287-293.

Liu, Z., Kutzbach, J., & Wu, L. (2000). Modeling climate shift of El Niño variability in the Holocene. *Geophysical Research Letters*, 27(15), 2265-2268.

Liu, Z., Otto-Bleisner, B. L., He, F., Brady, E. C., Tomas, R., Clark, P. U., Carlson, A. E., Lynch-Stieglitz, J., Curry, W., Brook, B. E., Erickson, D., Jacob, R., Kutzbach, J., & Cheng, J. (2009). Transient simulation of last deglaciation with a new mechanism for Bølling-Allerød warming. *Science*, 325(5938), 310-314.

Majoube, M. (1970). Fractionation factor of 18O between water vapour and ice.

Mann, M. E., & Lees, J. M. (1996). Robust estimation of background noise and signal detection in climatic time series. *Climatic change*, 33(3), 409-445.

Maselli, O. J., Fritzsche, D., Layman, L., McConnell, J. R., & Meyer, H. (2013). Comparison of water isotope-ratio determinations using two cavity ring-down instruments and classical mass spectrometry in continuous ice-core analysis. *Isotopes in environmental and health studies*, 49(3), 387-398.

Masson-Delmotte, V., Hou, S., Ekaykin A., Jouzel J., Aristarain A., R. T. Bernardo, D. Bromwich, O. Cattani, M. Delmotte, S. Falourd, M. Frezzotti, H. Gallée, L. Genoni, E. Isaksson, A. Landais, M. M. Helsen, G. Hoffmann, J. Lopez, V. Morgan, H. Motoyama, D. Noone, H. Oerter, J. R. Petit, A. Royer, R. Uemura, G. A. Schmidt, E. Schlosser, J. C. Simões, E. J. Steig, B. Stenni, M. Stievenard, M. R. van den Broeke, R. S. W. van de Wal, W. J. van de Berg, F. Vimeux, and J. W. C. White (2008). A review of Antarctic surface snow isotopic composition: Observations, atmospheric circulation, and isotopic modeling*. *Journal of Climate*, 21(13), 3359-3387.

Matthews, J. A., & Briffa, K. R. (2005). The 'Little Ice Age': Re‐evaluation of an evolving concept. *Geografiska Annaler: Series A, Physical Geography*, 87(1), 17-36.

McGregor, H.V., M.J. Fischer, M.K. Gagan, D. Fink, S.J. Phipps, H. Wong, and C.D. Woodroffe. (2013). A weak El Niño-Southern Oscillation with delayed seasonal growth around 4,300 years ago. *Nature Geoscience* 6.11 (2013): 949-953.

Merlivat, L., & Nief, G. (1967). Isotopic fractionation of solid-vapor and liquid-vapor changes of state of water at temperatures below 0◦ C. *Tellus*, *19*, 122-127.

Merlivat, L., & Jouzel, J. (1979). Global climatic interpretation of the deuterium‐oxygen 18 relationship for precipitation. *Journal of Geophysical Research: Oceans (1978–2012)*, *84*(C8), 5029-5033.

Meyerson, E. A., Mayewski, P. A., Kreutz, K. J., Meeker, L. D., Whitlow, S. I., & Twickler, M. S. (2002). The polar expression of ENSO and sea-ice variability as recorded in a South Pole ice core. *Annals of Glaciology*, 35(1), 430-436.

Milankovitch, M. *Kanon der Erdebestrahlung und seine anwendung auf das eiszeitenproblem*. *Königlich Serbische Akademie*, 1941.

Mo, K. C., & Higgins, R. W. (1998). The Pacific-South American modes and tropical convection during the Southern Hemisphere winter. *Monthly Weather Review*, 126(6), 1581-1596.

Mo, K. C., & Paegle, J. N. (2001). The Pacific–South American modes and their downstream effects. *International Journal of Climatology*, 21(10), 1211-1229.

Mook, W. (2000). Environmental Isotopes in the Hydrological Cycle. IHP-V Technical Documents in Hydrology No. 39. *UNESCO/IAEA*: Paris/Vienna.

Moritz, C., & Agudo, R. (2013). The future of species under climate change: resilience or decline?. *Science*, *341*(6145), 504-508.

Morse, D. L., Blankenship, D. D., Waddington, E. D., & Neumann, T. A. (2002). A site for deep ice coring in West Antarctica: results from aerogeophysical surveys and thermo-kinematic modeling. *Annals of Glaciology*, 35(1), 36-44.

Motta, R., & White, J. W. C. "A Tale of Two Cities: Miami, New York & Life on the Edge." *Climate Central*. Climate Central, 22 August 2014. Web. 05 January 2015. <http://www.climatecentral.org/news/sea-level-rise-miami-new-york-17925>.

Nereson, N. A., Raymond, C. F., Waddington, E. D., & Jacobel, R. W. (1998). Migration of the Siple Dome ice divide, West Antarctica. *Journal of Glaciology*, 44(148), 643-652.

Nereson, N. A., Raymond, C. F., Jacobel, R. W., & Waddington, E. D. (2000). The accumulation pattern across Siple Dome, West Antarctica, inferred from radar-detected internal layers. *Journal of Glaciology*, 46(152), 75-87.

Newman, B., Tanweer, A., & Kurttas, T. (2009). IAEA standard operating procedure for the liquid-water stable isotope analyser. *IAEA water resources programme.*

Nicolas, J. P., & Bromwich, D. H. (2011). Climate of West Antarctica and influence of marine air intrusions*. *Journal of Climate*, 24(1), 49-67.

Noone, D., & Simmonds, I. (2002). Annular variations in moisture transport mechanisms and the abundance of δ18O in Antarctic snow. *Journal of Geophysical Research: Atmospheres* (1984–2012), 107(D24), ACL-3.

Noone, D., & Simmonds, I. (2002). Associations between $\delta^{18}O$ of Water and Climate Parameters in a Simulation of Atmospheric Circulation for 1979-95. *Journal of Climate*, *15*(22), 3150-3169.

Noone, D. (2008). The influence of midlatitude and tropical overturning circulation on the isotopic composition of atmospheric water vapor and Antarctic precipitation. *Journal of Geophysical Research: Atmospheres (1984–2012)*,*113*(D4).

North Greenland Ice Core Project members. (2004). High-resolution record of Northern Hemisphere climate extending into the last interglacial period. *Nature*, v.431, No. 7005, pp. 147-151

NRC (National Research Council). 2002. *Abrupt Climate Change: Inevitable Surprises*. Washington, DC: National Academy Press.

NRC (National Research Council). 2013. *Abrupt Impacts of Climate Change: Anticipating Surprises.* Washington, DC: National Academy Press.

Nye, J. F. (1998). Diffusion of isotopes in the annual layers of ice sheets. *Journal of Glaciology*, *44*(148), 467-468.

O'Brien, K. (1979). Secular variations in the production of cosmogenic isotopes in the Earth's atmosphere. *Journal of Geophysical Research: Space Physics* (1978–2012), 84(A2), 423-431.

Osterberg, E. C., Handley, M. J., Sneed, S. B., Mayewski, P. A., & Kreutz, K. J. (2006). Continuous ice core melter system with discrete sampling for major ion, trace element, and stable isotope analyses. *Environmental science & technology*, 40(10), 3355-3361.

Otto‐Bliesner, B. L., Brady, E. C., Shin, S. I., Liu, Z., & Shields, C. (2003). Modeling El Niño and its tropical teleconnections during the last glacial‐interglacial cycle. *Geophysical Research Letters*, 30(23).

Park, J. (1992). *Envelope estimation for quasi-periodic geophysical signals in noise: A multitaper approach, in Statistics in the Environmental and Earth Sciences*, edited by A.T. Walden and P. Guttorp, 189-219, Edward Arnold, London.

Percival, D. B., & Walden, A. T. (1993). *Spectral Analysis for Physical Applications: Multitaper and Conventional Univariate Techniques* (Cambridge. Press, New York.

Peterson, L. C., Haug, G. H., Hughen, K. A., & Röhl, U. (2000). Rapid changes in the hydrologic cycle of the tropical Atlantic during the last glacial. *Science*, 290(5498), 1947-1951.

Petit, J. R., White, J. W. C., Young, N. W., Jouzel, J., & Korotkevich, Y. S. (1991). Deuterium excess in recent Antarctic snow. *Journal of Geophysical Research: Atmospheres* (1984–2012), 96(D3), 5113-5122.

Pisias, N. G., & Mix, A. C. (1997). Spatial and temporal oceanographic variability of the eastern equatorial Pacific during the late Pleistocene: Evidence from radiolaria microfossils. *Paleoceanography*, 12(3), 381-393.

Press, W. H.; Flannery, B. P.; Teukolsky, S. A.; and Vetterling, W. T. (1989). Fourier Transform of Discretely Sampled Data. *§12.1 in Numerical Recipes in FORTRAN: The Art of Scientific Computing*, 2nd ed. Cambridge, England: Cambridge University Press, pp. 494-498.

Rahmstorf, S. (2003). Timing of abrupt climate change: A precise clock. *Geophysical Research Letters*, *30*(10).

Ramseier, R. O. (1967). Self‐Diffusion of Tritium in Natural and Synthetic Ice Monocrystals. *Journal of Applied Physics*, *38*(6), 2553-2556.

Redman, C. L. (1978). *The rise of civilization: from early farmers to urban society in the ancient Near East*. San Francisco: WH Freeman.

Reijmer, C. H., Van den Broeke, M. R., & Scheele, M. P. (2002). Air Parcel Trajectories and Snowfall Related to Five Deep Drilling Locations in Antarctica Based on the ERA-15 Dataset*. *Journal of Climate*, 15(14), 1957-1968.

Rempel, A. W., Waddington, E. D., Wettlaufer, J. S., & Worster, M. G. (2001). Possible displacement of the climate signal in ancient ice by premelting and anomalous diffusion. Nature, 411(6837), 568-571.

Rempel, A. W., Wettlaufer, J. S., & Waddington, E. D. (2002). Anomalous diffusion of multiple impurity species: predicted implications for the ice core climate records. Journal of Geophysical Research: Solid Earth (1978–2012), 107(B12), ECV-3.

Rempel, A. W., & Wettlaufer, J. S. (2003). Isotopic diffusion in polycrystalline ice. *Journal of Glaciology*, *49*(166), 397-406.

Rial, J. A., & Saha, R. (2011). Modeling abrupt climate change as the interaction between sea ice extent and mean ocean temperature under orbital insolation forcing. *Abrupt Climate Change: Mechanisms, Patterns, and Impacts*, 57-74.

Rignot, E., Mouginot, J., Morlighem, M., Seroussi, H., & Scheuchl, B. (2014). Widespread, rapid grounding line retreat of Pine Island, Thwaites, Smith, and Kohler glaciers, West Antarctica, from 1992 to 2011. *Geophysical Research Letters*.

Robin, G. (1983). The climatic record from ice cores. *The climatic record in polar ice sheets*, 180-195.

Rodbell, D. T., Seltzer, G. O., Anderson, D. M., Abbott, M. B., Enfield, D. B., & Newman, J. H. (1999). An~ 15,000-year record of El Niño-driven alluviation in southwestern Ecuador. *Science*, 283(5401), 516-520.

Roe, G. (2006). In defense of Milankovitch. *Geophysical Research Letters*, 33(24).

Röthlisberger, R., Bigler, M., Hutterli, M., Sommer, S., Stauffer, B., Junghans, H. G., & Wagenbach, D. (2000). Technique for continuous high-resolution analysis of trace substances in firn and ice cores. *Environmental Science & Technology*, 34(2), 338-342.

Sandweiss, D. H., Maasch, K. A., Burger, R. L., Richardson, J. B., Rollins, H. B., & Clement, A. (2001). Variation in Holocene El Niño frequencies: Climate records and cultural consequences in ancient Peru. *Geology*, 29(7), 603-606.

Schilla, A. S. (2007). *The stable isotopes and deuterium excess from the Siple Dome ice core: implications for the late Quaternary climate and elevation history of the Ross Sea Region, West Antarctica.* ProQuest.

Schneider, D. P., Steig, E. J., & Comiso, J. C. (2004). Recent climate variability in Antarctica from satellite-derived temperature data. *Journal of Climate*, 17(7), 1569-1583.

Schneider, D. P., Steig, E. J., & Van Ommen, T. (2005). High-resolution ice-core stable-isotopic records from Antarctica: towards interannual climate reconstruction. *Annals of Glaciology*, 41(1), 63-70.

Schwabe, M. (1849). Solar sunspot cycle of 11 years. *Astron. Nachr*, 21, 234.

Schwander, J., Stauffer, B., & Sigg, A. (1988). Air mixing in firn and the age of the air at pore close-off. *Ann. Glaciol*, 10, 141-145.

Severinghaus, J. P., Bender, M. L., Keeling, R. F., & Broecker, W. S. (1996). Fractionation of soil gases by diffusion of water vapor, gravitational settling, and thermal diffusion. *Geochimica et Cosmochimica Acta*, 60(6), 1005-1018.

Shindell, D. T., Schmidt, G. A., Mann, M. E., Rind, D., & Waple, A. (2001). Solar forcing of regional climate change during the Maunder Minimum. *Science*, 294(5549), 2149-2152.

Shulmeister, J., & Lees, B. G. (1995). Pollen evidence from tropical Australia for the onset of an ENSO-dominated climate at c. 4000 BP. *The Holocene*, 5(1), 10-18.

Sigl, M., Cole-Dai, J. , Ferris, D., Fudge, T.J., McConnell, J.R., Welten, K., Winstrup, M., Woodruff, T.E., Brook, E.J., Buizert, C., Dunbar, N., Iverson, N., Koffman, B., Maselli, O.J., McGwire, K., Muscheler, R., Pasteris, D.R., Sowers Sowers, T.A. and Taylor, K. C., The WAIS-Divide deep ice core WD2014 chronology - Part 1: Annual layer counting (31-0 ka BP). *Climate of the Past Discussions* (in preparation)

SILSO, World Data Center (2015). Sunspot Number and Long-term Solar Observations, Royal Observatory of Belgium, on-line Sunspot Number catalogue: http://www.sidc.be/SILSO/, '1951-2003'

Solanki, S. K., Usoskin, I. G., Kromer, B., Schüssler, M., & Beer, J. (2004). Unusual activity of the Sun during recent decades compared to the previous 11,000 years. *Nature*, 431(7012), 1084-1087.

Souney, J. M., Twickler, M. S., Hargreaves, G. M., Bencivengo, B. M., Kippenhan, M. J., Johnson, J. A., Cravens, E. D., Neff, P. D., Nunn, R. M., Orsi, A. J., Popp, T. J., Rhoades, J. F., Vaughn, B. H., Voight, D. E., Wong, G. J., & Taylor12, K. C. (2014). Core handling and processing for the WAIS Divide ice-core project. *Annals of Glaciology*, 55, 68.

Steffensen, J. P., Andersen, K. K., Bigler, M., Clausen, H. B., Dahl-Jensen, D., Fischer, H., Goto-Azuma, K., Hansson, M., Johnsen, S. J., Jouzel, J., Masson-Delmotte, V., Popp, T., Rasmussen, S. O., Rothlisberger, R., Ruth, U., Stauffer, B., Siggaard-Andersen, M. L., Sveinbjornsdottir, A. E., Svensson, A., & White, J. W. (2008). High-resolution Greenland ice core data show abrupt climate change happens in few years. *Science*, 321(5889), 680-684.

Steig, E. J., Ding, Q., White, J. W. C., Kuttel, M., Rupper, S. B., Neumann, T. A., Neff, P. D., Gallant, A. J. E., Mayewski, P. A., Taylor, K. C., Hoffmann, G., Dixon, D. A., Schoenemann, S. W., Markle, B. R., Fudge, T. J., Schneider, D. P., Schauer, A. J., Teel, R. P., Vaughn, B. H., Burgener, L., Williams, J., & Korotkikh, E. (2013), Recent climate and ice-sheet changes in West Antarctica compared with the past 2,000 years, *Nature Geoscience*, 6(5), 372–375.

Stuiver, M. (1978). Radiocarbon timescale tested against magnetic and other dating methods. *Nature*, 273(5660), 271-274.

Suess, H. E. (1980). The radiocarbon record in tree rings of the last 8000 years. *Radiocarbon*, 22(2), 200-209.

Taylor, K. C., Mayewski, P. A., Alley, R. B., Brook, E. J., Gow, A. J., Grootes, P. M., ... & Zielinski, G. A. (1997). The Holocene-Younger Dryas transition recorded at Summit, Greenland. *Science*, 278(5339), 825-827.

Thomson, D. J. (1982). Spectrum estimation and harmonic analysis. *Proceedings of the IEEE*, 70(9), 1055-1096.

Thompson, D. W., & Wallace, J. M. (2000). Annular modes in the extratropical circulation. Part I: month-to-month variability*. *Journal of Climate*, 13(5), 1000-1016.

Torrence, C., & Compo, G. P. (1998). A practical guide to wavelet analysis. *Bulletin of the American Meteorological society*, 79(1), 61-78.

Tudhope, A. W., Chilcott, C. P., McCulloch, M. T., Cook, E. R., Chappell, J., Ellam, R. M., Lea, D. W., Lough, J. M., & Shimmield, G. B. (2001). Variability in the El Niño-Southern Oscillation through a glacial-interglacial cycle. *Science*, 291(5508), 1511-1517.

Turner, J. (2004). The El Niño–Southern Oscillation and Antarctica. *International Journal of Climatology*, 24(1), 1-31.

Turner, J., Phillips, T., Hosking, J. S., Marshall, G. J., & Orr, A. (2013). The Amundsen Sea low. *International Journal of Climatology*, 33(7), 1818-1829.

Urban, F. E., Cole, J. E., & Overpeck, J. T. (2000). Influence of mean climate change on climate variability from a 155-year tropical Pacific coral record. *Nature*, 407(6807), 989-993.

Vasiliev, S. S., & Dergachev, V. A. (2002). The~ 2400-year cycle in atmospheric radiocarbon concentration: bispectrum of 14 C data over the last 8000 years. In *Annales Geophysicae* (Vol. 20, No. 1, pp. 115-120).

Vaughn, B. H., White, J. W. C., Delmotte, M., Trolier, M., Cattani, O., & Stievenard, M. (1998). An automated system for hydrogen isotope analysis of water. *Chemical Geology*, 152(3), 309-319.

WAIS Divide Project Members. (2013). Onset of deglacial warming in West Antarctica driven by local orbital forcing. *Nature*, 500(7463), 440-444.

Wang, Y. J., Cheng, H., Edwards, R. L., An, Z. S., Wu, J. Y., Shen, C. C., & Dorale, J. A. (2001). A high-resolution absolute-dated late Pleistocene monsoon record from Hulu Cave, China. *Science*, 294(5550), 2345-2348.

Wang, X., Auler, A. S., Edwards, R. L., Cheng, H., Cristalli, P. S., Smart, P. L., Richards, D. A., & Shen, C. C. (2004). Wet periods in northeastern Brazil over the past 210 kyr linked to distant climate anomalies. *Nature*, 432(7018), 740-743.

Ward, M. N. (1998). Diagnosis and short-lead time prediction of summer rainfall in tropical North Africa at interannual and multidecadal timescales. *Journal of Climate*, 11(12), 3167-3191.

Weiss, H., Courty, M. A., Wetterstrom, W., Guichard, F., Senior, L., Meadow, R., & Curnow, A. (1993). The genesis and collapse of third millennium north Mesopotamian civilization. *SCIENCE-NEW YORK THEN WASHINGTON*-, 261, 995-995.

Wettlaufer, J. S. (1999). Impurity effects in the premelting of ice. *Physical Review Letters*, 82(12), 2516.

Whillans, I. M., & Grootes, P. M. (1985). Isotopic diffusion in cold snow and firn. *Journal of Geophysical Research: Atmospheres (1984–2012)*, *90*(D2), 3910-3918.

William, H. G. R., & Valdesa, P. J. (2015). On the tropical Pacific climate during the last 120 thousand years. *BRIDGE, School of Geographical Sciences, University of Bristol.* Bristol, England.

Xapsos, M. A., & Burke, E. A. (2009). Evidence of 6000-year periodicity in reconstructed sunspot numbers. *Solar Physics,* 257(2), 363-369.

Zebiak S. & Cane, M. A. (1987). Model ENSO. *Mon. Wea. Rev*., 115, 2262- 2278

Zhang, C. (1993). Large-scale variability of atmospheric deep convection in relation to sea surface temperature in the tropics. *Journal of Climate*, 6(10), 1898-1913.

Zheng, W., Braconnot, P., Guilyardi, E., Merkel, U., & Yu, Y. (2008). ENSO at 6ka and 21ka from ocean–atmosphere coupled model simulations. *Climate Dynamics*, 30(7-8), 745-762.

Zwally, H. J., & Gloersen, P. (1977). Passive microwave images of the polar regions and research applications. *Polar Record*, 18(116), 431-450.